2019

# HIDRAULICA

HYDRAULICS-PNEUMATICS-TRIBOLOGY-ECOLOGY-SENSORICS-MECHATRONICS

No. 4

ISSN 1453-7303
ISSN-L 1453-7303

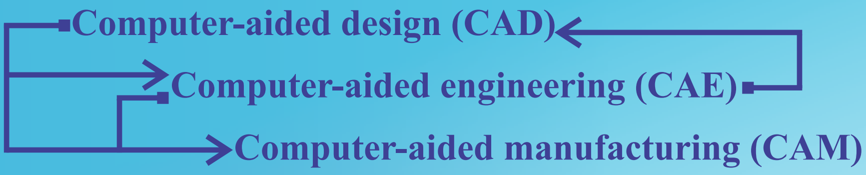

Computer-aided design (CAD)
Computer-aided engineering (CAE)
Computer-aided manufacturing (CAM)

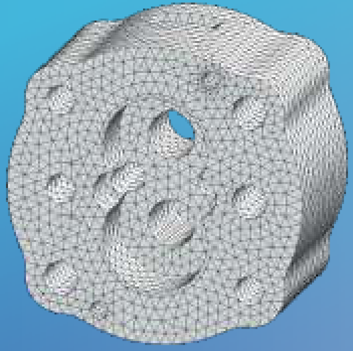

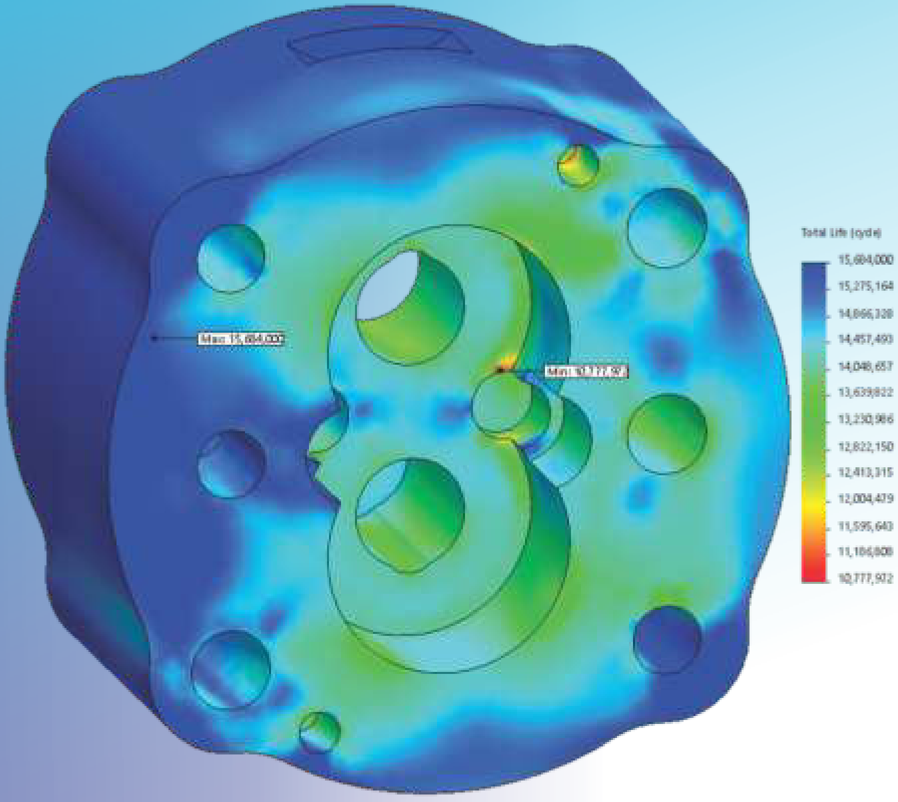

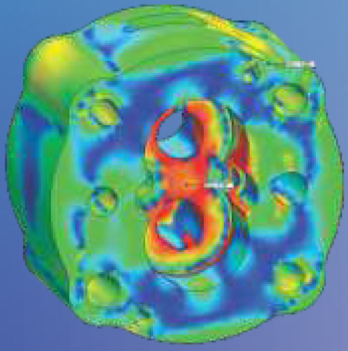

hidraulica.fluidas.ro

## CONTENTS

## BOARD

***MANAGING EDITOR***

- PhD. Eng. Petrin DRUMEA - Hydraulics and Pneumatics Research Institute in Bucharest, Romania

***EDITOR-IN-CHIEF***

- PhD.Eng. Gabriela MATACHE - Hydraulics and Pneumatics Research Institute in Bucharest, Romania

***EXECUTIVE EDITOR, GRAPHIC DESIGN & DTP***

- Ana-Maria POPESCU - Hydraulics and Pneumatics Research Institute in Bucharest, Romania

***EDITORIAL BOARD***

PhD.Eng. Gabriela MATACHE - Hydraulics and Pneumatics Research Institute in Bucharest, Romania
Assoc. Prof. Adolfo SENATORE, PhD. – University of Salerno, Italy
PhD.Eng. Cătălin DUMITRESCU - Hydraulics and Pneumatics Research Institute in Bucharest, Romania
Assoc. Prof. Andrei DRUMEA, PhD. – University Politehnica of Bucharest, Romania
PhD.Eng. Radu Iulian RĂDOI - Hydraulics and Pneumatics Research Institute in Bucharest, Romania
Assoc. Prof. Constantin RÂNEA, PhD. – University Politehnica of Bucharest; National Authority for Scientific Research and Innovation (ANCSI), Romania
Prof. Aurelian FĂTU, PhD. – Institute Pprime – University of Poitiers, France
PhD.Eng. Małgorzata MALEC – KOMAG Institute of Mining Technology in Gliwice, Poland
Prof. Mihai AVRAM, PhD. – University Politehnica of Bucharest, Romania
Lect. Ioan-Lucian MARCU, PhD. – Technical University of Cluj-Napoca, Romania

***COMMITTEE OF REVIEWERS***

PhD.Eng. Corneliu CRISTESCU – Hydraulics and Pneumatics Research Institute in Bucharest, Romania
Assoc. Prof. Pavel MACH, PhD. – Czech Technical University in Prague, Czech Republic
Prof. Ilare BORDEAȘU, PhD. – Politehnica University of Timisoara, Romania
Prof. Valeriu DULGHERU, PhD. – Technical University of Moldova, Chisinau, Republic of Moldova
Assist. Prof. Krzysztof KĘDZIA, PhD. – Wroclaw University of Technology, Poland
Prof. Dan OPRUȚA, PhD. – Technical University of Cluj-Napoca, Romania
PhD.Eng. Teodor Costinel POPESCU - Hydraulics and Pneumatics Research Institute in Bucharest, Romania
PhD.Eng. Marian BLEJAN - Hydraulics and Pneumatics Research Institute in Bucharest, Romania
Assoc. Prof. Ph.D. Basavaraj HUBBALLI - Visvesvaraya Technological University, India
Ph.D. Amir ROSTAMI – Georgia Institute of Technology, USA
Prof. Adrian CIOCĂNEA, PhD. – University Politehnica of Bucharest, Romania
Prof. Carmen-Anca SAFTA, PhD. - University Politehnica of Bucharest, Romania
Assoc. Prof. Mirela Ana COMAN, PhD. – Technical University of Cluj-Napoca, North University Center of Baia Mare, Romania
Ph.D.Eng. Mihai HLUȘCU – Politehnica University of Timisoara, Romania
Prof. Ion PIRNĂ, PhD. – The National Institute of Research and Development for Machines and Installations Designed to Agriculture and Food Industry - INMA Bucharest, Romania
Assoc. Prof. Constantin CHIRIȚĂ, PhD. – “Gheorghe Asachi” Technical University of Iasi, Romania

***Published by:***
***Hydraulics and Pneumatics Research Institute, Bucharest-Romania***
Address: 14 Cuţitul de Argint, district 4, Bucharest, 040558, Romania
Phone: +40 21 336 39 91; Fax: +40 21 337 30 40; e-Mail: ihp@fluidas.ro; Web: www.ihp.ro
***with support from:***
***National Professional Association of Hydraulics and Pneumatics in Romania - FLUIDAS***
e-Mail: fluidas@fluidas.ro; Web: www.fluidas.ro

**HIDRAULICA Magazine** is indexed by international databases

**ISSN 1453 – 7303; ISSN – L 1453 – 7303**

# EDITORIAL

## Who Evaluates the Evaluators?

Ph.D.Eng. Petrin DRUMEA
MANAGING EDITOR

It seems that the main element for the advancement of society on the scale of technology and science has been, to a large extent, the distribution of funds from national assets to the specialists who managed to convince that their ideas are valuable and will lead to high impact results. The criteria for allocating funds were either discretionary, when a person or a group have taken the right to select the ideas to be funded, or a theoretically better solution was reached by which groups of expert evaluators were established to decide what is good and what is not.

The solution of selection made by evaluators selected from among specialists is a correct one, but it implies the existence of precise criteria and a base of specialists who have proven their expertise in various technical and scientific issues. The hope that a theoretician can make the right decisions in production development programmes, or a machine tool specialist can decide what would be best for the aviation industry is illusive, if not fully dangerous. Therefore, a first problem would be to find the right specialists for each field.

A second major problem is to set clear criteria specific to the programme under discussion. I do not think that it is useful for the number and type of articles to be the main criterion neither in an industrial development programme nor when selecting evaluators in the same idea.

Obviously, for the first problem things are complicated, I can even say with no solution in the short term, because it is difficult to find the specialists able to make a correct assessment and be willing to participate in such a difficult process. Maybe one should work on the remuneration process and the involvement of professional associations to help the programme coordinators in selecting the evaluators.

For the second problem, things are easier to solve because it is not so difficult for evaluation criteria specific to each programme and not some general ones to be established by specialists. In principle, one should give up the idea of the omniscient specialist, who actually has little in common with the programme that he / she will have to evaluate.

In the end, the natural question is who selects the evaluators, or, in most situations, who evaluates the evaluators randomly introduced in the list of evaluators, regardless of the type of programme? It would be extremely unpleasant to find that there is no such assessment, or it is replaced by a selection procedure that regards only the tradition, or, even worse, the relational system.

I wish all of you a better new year!

P. Drumea

**ISSN 1453 – 7303** **“HIDRAULICA” (No. 4/2019)**
**Magazine *of Hydraulics, Pneumatics, Tribology, Ecology, Sensorics, Mechatronics***

# Examining Centrifugal Pump on Cavitation

Assist. Prof. PhD. Stud. Eng. **Nikolett FECSER**[1]**,** Senior Seal System Project and Standardization Eng. **Balázs SÁRA**[2]**,** Associate. Prof. PhD. **Rajmund KUTI**[3]

[1] Széchenyi István University, Department of Mechatronics and Machine Design H-9026 1 Egyetem tér, Győr, fecser.nikolett@sze.hu

[2] FLOWSERVE HUNGARY SERVICE, H-1097 6/b Gubacsi út, Budapest, bsara@flowserve.com

[3] Széchenyi István University, Department of Mechatronics and Machine Design, H-9026 1 Egyetem tér, Győr, kuti.rajmund@sze.hu

***Abstract:*** *Pumps influence all our lives directly or indirectly. Pumps are one of the most well-known and widespread type of a machine. Their task is to move fluid from one place to another, generally from a lower place to a higher one in a certain distance. For the safe operation of the pumps, it is essential to examine the operating parameters. The majority of specialists who are experts in pump technologies are familiar with cavitation. They are aware of its detrimental effects. Firstly, in our study we will briefly present the cavitation as a phenomenon. We will briefly present the place of measurement. Then we state the results of our measurements carried out type BKS 300. Finally, we present regression calculation for BKS 300 type pump for H-NPSH curve. Our goal is to call attention to the proper way of operating centrifugal pumps, the cavitation generated during operation as a harmful phenomenon and its development examined in practice by us.*

***Keywords:*** *Pumps, cavitation, operating parameters, regression, H-NPSH curve*

## 1. Introduction

Our literature research aiming at determining cavitation has revealed several definitions in use. Until the 1970s, cavitation did not have a common definition. According to Ackeret’s definition (1930), the formation of vapour cavities (bubbles) in a liquid occurs when the pressure at a given point of the flow compared to a given pressure reaches the saturated-water-vapour pressure belonging to the given fluid temperature. Then the fluid starts boiling and due to the formation of bubbles, it turns into a heterogeneous mixture of vapour-fluid phase [1].

As Knapp-Daily–Hammitt (1970) defined, cavitation is a phenomenon in which bubbles grow in the stationary or moving fluid and this growing phase is followed by a collapse phase. If the collapse of the bubbles fails to happen, due to gas release and vapourisation affecting the growing phase, effervescence or boiling occur. Accordingly, we make a distinction between gaseous and vaporous cavitation, which mainly differ in their damaging effect on the material. Gaseous cavitation precedes vaporous cavitation. At a given pressure, bubbles start growing under the influence of the gases dissolving from the fluid. Reaching a critical size, their static equilibrium gets imbalanced and they start a quick growing phase. This is vaporous cavitation, which has a damaging effect [2]. István Józsa (2013) claims that the physical process of cavitation is linked to the phenomenon of the boiling point, because if “saturated steam pressure” corresponding to the temperature develops at a given location in the flowing fluid, there the fluid turns into vapour and a bubble filled with steam evolves. The head space of the bubble is condensed if the flow travels the vapour cavity (i.e. bubble) into a location of higher pressure and the bubble implodes as a result of the thus created space. This bubble implosion is called cavitation [3]. As Tamás Lajos defined, when the pressure in a fluid flowing in a pump decreases to the level of saturated steam pressure, steam bubbles/voids evolve. When these bubbles travel to a place of higher pressure, the steam condenses and the bubbles implode causing significant damage on the surface of the nearby solid object. The formation and implosion of the bubbles are called cavitation, while the damage is cavitation erosion [4].

## 2. Ganz hydro-plant laboratory

In the Ganz hydro-plant laboratory there is an open and a closed test loop.
The measurements feasible in the open test loop are the following:

- Measurement on a pool with a weir
- Measurement on a pool with an induction device
- Measurement in measurement wells

The weir is applied for doing measurements with high volume pumps. This range is between 3.5 - 10 $m^3/s$. The drawback of a weir is that its difference in water level is a limit under which heads cannot be measured. The induction devices are the size of NA200, 300, 400 and 600, meaning that below 3.5 $m^3/s$ flowrate these devices are used since their loss is insignificant but they are relatively precise.
At the measurement well machines of studs with 100-400 mm can generally be examined. Cavitation breakdowns can also be examined by reducing the water level in the well. At the measurement wells, it is important to ensure that during the cavitation measurement the pump is provided with a smooth and bubbleless flow from the well water getting deeper and deeper.

Figure 1 shows the closed test loop of the Ganz factory, which was put into operation in 2012.

**Fig. 1.** The closed test loop of the Ganz factory

Besides low energy input, in order to be cavitated easily, the test machine is placed at the highest point of the 5 m high scaffold of the closed test loop. The figure shows the model of the cooling pumps of the Rostov Nuclear Power Plant installed in horizontal shaft arrangement. In the background, the tank on the suction side can be seen. The pump draws from here. In this tank, it is not recommended the vacuum to drop under 2 vom absolute pressure because air secession becomes intense and the operation water becomes “gassy”, which ruins the cavitation measurement. The circulator can never cavitate as it would interfere the measurement. For this reason, it is installed at about 2 metres deep in the pool.

## 3. Steps of measurement of BKS 300 type pump

In parallel with closing the sliding valves on the suction side, we open the one on the discharge side. This makes the flow rate constant. In our case, the only alteration from the conventional cavitation measurement was that a supply pump got built into the suction side (needed because of low water level) [5].

Table 1 shows the measured and readings values.

**Table 1:** Measured values/Readings

| **Name** | **Labels** | **Unit of Measure** |
|---|---|---|
| Time of Measurement | t | hh:mm |
| Revolution per minute | n | rpm |
| Flow rate | $Q_m$ | $m^3/h$ |
| Height difference between the centre lines of the tube entering the pressure gauge and the suction tube | $Z_m$ | m |
| Absolute suction pressure | $p_{m1}$ | kPa |
| Absolute discharge pressure | $p_{m2}$ | kPa |
| Absorbed electrical power | $P_{electric}$ | kW |
| Water temperature | $T_w$ | °C |
| Ambient temperature | $T_a$ | °C |
| Electric motor's efficiency | $\eta_{motor}$ | % |

Table 2 shows the calculated values.

**Table 2:** Calculated values

| **Name** | **Labels** | **Unit of Measure** |
|---|---|---|
| Water density | ϱw | $kg/m^3$ |
| Saturated vapour pressure | Ps | Pa |
| Flow rate | Qc | $m^3/s$ |
| Inlet flow velocity | vm1 | m/s |
| Outlet flow velocity | vm2 | m/s |
| Delivery head calculated at measured rpm | Hc | m |
| NPSH at measured rpm | $\Delta h_c(NPSH_c)$ | m |
| Calculated shaft power | $P_{mech}$ | kW |
| Aggregate performance | $P_{agg}$ | kW |
| Pump's Best Efficiency Point | $\eta_{pump}$ | % |
| Aggregate Efficiency | $\eta_{agg}$ | % |
| Converted delivery head | H | m |
| Converted NPSH | Δh(NPSH) | m |
| Converted flow rate | Q | $m^3/h$ |
| Converted shaft power | P | kW |

Inlet flow velocity

$$v_{m1} = \frac{Q_C}{\left(\frac{d_1}{1000}\right)^2 * \pi/4} \tag{1}$$

Outlet flow velocity

$$v_{m2} = \frac{Q_C}{\left(\frac{d_2}{1000}\right)^2 * \pi/4} \tag{2}$$

Delivery head calculated at measured rpm

$$\mathrm{H_c} = 0{,}102 * \frac{\mathrm{p_{m2}} * 1000 - \mathrm{p_{m1}} * 1000}{\varrho\mathrm{w}} + 0{,}827 * \mathrm{Q_c^2} * \left(\frac{1}{\mathrm{d_2^4}} - \frac{1}{\mathrm{d_1^4}}\right) + \mathrm{Z_m} \tag{3}$$

NPSH at measured rpm

$$\Delta \mathrm{h_c}(\mathrm{NPSH})_\mathrm{c} = 0{,}102 * \frac{\mathrm{p_{m1}} * 1000 + \mathrm{P_a} - \mathrm{P_s}}{\varrho_\mathrm{w}} + 0{,}827 * \mathrm{Q_c^2} * \frac{1}{\mathrm{d_1^4}} + \mathrm{Z_m} \qquad (4)$$

Calculated shaft power

$$\mathrm{P_{mech}} = \frac{\mathrm{P_{mech}}}{100} * \eta_{\eta\mathrm{motor}} \qquad (5)$$

Pump Efficiency

$$\eta_\mathrm{pump} = 0{,}981 * \mathrm{Q_c} * \frac{\mathrm{H_c}}{\mathrm{P_{mech}}} \qquad (6)$$

Aggregate Efficiency

$$\eta_{agg} = \eta_{\eta motor} * \frac{\eta_{pump}}{100} \qquad (7)$$

Converted delivery head

$$\mathrm{H} = H_c * \left(\frac{n}{n_{guar}}\right)^2 \qquad (8)$$

Converted NPSH

$$\Delta h(NPSH) = \Delta h_c(NPSH)_c * \left(\frac{n}{n_{guar}}\right)^2 \qquad (9)$$

Converted flow rate:

$$\mathrm{Q} = Q_c * \left(\frac{n}{n_{guar}}\right) * 3600 \qquad (10)$$

Converted shaft power:

$$\mathrm{P} = P_{mech} * \left(\frac{n}{n_{guar}}\right)^3 \qquad (11)$$

## 4. Presenting measurement results

Table 3 shows the readings.

**Table 3:** Readings

| No. | Readings | | | | | | | | | |
|---|---|---|---|---|---|---|---|---|---|---|
| | t | n | Qm | Zm | pm1 | pm1 | Pelectric | Tw | Ta | ηmotor |
| | h/min | rpm | m3/h | m | kPa | kPa | kW | ° C | ° C | % |
| 1 | 10:03 | 1491 | 1300 | -0.095 | 138.9 | 584.4 | 207.9 | 21.9 | 24.1 | 93.0 |
| 2 | 10:12 | 1491 | 1300 | -0.095 | 46.9 | 494.1 | 207.5 | 21.9 | 24.1 | 93.0 |
| 3 | 10:17 | 1492 | 1303 | -0.095 | 5.6 | 452.7 | 207.9 | 21.9 | 24.1 | 93.0 |
| 4 | 10:21 | 1491 | 1301 | -0.095 | -35.0 | 412.2 | 207.8 | 21.9 | 24.1 | 93.0 |
| 5 | 10:27 | 1492 | 1300 | -0.095 | -39.8 | 406.8 | 207.8 | 21.9 | 24.1 | 93.0 |
| 6 | 10:32 | 1492 | 1300 | -0.095 | -47.8 | 392.3 | 207.8 | 21.9 | 24.1 | 93.0 |
| 7 | 10:40 | 1491 | 1300 | -0.095 | -53.7 | 382.5 | 206.7 | 21.9 | 24.1 | 93.0 |
| 8 | 10:51 | 1491 | 1300 | -0.095 | -57.7 | 365.6 | 205.7 | 21.9 | 24.1 | 93.0 |
| 9 | 11:04 | 1491 | 1300 | -0.095 | -61.7 | 333.2 | 201.8 | 21.9 | 24.1 | 93.0 |
| 10 | 11:10 | 1491 | 1302 | -0.095 | -62.5 | 262.3 | 188.4 | 21.9 | 24.1 | 93.0 |

Table 4 shows the calculated values.

**Table 4:** Calculated values

| No. | Calculated values | | | | | | | | | | |
|---|---|---|---|---|---|---|---|---|---|---|---|
| | **ϱw** | **ps** | **Qc** | **vm1** | **vm2** | **Hc** | **Δhc** | **Pmech** | **Pagg** | **ηpump** | **ηagg** |
| | kg/m3 | Pa | m3/s | m/s | m/s | m | m | kW | kW | % | % |
| 1 | 997.7 | 2642 | 0.3611 | 5.1087 | 5.1087 | 44.5 | 23.4 | 193.3 | 207.9 | 81.4 | 75.7 |
| 2 | 997.7 | 2642 | 0.3611 | 5.1087 | 5.1087 | 44.7 | 14.0 | 193.0 | 207.5 | 81.9 | 76.2 |
| 3 | 997.7 | 2642 | 0.3619 | 5.1205 | 5.1205 | 44.7 | 9.7 | 193.3 | 207.9 | 81.9 | 76.2 |
| 4 | 997.7 | 2642 | 0.3614 | 5.1126 | 5.1126 | 44.7 | 5.6 | 193.3 | 207.8 | 819 | 76.1 |
| 5 | 997.7 | 2642 | 0.3611 | 5.1087 | 5.1087 | 44.7 | 5.1 | 193.3 | 207.8 | 81.7 | 76.0 |
| 6 | 997.7 | 2642 | 0.3611 | 5.1087 | 5.1087 | 44.0 | 4.3 | 193.3 | 207.8 | 80.5 | 74.8 |
| 7 | 997.7 | 2642 | 0.3611 | 5.1087 | 5.1087 | 43.6 | 3.7 | 192.2 | 206.7 | 80.2 | 74.6 |
| 8 | 997.7 | 2642 | 0.3611 | 5.1087 | 5.1087 | 42.3 | 3.3 | 191.3 | 205.7 | 78.1 | 72.6 |
| 9 | 997.7 | 2642 | 0.3611 | 5.1087 | 5.1087 | 39.4 | 2.9 | 187.7 | 201.8 | 74.2 | 69.0 |
| 10 | 997.7 | 2642 | 0.3617 | 5.1165 | 5.1165 | 32.2 | 2.8 | 175.2 | 188.4 | 65.1 | 60.5 |

Table 5 shows Converted values.

**Table 5:** Converted values

| No. | Converted values | | | |
|---|---|---|---|---|
| | H | Δh | Q | P |
| 1 | 44.2 | 23.2 | 1294.8 | 191.0 |
| 2 | 44.4 | 13.8 | 1294.8 | 190.7 |
| 3 | 44.3 | 9.6 | 1269.9 | 190.6 |
| 4 | 44.4 | 5.5 | 1295.8 | 190.9 |
| 5 | 44.2 | 5.0 | 1293.9 | 190.5 |
| 6 | 43.6 | 4.2 | 1293.9 | 190.5 |
| 7 | 43.2 | 3.6 | 1294.8 | 189.9 |
| 8 | 41.9 | 3.2 | 1294.8 | 189.0 |
| 9 | 39.1 | 2.8 | 1294.8 | 185.4 |
| 10 | 32.0 | 2.8 | 1296.8 | 173.1 |

Table 6 shows the Measuring instruments’ accuracy errors.

**Table 6:** Measuring instruments’ accuracy errors

| **Amount of Delivered Water** | **Symbol** | **Measurement accuracy** |
|---|---|---|
| Measuring instrument’s accuracy | | |
| Delivery Height | H | ±0.1% |
| Amount of Delivered Water | Q | ±0,2% |
| Shaft torque | M | ±0.1% |
| Revolution per minute | n | ±0.05% |
| Operation water temperature | Tw | ±0,1C° |
| Atmospheric pressure | Pa | ±0.5 mbar |
| Suction pressure | p1 | ±0.1% |

Figure 2 shows the H-NPSH curve.

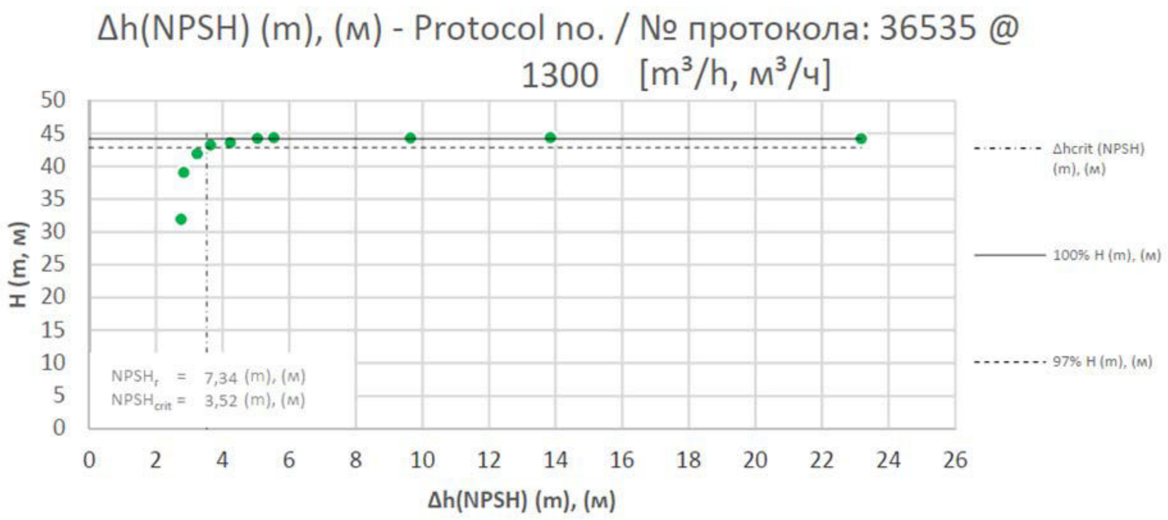

**Fig. 2.** H-NPSH curve

## 5. Regression calculation for BKS 300 type pump for H-NPSH curve

In regression analysis we use the term non-linear regression calculation when the relationship between dependent and independent variables cannot be described by a linear function. In this case, a curve line fits the dots the best. The procedure for finding the equation of the curve that fits the set of points best is called a curve fitting. In practice, Measurement data is used in different ways. If we know the shape of the physical quantity with which it can be described and function parameters are called by a function fit, this is called regression. In the case of regression, we determine the parameters of the best-fit function.

Preferably selected nonlinear functions are:

- logarithmic
- polynomial
- exponential
- hyperbolic
- exponential

Based on measurements by Ganz, I determined an exponential function.
Based on the measured data I determined and plotted an exponential function, which fits to the measured data. I used Python for curve fitting.

An exponential equation from the measurement data:

$$f(x) = A \cdot \left(1 - e^{-\theta \cdot (x - x_0)}\right) \tag{12}$$

Figure 3 shows a curve fitting using the Pyton software package. The curve fits well with the measurement points.

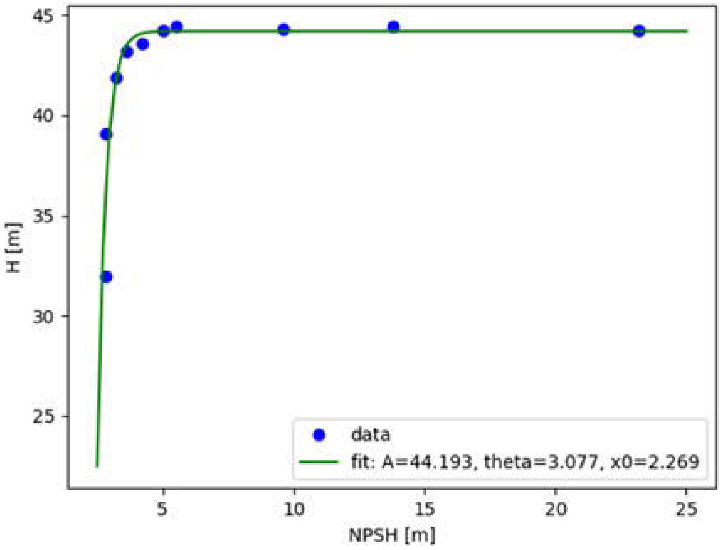

**Fig. 3.** Exponential function fitting

## 6. Conclusions

The scientific examination of cavitation assists manufacturers and users to avoid this undesirable phenomenon. Its possible solution is to determine the NPSH parameter and to take it into account when you are choosing and installing the pump and during its operation. In my study I presented Ganz hydro-plant laboratory and I described the measurement results carried out by a BKS 300 type pump. It is important to note that measurements during operation we were carried out under standard conditions. Based on the measured data I determined and plotted an exponential function, which fits to the measured data. I used Python for curve fitting. The curve fits well with the measurement points.

### References

[1] Ackeret, J. *Cavitation, Handbook of Experimental Physics / Kavitation, Handbuch der Experimentalphysik*. Leipzig, Akademische Verlagsgesellschaft, 1931.
[2] Knapp, Robert T., James W. Daily, and Frederick G. Hammitt. *Cavitation*. New York, McGraw-Hill Book Company, 1970.
[3] Józsa, I. *Vortex pumps in practice / Örvényszivattyúk a gyakorlatban*. Budapest, Invest-Marketing Bt., 2013, pp. 10-128.
[4] Lajos, T. *Fundamentals of hydrodynamics / Az áramlástan alapjai.* Mackensen Kft., 2008, p. 31.
[5] Fecser, Nikolett. "Examining Fire Pump Nocchi CB8038T on Cavitation." *Periodica Polytechnica Transportation Engineering* (2018): 1-5.
[6] Sara, B. Annex 3 of test report. Budapest, 2018.

# The Influence of the Fluid Nature on the Driving Power of a Rotating Volumetric Pump with Profiled Rotors

PhD Student **Mariana Mirela STOICAN (PRISECARU)**[1], Prof. Dr. Eng. **Nicolae BĂRAN**[1],
PhD Student **Almaslamani Ammar Fadhil SHNAWA**[1], Sl. Dr. Eng**. Mihaela CONSTANTIN**[1]

[1] University Politehnica of Bucharest, i.mihaelaconstantin@gmail.com

***Abstract:*** *The term rotating volumetric machine with profiled rotors refers to the following:*
*- The constructive solution of the rotating machine can be used as a force machine (steam engine, pneumatic engine);*
*- Or it can be used as a working machine (pump, fan, and compressor).*
*The constructive solution and the operation mode of the volumetric pump with profiled rotors are presented, and based on the functional parameters (speed and flow rate) the correlation between the driving power and the conveyed fluid nature is established.*
*The data obtained theoretically are verified by means of an experimental installation built for this purpose.*

***Keywords:*** *Volumetric pump, profiled rotors.*

## 1. The constructive solution and the operation of a volumetric pump with profiled rotors

The rotating machine can convey clean or suspended liquids, multiphase fluids, wastewater, rheological fluids, gases, vapours, etc.

In this paper it was considered that the machine functions as a rotating volumetric pump with profiled rotors that convey water, engine oil.

The rotating volumetric pump with profiled rotors is composed (figure 1) of two profiled rotors (2), which rotate at the same speed inside a case (1); the profiled rotors are engaged by two gear wheels (7), thus ensuring their synchronization. The gear wheels are mounted on the outside of the pump on the shafts of the two rotors [1] [2].

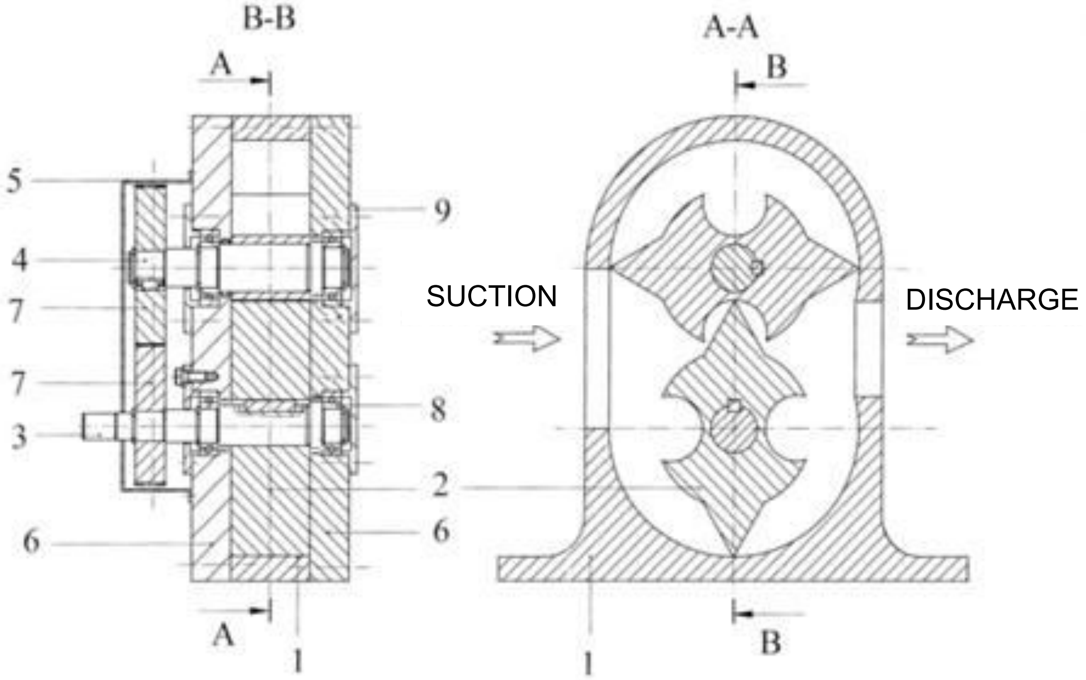

**Fig. 1.** Constructive solution of the rotating volumetric pump with profiled rotors
1 - oval case; 2 - profiled rotor; 3 - driving shaft; 4 - driven shaft; 5 - oil box; 6 - side wall; 7 - gear wheel; 8 - bearing; 9 - bearing cover

Figure 2 shows the operating mode of the rotating volumetric pump with profiled rotors. One can observe that after a rotation of 180 ° the useful volume of the transported fluid ($V_u$), is discharged into the chamber (8).

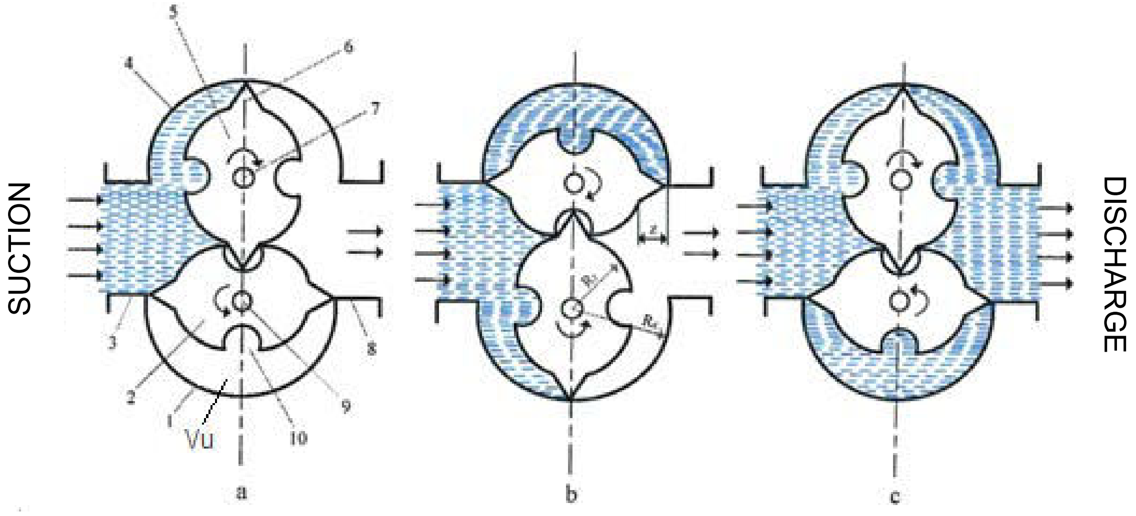

**Fig. 2.** Position of the rotors after a rotation of 90 °
1 - lower case; 2 - lower rotor; 3 - the suction chamber; 4 - upper case; 5 - upper rotor; 6 - rotating piston; 7 - driven shaft; 8 - discharge chamber; 9 - driving shaft; 10 - cavity in which the piston of the upper rotor enters

The useful volume is the volume between two pistons and the case (figure 2.a).

## 2. Calculation relations for the determination of the volumetric flow rate and the driving power of the pump

When operating as a rotating volumetric pump with profiled rotors, at a complete rotation of the shaft (9) two volumes will be transported from suction to discharge [3] [4] [5]:

$$V_u = \left(\pi R_c^2 - \pi R_r^2\right)\cdot l\left[m^3 / rot\right] \tag{1}$$

where l - the length of the rotor [m].
Case radius ($R_c$) is the sum of rotor radius ($R_r$) and piston height (z):

$$R_c = R_r + z\left[m\right] \tag{2}$$

The flow rate conveyed by a rotor is obtained:

$$\dot{V} = \pi l z\left(z + 2R_r\right)\cdot \frac{n}{30}\left[m^3 / s\right] \tag{3}$$

One can observe that the volumetric flow rate increases linearly with the length (l), with the rotor radius ($R_r$) and with the speed (n).
For the volumetric pump with profiled rotors the theoretical driving power is obtained with the relation [6] [7]:

$$P = \dot{V}\cdot \Delta p\left[W\right] \tag{4}$$

$$\Delta p = \rho_l \cdot g \cdot H\left[N / m^2\right] \tag{5}$$

* $\dot{V}$ – volumetric flow rate [$m^3$ / s];
* $\Delta p$ - pressure increase [N / $m^2$];
* $\Delta H$ - pumping height [m];

* $\rho_l$ - the density of the conveyed fluid [kg / m$^3$].
Replacing the flow rate in relation (3) one can obtain:

$$P_m = \pi l z\left(z+2R_r\right)\cdot\frac{n}{30}\cdot\rho_l\cdot g\cdot H\left[W\right] \tag{6}$$

It is observed that $P_m = f(l, z, R_r, n, \rho_l, \Delta H)$. (7)

### 3. Determination of the fluid nature influence on the driving power of a rotating volumetric pump with profiled rotors

For the experimental installation the following are specified:
- l = 0.05 m; z = 0.03 m; $R_r$ = 0.05 m;
- machine speed n: 200, 300, 400, 500 [rot / min];
- the working fluid is water and engine oil [5] [8]:
- $\rho_{H2O} = 10^3$ [kg/m$^3$];
- $\rho_u = 0.9 \cdot 10^3$ [kg /m$^3$].

### 3.1 Calculation of the driving power of the volumetric pump for the two fluids

### I. The working fluid is water

$$P_{H_2O} = \pi l z\left(z+2R_r\right)\cdot\frac{n}{30}\cdot\rho_{H_2O}\cdot g\cdot H\left[W\right] \tag{8}$$

For the speed of 200 rpm:

$$P_{H_2O} = 3.14\cdot0.05\cdot0.03\cdot\left(0.03+2\cdot0.05\right)\cdot200/30\cdot10^3\cdot9.81\cdot4 \;=\; 160.18\left[W\right]$$

Performing the calculations, the data from table 1 are similarly obtained.

**Table 1:** The values of the theoretical driving power of the pump

| n [rot/min] | 200 | 300 | 400 | 500 |
|---|---|---|---|---|
| $P_{H_2O}$ [W] | 160.18 | 240.27 | 320.36 | 400.44 |

Based on the data in the table, the function $P_{H_2O}$ = f (n) was graphically constructed for the conveyed liquid, the water (figure 3).

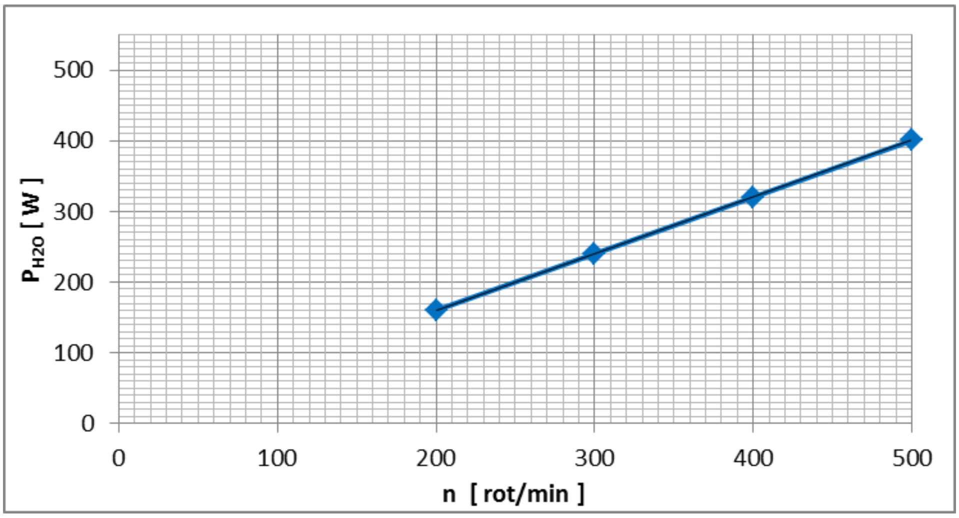

**Fig. 3.** The theoretical driving power of the pump function the speed of the rotating machine

From figure 3 one can observe that the dependence $P_{H_2O}$ = f (n) is a linear function.

**II. The working fluid is engine oil**

The relationship (6) becomes:

$$P_u = \pi lz\left(z + 2R_r\right)\cdot\frac{n}{30}\cdot\rho_u\cdot g\cdot H\left[W\right] \tag{9}$$

For the speed of 200 rpm:

$$P_u = 3.14\cdot 0.05\cdot 0.03\cdot\left(0.03 + 2\cdot 0.05\right)\cdot 200/30\cdot 0.9\cdot 10^3\cdot 9.81\cdot 4 \;=\; 144.16\left[W\right]$$

Performing the calculations, the data in table 2 are similarly obtained.

**Table 2:** The values of the theoretical driving power of the pump

| n [rot/min] | 200 | 300 | 400 | 500 |
|---|---|---|---|---|
| $P_u$[W] | 144.16 | 216.24 | 288.32 | 360.40 |

Based on the data in the table 2, the function $P_u$= f (n) was graphically constructed for the conveyed liquid, the engine oil (figure 4).

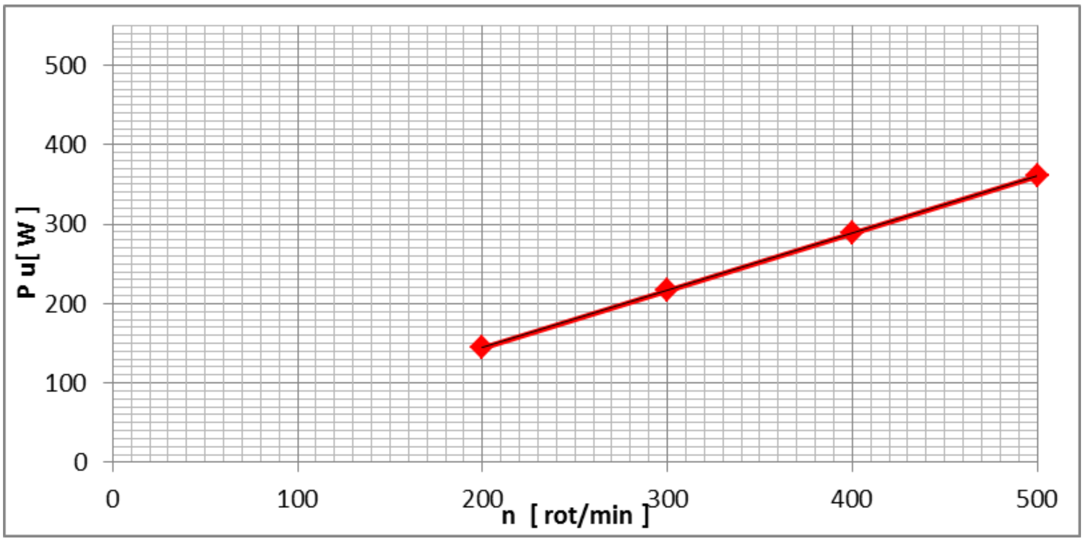

**Fig. 4.** The theoretical driving power of the pump function the speed of the rotating machine

The data for the theoretical driving power of the pump for the two fluids are presented in table 3.

**Table 3:** The values of the theoretical driving power of the pump depending on the conveyed fluid

| **n** [rot/min] | 200 | 300 | 400 | 500 |
|---|---|---|---|---|
| $P_{H_2O}$ [W] | 160.18 | 240.27 | 320.36 | 400.44 |
| $\mathbf{P_u}$ [W] | 144.16 | 216.24 | 288.32 | 360.40 |

Based on the data in table 3, the graph in figure 5 was plotted.

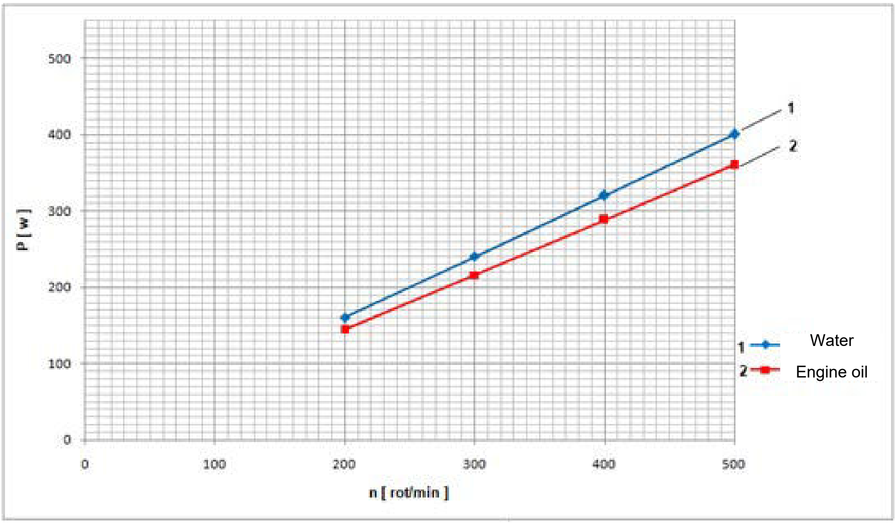

**Fig. 5.** Theoretical driving power depending on the speed of the rotating machine and the conveyed liquid nature

From figure 5 one can observe that the theoretical driving power of the pump has lower values in the case when the fluid conveyed is engine oil, this because the $\rho_{oil} < \rho_{water}$.

## 4. Experimental researches

### 4.1 Sketch of the experimental installation

Figure 6 shows the sketch of the experimental installation. This installation was developed, designed and built to validate the theoretical results previously presented [9] [10] [11].

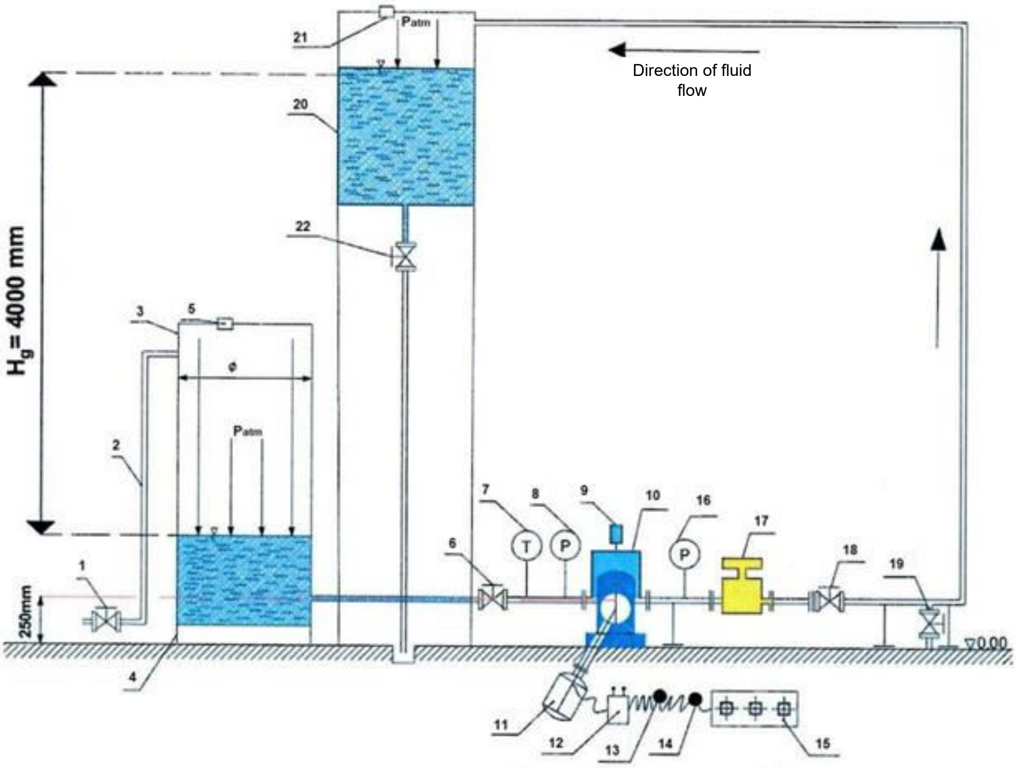

**Fig. 6.** The sketch of the experimental installation
1-tap; 2-pipe; 3- water tank; 4- the water tank support; 5- air vent; 6- valve Dn 60 Pn 2 bar; 7- thermometer; 8- pump suction manometer; 9- differential pressure manometer; 10-volumetric pump; 11 - electric motor; 12- frequency converter; 13-ampermeter; 14-multimeter; 15 - AC 380 V; 16- manometer at pump discharge, 17- electromagnetic flow meter, 18- adjusting valve, 19- drain valve; 20 - water tank; 21- air vent; 22 - drain tap.

The experimental installation consists of a tank (3) from which the working fluid (water, engine oil) is aspired in by a rotating volumetric pump with profiled rotors (10), driven by an electric motor (11) whose speed is controlled by a frequency converter (20).

### 4.2 Experimental obtained results

For the two types of fluids the voltage (U) and the intensity of the electric current (I) were measured at the rotational speed variation from 200 to 500 rot / min [12] [13].
The active power absorbed by the electric motor ($P_{me}$) is calculated with the relation [14]:

$$P = \sqrt{3}\ U.\ I\cos\phi[W] \tag{10}$$

Where:
U- electrical voltage [V]
I - current intensity [A]
cosφ - power factor of the electric motor
From supplier data (UMEB) cosφ = 0.71.
The power at the electric motor torque is calculated by the relation [15]:

$$P_{c,me} = P_{me} \cdot \eta_{me}\ \ [W] \tag{11}$$

where:
$P_{c,\,me}$ - the power at the torque of the electric motor [W];
$P_{me}$ - the active power absorbed by the electric motor [W];
$\eta_{me}$ - efficiency of the electric motor.
$\eta_{me}$ = 74.7%.

### I. The values of the measured quantities and the calculation obtained results when the fluid conveyed is water

For the speed of 200 rpm:

$$P = \sqrt{3}\ U.\ I\cos\phi = 1.73\ \cdot 0.75 \cdot 384.7 \cdot 0.71 = 354.40[\mathrm{W}]$$

$$P_{c,me} = P_{me} \cdot \eta_{me} = 345.4 \cdot 0.747 = 264.73\ [W]$$

Performing the calculations, the data presented in tables 4 and 5 are similarly obtained.

**Table 4:** Values of $P_{me}$, $P_{c,me}$ experimentally established

| **n** [rot/min] | **200** | **300** | **400** | **500** |
|---|---|---|---|---|
| **U** [V] | 384.70 | 384.00 | 381.00 | 381.00 |
| **I**I [A] | 0.75 | 1.1 | 1.45 | 1.8 |
| $P_{me}$ [W] | 354.40 | 518.83 | 678.57 | 842.37 |
| $P_{c,me}$ [W] | 264.73 | 387.57 | 506.90 | 629.25 |

### II. The values of the measured quantities and the calculation obtained results when the conveyed fluid is engine oil

**Table 5 :** Values of $P_{me}$, $P_{c,me}$ experimentally established

| **n** [rot/min] | **200** | **300** | **400** | **500** |
|---|---|---|---|---|
| **U** [V] | 383.90 | 384.40 | 384.00 | 381.00 |
| **I** [A] | 0.70 | 1.00 | 1.30 | 1.60 |
| $P_{me}$ [W] | 330.08 | 472.16 | 613.17 | 748.77 |
| $P_{c,me}$ [W] | 246.57 | 352.70 | 458.04 | 559.33 |

The power from the electric motor coupler is used to drive the fluid conveyed by the pump. Taking into account the actual efficiency of the pump ($\eta_p$) [16] [17], the actual power used to drive the fluid ($P_r$) results.

$$P_r = P_{c,me} \cdot \eta_p \; [W] \tag{12}$$

$\eta_p$ = 77%.

For the two fluids, at a speed of 200 rpm is obtained:

$$P_{r,H_2O} = 264.73 \cdot 0.77 = 203.84 \; [W]$$

$$P_{r,u} = 246.57 \cdot 0.77 = 189.86 \; [W]$$

Performing the calculations in a similar manner to the data in tables 4 and 5, the data in table 6 are obtained.

**Table 6:** The values of the power required to circulate the fluid

| **n** [rot/min] | **200** | **300** | **400** | **500** |
|---|---|---|---|---|
| $P_{r,H_2O}$ [W] | 203.84 | 298.43 | 390.31 | 484.52 |
| $P_{r,u}$ [W] | 189.86 | 271.58 | 352.69 | 430.69 |

Based on the data in table 3 and table 6, the graph P = f (n) in figure 7 was plotted.

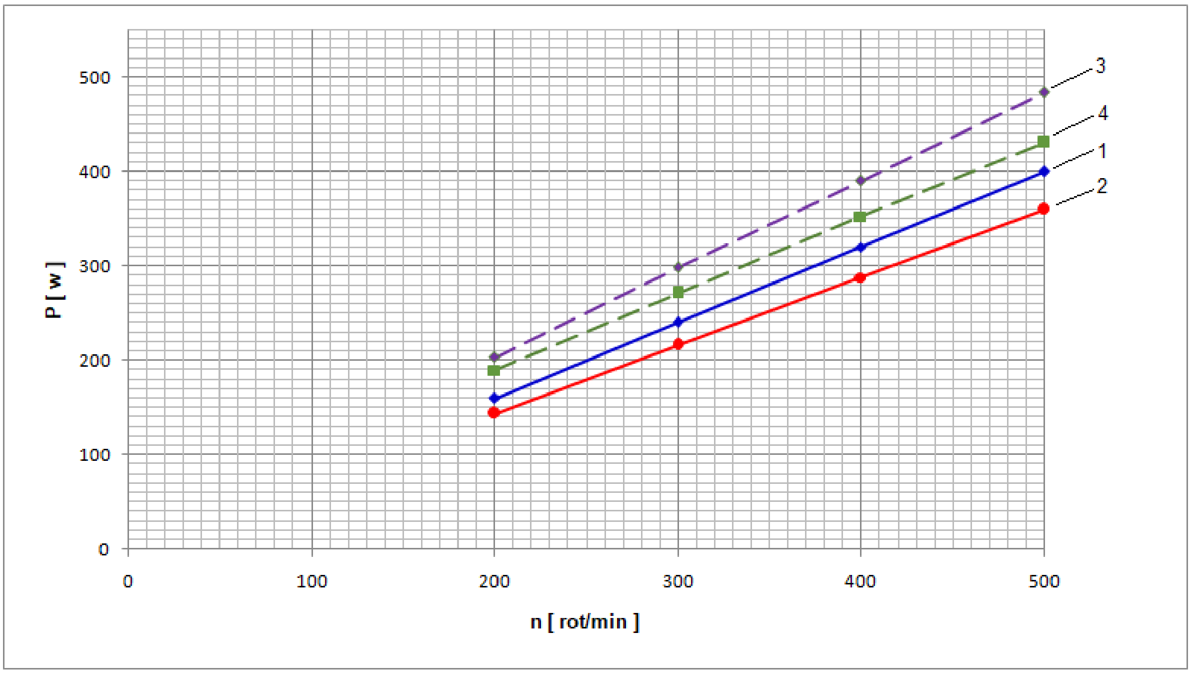

**Fig. 7.** Theoretical power and actual power required for fluid transport
1-2 calculation results for water, oil
3-4 experimental results for water, oil

The actual power consumed by the pump in the case of transporting engine oil is lower than in the case of transporting water, because the losses due to mechanical friction between the rotors and the case are lower in the case of transporting engine oil.

## 5. Conclusions

1. The constructive presented solution can transport clean or suspended liquids, as well as rheological fluids or gases.

2. The driving power of the machine is influenced by the nature of the conveyed fluid and by the density of the fluid.
3. Volumetric pumps with profiled rotors can be used in the field of land improvements, in wastewater treatment plants, in the: mining industry, energy industry, petrochemical industry.
4. From figure 7 one can observe that there is a satisfactory accordance between the theoretical and the experimental data.

**References**

[1] Băran, N., I. Căluşaru, and A. Detzortzis. “Research Regarding the Testing of a New Type of Rotating Machine with Profiled Rotors. ˝ *Journal of Materials Science and Engineering A* 2, no. 3 (2012): 372-376.
[2] Motorga, A. “Influența parametrilor constructivi și funcționali asupra performanțelor mașinilor rotative cu rotoare profilate.˝ PhD. Thesis. Politehnica University of Bucharest, 2011.
[3] Băran, N., P. Răducanu, et. al. *Bases of Technical Thermodynamics*. Bucharest, Politehnica Press Publishing House, 2010.
[4] Băran, N., D. Despina, D. Besnea, and A. Detzotzis. “Theoretical and experimental researches regarding the performances of a new type of rotating machine with profiled rotors.˝ *Advanced Materials Research* 488-489: 1757-1761.
[5] Hawas, M. PhD Thesis, “The influence of fluid viscosity on the performance of rotating machine with profiled rotors.˝ Politehnica University of Bucharest, 2015.
[6] Băran, N., D. Ion, and Al. Motorga. “Un nou tip de mașină de lucru și de forță în domeniul fluidelor.˝ Lucrările celei de a cincea conferință a Hidroenergeticienilor din România, Universitatea POLITEHNICA din București, 2008, pp. 376-381.
[7] Băran, N., D. Ion, and Al. Motorga. “Un nou tip de mașină care poate funcționa ca pompă sau ca motor hidraulic. ˝ *Revista Hidrotehnica* 53, no. 7-8 (2008).
[8] Motorga, A. “Influence of constructive and functional parameters on the performances of rotating machines with profiled rotors.” PhD Thesis. Faculty of Mechanical Engineering and Mechatronics, Politehnica University of Bucharest, 2011.
[9] Exarhu, M. “Pneumatic and hydraulic machine and installations.” (in Romanian). Bucharest, S.C. ANDOR SRL, 2011.
[10] Băran, N., D. Besnea, and A. Motorga. “Elements of computing the architecture and manufacturing technology for a new type of profiled rotor.˝ Proceedings International Conference, 6th Workshop on European Scientific and Industrial Collaboration on promoting Advanced Technologies in Manufacturing, WESIC’08, Bucharest, Romania, 2008, pp. 233-241.
[11] Băran, N., A. Motorga, and D. Duminică. “Research Regarding the Building of an Experimental Setup for the Testing of a New Type of Rotating Machine with Profiles Rotors.˝ *Rev. Mecatronica*, no.1 (2011): 27-30.
[12] Detzortzis, A., N. Băran, and M. Hawas. “The influence of the rotor architecture of a rotating working machine on the driving power.˝ *U.P.B. Sci. Bull. Series D* 77, no. 1 (2015):155-166.
[13] Hawas, M., N. Băran, and A. Detzortzis. ”Influence of the rotor architecture and of the speed on the volumetric efficiency of a new type of rotating volumetric machine.˝ *Advanced Materials Research* 905, (2014): 487-491.
[14] Hawas, M. “Research regarding the establishment of efficiency for a new type of rotating volumetric pump.˝ *International Research Journal of Engineering and Technology (IRJET)* 2, no. 2 (2015): 796-800.
[15] Băran, N., D. Duminică, D. Besnea, and A. Detzortzis. “Theoretical and Experimental Researches Regarding the Performances of a New Type of Rotating Machine with Profiled Rotors.˝ *Advanced Materials Research* 488-48 (2012): 1757-1761.
[16] Băran, N., Gh. Băran, D. Duminică, and D. Besnea. “Determinarea experimentală a randamentului efectiv pentru un nou tip de pompă volumică rotativă. ˝ *Revista de Chimie* 57, no. 12 (2006): 1294-1297.
[17] Băran, N., A. Detzortzis, M. Hawas, and D. Besnea. “The correlation between the rotor shape and the energetic performance of a rotating machine with profile rotors.˝ *The Romanian Review Precision Mechanics, Optics & Mechatronics*, no.45 (2014):18-26.

**ISSN 1453 – 7303** **“HIDRAULICA” (No. 4/2019)**
**Magazine *of Hydraulics, Pneumatics, Tribology, Ecology, Sensorics, Mechatronics***

# Design of a Bionic Arm Using Rapid Prototyping Technology

Ph.D. **Ștefan Adrian ȚÎMPEA**[1]**,** S.L.Dr.Ing. **Cristian COSMA**[2]**,** Conf.Dr.Ing. **Cosmin CODREAN**[3], S.L.Dr.Ing. **Aurelian MAGDA**[4]

[1]University Politehica of Timisoara, Piata victoriei nr. 2, 300006 Timisoara, Romania, stefantimpea@gmail.com

[2] University Politehica of Timisoara, Piata victoriei nr. 2, 300006 Timisoara, Romania, cristian.cosma@upt.ro

[3] University Politehica of Timisoara, Piata victoriei nr. 2, 300006 Timisoara, Romania, cosmin.codrean@upt.ro

[4] University Politehica of Timisoara, Piata victoriei nr. 2, 300006 Timisoara, Romania, aurelian.magda@upt.ro

***Abstract:*** *This paper presents a 3D printable design for a myoelectric prosthetic arm which is electronically actuated and controlled by a user flexing muscles. The prototype has the potential to be used by an amputee or person born without a limb. In these days, a rapid prototyping (RP) technology as Fused Deposition Modeling (FDM) allows individuals to become small-scale manufacturers. Using RP technology to obtain physical parts for the bionic arm has a high impact due to the final price. The main purpose of this project is to design a low-cost bionic arm controlled by EMG signals.*

***Keywords:*** *Bionic arm, rapid prototyping, additive manufacturing, fused deposition modelling FDM*

## 1. Introduction

In medicine, a prosthetic implant is an artificial device designed to replace missing parts of the body, which may be lost through trauma, disease, or congenital conditions [1]. The prostheses are intended to restore the normal functioning of the missing parts of the body. The replacement of a part of the body, especially replacement of an arm, is indeed a challenging task, which makes the person truly appreciate the complexity of the human body. For centuries innovators have tried to replace lost limbs with various devices. Several prosthetic devices have been discovered by ancient civilizations around the world, which demonstrate the continuous progress of prosthetic technology [7]. For many people, an artificial limb can improve mobility and the ability to manage daily activities, and to be independent. Rapid prototyping technology has a major impact on low-cost bionic arms. RP gives a big chance to test the prototypes and upgrade them, to create the plastic parts of the bionic arm I took in consideration a field of RP called fused deposition modeling, FDM is one of the most popular technology on the market. Nowadays RP is used in medicine, especially in implantology area. Many implants for e.g. hip are made by selective lase sintering (SLS) technology using biocompatible materials as Titanium alloy Ti-6Al-4V [2].

## 2. The current state

In this moment, the price of a bionic hand is relatively high. A bionic hand with different functions costs between 20,000 - 30,000 $. An advanced bionic hand can cost up to $ 100,000. More than that, the price of a bionic hand is closely linked to the degree of amputation [3]. The price of a bionic hand with a myoelectric arm up to the shoulder is three times higher than a bionic hand which replace a partial part of hand.

### 2.1 EMG signals. Electromyography

Myoelectric signals are electrical impulses located inside the body produced by muscles fibers when they are contracting, base of this generate a change in electrical potential and can be measured of the surface of the skin by an electromyogram (EMG). The amplitude of the EMG signal is directly correlated with the force generated by the muscle. Most of prosthetics are using the amplitude of the steady state (Fig 1) EMG signal where the subject exerts constant effort with a chosen muscle, the device has a single degree of freedom such as a gripper for grasping and releasing objects [4].

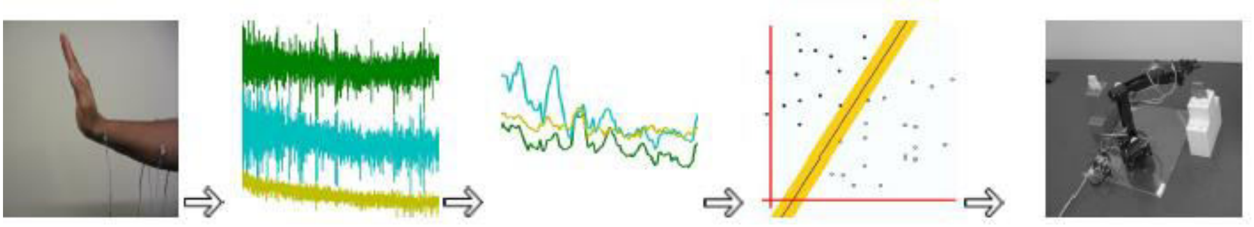

a) Static gesture b) steady-state EMG c) extracted features d) SVM classification e) robot arm control

**Fig. 1.** Schematic for EMG-based robotic control [4]

Medical electrodes placed on the user's skin (Fig 2) can detect these small signals and can be used to control the device. The electrical signals are very small, myoelectric sensors pick up signals generated in the muscle tissue that are amplified filtered and undergo signal processing to control artificial hand. [5], [6]. The figure 3 shows standard model of myoelectric hand functionality.

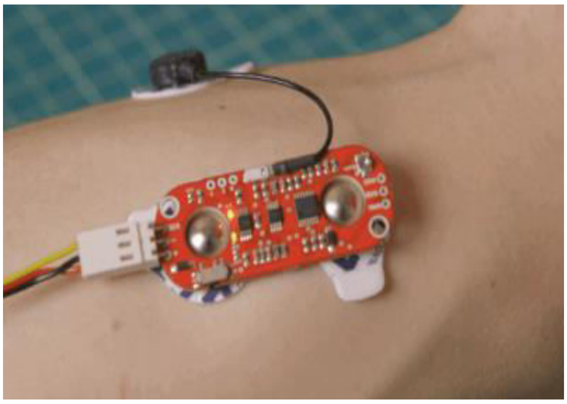

**Fig. 2.** Location of electrodes

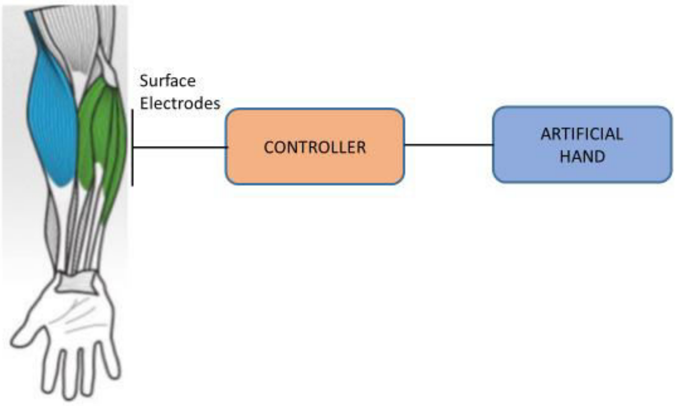

**Fig. 3.** Myoelectric hand [5]

### 2.2 Rapid prototyping. Fused deposition modelling FDM

To create the physical parts of the bionic arm is taken into consideration a field of rapid prototyping (RP) technology, called fused deposition modeling (FDM).

In RP, the term "rapid" is relative, it aims at the automated step from CAD data to machine, rather than at the speed of the techniques. Depending on the dimensions of the object, production times can be as a few days, especially with complex parts or when long cooling times are required. The manufacturing process is slow, but compared to traditional production techniques it can provide the physical parts in a very short time. This relatively fast production allows analysing parts in a very early stage of designing, which decreases the resulting design cost [6].

‘’Additive manufacturing AM is the generic term for the collective advanced manufacturing technologies that build parts layer by layer. The layers are produced by adding material instead of removing it as opposed to subtractive manufacturing such as machining. The material addition or fusion is controlled by G-codes generated directly from 3D CAD models. FDM, one of the AM technologies, builds parts layer by layer by heating a thermoplastic filament to a semi-liquid state and extruding it through a small nozzle per 3D CAD models usually in STL format as shown in Figure 4. The filament is usually of circular cross section with specific diameters for each FDM system. The most widely used diameters are either 1.75 mm or 3.0 mm. Due to the nature of FDM process, many advantages arise, such as the design freedom to produce complex shapes without the need to invest in dies and molds, the ability to produce internal features, which is impossible using traditional manufacturing techniques. FDM enables the reduction of the number of assemblies by producing consolidated complex parts [7].’’

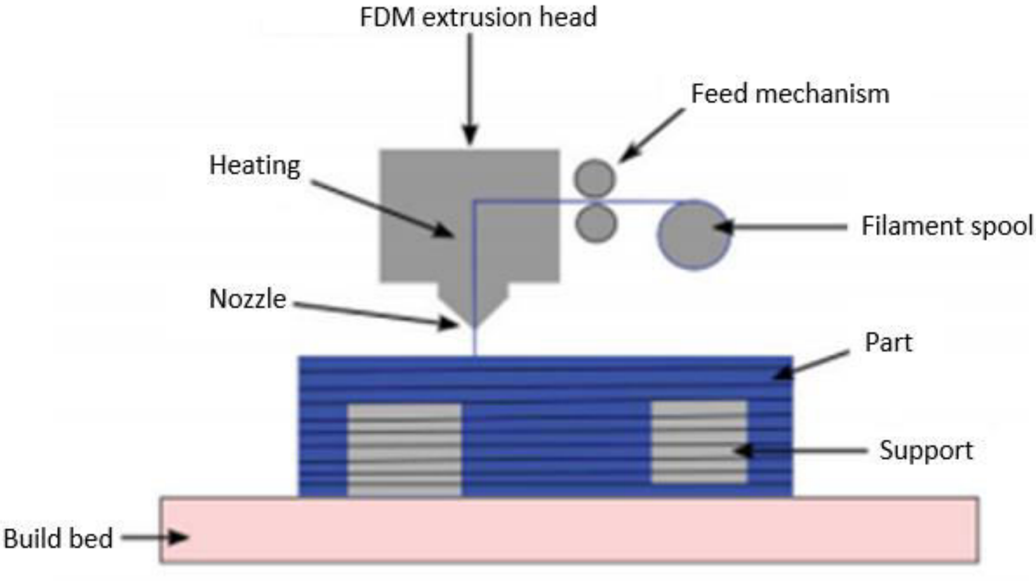

**Fig. 4.** FDM process schematic [5]

## 3. Description of the bionic arm

In order to design a bionic arm (Fig. 5), it is important to have a well-designed mechanic that mimics the functionality of the human arm as good as possible. Among many other aspects, the mechanical scheme involves how joints are operated, what type of linear motors used for fingers actuation, the centering and fixing of the components. The design of the bionic arm presented in this sketch can be entirely made with a 3D printer and basic tools. The bionic arm can be used in many applications like a human arm, this requires a high speed of response from the sensors to make a certain task.

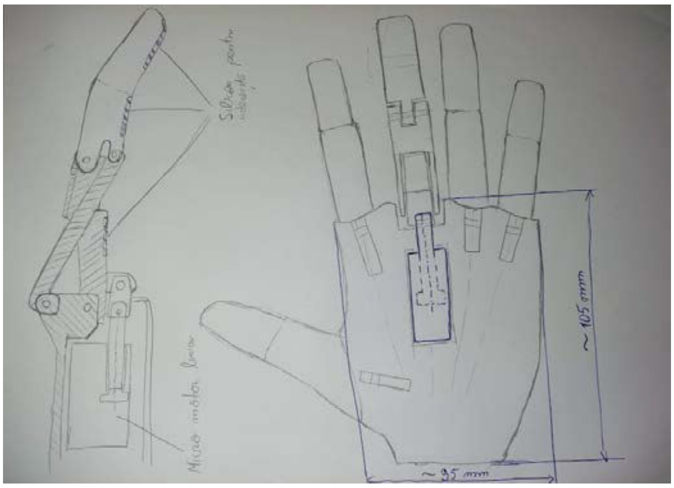

**Fig. 5.** Isometric view and schematic of the bionic arm

Figure 6 represents an isometric view of the finger assembly, the only piece that differs from one finger to another is the tip of the finger that is longer or shorter depending on the position of each.

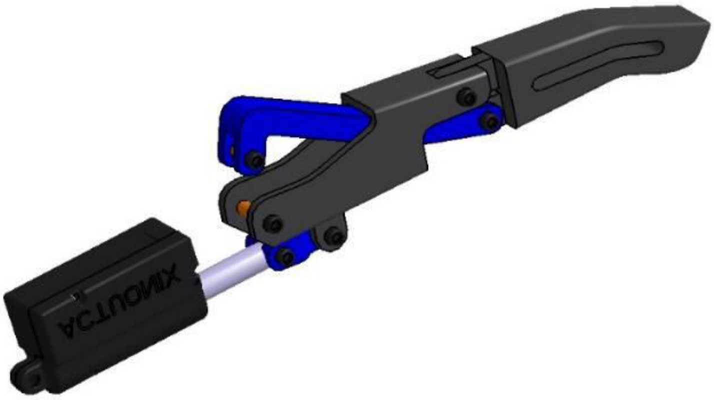

**Fig. 6.** Finger subassembly

In the figure 7 the Kinematic model for prosthetic finger is presented. The finger incorporates own mechanism to mechanically couple joints together. Rotating the metacarpal joint (knuckle) simultaneously rotates the higher phalange joint [8].

**Fig. 7.** Kinematic model for prosthetic finger [6]

Figure 8 shows an exploded view of the finger assembly, the assembly steps can be observed as well as the name of each component of the finger. In order to avoid damage to the plastic parts is used brass bushing. Also, to avoid the unscrew process is chosen self-locking nut.

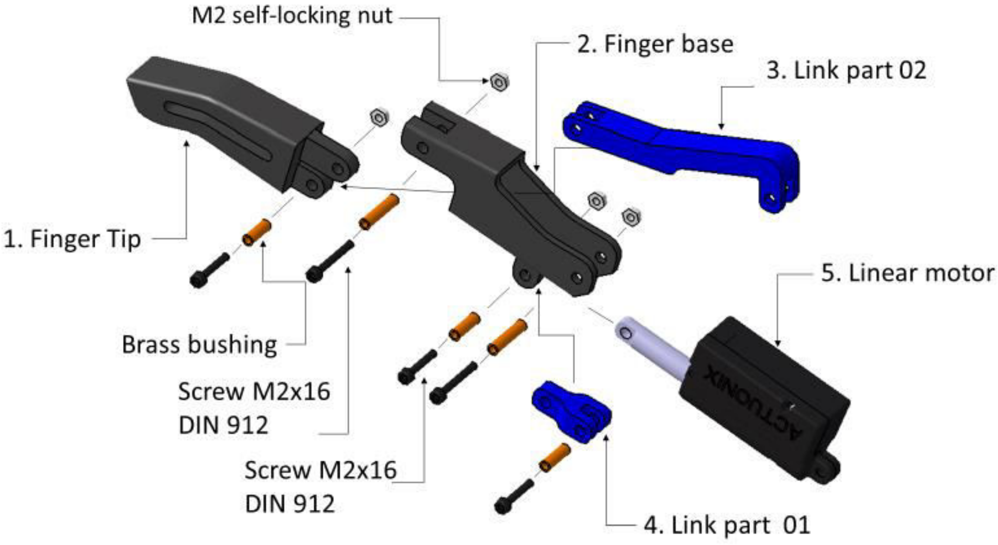

**Fig. 8.** Exploded view of the finger subassembly

In figure 9 one can see an exploded view of the palm assembly, the assembly steps can be observed as well as the name of each component.

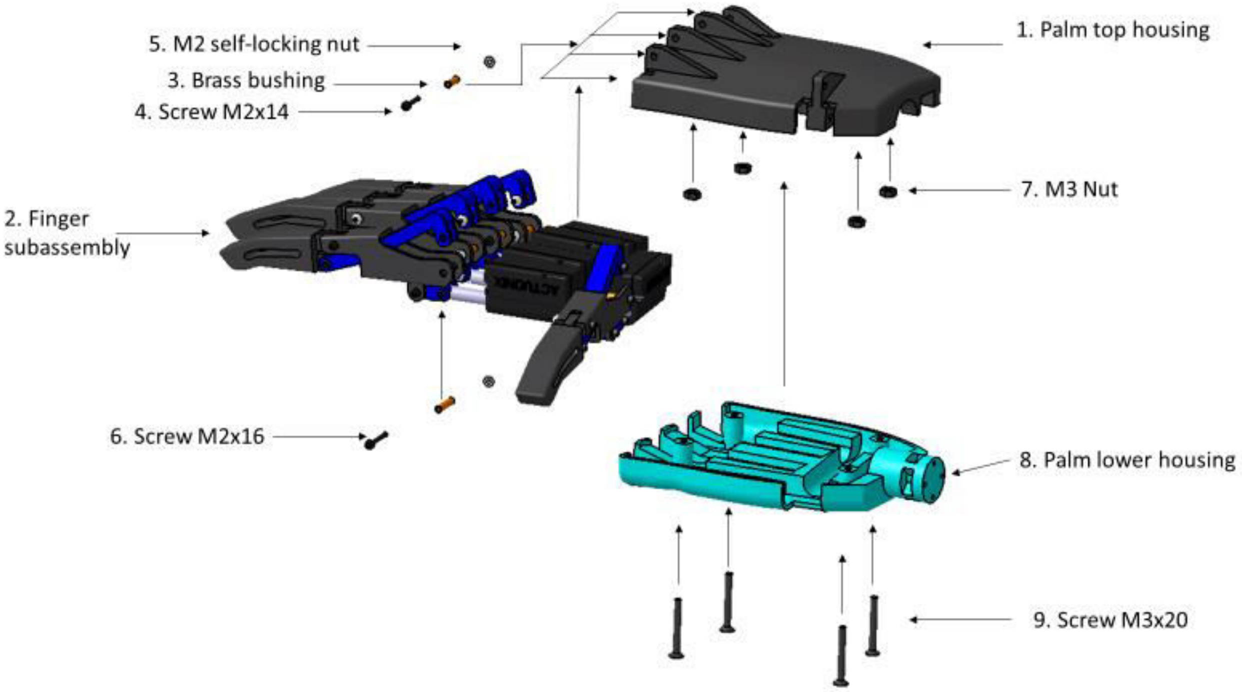

**Fig. 9.** Exploded view of the palm subassembly

Figure 10 shows an exploded view of the finger assembly; the assembly steps can be observed as well as the name of each component of the finger.

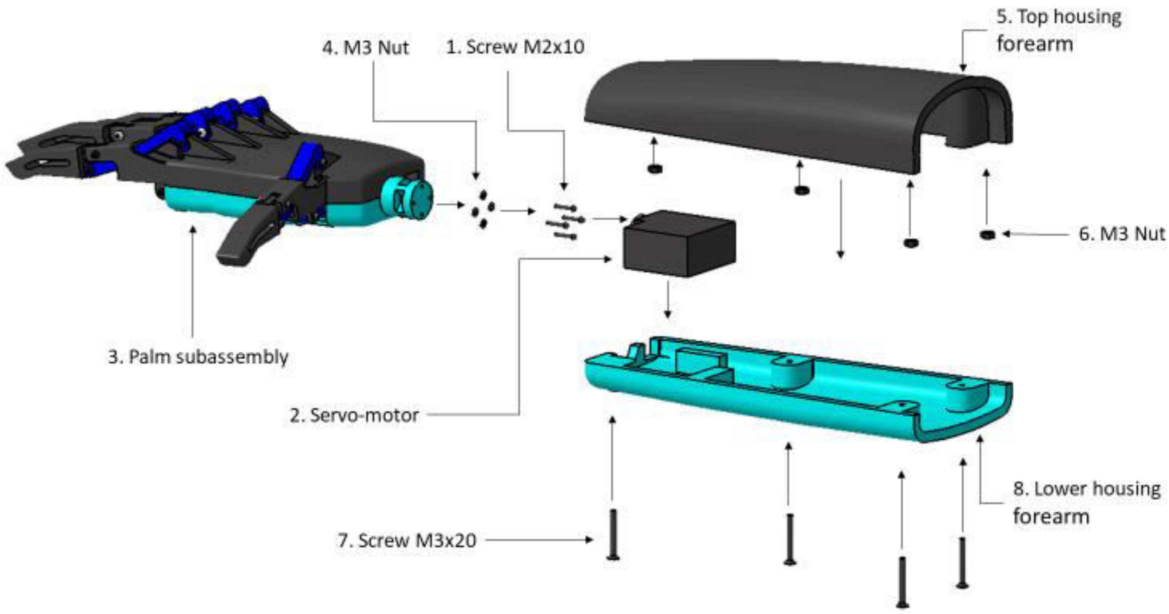

**Fig. 10.** Exploded view of the bionic arm

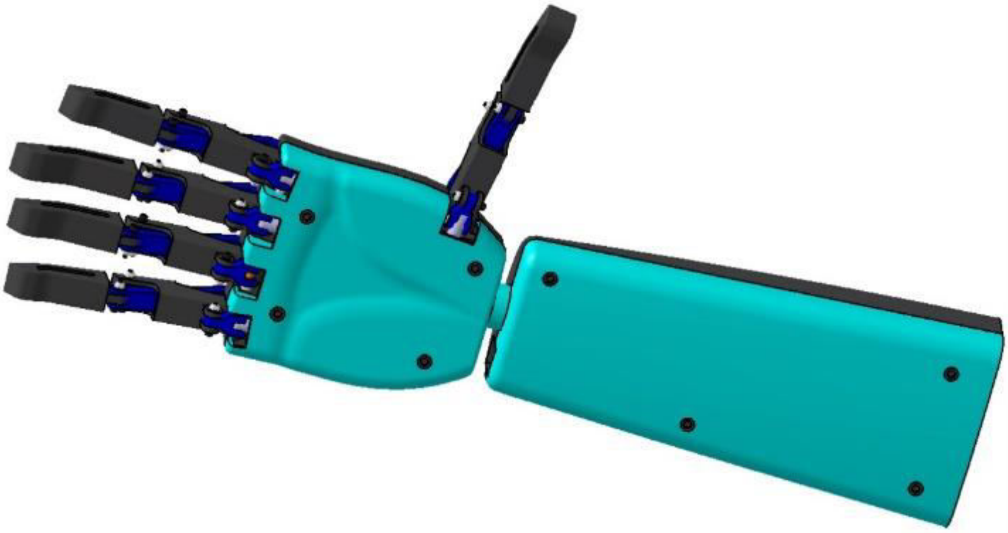

**Fig. 10.1.** Final assembly

### 3.1 Simulation of bionic arm movements

During the mechanical design I made a series of finger simulations (Fig 11 and 12), how they close, how much to close. Doing these simulations, a very well-structured concept has resulted. The following figures show the bionic arm movements.

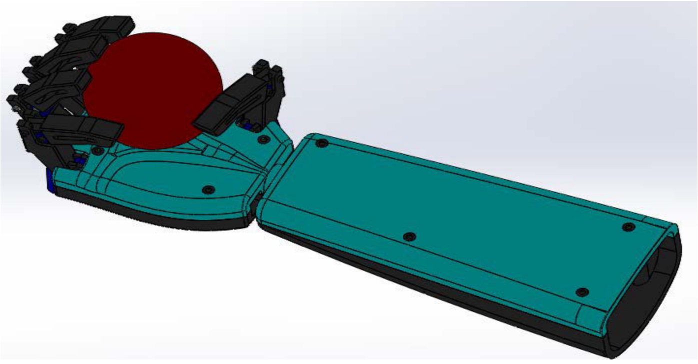

**Fig. 11.** Catching a sphere with diameter 70mm

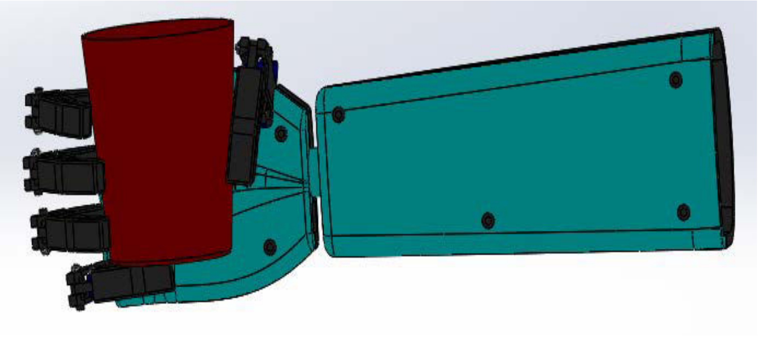

**Fig. 12.** Catching a glass with diameter ~70mm

### 3.2 Price of the bionic arm

One of the goals of the project was to design an affordable bionic arm for all patients. The hand developed within the project is still in the prototype phase. Therefore, a cost analysis is needed to estimate future costs and price per unit. The current cost of an arm is $ 503.38, and the costs are shown in Table 1. Compared to the myoelectric prostheses available on the market, which cost about $ 60,000, the goal of creating the bionic arm with reduced costs was achieved.

**Table 1:** Price of the components

| Description | Nr Part | Price in $ | Total price in $ |
|---|---|---|---|
| Myo-Ware Muscle sensor | 3 | 30.53 | 91.59 |
| Linear Motor PQ12 | 5 | 65 | 325 |
| Battery | 1 | 19.34 | 19.34 |
| Tower Pro MG996R Servo | 1 | 7.45 | 7.45 |
| Filament PLA | 24 | 15$/kg | 10 |
| Other components | N/A | N/A | 50 |
| | | | 503.38 |

### Conclusions

The main purpose of this project was to design a bionic arm controlled myoelectric with low manufacturing costs, which can be made by 3D printing technology. The purpose of this project was achieved resulting a prototype controlled by EMG signals captured by the biomedical electrodes and converted into movements. The final prototype is designed to be user-friendly with a simplistic design. However, many aspects still require further work to develop a fully functional bionic arm.

The project shows the advantages of rapid prototyping technology, this have the potential to produce bionic arm parts personalized, cheaper and faster. The bionic arm is designed to be easy to assemble. For people who lost the upper limbs trough trauma, disease, or a condition present at birth, they may have a chance at a normal life. For a highest precision of the finger movements, a medical check is recommended to highlight the area where the biomedical electrodes are placed that capture the electrical signals from the movements.

During the development of the bionic arm, we made several finger actuation systems, one of the tried systems was to actuation finger using a tendon cord, the problem encountered in this system was to return to the natural position of the finger. To restore the finger to the natural state it was necessary to implement two or three springs depending on the system used, which was quite difficult for the small space of the finger joint.

### References

[1] Evdokia, K.N. *AI and Prosthetics*. Universitat Politecnica de Catalunya, Final Master Thesis, 2016.
[2] Popovich, A., V. Sufiiarov, I. Polozov, E. Borisov, and D. Masaylo. “Producing hip implants of titanium alloys by additive manufacturing.” *International Journal of Bioprinting* 2, no. 2 (June, 2016): 78–84.
[3] ***. What a $100,000 Bionic Arm Can Do. Accessed November 8, 2019. https://www.vocativ.com/money/industry/prosthetic-boom-3d-printed-mind-controlled-limbs/index.html.
[4] Crawford, B., K. Miller, P. Shenoy, and R. Rao. “Real-Time Classification of Electromyographic Signals for Robotic Control.” Paper presented at AAAI'05 the 20th National Conference on Artificial Intelligence, Pittsburgh, Pennsylvania, USA, July 09 - 13, 2005.
[5] Geizans, R. *Developing 3D Printed Prosthetic Hand Model Controlled by EMG Signal from Forearm*. Metropolia University of Applied Sciences, Bachelor of Engineering, Electronics, Thesis, May, 2018.
[6] Tut, V., A. Tulcan, C. Cosma, and I. Serban. "Application of CAD/CAM/FEA, Reverse engineering and rapid prototyping in manufacturing industry.” *International Journal of Mechanics* 4, no. 4 (2010): 79-86.

[7] Alafaghani, A., A. Qattawi, B. Alrawi, and A. Guzman. "Experimental Optimization of Fused Deposition Modelling Processing Parameters: a Design-for-Manufacturing Approach." *Procedia Manufacturing* 10 (2017): 791-803.
[8] Hussein, M.E. *3D Printed Myoelectric Prosthetic Arm.* Thesis Bachelor degree Engineering (Mechatronics), October 2014.

# Dynamic Analysis of a Centrifugal Pump using CFD and FEM Methods

PhD Student Eng. **Nicolae IACOB**[1], Assoc. Prof. PhD Eng. **Nicușor DRĂGAN**[2]

[1] Institute of Solid Mechanics, Romanian Academy Bucharest, nicolaeiacob84@yahoo.com

[2] "Dunarea de Jos" University Galati, Engineering and Agronomy Faculty of Braila, The Research Center of Machines, Mechanic and Technological Equipment - MECMET, ndragan@ugal.ro

***Abstract:*** *The article analyses the performances of a centrifugal pump using the Computational Fluid Dynamic (CFD) method, a computer numerical simulation method that was performed with specialized software in dynamic fluid flow analysis, ANSYS Workbench, using the FluidFlow (CFX) module. With this, the performances parameters of a centrifugal pump were determined: the inlet pressure and the outlet pressure of the pump, the flow of the pump, the speed of the fluid through the pump, the cavity of the pump. Using the finite element method (FEM) for solid bodies, the stresses and deformations occurring in the rotor blades were determined. For this part of the study, the Static Structural module from the ANSYS Workbench work platform was used. The 3D geometry of the centrifugal pump was modelled with the Siemens PLM NX 7.5 CAD/CAM software, then imported into the ANSYS Workbench to perform the analysis. The results of numerical simulations were interpreted and the conclusions of the study were drawn. This study emphasizes the advantages of using numerical modelling and simulation by CFD method and by the finite element method.*

***Keywords:*** *Dynamic analysis, current lines, centrifugal pump, CFD, FEM*

## 1. Introduction

Centrifugal pumps are rotary hydraulic machines that create hydraulic energy based on the centrifugation of the liquid passing through the pump rotor. Centrifugal pumps are widely used in technical applications.

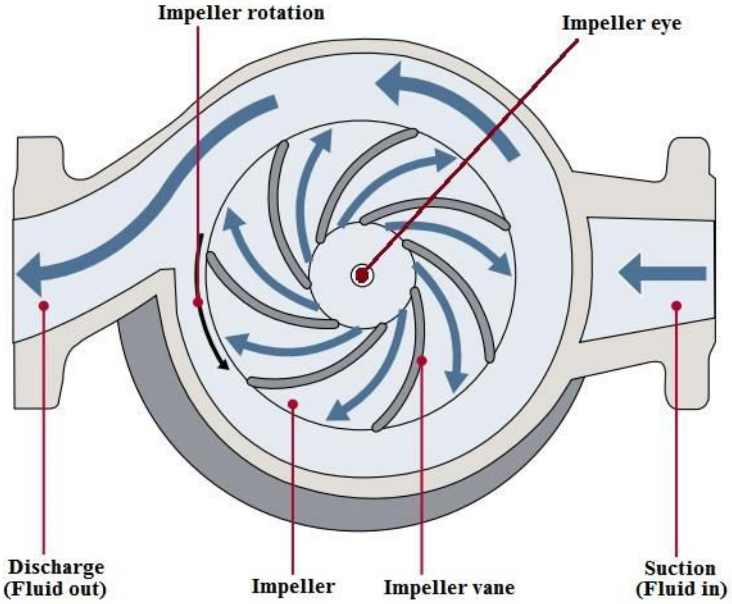

**Fig. 1.** Centrifugal pump - operation principle [1]

Due to the development of the centrifugal pump construction industry, the field of use of piston pumps has been narrowing lately, being used only for low flows and high pressures, an area where the use of centrifugal pumps is uneconomical, but even this area it narrows. The principle of operation of centrifugal pumps is relatively simple. This can also be seen in Fig. 1. The centrifugal pump creates a increased pressure inside it by transferring the mechanical energy from an engine through an axis to the pump rotor. The fluid flows from the inlet to the center of the rotor, then flows along the blades of the rotor outward due to centrifugal force. The kinetic energy created by the rotation of the rotor is converted to pressure at the output of the pump (discharge area).

## 2. Performance parameters of centrifugal pumps

The performance parameters of the centrifugal pumps can be determinate by a set of performance curves diagrams. Figure 2 shows the performance curves of the centrifugal pumps. The first diagram shows the curves for the height of the fluid rise in relation to the flow produced by it and the yield curve. The optimum power consumption of a centrifugal pump is found at the intersection of the height curve and the pump yield curve.

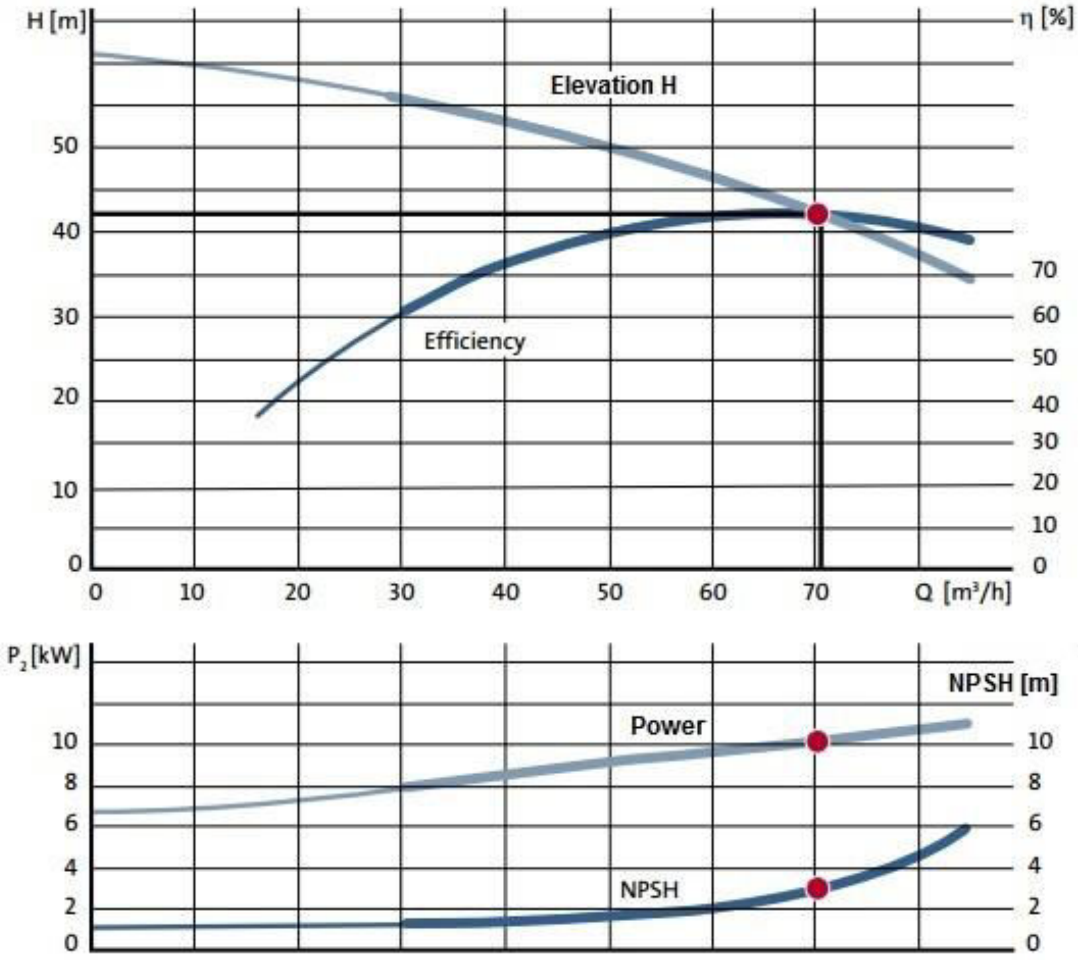

**Fig. 2.** Centrifugal pumps - performance curves diagrams [1]

The second diagram shows the power curves and the suction height of the pump. The NPSH (Net Positive Suction Head) abbreviation in the second diagram represents the suction height. For example, for a suction height of 2.5 m, a power consumption of 10 [kW] is required, as can be seen in the second diagram by marking the points in red.

The performance of centrifugal pumps is characterized by static pressure, dynamic pressure, fluid flow rate, suction height and fluid rise height. All of these performances are based on more complicated mathematical computing formulae, determining the performance of centrifugal pump by an analytical becoming almost impossible.

Another method of determining the performance of a pump is the experimental one, but this means consumption of material, time and money. The method proposed in this paper is the numerical simulation through the dynamic CFD fluid analysis performed with the ANSYS software.

## 3. Dynamic Analysis of a Centrifugal Pump using CFD Method

In order to determine the performances of the centrifugal pumps in this work, the CFD method was proposed. For this, the Fluid Flow (CFX) module from the Workbench Ansys 14.5 work platform was used. There are numerous work programs that can perform numerical simulation but Fluid Flow (CFX) is easy to use and has an algorithm with a very high computing power compared to other dynamic flow analysis software. The pump geometry was performed in the 3D modelling software NX 7.5 from the company Siemens PLM (Fig. 3, Fig. 4).

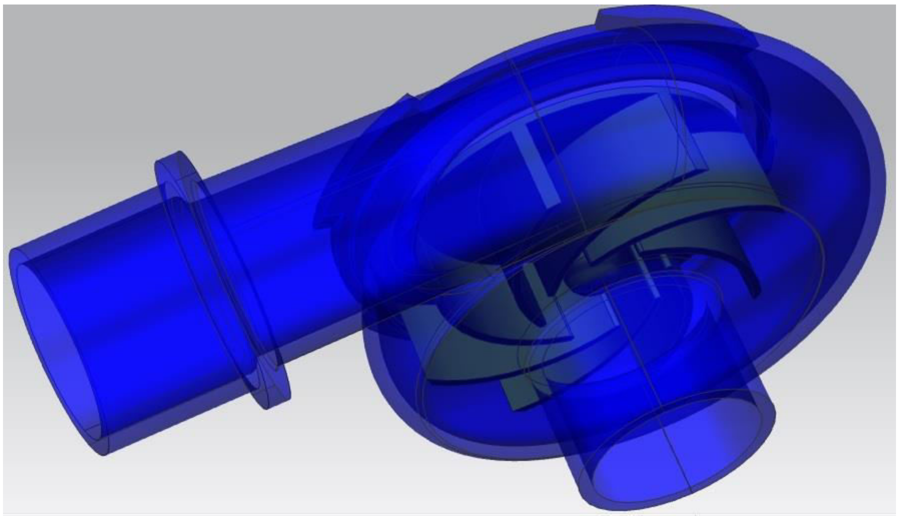

**Fig. 3.** Centrifugal pump geometry (model assembly)

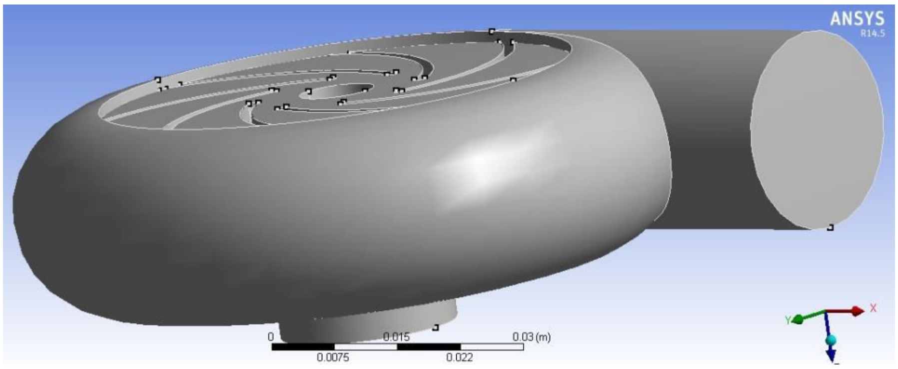

**Fig. 4.** Centrifugal pump - fluid flow geometry

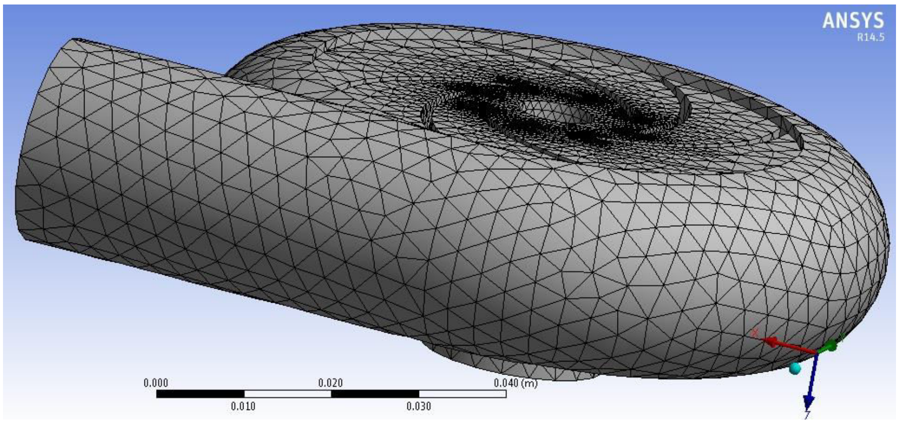

**Fig. 5.** Centrifugal pump - 3D mesh model of the flow area

After the discretization of the working model (Fig. 5), we proceeded to the next stage in which the boundary conditions for the dynamic flow analysis were imposed. The limit condition that was imposed on the analysis was the rotational speed of the rotor of 1500 rpm under the conditions of atmospheric pressure. This condition was imposed due to the operation of the centrifugal pumps. The centrifugal pumps as mentioned in the first part of the work are hydraulic machines that operate on the basis of fluid centrifugation. And centrifugation is a phenomenon that is obtained under the conditions of high angular velocities. In the case of the centrifugal pump, it is the rotor that drives the fluid in rotational motion and generates the phenomenon of centrifugation.
After imposing a boundary condition, the order for analysis was executed, and after the analysis was completed, the results were exported to a special post-processing module within the WORKBENCH ANSYS 14.5 platform. to be interpreted. This module gives the user the opportunity to observe the results of the analysis both numerically and through graphical illustrations.

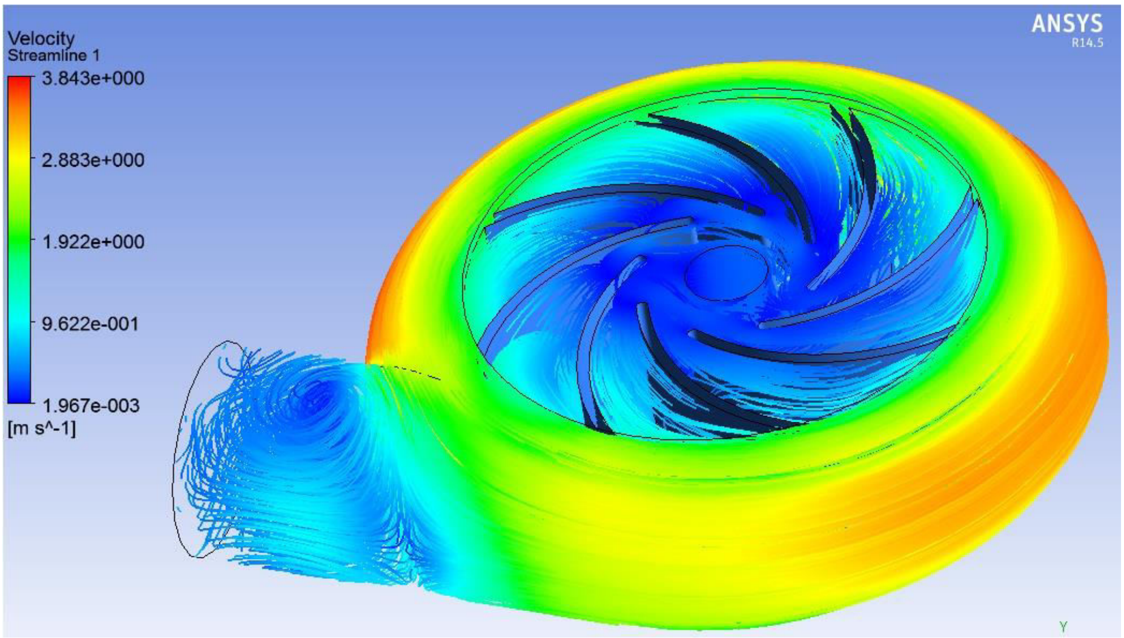

**Fig. 6.** Streamlines and flow velocity distribution inside the centrifugal pump [m/s]

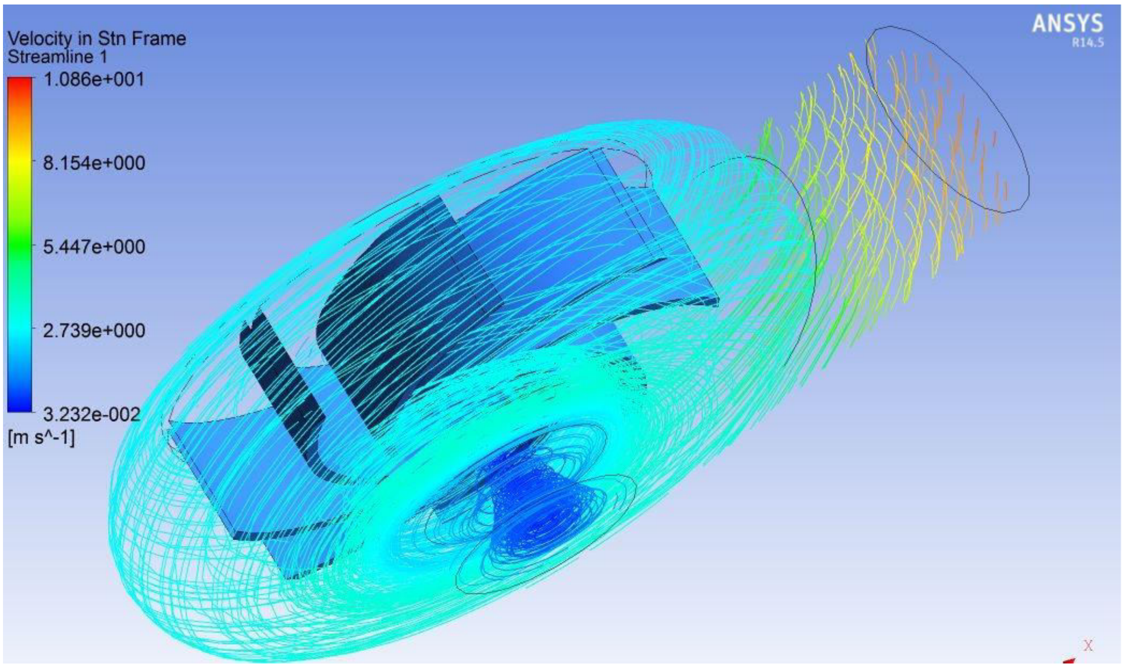

**Fig. 7.** Streamlines inside the centrifugal pump [m/s]

Fig. 6 and fig. 7 show the current lines of the fluid. As noted, the fluid ascends into the centrifugal pump having a cycloid motion. The fluid is sucked in due to the Coandă effect [2]. This can be seen very well in fig. 6 where in the middle of the rotor there is a decrease in the flow velocity of the fluid, which leads to the decrease of the dynamic pressure and the increase of the static pressure.

In the middle area of the rotor a depression is formed that sucks the fluid and raises it in the pump. Once reached the centrifugal pump the fluid is pushed outward from the pump walls and compressed due to the centrifugal force. With the compression of the fluid, there is an increase in pressure inside the pump. This pressure is much higher than the atmospheric pressure, and when it reaches the pump outlet, the fluid is discharged out.

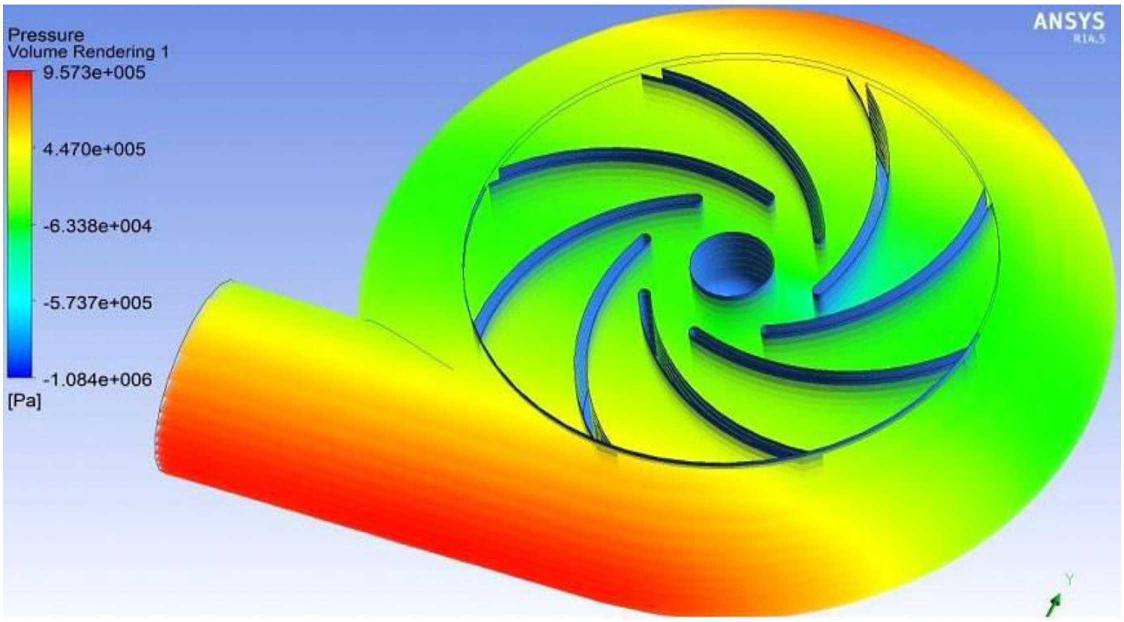

**Fig. 8.** Static pressure distribution [Pa] - fluid volume rendering

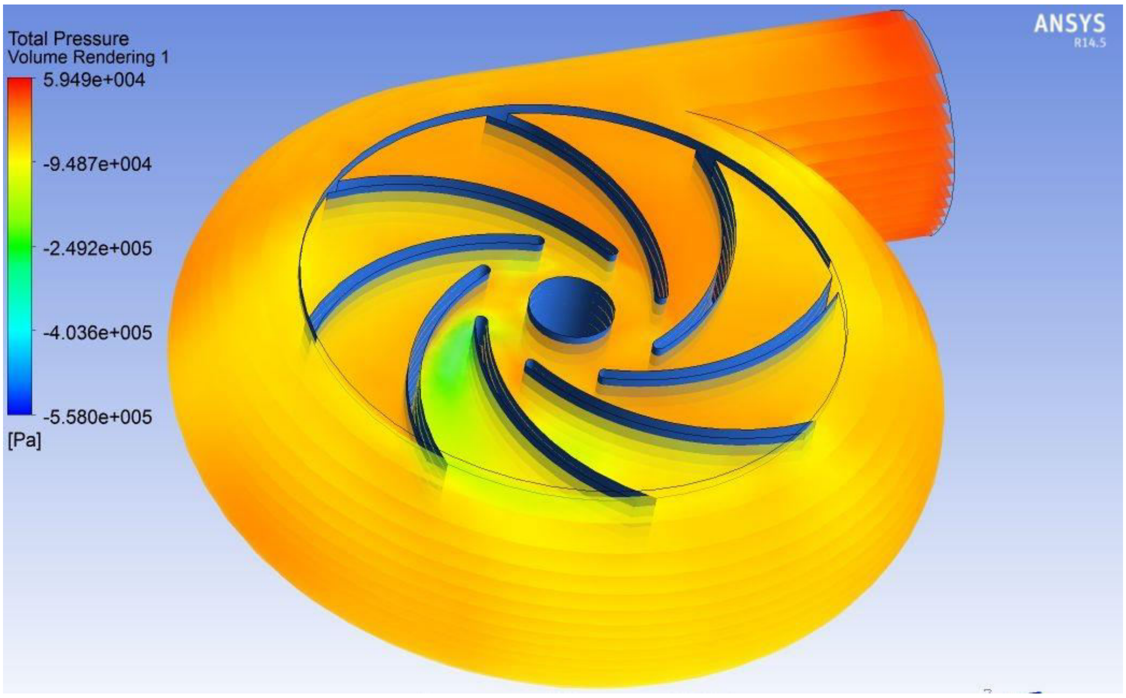

**Fig. 9.** Total pressure distribution [Pa] - fluid volume rendering

Figures 8 and 9 show the distribution of static pressures and total pump pressure. Static pressure is formed at the inside walls of the pump. As shown in figure 8, in the middle of the rotor a depression of $-6.3\times10^4$ Pa is formed. This is the suction pressure of the pump.

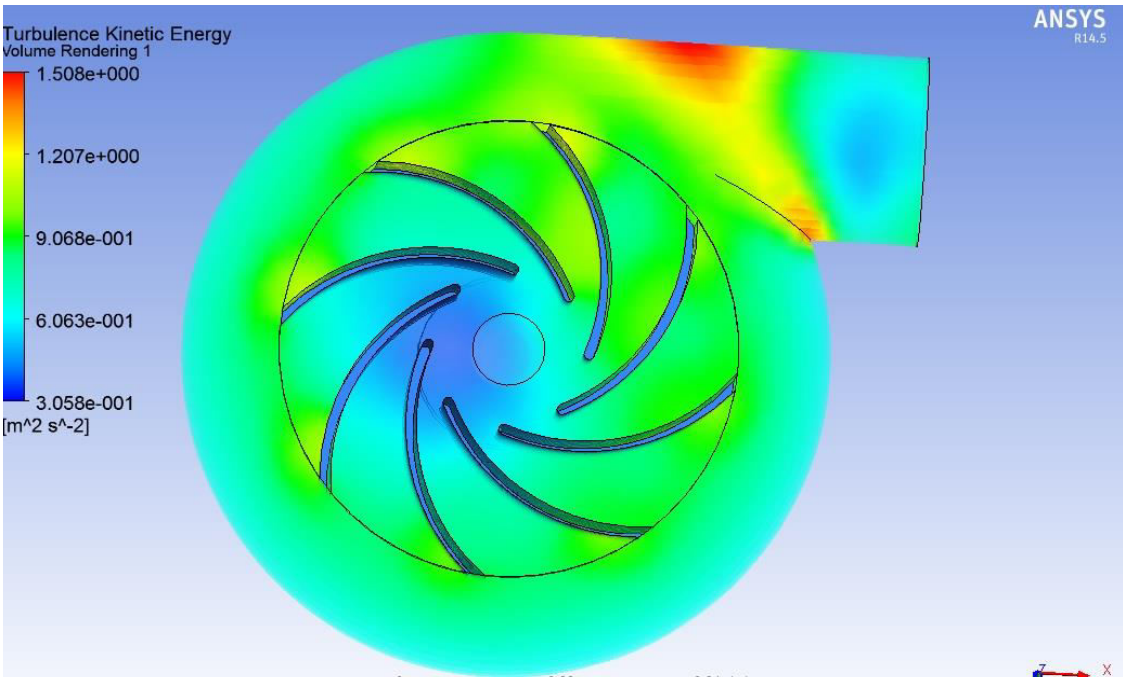

**Fig. 10.** Turbulence kinetic energy distribution [$m^2/s^2$] - fluid volume rendering

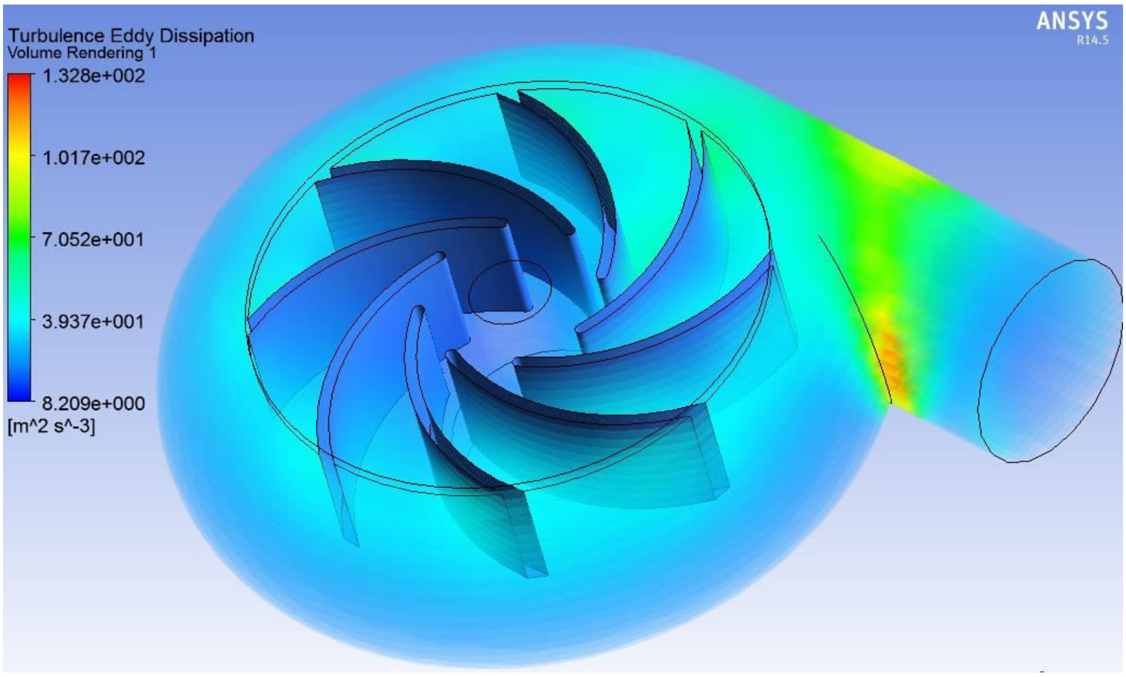

**Fig. 11.** Turbulence Eddy dissipation of kinetic energy [$m^2/s^3$] - fluid volume rendering

Figures 10 and 11 show the distribution of the turbulence occurring at the centrifugal pump level. These turbulences produce the phenomenon of cavitations, an undesirable phenomenon because it leads to damage to the pump. As shown in Figure 10, the cavitations appear in the area of the pump rotor.

When the pumped fluid reaches the impeller, because the inlet section is small, a speed increase occurs, accompanied by a drop in pressure. The higher the flow rate of the pump, the more this pressure drop is more pronounced. If this pressure drop exceeds a certain threshold or if the fluid temperature is high enough (or a combination of the two) the fluid vaporizes (the local pressure drops below the saturated pressure of the pumped fluid). The vapour bubbles get trapped on the rotor and after it exits, it enters a high pressure area, where it suddenly passes from the vapour state to the liquid state (it is destroyed), that means cavitations phenomenon.

## 4. FEM Analysis of Tension and Deformation Distributions in the Rotor Blades

The determination of the tensions and deformations in the rotor blades was performed using the FEM method (Static Structural module from the ANSYS Workbench platform).

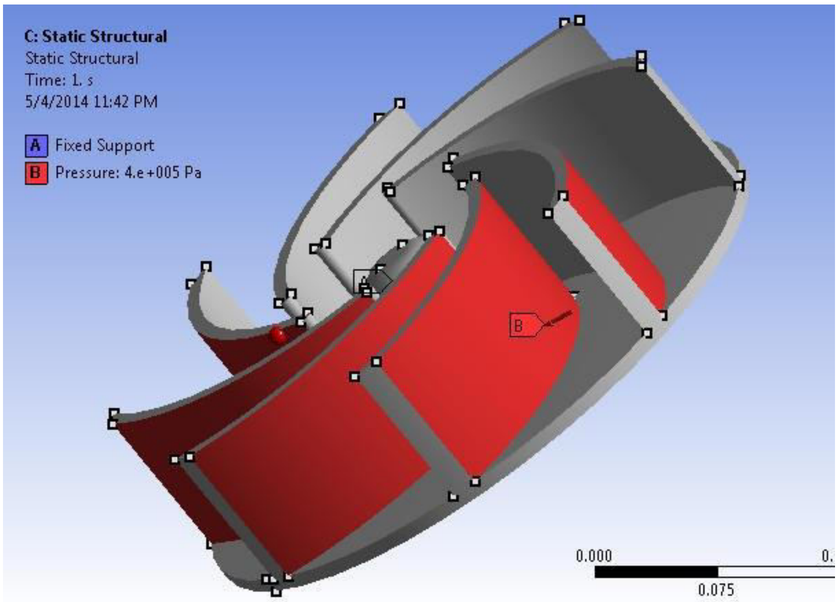

**Fig. 12.** The boundary conditions imposed to the rotor

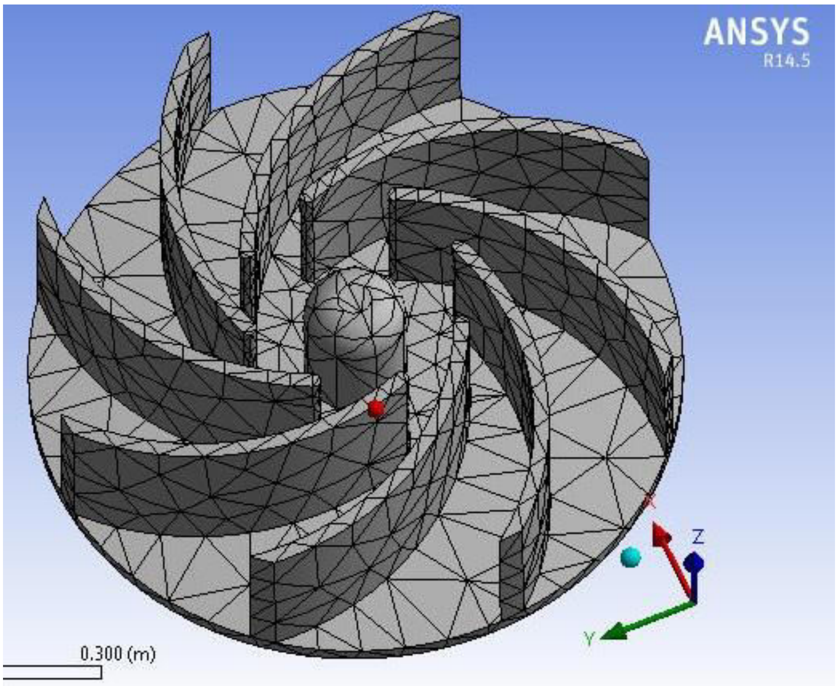

**Fig. 13.** Mesh model of the rotor

The geometry of the rotor was realized in the software Siemens PLM NX 7.5. The imported model was discretized and the material from which the rotor is made was declared as alloy steel. The boundary conditions imposed for the structural analysis of the rotor can be seen in figure 12. The maximum static pressure resulting from the CFD analysis was applied to each rotor pallet surface. After applying the boundary conditions, the command to solve the calculation was launched.

The 3D model discretion of the rotor can be seen in figure 13. The model was discretized into 51517 knots and 192526 tetrahedron type finite elements [3]. The rotor was analyzed under the conditions in which it is blocked and the maximum static pressure in the pump acts on the pallets. The maximum static pressure value on the rotor blades was taken from the results of the CFD analysis performed in §3.

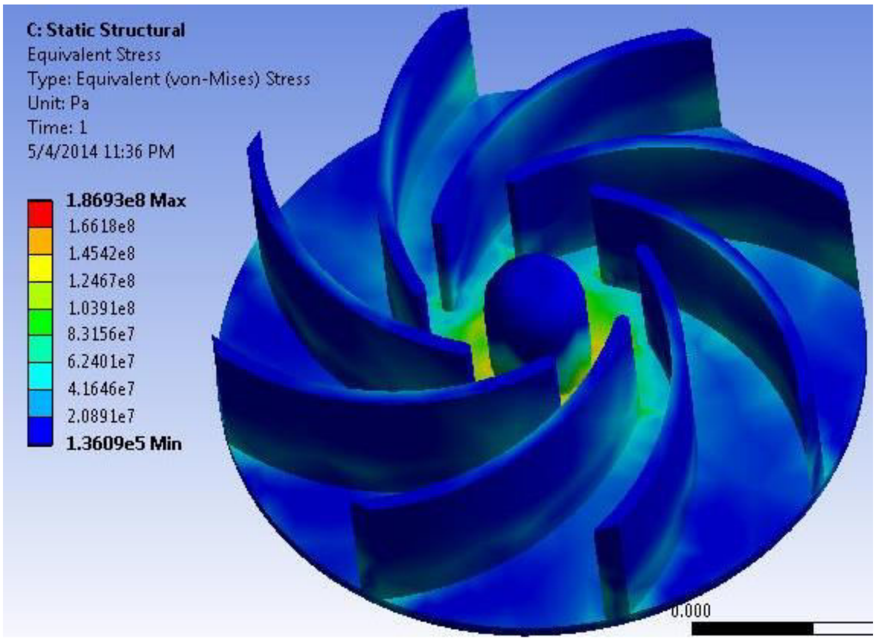

**Fig. 14.** Tensions distribution in the rotor [Pa]

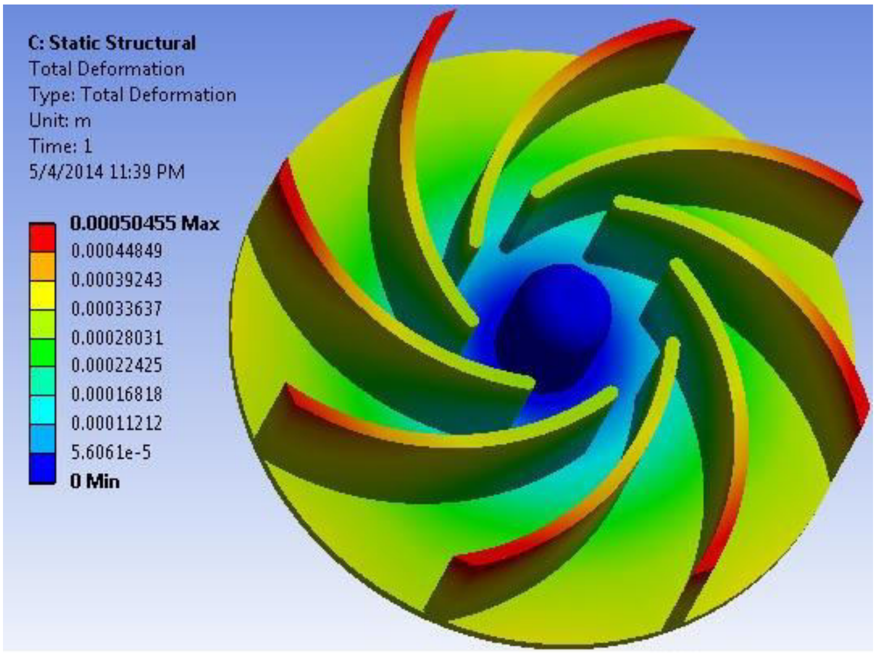

**Fig. 15.** Deformations distribution in the rotor [m]

Figure 14 shows the tensions distribution in the rotor blades, and figure 15 shows the deformations that appear in the rotor. In the rotor blades there is a maximum tension of $41.6\times10^6$ Pa, that means 41 $N/mm^2$. The maximum tensions in the rotor are below the material breaking limits. And the maximum deformations that occur in the rotor blades are $5.04\times10^{-4}$ m, that means 0.504 mm. These deformations are very small (of the order of tenths of a millimeter). Maximum deformations occur in the end zones of the rotor.

## 5. Conclusions

In this paper, the functional parameters of a centrifugal pump were determined using CFD analysis and at the same time showed the efficiency of the finite element analysis method.
Also with the CFD method, the Coanda effect created by the rotor of the centrifugal pump was highlighted.

### References

[1] Anton, Viorica, Mircea Popoviciu and Ioan Fitero*. Hydraulics and hydraulic machines/Hidraulică şi maşini hidraulice*. Bucharest, Didactic and Pedagogical Publishing House, 1978.

[2] Coanda, Henri. *Perfectionnement aux pompes centrifuges*. Brevet d'invention no. 1.030.088/23.12.1953, France.

[3] Moeykens, Shane. "From CAD to CAE. FLUENT software now offers support for Autodesk Inventor" *ANSYS Advantage, Volume II, Issue 1*, 2008. Accessed September 30, 2019. https://www.ansys.com/-/media/ansys/corporate/resourcelibrary/article/aa-v2-i1-from-cad-to-cae.pdf.

# Modelling and Sensitivity Study of a Firefighting System

Assistant Lecturer PhD. Student **Flóra HAJDU**[1], Associate Professor PhD. **Rajmund KUTI**[2]

[1]Széchenyi István University, Department of Mechatronics and Machine Design H-9026 Győr, Egyetem Square 1., hajdfl@sze.hu

[2] Széchenyi István University, Department of Mechatronics and Machine Design, H-9026 Győr, Egyetem Square 1., kuti.rajmund@sze.hu

***Abstract:*** *For safe operation of firefighting systems it is essential to study the operation conditions, especially in case of mobile fire pumps, which are sometimes used by firefighters under extreme conditions. Changes in operation parameters can have a serious impact on the amount of water that can be extracted from the system, and thus on the effectiveness of firefighting itself. Therefore, the study of the topic is an important current issue. During this research a simulation model of a firefighting system was created. In this paper the developed model is presented first, which is followed by numerical simulations and a Fuzzy-set based sensitivity study using the model. The aim of the research is to facilitate the optimal operation of firefighting systems and the work of firefighters and to increase the efficiency of firefighting.*

***Keywords***: *Firefighting system, operation parameters, numerical simulation, sensitivity study*

## 1. Introduction

Various pumps allow the transport of liquids in piping systems. Within pumps there is a separate group of fire pumps. The continuous examination of their operating conditions is essential for effective firefighting and continuous water supply. Their operation sometimes takes place under extreme conditions, which greatly affects the pump performance and thus the amount of water that can be extracted from the system. In order to facilitate accurate investigations and practical applications a simulation model of a mobile pump-operated firefighting system based on [1] was created as first step. The paper is organized as follows: first the technical parameters of the firefighting system are described, which is followed by the development of the simulation model and a parameter sensitivity study. The paper concludes with the summary of the results and further research tasks.

## 2. Examined firefighting system

In most cases the performance parameters of fire pumps are measured at a suction depth of 1.5 to 3 meters by means of a measuring device placed directly on the discharge port of the pump at various speed limits .During firefighting tasks suction depth of 3 m or less is required in case of built-up basins, therefore this is the starting point for developing our system. During operation of firefighting systems, the change in head may result in a significant performance difference in the amount of water that can be extracted from the system. It can even be decreased to a quarter of the expected amount within a given time interval. Creating optimal operation conditions for firefighting tasks is important, but the on-site conditions and available equipment do not always allow them, so actual pressure and flow rate values are usually below expectations. By studying the available literature [2,3,4,5] only partial solutions were found to the problem. It requires complex calculations to take into account all potential losses [1], but there is no time for time-consuming calculations in case of an accident [6]. As a solution a simplified calculation model was developed [1]. To facilitate and accelerate the calculations a modular simulation model was developed in Matlab/Simulink. The basic model can be easily expanded with additional elements if necessary. The subsystems of the simulation model are the following:

- mobile centrifugal pump
- standardized fire hoses
- adapters
- nozzle

The examined system consists of a fire pump, an adapter, a B type hose and 2 C type hoses as shown in Fig 1.

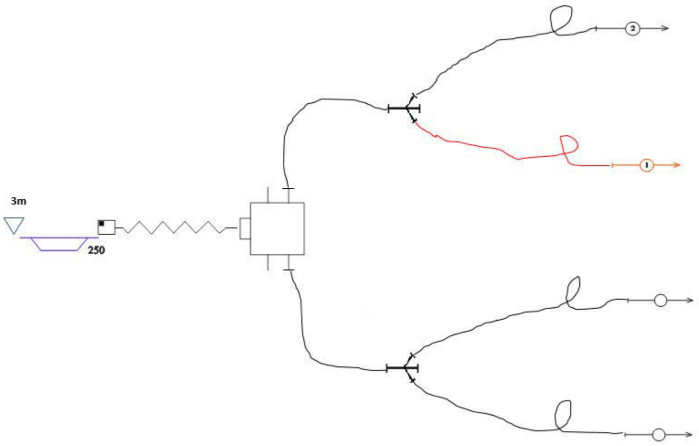

**Fig. 1.** Scheme of the examined firefighting system

The pump model was based a Rosenbauer Fox II type used in everyday practice in EU countries. The pump is powered from an underground water reservoir in suction mode. It was defined as an additional requirement for the firefighting system that the pump to provide the necessary amount of water and a pressure of 5 bar required for the operation of nozzles of DIN EN 15182-3 at a height of 10 meters. In order to meet our expectations a Q=0.00343 $m^3/s$ (206 l/min) flow rate should be provided at each water spray jet of the system. The diameter of the inlet is 52 mm and the diameter of the outlet is 12 mm of the nozzle. The length of the hoses all together is 40 m.

## 3. Simulation model

The simulation model was created in Simulink (Fig. 2). It is modular, easily expandable and made of subsystems.

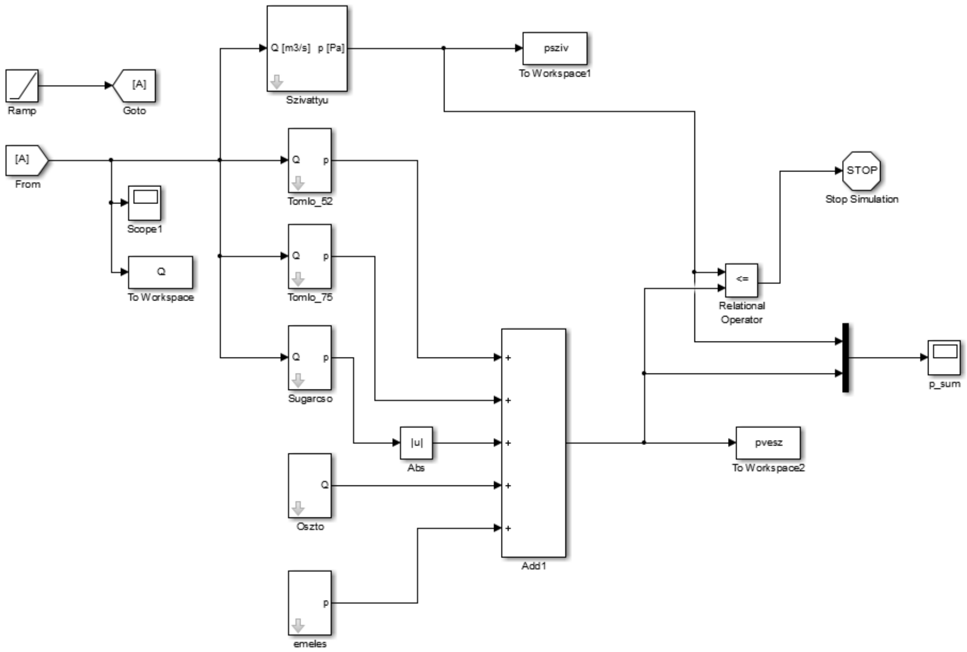

**Fig. 2.** Simulink model of the firefighting system

The subsystems are the following: pump, hoses, nozzle, adapter and lifting height. The subsystems are masked in order to change the parameters easily. The input variable is the flow rate and the output variables are the pressure of the pump (pressure side) and the total pressure loss in the system.

The pump subsystem is shown in Fig 3.

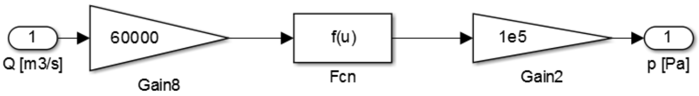

**Fig. 3.** Pump subsystem

The equation describing the subsystem is the following [1]:

$$p\,[bar] = n^2 \sqrt{1 - \left( i \frac{Q\,\left[\frac{l}{min}\right]}{2000} \cdot \frac{1}{n} \right)^2} \tag{1}$$

where *Q* is the flow rate, *p* is the pressure of the pump, *n* is the speed ratio compared to the maximum speed ($n_{max}$=4500 RPM) and *i* is the number of water spray jets. In the subsystem the speed ratio (n) and the number of water spray jets (i) are the variable parameters.

The pressure loss in the hoses can be calculated by the following equation [1]:

$$p_{hose} = c_d \cdot L \cdot (k \cdot Q)^2 \tag{2}$$

where $c_d$ is the proportionality constant depending on the diameter of the hose, *L* is the length of the hose and *k* is the number of hoses. The subsystem is shown is Fig 4.

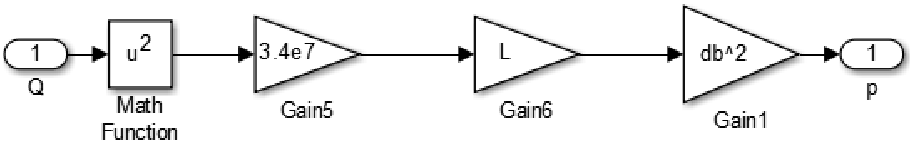

**Fig. 4.** Hose subsystem (C type)

The length (L) and the number of hoses (i) are the variable parameters. The diameter of the hoses was 52 (C type) and 75 mm (B type), which are standardized diameters. The proportional factor was only known for standardized hoses; therefore, the diameter of the hoses was constant in this study. In the future the diameter of the hose is also planned to be variable to test the systems behaviour in configurations different from the standardised hoses.

The pressure drop in the nozzle can be calculated with the following equation:

$$p_n = \frac{\rho}{2} \cdot \left( \frac{1}{A_1^2} - \frac{1}{A_2^2} \right) \tag{3}$$

where ρ=1000 kg/m$^3$ is the density of water, $A_1$ is the cross section at the inlet of the nozzle and $A_2$ is the cross section at the outlet of the nozzle. The cross section can be calculated with the following equation:

$$A = \frac{d^2}{4\pi} \tag{4}$$

From equations (3)-(4) the subsystem of the nozzle can be created (Fig. 5). A 96% efficiency is given in the standard, which is also taken into account.

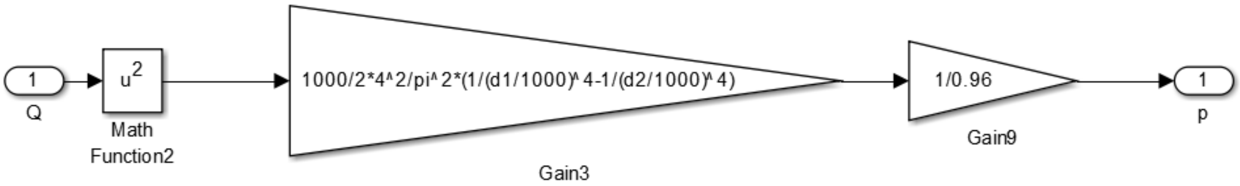

**Fig. 5.** Nozzle subsystem

The variable parameters of the subsystem are the inlet and outlet diameters.

The subsystem of the adapter is shown in Fig 6. According to literature the pressure drop in case of an adapter is 0.69 bar [7]. It has only a single variable parameter, which is the number of adapters.

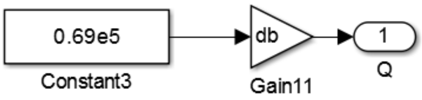

**Fig. 6.** Adapter subsystem

The subsystem of the lifting height is shown in Fig 7. Theoretically a 10 m height causes 1 bar pressure drop [2]. The height is the variable parameter.

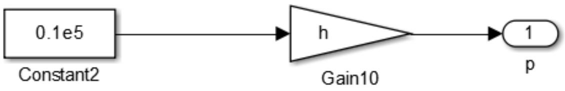

**Fig. 7.** Lifting height subsystem

## 4. Simulation results and parameter sensitivity study

First the pressure at the pump and the pressure loss in the system were calculated in case of the initial configuration (Q=3.43e-3 [$m^3/s$], i=4, n=0.78). The pressure can be seen in Fig. 8 left. It can be observed that the pressure at the pump is 6.8734e5 Pa and the pressure loss is 6.7989e5 Pa. The results are the same as calculated in [1]. There are only small differences in the pressure loss compared to the results of [1], because a slightly different nozzle model was used for easier testing and expandability. The model was then tested with increasing flow rate. The simulation was stopped, when the pressure loss was greater than the pressure at the pump (Fig. 8 right).

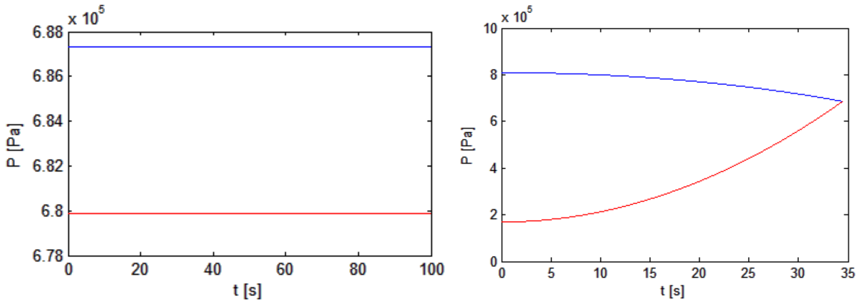

**Fig. 8.** Pressure in the original configuration (left) and increasing flow rate (right) (blue: pressure of the pump, right: pressure loss)

For sensitivity study the maximum flow rate which can be extracted in case of a configuration was selected. The flow rate was increased until the simulation stopped and the last value was stored in a list. Then the maximum flow rate versus the varied parameter was plotted in a diagram. From the diagrams the sensitivity can be measured with a sensitivity index, which can be calculated as follows:

$$SI = \frac{\Delta Q_{max}\ [\%]}{\Delta a\ [1\%]} \tag{5}$$

where *Δa* is the 1% change in the selected parameter. To measure sensitivity the following Fuzzy sets were established [8]:

- not sensitive: SI<=1
- moderately sensitive: 1<SI<=5
- sensitive: 5<SI<=10
- extremely sensitive: 10<SI

The parameter is considered sensitive, when there is a parameter range in the extremely sensitive or the sensitive Fuzzy set.

The sensitivity of the speed ratio and the lifting height are shown in Fig 9.

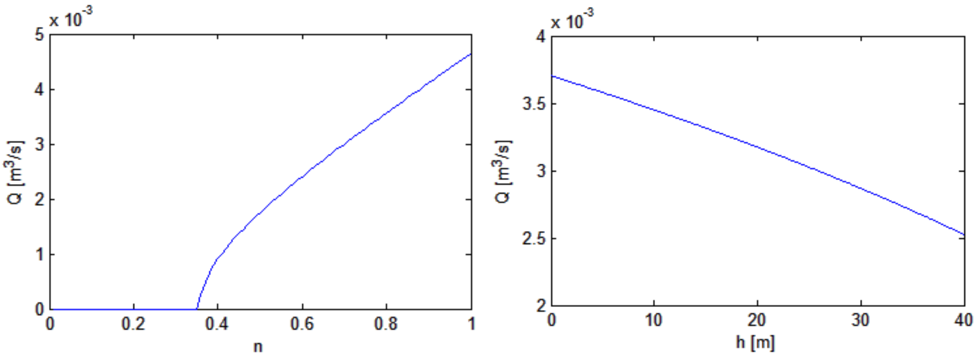

**Fig. 9.** Sensitivity of the speed ratio (left) and the lifting height (right)

The speed ratio is not sensitive when n<0.36. Till this speed ratio there is no fluid flow in the system. When 0.36<n<0.4 the parameter is extremely sensitive, SI=19.5. When 0.4<n $Q_{max}$ increases linearly. In this range SI=4.68, therefore the parameter is moderately sensitive.

The sensitivity of the lifting height changes almost linearly during the entire examination range. SI=0.3, therefore this parameter is not sensitive.

In Fig.10 the sensitivity of the nozzle inlet and output diameters are shown.

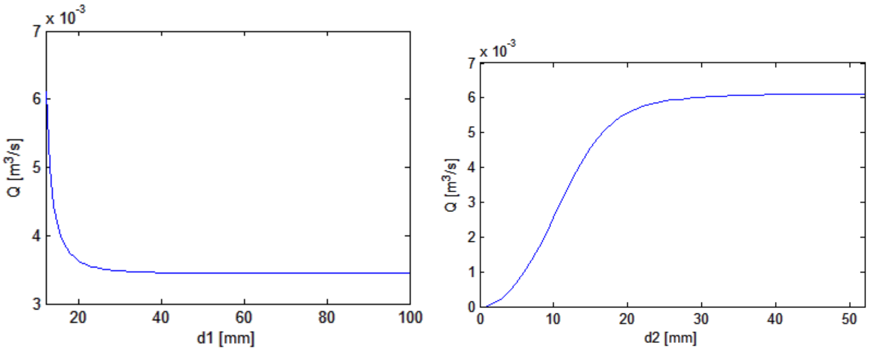

**Fig. 10.** Sensitivity of the inlet diameter (left) and the outlet diameter (right) of the nozzle

When the inlet diameter is small ($d_1$<10 mm) it is moderately sensitive with SI=2.667. When 10<$d_1$<22 mm it is not sensitive, SI=0.5. When $d_1$ is further increased the maximum flow rate remains the same, therefore this parameter is not sensitive. When the outlet diameter of the nozzle is small ($d_2$<4) it is moderately sensitive with SI=3.2. When 4<$d_2$<18 it is moderately sensitive (SI=4.33). When this parameter is further increased it is not sensitive (SI=0.17). It can be observed that the inlet diameter is more sensitive than the outlet diameter.

In Fig.11 the sensitivity of the hose lengths is shown.

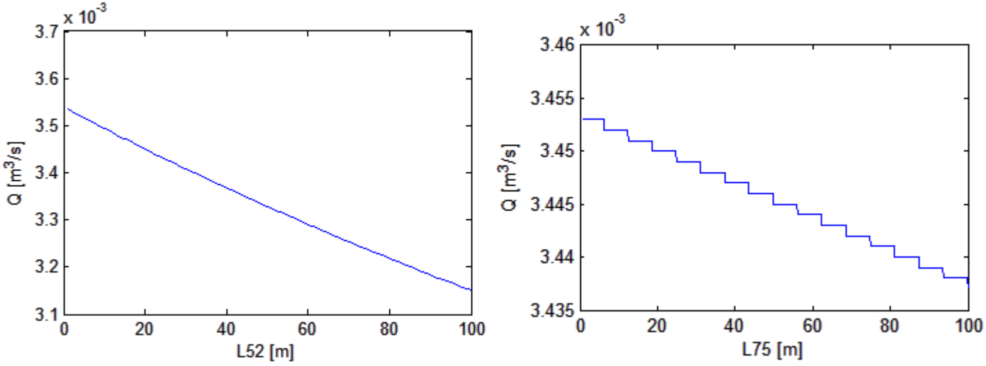

**Fig. 11.** Sensitivity of the hose length (left: C type, right: B type)

It can be seen that the maximum flow rate decreases almost linearly as the length of the hoses is increased. These parameters are not sensitive, $SI_{max}$=0.067 and $SI_{max}$=0.0026.

It can be concluded that the speed ratio of the pump is the most sensitive parameter, only it has range in the extremely sensitive Fuzzy set. All the other parameters are moderately sensitive or not sensitive. With this study it was proved that the examined firefighting system is well designed, there are no weak points. Except the speed ratio of the pump the parameter values are in the not sensitive range. With this study it was shown that the pump is the most critical element of the system. Therefore, an important further research task is to develop a pump model and carry out its sensitivity analysis in more detail.

## 6. Conclusions

In this study the operation parameters of a firefighting system were examined. In order to facilitate and accelerate calculations a modular, easily expandable simulation model was created in Simulink and numerical simulations were performed. Analyzing the results it can be concluded that in case of water spray jets operated in different system configurations there are differences in the maximum amount of water that can be extracted. It should be taken into account during firefighting tasks. It was also observed that significant pressure losses occur inside the system. With the simulation model the parameter sensitivity study of the subsystems was carried out. From the sensitivity study it was concluded that the pump is the most critical element, therefore in the future it will be further examined with more detailed simulation models and field measurements. All the other elements are moderately sensitive or not sensitive. Another research task is to expand the model further and examine other configurations as well. In the future using the model and numerical simulations, fire department exercises can easily be used to test assembled firefighting systems. Experience from the simulations can also be put into practice to avoid problems with water supply due to improper operation.

### Acknowledgments

This study was supported by the ÚNKP-19-3-III-SZE-11 New National Excellence Program of the Ministry for Innovation and Technology.

## References

[1] Hajdu F., P. Horváth, and R. Kuti. "Examination of useful fluid transport in case of centrifugal pumps/ Hasznos folyadékszállítás vizsgálata centrifugálszivattyúk alkalmazásánál." *Védelem Tudomány* 2, no. 1 (2017): 304-317.

[2] Szabó, B.L. *Knowledge of water supply/ Vízellátási ismeretek*. Budapest, BM Könykiadó, 1983.

[3] Lajos, T. *Basics of hydrodynamics/ Az áramlástan alapjai*. Budapest, Műegyetemi Kiadó, 2004.

[4] Spurgeon, P. "Every Pump Operator' Basic Equation." *Fire Engineering* 165, no. 10 (2012): 51-64.

[5] Pázmándy, M. *Water supply of firefighting / A tűzoltás vízellátása*. Budapest, BM Könyvkiadó, 1979.

[6] Hajdu, Cs., and R. Kuti. "Designing Complex Technical Rescues with a Proprietary Application (Computer Program)." *Academic and Applied Research in Military and Public Management Science* 17, no. 1 (2018): 45-52.

[7] ***. Fire Department Hydraulics: Basic Concepts & Formulas, *Studylib*. Accessed 19.11.2019. http://studylib.net/doc/8256726/fire-department-hydraulics.

[8] Hajdu, F. "Sensitivity Study of a Nonlinear Semi-Active Suspension System." *Acta Technica Jaurinensis* 12, no. 3 (2019): 205-217.

# Marine Impressed Current Cathodic Protection System

PhD. Student **Mihail-Vlad VASILESCU**[1]**,** Prof.PhD.Eng. **Mariana PANAITESCU**[2]**,**
Prof.PhD.Eng. **Fănel-Viorel PANAITESCU**[3]

[1] Maritime University of Constanta, vladmihail_2005@yahoo.com

[2] Maritime University of Constanta, panaitescumariana1@gmail.com

[3] Maritime University of Constanta, viopanaitescu@yahoo.ro

***Abstract:*** *The paper presents Marine Impressed Current Cathodic Protection system like a method of protection of the ship against corrosion. By installing and developing ICCP systems, we minimize the risk of failures or major renewals of hull structures, propeller and other still or iron parts of the vessel, which can be attacked by corrosion, during the ship's expected life time and like this also ship owners can cut down repair costs.*
*This article major points are: how to design and choose the best Impressed Current Cathodic Protection system - ICCP for a ship, what are the main components and how it works an ICCP system, types of anodes, what parts of the ship the ICCP system can protect, installation of the system components and maintenance.*

***Keywords:*** *ICCP, ship, protection, corrosion, design*

## 1. Introduction

For improving the corrosion protection design and for extension of ship's life time, marine industry had given a great attention to modelling and understanding of electrochemistry-current distribution. Because steel and iron are used as a shipbuilding material, corrosion of ship's hull was identified as a serious problem.
The area most affected is at the after end of a vessel - an area of high wave turbulence and adjacent to the bronze propeller which creates a galvanic couple causing pitting of the adjacent steel.
Some ship owners have a bad habit. In order to decrease dry dock stay costs, they cut anodes and put them away soon after the ship has been cleaned and inspected for repair, not thinking about the purpose of the anodes and about life and environment protection. They do not understand that in time expenses will be much higher, then the economy that they try to achieve now by cutting the anodes.
Cathodic Protection has been widely used for protecting structures from corrosion. The design of Cathodic Protection Systems normally relies on a combination of experience and experimental data.
Problems and failures of Cathodic Protection systems is not only an economic cost, but it can also present a threat to life and the environment.
Impressed Current Cathodic Protection (ICCP) systems can be installed on all types of ships:

- Cruise Ships
- Container Vessels
- VLCCs
- Ferries
- FPSOs
- Ice Class Vessels

Most operators recognize the need to combine modern hull coatings with a purpose designed Impressed Current Cathodic Protection system.

## 2. Computer modelling

Modelling is more than just a representation of the actual structure. It is a methodology for advancing the understanding of system performance. It is a methodology for determine relative importance of the many factors that have an influence on system performance.

Recent research in computer modelling, are using different programs like Ansys Fluid, AutoCAD 3D. They have enabled the performance of Cathodic Protection systems in protecting metallic surfaces, to be predicted by simulating the environment and the electrochemical processes on the metallic surfaces (Figure 1).
These advances have been applied on offshore, marine installations and on ships.

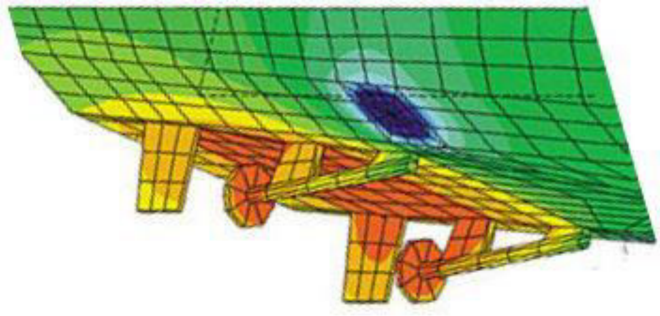

**Fig. 1.** Modelling of Cathodic Protection of ship

Predicting the Cathodic Protection systems in the marine environment is an important application area of computer modelling.
Using the software enables the designer to develop a full 3D virtual prototype of the vessel and its Cathodic Protection system.
**Advantages of using a computer modelling program:**

- The designer can assess the performance of ICCP system;
- Optimize the design by varying parameters such as anode location, reference electrode location and number of anodes;
- Investigate interference effects caused by nearby Cathodic Protection systems, electrical sources and metallic structures;
- Determine the protection potential, corrosion rates and the life of the Cathodic Protection system;
- Evaluate the effect of different operating environments and their impact on the effectiveness of the Cathodic Protection system;
- Evaluate the performance of the Cathodic Protection system under potential damage scenarios;
- Predict the ICCP Control system behaviour using the ICCP software which simulates its transient dynamic response under working condition
- Possibility of modelling any geometry including ships, platforms, pipelines, storage tanks and others.

The design process for Cathodic Protection of marine structures includes various necessary input parameters and the decisions, which must be made.
**There are design considerations to take in account like:**

- Determine the current density requirement, which is based largely upon environmental parameters.
- The net cathodic current is then calculated.

They are determined various aspects in the design like anode selection, sizing, number and placement [1][2].

## 3. Corrosion

**In principle, the major factors that must be considered in protecting a hull from corrosion are:**

- The nominal wetted surface area which requires protection;
- The material characteristics of metallic components exposed to the seawater

- The chemical aspects of the bulk electrolyte (seawater) under operational conditions (seawater conductivity, pH, dissolved oxygen and surface reactions).

These reactions are influenced by: the temperature, velocity and diffusion properties of the surfaces, both with and without Cathodic Protection applied.

The growth of calcareous deposits, on the ship hull, while cathodic ally protected, all surfaces may foul with marine organisms, resulting in a biological system that will further influence the surface properties of the metals involved.

The principle of Cathodic Protection is that, when connecting an external anode to the metal, to be protected and the passing of an electrical DC current so that all areas of the metal surface become cathodic and therefore do not corrode. The external anode may be a galvanic anode, where the current is a result of the potential difference between the two metals, or it may be an impressed current anode, where the current is impressed from an external DC power source [3].

**This corrosion process is caused by:**

- Difference in natural potential, in galvanic couples;
- Metallurgical variations in the state of the metal at different points on the surface;
- Local differences in the environment, such as variations in the supply of oxygen at the surface.

Corrosion takes many forms in the marine environment. It can be seen as pitting on hull plates; in the disintegration of weld seams; around bow thrusters and on the surfaces of rudders and other vital components (Figure 2).

**Fig. 2.** Corrosion on hull plate

A well designed ICCP system can eliminate these problems, safeguarding the structural integrity of the vessel and significantly reducing maintenance costs throughout its operational life.

Metallic corrosion is an electro-chemical reaction in which the metal combines with a non-metal, such as oxygen, to form a metal oxide or other compound. This depends upon the nature of the environment.

Different metals have different tendencies to corrode, activity or potential. These potentials can be tabulated and form the electro-chemical series.

A more practical approach is the determination of the tendency of certain metals to corrode in a particular electrolyte, such as sea water [4][5].

## 4. Cathodic Protection

### 4.1 Introduction

Some metals and alloys have two positions in the series, marked Active and Passive.

The active position is equivalent to the position if corrosion is occurring and approaches the electro-chemical series position for the material.

The passive position relates to a non-corroding situation where the material is protected by a self-forming surface film.

If two metals are placed in an electrolyte (e.g. sea water or damp soil) and are in direct electrical contact, a current will pass through the electrolyte from the more active metal onto the least active metal (Figure 3). The least active metal does not corrode and is termed the cathode. The more active metal, the anode, passes into solution and the flow of electrical current increases. This is a metal ion and electron transfer process - corrodes.

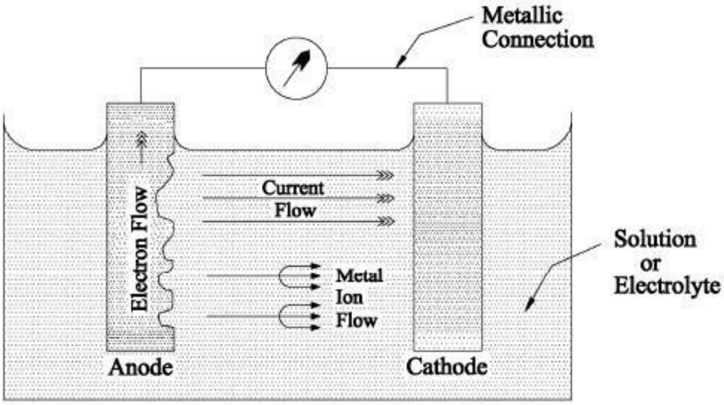

**Fig. 3.** Simple Corrosion Cell

The anodic and cathodic areas in a corrosion cell may be due to the electrical contact of two dissimilar metals, galvanic corrosion. Anodic and cathodic areas may be formed on a single metal surface as micro-cells for instance by rain drops on uncoated steel. Alternatively, they may be close but discrete cells found when accelerated corrosion occurs at uncoated anodic areas on a generally coated cathodic structure.

In addition, there are long line type cells that occur on pipelines that pass through aggressive low resistivity soils. These sections form anodic areas and corrode in preference to cathodic areas in less aggressive higher resistivity soils.

Large currents can occur at small anodic areas and lead to rapid corrosion of marine structures such as ship's internal tanks, external hull plates, sheet steel piling in harbors and tubular structures common in jetties and petrochemical drilling and production platforms.

Cathodic Protection is a system of preventing corrosion by forcing all surfaces of a structure to be cathodes by providing external anodes.

As described above, a galvanic corrosion cell occurs when dissimilar metals are in contact with each other within an electrolyte. Care should be taken in the construction of structures that will be buried or immersed in an electrolyte to ensure a galvanic cell is not created [6].

**Galvanic cells can be:**

- Steel or cast iron water boxes in contact with nonferrous (often copper based) tube plates in condenser water boxes in ships or generating plant. Rapid corrosion of the ferrous water box occurs close to the tube plate.
- Brass or bronze valves fitted to immerse steel buoyancy tanks or flooding chambers on marine petrochemical structures. Accelerated corrosion of the steel occurs near the valve.
- The connection of steel pipes into an otherwise cast iron system. Accelerated corrosion of the steel occurs near the cast iron sections.

Sacrificial anode Cathodic Protection achieves corrosion prevention on a particular structure or component by forming galvanic cell where an additional anode of zinc, magnesium or aluminium corrodes in preference to the structure. The galvanic corrosion current (see simple cell before) available from this anode/electrolyte/structure combination should be sufficient to overcome the local surface corrosion currents on the structure until no current flows from anodic areas of the structure. The structure is entirely cathodic or under complete Cathodic Protection [7][8].

The potential, or measure of activity, between the structure and the electrolyte is a relatively easily measured indication of whether the structure is anodic or cathodic.

For steel under normal non anaerobic conditions it can be shown theoretically, and is accepted practically, that a steel / electrolyte potential more negative than -0.85 volts measured against a standard copper / copper sulphate ref cell indicates that Cathodic Protection is achieved. This is equivalent to -0.80 volts measured against silver / silver chloride ref cell and + 0.24 volts against a zinc ref cell.

### 4.2 Sacrificial anode Cathodic Protection

As indicated previously, a metal can be made cathodic by electrically connecting it to a more anodic metal within the electrolyte. The most commonly used anodic metals are alloys of aluminium, zinc and magnesium. Anodes of these metals corrode preferentially, the corrosion current of the anode achieving cathodic protection of the structure to which they are connected. The anodes deteriorate as an essential part of their essential part of their function and they are therefore termed sacrificial.

Cathodic-protection systems can be monitored effectively by the measurement of structure-to-electrolyte potentials, with a high input impedance voltmeter and suitable half-cell (copper/copper sulphate, silver/silver chloride/seawater, silver/silver chloride/potassium chloride and zinc) [9].

### 4.3 Impressed current Cathodic Protection

Impressed Current Cathodic Protection system consists essentially of several anodes, reference electrodes and control units. All of them being inter-connected. Types, sizes, positions of the components are all around the hull, being specified according to design parameters.

A metal also can be made cathodic by electrically connecting it to another metallic component in the same electrolyte through a source of direct electric current and directing the current flow to occur off the surface of added metallic component (anode), into the electrolyte and onto the metal (cathode). This can easily be visualized by reference to the simple cell and assuming yet another ref cell with a power source is introduced and that the current flow from this ref cell is sufficient to overcome the natural corrosion current.

Because an external current source is employed, this type of protection is termed 'Impressed Current Cathodic Protection' – ICCP (Figure 4).

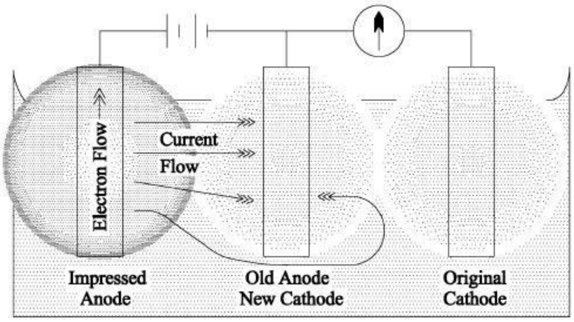

**Fig. 4.** Cathodic Protection Applied to a Simple Corrosion Cell

A source of direct current is required. This is generally obtained from mains power units that contain a transformer and rectifier.

The magnitude of this current may be automatically controlled in response to a continuous monitor of the cathode/electrolyte potential or may be manually controlled after intermittent measurement.

The impressed current anode material is ideally non-consumed by the passage of current from it into the electrolyte, in practice the materials used are a compromise between this ideal and the cost and physical properties of available materials. Impressed current anodes are made from graphite, silicon iron, lead alloys some with platinum di-electrodes, platinized titanium or more exotic combinations such as platinum clad niobium. The selection of the correct anode material is critical in the formulation of an effective and economic Cathodic Protection scheme [10].

Generally, for a given current demand, less impressed current anodes than sacrificial anodes are required for protection, as high anode currents are feasible (Figure 5).

Impressed current systems of cathodic protection are more sophisticated in design than sacrificial systems (Figure 5, Figure 7).

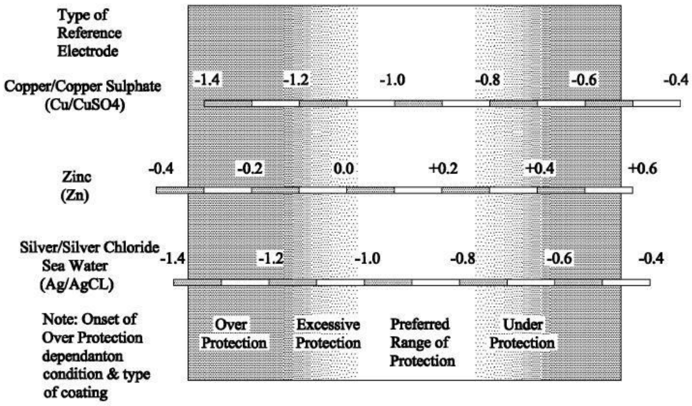

**Fig. 5.** Comparison of Reference Electrodes and Interpretation

Attention must be given to the propeller, any exposed shafting and to the rudder with the main hull structure protected. The propeller and the exposed shaft are protected by grounding the shaft to the hull structure with a shaft slip ring to make this appendage electrically common with ship's hull. Bonding rudder stock to ship’s hull grounds the rudder and in this way the rudder is also protected by the digital system (Figure 6).

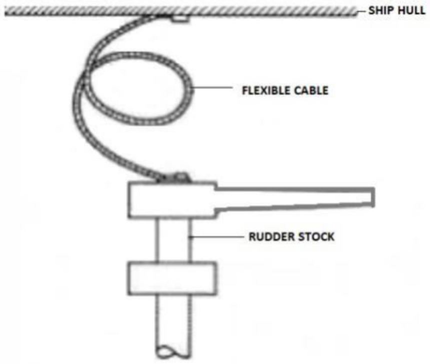

**Fig. 6.** Rudder stock bond

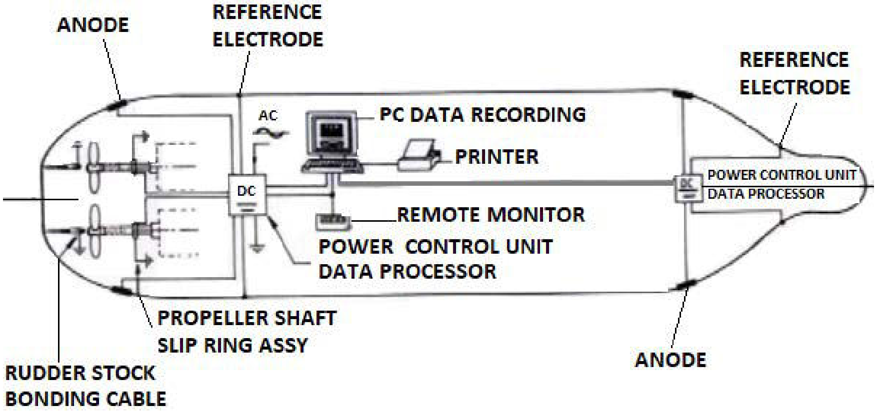

**Fig. 7.** Impressed Current system for ship

## 4.4 Marine Impressed Current system components

The Marine Impressed Current system comprises the following components (Figure 8):

- Rudder bonding;
- Linear loop anode;
- Remote monitoring unit;
- Shaft earthing assembly;

- Control panel;
- Reference cell.

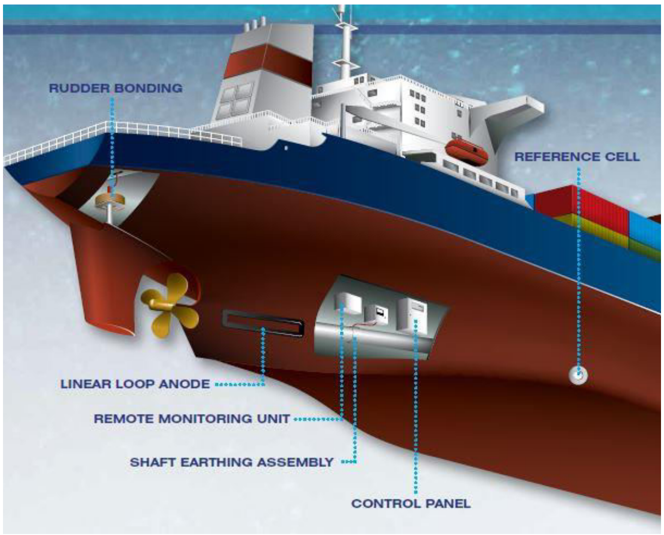

**Fig. 8.** Marine Impressed Current system

### 4.4.1 Impressed Current anodes

The driving voltage for Cathodic Protection in this type of system is provided by an external power supply and so, inherent electrochemical potential difference between structure and anode have no consequences. In this case also the type of anode is important for an effective and efficient operation.

**Anodes can be:**

- Linear loop anodes (Figure 9);
- Circular anodes (Figure 10);
- Elliptical anodes (Figure 11).

**Linear Loop Anodes**

Produce a powerful output from a relatively small surface area. Light weight and easy to install.

**Fig. 9.** Linear Loop Anodes

Ideally suited to vessels where a smooth hull profile is required. Can be flush mounted in areas where space is limited.

**Fig. 10.** Circular Anodes

**Elliptical Anodes**

The elliptical shape enhances current distribution. Provides the flexibility to fit into complex hull profiles.

**Fig. 11.** Elliptical Anodes

It is necessary that anode must be surrounded with a protective shield to avoid very high cathodic current density in the immediate vicinity of the anode, like enclosing anode with neoprene shield. An electrical control device automatically changes current required for cathodic protection. Reference electrodes are used to monitor the protection and to know whether all the structures are protected.

The function of the anode is to conduct the DC protective current into the sea water. Anodes have been designed to perform this function whilst maintaining a low electrical resistance contact with the sea water. Standard surface mounted anodes are available with from 50 to 300 Ampere ratings. For forward mounted systems and for special applications 50 ~ 175 Ampere recessed anodes are available.

Materials now used by Anodes have now gone beyond lead alloy with specialist coated titanium based Anodes now available. All anode designs utilize a tough, chlorine resistant, but slightly flexible plastic carrier.

The use of a 24-volt system reduces the number and length of the anodes from that required with a 12-volt system. The increased anode / sea water resistance resulting from this decrease in anode size is overcome by the additional voltage.

The potential of the hull steel to the sea water is unaffected by this increase in driving voltage, as the resistive effects are local to the anode and the hull/sea potential is a function of the current flow, the sea water and the coating condition, not the driving voltage.

The electrical connections to the active surface are made at the back of the anode and are fully encapsulated and protected by the hull penetration. Recessed anodes of essentially similar construction are provided for bow section applications.

All hull penetrations are provided with substantial double plates and cofferdams. The penetrations themselves are made watertight with heavy duty packing glands, the cofferdams are full sealed and provided with watertight cable glands, all conforming to the requirements of Classifications Societies [11].

### 4.4.2 Impressed current reference electrode

The high purity, high stability, zinc ref cells are designed to give a stable reference against which the hull/sea potentials can be measured and a small current flow that is used in the closed loop circuit to maintain the present levels of protection. The construction and the quantity of zinc employed within the electrodes are such that a minimum life of ten years is available without maintenance or replacement.

The minimum number of ref cell per power supply is one although normally two will be fitted. Ideally, these should be located a minimum of 7.5 meters distant from the anodes. In the case of a stern only installation with the anodes more than 200 meters from the bows, one ref cell may be located in the bows.

A novel feature of the closed circuit is that additional reference cells may be placed at areas that may be susceptible to over-protection such as adjacent to the anode dielectric shields. These additional reference cells provide a permanent check, thus preventing any coating damage due to over-protection if conditions of operation change from those anticipated. This feature is offered as an optional extra to the standard schemes.

All hull penetrations are provided with substantial cofferdams. The penetrations themselves are made watertight with heavy duty packing glands. The cofferdams are fully sealed and provided with watertight cable glands [12][13].

### 4.4.3 Bonding

To enable the rudder to receive protection it is provided with a dedicated electrical bond in the form of a flexible cable from the top of the rudder stock to the main ship structure. In the same way any stabilizers are bonded to allow protective current to these surfaces.

To allow protection of the bare propeller and any exposed shafting and to prevent electrical arcing between shaft and bearings the propeller shaft is fitted with a slip ring assembly as optional items. A set of brushes provide the completion of a low resistance path to allow current to flow to the propeller blades along the shaft and back to the hull.

The slip ring track is silver plated as standard and in addition silver graphite brushes are used to minimize contact resistance [14][15][16].

### 4.4.4 Shaft earthing

#### 4.4.4.1 Introduction

A turning propeller shaft on a ship becomes electrically insulated from the hull by the lubricating oil film in the bearings and by the use of non-metallic bearing materials in the tail shaft. When the shaft is insulated in this way an electrical potential can be measured between the shaft and the hull and this can accelerate corrosion in the ship. If the ship has a system of cathodic protection, whether it is sacrificial anode or an impressed current system, the shaft insulation will prevent the propeller and the boss from receiving protection.

The electrical potential between the shaft and the hull can also cause a heavy current to flow in bearings when the oil film breaks down or is contaminated with seawater. This current can cause deep pitting of the bearing surface. Excessive wear on the shaft bearings can often be traced to this cause.

Now in addition it's necessary to reduce the spark erosion causing the excessive wear on main engine metal bearings and this shaft earthing is the most appropriate method. All the troubles can be avoided and cathodic protection can be extended to the propeller if the shaft is properly earthed with a propeller shaft slip ring. The effectiveness of the shaft earthing system should ensure a maximum contact resistance of no greater than 0.001 ohms for a water filled bearing and 0.01 ohms for an oil filled bearing.

Our own tests indicate that high silver content brushes running on a silver track have repeatable low conductivity that can maintain these limits and ensure a low resistance contact is maintained even under dirty conditions.

The shaft earthing assembly comprises a pair of high silver content/graphite compound brushes mounted in balanced brush holder, running on a silver alloy slip ring.

Each brush holder has an adjustable spring tensioner which is supplied present to the minimum [17][18].

At this pressure the expected life of the brush is approximatively one year.

#### 4.4.4.2 Design base

- Intermediate shaft diameter: Ø 655 mm

#### 4.4.4.3 Installation work by shipyard

- Assembling the intermediate shaft earthing assembly;
- Attaching the intermediate shaft monitoring millivolt meter & wiring;
- Welding the brush holder support bar and assembling the brush holder.

#### 4.4.4.4 Installation

- Weld the mounting post(s) nearby shaft where slip ring is installed (Figure 12).
- Weld the support bar(s) carefully on mounting post according to the drawing.

- Slip ring.

It is strictly required to install slip ring correctly according to following procedure for the good performance of shaft earthing and longer life time of brushes.

- Make clean the area where slip ring is positioned.

The area should be cleaned and prepared for bright bare steel.

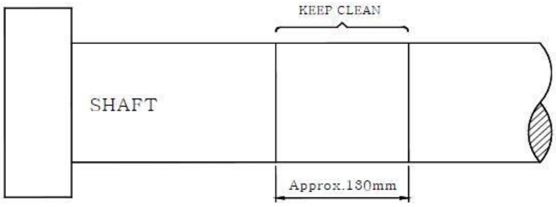

**Fig. 12.** Slip ring position

- Fasten stainless steel bands (A & B) temporarily (Figure 13).

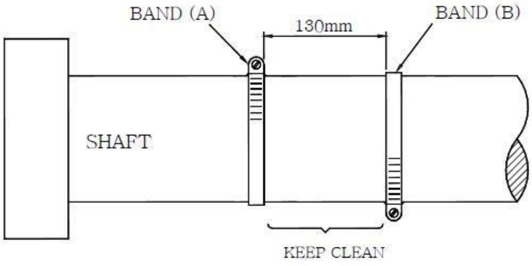

**Fig. 13.** Fasten stainless steel bands

- Put the slip ring around the shaft and mark the overlapped part. Cut the overlapped part at an angle of 45 Ø carefully (Figure 14).

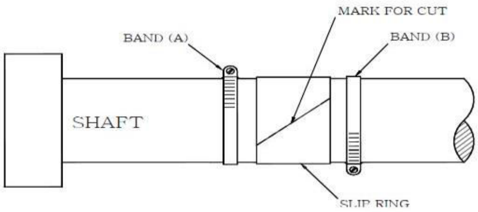

**Fig. 14.** Slip ring around the shaft

After cutting properly rub the both edges of inner surface of slip ring with a fine-mesh file or sand paper as below. Then secure slip ring very tightness around shaft (Figure 15).

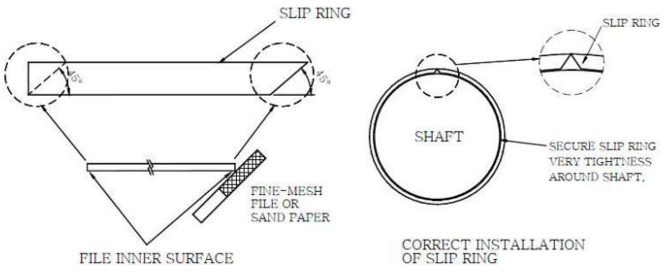

**Fig. 15.** Inner surface of slip ring

- Fasten the slip ring around the shaft by the tightening stainless steel band (B) (Figure 16). When the slip ring is tightly installed no protrusion or gap is found. In case there happens with protrusion or gap smoothly rub the protrusion with sand paper.

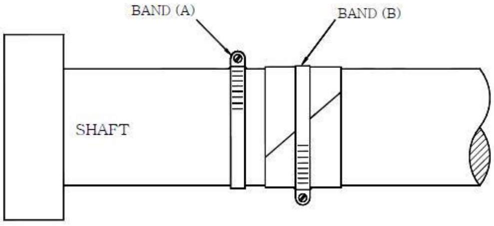

**Fig. 16.** Fasten the slip ring around the shaft

- Fasten the both edges of slip ring with 3/4” (19mm) pressure tape for a preparation of tight fastening of stainless steel band (Figure 17). Apply the tape to the slip ring five times at the opposite direction of the shaft rotation.

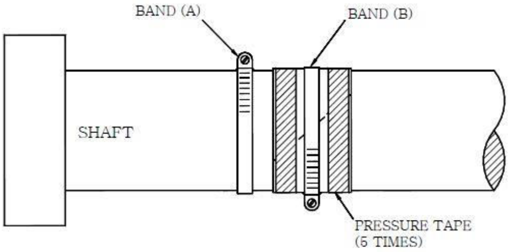

**Fig. 17.** Fasten the both edges of slip ring

- Fasten the stainless steel band (A) over the pressure tape tightly by tightening fixing bolt around the edge of slip ring (Figure 18).

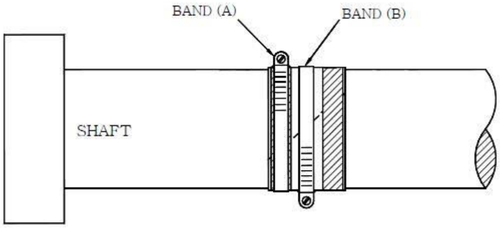

**Fig. 18.** Fasten the stainless steel band (A)

- Fasten the stainless steel band (B) over the pressure tape tightly by tightening fixing bolt around the edge of slip ring (Figure 19). After tightening bands (A, B), bend the end part of band to the opposite direction to prevent loosening when the shaft rotates.

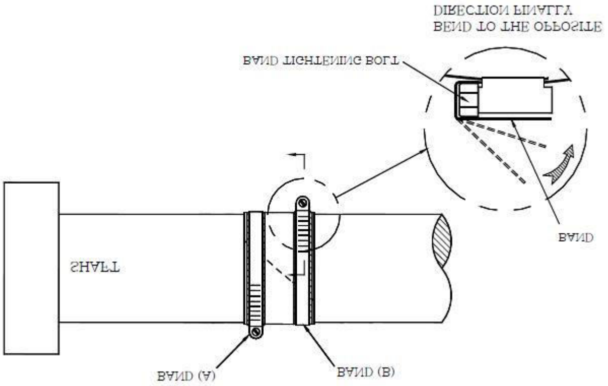

**Fig. 19.** Fasten the stainless steel band (B)

- Apply 2"(50mm) tape over both stainless steel bands (A & B) at the opposite direction of the shaft rotation finally (Figure 20). Keep the minimum 30 mm width of slip ring where brushes run.

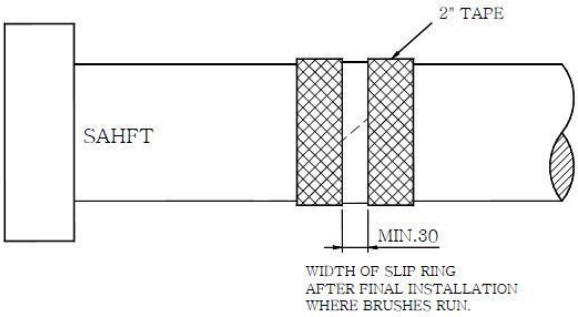

**Fig. 20.** Apply tape over both stainless steel bands (A & B)

➢ **Brush holder**

- Carefully study the drawing for correct installation and keep the distance of 3mm between bottom of brush holder and slip ring surface.
- Fit the brush holder to the support bar and align the assembly so that the brushes are able to run centrally on the slip ring, and the brush holders assembly is to be clear of the slip ring securing brackets when the shaft rotates.

Secure the assembly in this position by tightening the hexagon headed bolt at the top of the brush holder bod [19][20].

- The support bar for double brush holder should be connected to the hull electrically. So, the bracket(support) supplied by shipyard should be welded on the hull plate. The touched bracket surface should be galvanized to ensure metal touch in case the bracket will be installed by bolting.

➢ **Shaft monitoring millivolt meter (Digital type)**

- The system comprises a bulkhead mounted panel that incorporates terminals and a digital display meter.
- The meter has a high internal resistance that restricts current flow in the circuit to minimal levels and thus minimizes the volt drop between the slip ring and the monitor brush. The meter therefore accurately displays the potential difference between the shaft and hull.
- For ease of interpretation the display meter is scaled up to 250mV. As the meter reading rises above 80mV it is recommended that the slip ring and brushes to be checked and cleaned.
- The earthing cables of mV meter and double brush holder should be connected separately.

#### 4.4.4.5 Operation

➢ The millivolt meter normally reads 250mV full scale.

➢ Reading of below 80mV when shaft is turning at sea indicate proper grounding. If readings are above 80mV, clean the faces of slip ring and brush with a clean cloth.

➢ The millivolt meter will read '0' when shaft is at rest because of the current entering the propeller will return to the hull through main engine bearings and engine foundation.

➢ Check according to troubleshooting in case the millivolt meter reading is '0' when shaft is turning at sea.

#### 4.4.4.6 Maintenance and service

➢ This grounding assembly should be checked at least twice a week for cleanliness.

➢ If there has been a build-up of oil, dirt, scale and rust on the slip ring face or between slip ring and shaft, this should be removed with a degreaser, emery paper and clean cloth.

➢ Inspect and clean the brushes and brush holder to prevent their moving due to dirt build-up. Inspect the brush copper leads (pig tails) to ensure they have not become loose or corroded. The brush wear-down should be noted.

- At the time of every dry dock, disassemble the slip ring and clean the surface of the shaft right thereunder.

### 4.4.4.7 The life time of brushes

- The brushes are getting worn out by metal touch with slip ring.

Therefore, it's strictly required to keep clean and smooth surface of slip ring, also to carry out proper installation/alignment of brush holders as per our manual and drawing. Otherwise it's very hard to obtain the proper earthing and the proper life time of brushes.

- The brushes are consumable parts with wearing ratio approximately 2~3mm per 1,000 hours shaft rotation under proper installation. The replacement time is shown by engraving the line (15mm from the top) on the brushes.

Customer is requested to replace brushes with spares when the time comes.

- Brushes are consumable parts as stated above and they are often consumed earlier but it's not a matter of guarantee claim for supplying extra brushes.
- Use only our genuine silver graphite brushes for longer life and higher earthing efficiency [21].

### 4.4.5 How to select the best ICCP system for a ship

**Designing steps for an ICCP system are as following:**

- Select the current density to be applied from the results of Cathodic protection tests and from any available data;
- Compute the total current requirement to achieve the required current density;
- Design the DC wiring systems for the most economical cable size in accordance with standard electrical practices and then calculate the total IR drop in the circuit;
- Select rectifier voltage and current outputs;
- Design the electrical circuits, fittings and switchgear in accordance with standard electrical practice;
- Select the location of cathodic protection test station;
- Prepare project drawing and specification [22][23][24].

### 4.4.6 Modern ICCP system C-Shield

### 4.4.6.1 Introduction

A modern ICCP system is C-Shield, which suppresses corrosion on the wetted surface of the hull using an arrangement of hull mounted anodes and reference cells connected to a control panel (Figure 21). This neutralizes 'corrosion cells' and eliminates problems that arise through dissimilar metals and the proximity of components such as propellers.

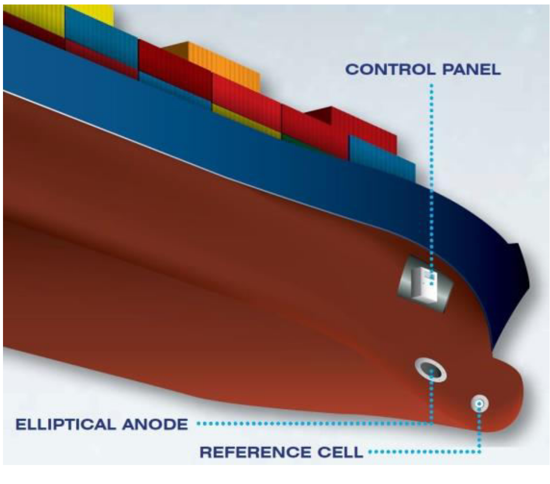

**Fig. 21.** C-Shield system

### 4.4.6.2 Thyristor control panels

C-Shield system is using thyristor control panels which combine cost effectiveness with rugged reliability that has been proved on vessels of all sizes worldwide. They also incorporate the latest computerized information systems enabling the status of the ICCP system to be monitored by ships' computers.
Thyristor control panels can be used for systems of up to 1,000 amps with 8 anodes and 4 reference cells being controlled by an individual panel. They are ideal for the requirements of cruise ships, VLCCs and many types of container and cargo vessels.
The popularity of these panels means that they can generally supplied within relatively short lead times.

**Thyristor control panel characteristics:**

- For ICCP systems of up to 1,000 amps.
- Reliable performance with minimum attention.
- Economical control for systems of all sizes.
- Combines computerised output displays, alarms and information systems.
- Can have up to 8 anodes and 4 reference cells per panel.
- Easily configured to clients' requirements.
- Relatively easy maintenance.

### 4.4.6.3 Maintenance

- Diver Change Anodes

Can be changed from the outside of the hull by a diver. Ideal for FPSOs and vessels with long intervals between dry docking (Figure 22).

**Fig. 22.** Anodes

- Reference Cell

Designed to measure the electrical 'potential' at the seawater/hull interface (Figure 23).

**Fig. 23.** Reference Cell

### 4.4.6.4 C-Shield modular control panels

Is based on advanced computerized electronics and is designed for installations of up to 350 amps. Extremely lightweight and compact in design, it can be easily installed in engine rooms and requires the minimum of attention from the crew. One of the major advantages of the unit is that the modules are interchangeable and can be quickly removed and replaced if necessary, thereby offering greater reliability.

**C-Shield modular control panel characteristics** (Figure 24)**:**

- For ICCP systems of up to 350 amps.
- Modular design for greater reliability and flexibility.
- Extremely lightweight and compact.
- Clear digital output displays.

- Incorporates 'under' and 'over' protection alarms
- Can be linked to bridge information systems

**Fig. 24.** C-Shield modular control panel

- **Minitek Panels**

The Minitek system has been designed to protect smaller steel hulled vessels against corrosion. It has been widely installed on tugs, fishing vessels and workboats where engine room space is at a premium.

**Minitek Panels characteristics** (Figure 25)**:**

- Operates from 230V AC electrical supply;
- Control panel measures 600mm x 600mm x 210mm;
- Far superior to sacrificial anode systems where output cannot be verified.

**Fig. 25.** Minitek Panel

- **Alutek Panels**

The Alutek system provides carefully controlled protection for aluminium hulls using an arrangement of flush mounted anodes, monitoring electrodes, controlling electrodes and di-electric shield sensors.

**Alutek Panels characteristics:**

- Operates from 230V or 115V AC electrical supply;
- Control panel measures 400mm x 500mm x 210mm;
- Lower yard installation cost than recessed sacrificial anode systems.

**4.4.6.5 Shaft Earthing** (Figure 26)

Even on ships fitted with ICCP or sacrificial anode systems, propeller shaft bearings are vulnerable to corrosion.

This is because turning propeller shafts are electrically insulated from the hull by the lubricating oil film in the bearings and by the use of non-metallic bearing materials in the tail shaft.

The problem can be eliminated if the shaft is earthed to the hull using a propeller shaft slip ring. A complete shaft earthing assembly is consisting of a pair of high silver content/ graphite compound brushes mounted in a balanced brush holder, running on a copper slip ring with a solid silver inlay track. This combination has been proved to give the optimum electrical continuity. The number of brushes depends on the size of the vessel. Smaller craft have a single brush holder [25] [26].

**Fig. 26.** Shaft Earthing

- **Installation**

Installation is simple. The shaft slip ring is supplied as two matched halves, complete with band and clamping arrangement.

The balanced brush holder is supplied ready for fitting to a shipyard-supplied 20mm diameter rod and mounting bracket.

Each brush holder has an adjustable tensioner to ensure good electrical contact and maximum brush utilization.

### 4.4.6.6 Propeller shaft potential monitoring (Figure 27)

It has a compact millivolt meters to monitor the potential between the shaft and the hull and verify the effectiveness of the system.

The meters can be located in a convenient position for monitoring by the crew.

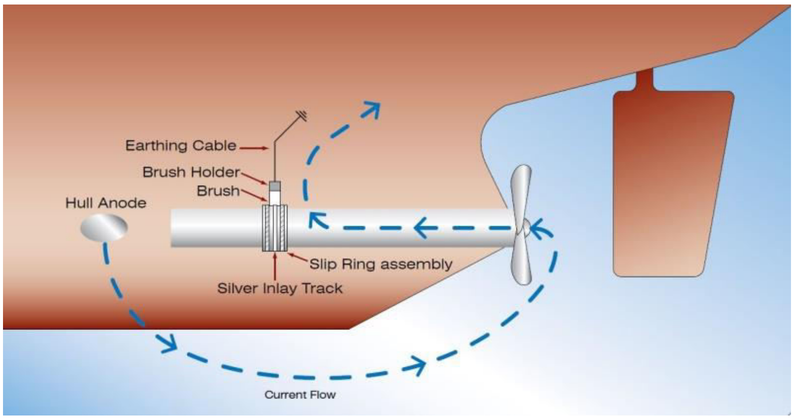

**Fig. 27.** Propeller shaft system

### 4.4.6.7 Large Thruster Tunnel ICCP Systems (Figure 28)

For bow and stern thruster protection there was developed a specialized system which is uniquely effective in providing corrosion protection.

Problems of corrosion arise because of the dissimilarity of the materials used in the hull and thruster tunnel construction and remain unchecked because they are outside the scope of conventional ICCP systems.

Specialized thruster tunnel systems are installed on ocean going vessels, harbor tugs and in offshore oil and gas applications.

The equipment consists of a power unit/controller and an arrangement of reference cells and anodes positioned on either side of the tunnel. The anodes and reference electrodes are flush mounted to maintain the optimum performance of the thrusters and reduce the effects of turbulence which can accelerate corrosion.

This has a number of advantages in comparison with sacrificial anode systems where anodes are much heavier, have to be checked at regular intervals and replaced at each dry docking. In contrast, this new specialized system for protection of bow and stern thruster provides carefully monitored, precisely delivered corrosion protection for a design life of up to 15 years (Figure 29).

The system operates continuously when the vessel is at sea, but when the impeller is activated during docking, the equipment is automatically shut down using a fail-safe switching system which is installed by the shipyard. This prevents any stray current damage occurring to the bearings and seals [27][28][29].

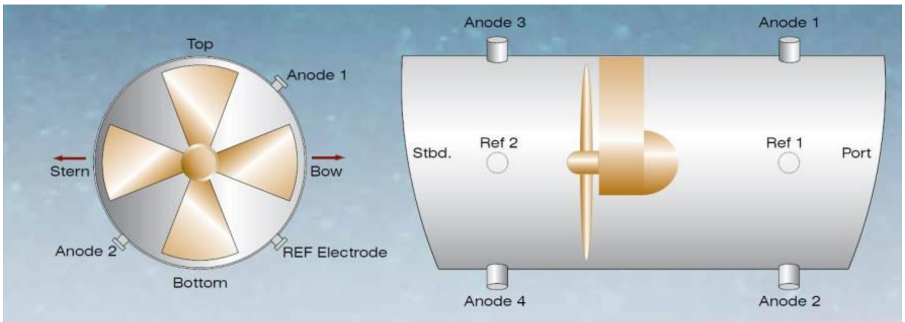

**Fig. 28.** Large Thruster Tunnel ICCP Systems

**Fig. 29.** Corrosion in and around thruster tunnel [30]

## 5. Conclusions

Cathodic Protection of steel in seawater is when a sufficient number of electrons from a preferred external source, are applied to the surface of the metal being protected. The electrons from external source, accommodate with the cathodic reaction such as hydrogen evolution or oxygen reduction. Without this protection, the electrons would react with oxygen at the cathodic surfaces and they would be covered by corrosion at the anodic areas. When additional electrons are supplied from an external source, they accommodate to the oxygen reduction reaction.
As a result, to the use of ICCP C-Shield, significant savings result had been demonstrated.
First time when they appeared ICCP systems had seem to be very expensive to install than sacrificial anode systems, but because of the escalating price of zinc, the differential cost between the two has been reduced, making ICCP systems competitive and even a more attractive proposition, from the economic point of view.
Sacrificial anodes have a lot of disadvantages. The main one is that they have to be renewed at periodic dry docking intervals as they become consumed, this resulting in on-going replacement costs for the ship owners.
By using a modern ICCP system like C-Shield, with special anodes, they can last for many years and achieve a more much reliable level of protection without the extra weight or drag which is inevitably associated with sacrificial methods.
Major operational savings result from the use of ICCP C-Shield. A smooth hull, free from corrosion ensures the lowest fuel consumption for the vessel that means more money saved by the ship owners.
Data collected in time, has shown that unprotected vessels, after as little as 2.5-3 years, can require an additional 30% increase in shaft power to maintain service speed, that means more money splendid on fuel, because of high consumption.
Throughout by using the ergonomic design of modern ICCP system like C-Shield, we can ensure the high reliability commensurate with minimal installation time. The lowest cost system may leave the installer with the highest work load.

By using a competitive ICCP system in combination with modern hull coatings, ship owners, can save money, protect life and environment.

**References**

[1] Mathiazhagan, A. “Design and Programming of Cathodic Protection for ships.” *International Journal of Chemical Engineering and Applications* 1, no. 3 (October, 2010): 217-221.
[2] Mathiazhagan, A. “Corrosion Management.” 2014. Accessed October 01, 2019. http://www.iacsit.org.
[3] Trethewey, K.R, and J. Chamberlain. *Corrosion for Science and Engineering*. UK, Longman Publishing Ltd, 1995, 375.
[4] Laque, F.L. *Marine Corrosion: Causes and Prevention.* New York, John Wiley & Sons, 1975, 203.
[5] DeGiorgi, V. G., E. Hogan, K.E. Lucas, and S.A. Wimmer. *Shipboard impressed current cathodic protection system (ICCP) analysis*. Naval Research Laboratory, Washington, DC, United States, WIT Press, 2005.
[6] DeGiorgi, V.G. ”Corrosion Prevention System Parameters”, 1997. Accessed October 04, 2019. http://www.witpress.com.
[7] ***. *Guidance for Corrosion Protection System of Hull Structure-CPS*. Japan, Class NK, 1995.
[8] Jones, D.A. *Principles and prevention of Corrosion*. New York, Maxmillan Publishing Co., 1992, 439.
[9] Pearson, J.M. *Fundamentals of Cathodic Protection for Marine Service*. Technical Report, New York, USA, Society of Naval Architects and Marine Engineers, 2010.
[10] Darchivio, F., A. Cassanelli, and S. Simison. *Cathodic protection of ship hull by galvanic anodes: design evaluation*. Mar del Plata, Buenos Aires, Argentina, NACE International, 2009.
[11] K.C. Ltd. “I.C.C.P. System”, 2018. Accessed October 02, 2019. http://www.iccp-mgps.com/iccp/iccp01.html.
[12] Thomas, E.D., and A.R. Parks. *Proceedings of Corrosion 89*. Houston, NACE International, 1989.
[13] Parks, A.R., E.D. Thomas, and K.E. Lucas. *Proceedings of Corrosion 90*. Houston, United States, NACE International, 1990.
[14] Gartland, O. *Proceedings of Corrosion 93*. Houston, United States, NACE International,1993.
[15] Bardel, E.R., R. Johnsen, and P.O. Gartland. *Corrosion.* Houston, United States, NACE International,1984.
[16] Morgan, J.H. *Cathodic Protection*. London, Leonard Hill, 1959.
[17] Shrier, L.L. *Corrosion*. Volume 2, London, Newnes-Butterworths, 1977.
[18] McGrath, J.N., D.J. Tighe-Ford, and L. Hodgkiss. *Corrosion Prevention and Control*. Washington, DC, United States, Alpha Science, April, 1985.
[19] Munn, R.S. *Computer Modeling in Corrosion.* West Conshohocken Pennsylvania, United States, ASTM International, 1992, 215-228.
[20] Adey, R.A. *Galvanic Corrosion*. West Conshohocken Pennsylvania, United States, ASTM International, 1988, 96-117.
[21] Adey, R.A. *Computer Modeling in Corrosion*. West Conshohocken Pennsylvania, United States, ASTM International, 1992.
[22] Ulhig, H.H., and R.W. Revie. *Corrosion and Corrosion Control*. New York, John Wiley and Sons, 1985.
[23] Frechette, E., C. Compere, and E. Ghali. *Corrosion Science*. Paris, France, Institut Français de Recherche pour l'Exploitation de la Mer,1991.
[24] Wimmer, S.A., V.G. DeGiorgi, E. Hogan, and K.E. Lucas. *Proceedings 2002 Tri Service Corrosion Conference*. Washington,DC, United States, In Press, 2003.
[25] Trethewey, K.R., and J. Chamberlain. *Corrosion for Science and Engineering*. UK, Longman Publishing Ltd, 1995, 375.
[26] Rietdekkerstraat, B.V. *Cathodic Protection Manual*. UK, Materials Metingen Europe, 2010.
[27] Laque, F.L. *Marine Corrosion: Causes and Prevention.* New York, John Wiley & Sons, 1975, 203.
[28] Mathiazhagan, A. “Corrosion Management” 2014. Accessed October 01, 2019. http://www.iacsit.org.
[29] Jotun. ”Paints & Coatings”, 2017. Accessed October 01, 2019. http://www.jotun.com.
[30] Evac Group. “*ICCP* hull corrosion prevention”, 2018. Accessed October 03, 2019. http://www.cathelco.com.

**ISSN 1453 – 7303** **“HIDRAULICA” (No. 4/2019)**
**Magazine *of Hydraulics, Pneumatics, Tribology, Ecology, Sensorics, Mechatronics***

# Experimental Research on the Processing of Convex Spherical Surfaces with Toroidal Mills versus Spherical Mills

PhD. Student Eng. **Andrei OȘAN**[1]

[1] Technical University of Cluj-Napoca - North University Center of Baia Mare, Romania,
osan.andrei@yahoo.com

***Abstract:*** *The surface roughness plays a very important role on the wear layer, on the precision as well as on the lubrication environment. In terms of determining the quality of the surface, this is a complex process and highly influenced by the process factors. The present paper aims to determine the roughness of the convex spherical surface by using two types of mills with different geometries. The toroidal and spherical mills are subject to comparison. The processing with the two types of milling machines presents the processing with three variable regimes the rest keeping cash. In addition to determining the best quality obtained and the shortest execution time.*

***Keywords:*** *Roughness, toroidal milling, spherical milling, optimum regimes, surface quality*

## 1. Introduction

Surface roughness is one of the most important parameters to determine the quality of the product. The process of forming the roughness is very dynamic, complex and process dependent. There are two types of factors that influence the surface finish and implicitly the surface quality of a workpiece. The first factors are the kinematic geometry of the tool which theoretically affects the surface and can be calculated from so-called processing parameters and controllable factors such as rotational speed, feedrate and cutting depth. The second category of factors is represented by the nongeometric components including tool wear, work material deformation, vibration, tool deformation as well as errors of movement of the machine axes.

The roughness, as an important parameter of the surface layer, has a special influence on the wear resistance, the fatigue resistance, the corrosion resistance and the precision of the adjustments. In the case of the free adjustments, the irregularities (asperities) determine the decrease of the actual bearing surface compared to the theoretical one, considered in calculations, which produces local increases of the contact pressure, sometimes, far above those considered in the dimensioning calculations. These have the effect of accelerated wear of the surfaces in contact and the increase of the games, especially during the first period of operation (the period of running), the more accentuated the higher the initial roughness (technological). These effects justify the application of correct rolling programs of the adjustments after assembly.

Mike S. Lou et al. [6] states that surface roughness is an important measure of the technological quality of a product and a factor that greatly influences the cost of production. Surface quality plays a very important role in the performance of the processing through a good quality processed surface that significantly improves wear resistance or corrosion resistance. In addition, surface roughness also affects the friction surface, light reflection, the ability to retain a lubricant as well as electrical or thermal resistance.

Nowadays, the researchers carry out active studies on the quality of the surface introduced by the milling process of the different orientations of the tools. Toh studied in high speed milling of hardened steel and obtained a high cutting force when using a negative feed angle and minimal surface roughness when positive [9]. Gani established a geometrical model of the machining process and discussed the influence of the tool orientation on the five-axis milling process, and the results were verified experimentally [3]. According to a previous paper the results indicate that the tool orientations have a great influence on the surface roughness, surface morphology and residual loading, but little on the microhydration [8].

Daymin achieved the best surface finish when the inclination angle of the workpiece is 25 ° and the average compression stress slightly decreased at a larger angle of the workpiece [2]. Ko considered the cutting force, surface roughness and tool wear, the results indicating 15 ° of the tilt angle of the workpiece were optimal [5]. Aspinwall studied the influence of tool orientation and tilt angle on surface integrity, results showed a downward horizontal orientation, providing better surface roughness, cutting force and tool wear obtained the highest residual compression pressure when the workpiece was machined without inclination angle [1]. Kalvoda indicated that positive or negative feed angle and tilt angle had a reduced effect on residual loading and provided the best surface roughness when both angles were negative, but the worst is when there is no inclination [4]. Min Fu studied the adjustment of the inclination angle which can optimize the cutting conditions, reduce the surface roughness and ensure the best surface quality when the angle between the tool axis and the vertical surface of the workpiece is 15 ° [7].

## 2. Presentation of the experimental stand

The experiments will be carried out on a 5-axis numerical control center OKUMA MU-400VA. This is a fast and precise vertical CNC that offers superior simultaneous workability in 5 axes simultaneously. The Okuma MU-400VA has a rotary table that offers a plus in 5-axis processing as well as a fast and precise positioning and at the same time a rigidity in offering outstanding performance.

The spherical-convex surface is represented by a recess at the top of the plate; it is positioned in the center of the plate representing the distance of 5mm from the maximum spherical recesses to the flat surface. The convex spherical shape has a diameter of Ø85 mm as shown in the following figure.

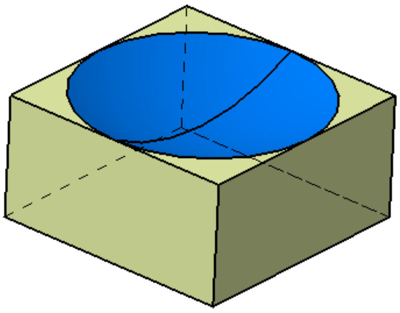

**Fig. 1.** The convex spherical surface

The TR200TIME roughness meter is used to measure the roughness, this tester is applied on the production site and can be used to measure the roughness of the surfaces of the different processed parts, to calculate the parameters according to the selected measuring conditions and to clearly display all the measuring parameters and on-screen profile graphics.

The two cutting tools used are: toroidal milling machine JHP780160E2R400.0Z4-M64 and spherical head milling machine JS534160D1B.0Z4-NXT.

## 3. The experimental part

During this research we will experimentally study the realization of 27 convex spherical surfaces with toroidal milling as shown in table 1 and 27 convex spherical surfaces processed with spherical milling as presented in table 2. In addition, these tables contain a column where the runtime of each test is passed. These times refer strictly to the moment of processing, the rest of the time being considered constant so that they were no longer considered for the study. Regarding the cutting regimes only the 3 presented in the tables vary the rest remain cash. Here we can talk about the cutting depth equal to 0.5 mm (ap = 0.5 mm) and the radial depth equal to 0.3 mm (ae = 0.3mm). During processing it is present as a cooling liquid, the emulsion. Discussing the clamping mode, the plates will be clamped in a fingerprint clamp being a rigid and secure system. In order for each experiment to be able to differentiate, I decided to write down with SFCX-TR the convex spherical surfaces processed with the toroidal milling and with SFCX-SF the convex spherical surfaces processed with the spherical milling.

**Table 1:** Carrying out experiments on the processing of convex spherical surfaces with toroidal milling

| No. | Cutting speed [m/min] | Tilt angle [°] | Feed/tooth [mm/dinte] | Program name SFCX-TR | Time [min] |
|---|---|---|---|---|---|
| **1** | 80 | 15° | 0.11 | SFCX-TR-1 | 06:05 |
| **2** | 80 | 15° | 0.15 | SFCX-TR-2 | 04:37 |
| **3** | 80 | 15° | 0.19 | SFCX-TR-3 | 03:46 |
| **4** | 80 | 35° | 0.11 | SFCX-TR-4 | 06:06 |
| **5** | 80 | 35° | 0.15 | SFCX-TR-5 | 04:38 |
| **6** | 80 | 35° | 0.19 | SFCX-TR-6 | 03:48 |
| **7** | 80 | 55° | 0.11 | SFCX-TR-7 | 06:43 |
| **8** | 80 | 55° | 0.15 | SFCX-TR-8 | 05:08 |
| **9** | 80 | 55° | 0.19 | SFCX-TR-9 | 04:13 |
| **10** | 170 | 15° | 0.11 | SFCX-TR-10 | 03:10 |
| **11** | 170 | 15° | 0.15 | SFCX-TR-11 | 02:29 |
| **12** | 170 | 15° | 0.19 | SFCX-TR-12 | 02:05 |
| **13** | 170 | 35° | 0.11 | SFCX-TR-13 | 03:13 |
| **14** | 170 | 35° | 0.15 | SFCX-TR-14 | 02:32 |
| **15** | 170 | 35° | 0.19 | SFCX-TR-15 | 02:08 |
| **16** | 170 | 55° | 0.11 | SFCX-TR-16 | 03:35 |
| **17** | 170 | 55° | 0.15 | SFCX-TR-17 | 02:50 |
| **18** | 170 | 55° | 0.19 | SFCX-TR-18 | 02:24 |
| **19** | 210 | 15° | 0.11 | SFCX-TR-19 | 02:41 |
| **20** | 210 | 15° | 0.15 | SFCX-TR-20 | 02:07 |
| **21** | 210 | 15° | 0.19 | SFCX-TR-21 | 01:48 |
| **22** | 210 | 35° | 0.11 | SFCX-TR-22 | 02:43 |
| **23** | 210 | 35° | 0.15 | SFCX-TR-23 | 02:10 |
| **24** | 210 | 35° | 0.19 | SFCX-TR-24 | 01:51 |
| **25** | 210 | 55° | 0.11 | SFCX-TR-25 | 03:03 |
| **26** | 210 | 55° | 0.15 | SFCX-TR-26 | 02:26 |
| **27** | 210 | 55° | 0.19 | SFCX-TR-27 | 02:06 |

**Table 2:** Carrying out experiments on the processing of convex spherical surfaces with spherical milling

| No. | Cutting speed [m/min] | Tilt angle [°] | Feed/tooth [mm/dinte] | Program name SFCX-SF | Time [min] |
|---|---|---|---|---|---|
| **1** | 280 | 15° | 0.05 | SFCX-SF-1 | 06:53 |
| **2** | 280 | 15° | 0.09 | SFCX-SF-2 | 04:13 |
| **3** | 280 | 15° | 0.13 | SFCX-SF-3 | 03:12 |
| **4** | 280 | 35° | 0.05 | SFCX-SF-4 | 07:18 |
| **5** | 280 | 35° | 0.09 | SFCX-SF-5 | 04:47 |
| **6** | 280 | 35° | 0.13 | SFCX-SF-6 | 03:49 |
| **7** | 280 | 55° | 0.05 | SFCX-SF-7 | 06:04 |

| | | | | | |
|---|---|---|---|---|---|
| **8** | 280 | 55° | 0.09 | SFCX-SF-8 | 03:58 |
| **9** | 280 | 55° | 0.13 | SFCX-SF-9 | 03:00 |
| **10** | 370 | 15° | 0.05 | SFCX-SF-10 | 05:25 |
| **11** | 370 | 15° | 0.09 | SFCX-SF-11 | 03:24 |
| **12** | 370 | 15° | 0.13 | SFCX-SF-12 | 02:38 |
| **13** | 370 | 35° | 0.05 | SFCX-SF-13 | 05:55 |
| **14** | 370 | 35° | 0.09 | SFCX-SF-14 | 04:01 |
| **15** | 370 | 35° | 0.13 | SFCX-SF-15 | 03:17 |
| **16** | 370 | 55° | 0.05 | SFCX-SF-16 | 04:52 |
| **17** | 370 | 55° | 0.09 | SFCX-SF-17 | 03:11 |
| **18** | 370 | 55° | 0.13 | SFCX-SF-18 | 02:32 |
| **19** | 430 | 15° | 0.05 | SFCX-SF-19 | 04:47 |
| **20** | 430 | 15° | 0.09 | SFCX-SF-20 | 03:03 |
| **21** | 430 | 15° | 0.13 | SFCX-SF-21 | 02:23 |
| **22** | 430 | 35° | 0.05 | SFCX-SF-22 | 05:19 |
| **23** | 430 | 35° | 0.09 | SFCX-SF-23 | 03:41 |
| **24** | 430 | 35° | 0.13 | SFCX-SF-24 | 03:03 |
| **25** | 430 | 55° | 0.05 | SFCX-SF-25 | 04:20 |
| **26** | 430 | 55° | 0.09 | SFCX-SF-26 | 02:53 |
| **27** | 430 | 55° | 0.13 | SFCX-SF-27 | 02:20 |

### 3.1 Surface processing

CAM programs were created with the help of Powermill software, a software capable of creating the tool with which to process, but more importantly, a software capable of generating the tool trajectories on the surface to be processed. As an optimum variant, we chose to work in one direction, the tool paths being parallel, with the corresponding inputs and outputs. For the processing of the surface with toroidal milling, the program contains in the case of the 15º inclination a number of 139 lines, for the inclination of 35º, 146 lines and for the 55º inclination, 150 lines. In the case of spherical milling, the trajectory for all three inclines consists of 149 lines. In figure 2 are presented 3 images with the simulation of the convex spherical surface processing in the 3 types of inclinations using the toroidal milling beam and in figure 3 the images during the simulation of the convex spherical surface processing with the spherical milling in the 3 cases of inclinations are presented.

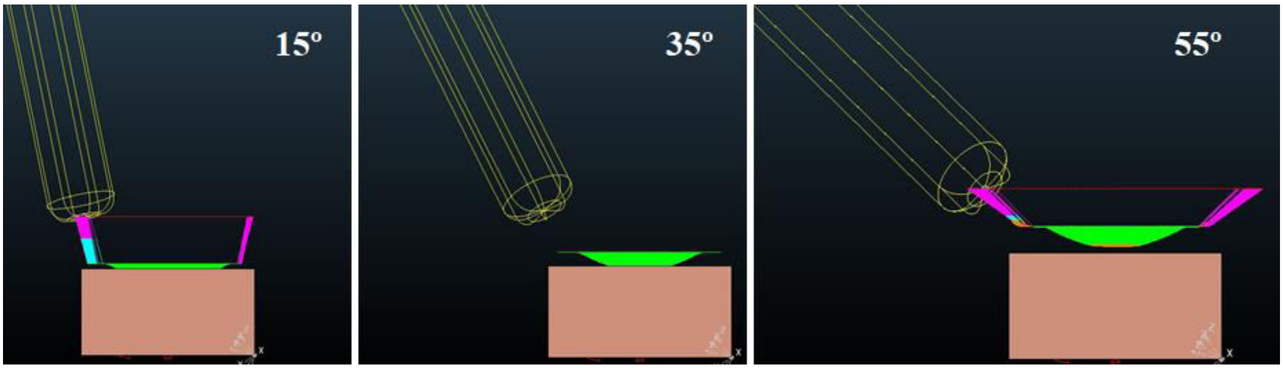

**Fig. 2**. Images taken following the simulation of the trajectory of the toroidal mill in Powermill on SFCX-TR

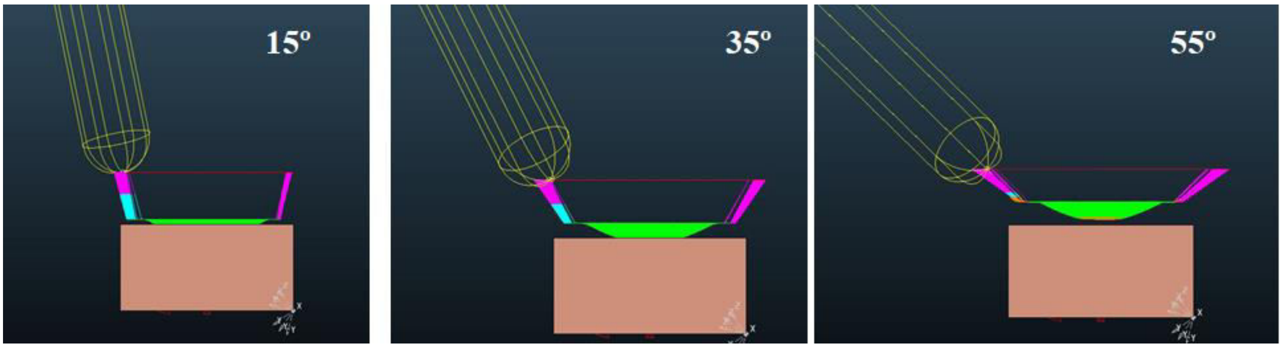

**Fig. 3**. Images taken following the simulation of the trajectory of the toroidal mill in Powermill on SFCX-SF

The practical experiment will be performed on the center with numerical control in 5 axes OKUMA MU-400VA as shown in figure 4 where 3 images are present during the processing of the convex spherical surface with the toroidal milling in the case of the 3 types of inclinations and in figure 5 it is presented processing of the convex spherical surface with the spherical mill in the case of the 3 types of inclinations.

**Fig. 4.** Processing of the convex spherical surface with the toroidal milling in the case of the 3 types of inclinations

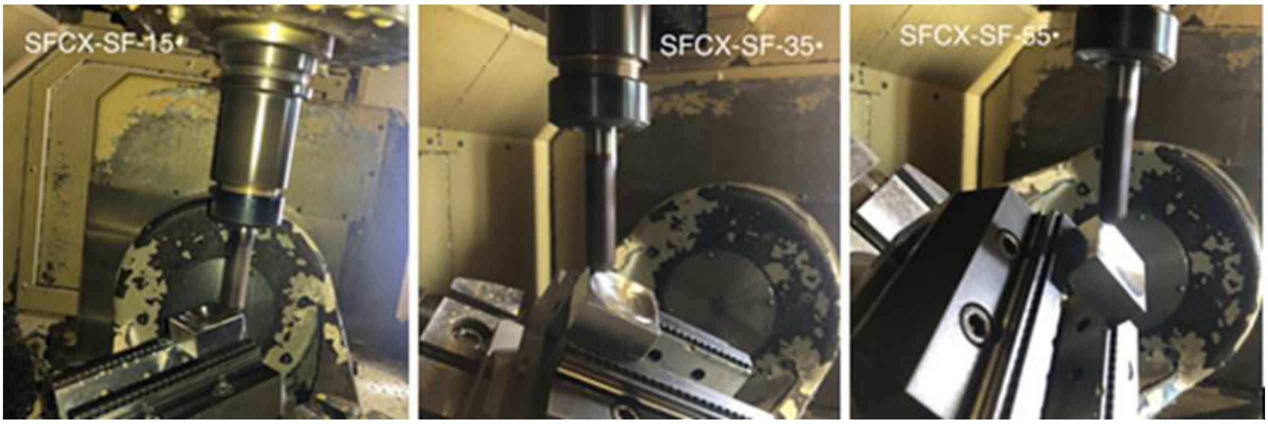

**Fig. 5**. Processing of the convex spherical surface with the spherical mill in the case of the 3 types of inclinations

It is necessary to emphasize that during the whole period of processing of the convex spherical surface with both the toroidal and the spherical mill, the axis of the tool constantly maintains its angle of inclination throughout the surface.

At the end of the experimental work performed on 27 convex spherical surfaces processed with toroidal milling and 27 convex spherical surfaces processed with spherical milling in the following figure are presented the plates prepared to be measured in terms of surface quality.

**Fig. 6.** The convex spherical surfaces processed with the two types of mills prepared for measurement

### 3.2 Runtime analysis

Regarding the execution time, the processing of the convex surface lasts the most in the case of the spherical milling machine with a time of 7 minutes and 18 seconds with the minimum speeds set but at an angle of inclination of 35° compared to the maximum time obtained by the toroidal milling machine of 6 minutes and 43 seconds in the case of minimum speeds and the inclination angle of 55°.

The fastest surface processing was done with the toroidal milling machine in one minute and 48 seconds in the case of maximum speeds at the angle of 15° compared to the minimum time obtained with the spherical milling machine of 2 minutes and 20 seconds also at maximum speeds but at 55° inclination.

From the point of view of the execution time of the most cost-effective surface is the toroidal milling machining at the inclination of the tool axis of 15° following the establishment of the best quality of the surface.

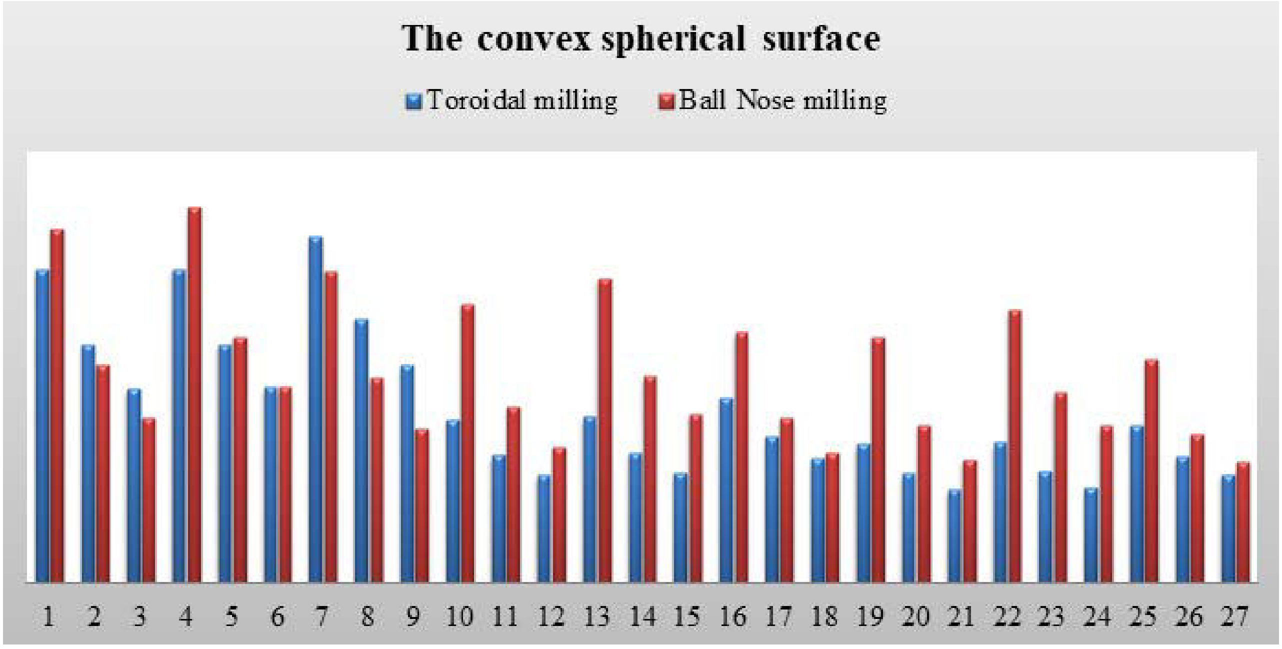

**Fig. 7.** Graphical analysis of the execution times for the processing of the convex spherical surface

### 3.3 Surface quality analysis

The analysis of table 3 reveals the measured values of the roughness on the convex spherical surface processed with the spherical mill. The smallest value of the arithmetic mean Ra was recorded in the parallel direction on the SFCX-SF-15 surface with the value Ra = 0.439 [µm] having variable processing parameters vc = 370 [m / min] fz = 0.13 [mm / tooth] and the inclination of the 35º tool axis. The highest value recorded for Ra is 1,194 [µm] for the SFCX-SF-11 surface processed with vc = 370 [m / min] fz = 0.09 [mm / tooth] and the tool axis inclination of 15º.
According to ISO, the minimum value of the theoretical roughness Rt is recorded with the value of, Rt = 2,567 [µm] on the surface SFCX-SF-15, where the smallest arithmetic mean of the roughness Ra is recorded and the highest value of the theoretical roughness Rt is recorded is 8.133 [µm] measured perpendicular to the feed direction on the SFCX-SF-11 surface where the highest roughness value Ra was recorded.
In the case of the convex spherical surface processed with the toroidal milling cutter the smallest value for Ra is 0.372 [µm] in the case of the SFCX-TR-8 surface processed with vc = 80 [m / min] fz = 0.15 [mm / tooth] and 55º tool axis inclination. The maximum value Ra is 1.199 [µm] measured perpendicular to the feed direction for the SFCX-TR-1 surface processed with vc = 80 [m / min] fz = 0.11 [mm / tooth] and the tool axis inclination of 15º. The minimum Rt value is 2.786 [µm] for the SFCX-TR-8 surface and the maximum value for Rt is 7.606 [µm] for the SFCX-TR-1 surface.

**Table 3:** The results related to the processing of the convex spherical surface with the spherical mill

| Surface type | Roughness Ra[µm] | | Roughness Rt[µm] | |
|---|---|---|---|---|
| | Direction of measurement in relation to the direction of advance | | | |
| | Parallel | Perpendicular | Parallel | Perpendicular |
| **SFCX-SF-1** | 0.595 | 0.492 | 4.101 | 3.246 |
| **SFCX-SF-2** | 0.717 | 0.440 | 4.466 | 3.609 |
| **SFCX-SF-3** | 0.630 | 0.722 | 4.012 | 4.926 |
| **SFCX-SF-4** | 0.563 | 0.582 | 4.613 | 3.746 |
| **SFCX-SF-5** | 0.511 | 0.592 | 3.602 | 4.180 |
| **SFCX-SF-6** | 1.218 | 0.958 | 7.286 | 6.920 |

| | | | | |
|---|---|---|---|---|
| **SFCX-SF-7** | 0.701 | 0.748 | 4.213 | 5.046 |
| **SFCX-SF-8** | 0.915 | 0.634 | 5.646 | 4.693 |
| **SFCX-SF-9** | 0.832 | 0.847 | 5.667 | 5.379 |
| **SFCX-SF-10** | 0.588 | 0.935 | 4.219 | 7.046 |
| **SFCX-SF-11** | 1.194 | 0.992 | 3.680 | 8.133 |
| **SFCX-SF-12** | 0.747 | 0.649 | 4.866 | 5.166 |
| **SFCX-SF-13** | 0.656 | 0.955 | 4.153 | 6.739 |
| **SFCX-SF-14** | 0.651 | 0.465 | 4.866 | 3.280 |
| **SFCX-SF-15** | 0.439 | 0.696 | 2.567 | 7.752 |
| **SFCX-SF-16** | 0.708 | 0.466 | 4.303 | 3.346 |
| **SFCX-SF-17** | 0.667 | 0.645 | 4.846 | 4.560 |
| **SFCX-SF-18** | 0.695 | 0.911 | 4.380 | 7.330 |
| **SFCX-SF-19** | 0.485 | 0.749 | 4.076 | 4.993 |
| **SFCX-SF-20** | 0.503 | 0.620 | 3.599 | 4.373 |
| **SFCX-SF-21** | 0.742 | 0.831 | 4.893 | 5.260 |
| **SFCX-SF-22** | 0.547 | 0.473 | 3.746 | 3.079 |
| **SFCX-SF-23** | 0.532 | 0.511 | 3.136 | 3.993 |
| **SFCX-SF-24** | 0.773 | 0.545 | 6.226 | 3.733 |
| **SFCX-SF-25** | 0.731 | 0.624 | 4.890 | 3.966 |
| **SFCX-SF-26** | 0.896 | 0.746 | 6.033 | 4.793 |
| **SFCX-SF-27** | 0.611 | 0.561 | 4.792 | 3.373 |

**Table 4:** The results of the processing of the convex spherical surface with toroidal milling

| **Surface type** | **Roughness Ra[µm]** | | **Roughness Rt[µm]** | |
|---|---|---|---|---|
| | **Direction of measurement in relation to the direction of advance** | | | |
| | **Parallel** | **Perpendicular** | **Parallel** | **Perpendicular** |
| **SFCX-TR-1** | 0.672 | 1.199 | 3.599 | 7.606 |
| **SFCX-TR-2** | 0.711 | 0.903 | 4.253 | 6.153 |
| **SFCX-TR-3** | 0.653 | 0.702 | 4.339 | 3.900 |
| **SFCX-TR-4** | 0.632 | 0.737 | 4.066 | 4.652 |
| **SFCX-TR-5** | 0.909 | 0.862 | 5.140 | 6.927 |
| **SFCX-TR-6** | 0.705 | 0.979 | 4.567 | 6.033 |
| **SFCX-TR-7** | 0.622 | 0.522 | 3.306 | 3.673 |
| **SFCX-TR-8** | 0.372 | 0.497 | 2.786 | 2.813 |
| **SFCX-TR-9** | 0.641 | 0.881 | 3.873 | 4.619 |
| **SFCX-TR-10** | 0.591 | 0.636 | 3.626 | 5.547 |
| **SFCX-TR-11** | 0.556 | 0.673 | 3.693 | 3.899 |
| **SFCX-TR-12** | 0.629 | 0.887 | 3.693 | 6.920 |
| **SFCX-TR-13** | 0.622 | 0.544 | 4.113 | 5.173 |
| **SFCX-TR-14** | 0.697 | 0.634 | 3.953 | 5.686 |
| **SFCX-TR-15** | 0.721 | 0.717 | 3.953 | 5.386 |
| **SFCX-TR-16** | 0.604 | 0.506 | 3.360 | 2.780 |

| | | | | |
|---|---|---|---|---|
| **SFCX-TR-17** | 0.530 | 0.551 | 2.927 | 3.580 |
| **SFCX-TR-18** | 0.588 | 0.798 | 3.486 | 4.506 |
| **SFCX-TR-19** | 0.520 | 0.453 | 3.827 | 4.287 |
| **SFCX-TR-20** | 0.624 | 0.486 | 4.020 | 4.073 |
| **SFCX-TR-21** | 0.540 | 0.999 | 4.400 | 6.566 |
| **SFCX-TR-22** | 0.673 | 0.488 | 6.587 | 3.286 |
| **SFCX-TR-23** | 0.691 | 0.760 | 5.146 | 4.792 |
| **SFCX-TR-24** | 0.763 | 1.003 | 3.899 | 7.100 |
| **SFCX-TR-25** | 0.550 | 0.480 | 3.039 | 2.793 |
| **SFCX-TR-26** | 0.625 | 0.599 | 3.767 | 3.226 |
| **SFCX-TR-27** | 0.599 | 0.572 | 3.273 | 2.086 |

Comparing the quality of the convex spherical surfaces, the smallest value of the roughness Ra is integrated by the toroidal milling process with a difference of 0.067 [µm]. Regarding Rt, the smallest value is recorded by the spherical milling process, with a difference of 0.219 [µm] compared to the toroidal milling.

The convex spherical surface was a challenge in the tool path, representative for me was the realization of a spherical convex surface with both spherical and toroidal milling. From the point of view of the surface quality, the toroidal mill has a slight advantage over the spherical mill, the inclination angle being 55º, where at this angle and the toroidal milling wear is smaller than the spherical milling wear.

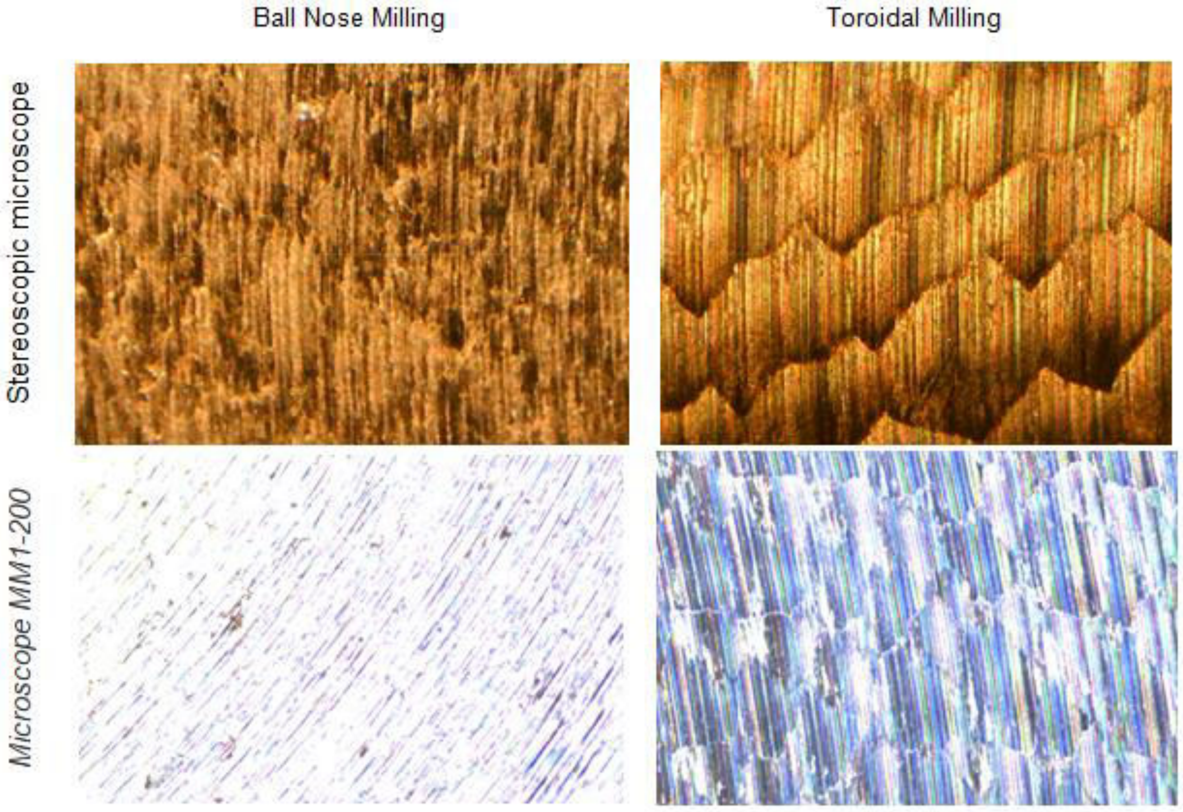

SFCX-SF-15 Ra=0,439 [µm]
Vc=370 [m/min] fz=0,13[mm/dinte]; angle of inclination 35°

SFCX-TR-8 Ra=0,372 [µm]
Vc=80[m/min] Fz=0,15[mm/dinte]; angle of inclination 55°

**Fig. 8.** Microscopic images of the quality of the surfaces processed with the two mills

Figure 8 illustrates the microscopic topography obtained with the IOR stereoscopic microscope and the MM1-200 microscope on the surfaces with the best roughness processed with the spherical and toroidal milling.

## 4. Conclusions

The purpose of this work is to determine the quality of the surface. Surface quality plays a very important role in the precision and lubrication of the surfaces. It was chosen to compare the processed surfaces with the toriodal milling, respectively the spherical milling. The surface on which the roughness was investigated is the convex cylindrical surface.

As variable parameters it was decided to juggle with the cutting speed, the tooth advance and the inclination angle of the tool. It was decided to process 27 surfaces with toroidal milling and 27 surfaces processed with spherical milling.

From the point of view of the execution time, the fastest processing was done with the toroidal milling machine in one minute and 48 seconds in the case of the maximum speeds at the angle of 15º compared to the fastest processing obtained with the spherical milling machine in 2 minutes and 20 of seconds also at maximum speeds but at 55º angle of inclination.

Regarding the surface quality, the best surface quality was obtained with the toroidal milling machine, having the value Ra = 0.372 [µm] with Vc = 80 [m / min], Fz = 0.15 [mm / tooth] and the angle inclination of 55º. In the case of spherical milling, the best surface quality was recorded using the regimes Vc = 370 [m / min], fz = 0.13 [mm / tooth] and the inclination angle of 35º recording the value Ra = 0.439 [µm ].

According to the aspects investigated in this paper, it is proved that depending on the surface geometry and the tool geometry, as regards the processing of convex spherical surfaces, one can exit the pattern to use the toroidal milling instead of the spherical milling. This statement is confirmed both by the evolution of the execution time and by determining the quality of the surface.

### Acknowledgments

The experimental research carried out with the support of the processing department of S.C. Ramira S.A., Baia Mare.

### References

[1] Aspinwall, D., and R. Dewes. “The influence of cutter orientation and workpiece angle on machinability when high-speed milling Inconel 718 under finishing conditions.” *International Journal of Advanced Manufacturing Technology* 47, no. 12-13 (October 2007): 1839-1846.

[2] Daymin, A., M. Bouljelbene, A. Ben, E. Bayraktar, and D. Katundi. “Surface integrity in high speed end milling of titanium alloy Ti-6Al-4V.” *Materials Science and Technology* 27, no.1 (January 2011): 387-394.

[3] Gani, E.A., J.P. Kruth, P. Vanherck, and B. Lauwers. “A geometrical model of the cut in five-axis milling accounting for the influence of tool orientation.” The *International Journal of Advanced Manufacturing Technology* 13, no.10 (October 1997): 677–684.

[4] Kaldova, T., and Y.R. Hwang. “Impact of various ball cutter tool positions on the surface integrity of low carbon steel.” *Materials and Design* 30, no. 9 (October 2009): 3360-3366.

[5] Ko, T.J., H.S. Kim, and S.S. Lee. “Selection of the Machining Inclination Angle in High-Speed Ball End Milling.” *The International Journal of Advanced Manufacturing Technology* 17, no.3 (January 2001): 163-170.

[6] Lou, Mike, Joseph Chen, and Caleb Li. “Surface Roughness Prediction Technique For CNC End-Milling.” *Journal of Industrial Tehnology* 15, no.1 (January 1999).

[7] Fu, M., M.L. Zheng, and Z.T. Yang. “Research of Surface Roughness in High-speed Ball-end Milling Al-alloy.” *Journal of Harbin University of Science and Technology*, no.3 (2004).

[8] Oșan, Andrei, Mihai Bănică, and Vasile Năsui. ”The influence of inclination of the axis of the toroidal on a flat surface roughness.” Paper presented at the 23nd edition of Innovative Manufacturing Engineering&Energy International Conference – ImanE&E 2019, Pitești, Romania, May 22 – 24, 2019.

[9] Toh, C.K. “Cutter path orientations when high-speed finish milling inclined hardened steel.” *Int J Adv ManufTechnol* 27, no. 5-6 (2006): 473–480.

**ISSN 1453 – 7303** **"HIDRAULICA" (No. 4/2019)**
**Magazine *of Hydraulics, Pneumatics, Tribology, Ecology, Sensorics, Mechatronics***

# Optimal Design of a CNG Storage Tank with a Combined Form Consisting of a Torus and a Sphere

Assoc. Prof. PhD. Eng. **Mihai ŢĂLU**[1], Assoc. Prof. PhD. Eng. **Ștefan ŢĂLU**[2,*]

[1] University of Craiova, Faculty of Mechanics, Department of Applied Mechanics and Civil Engineering, Calea București Street, no. 107, 200512 Craiova, Dolj county, Romania. E-mail: mihai_talu@yahoo.com

[2] Technical University of Cluj-Napoca, The Directorate of Research, Development and Innovation Management (DMCDI), Constantin Daicoviciu Street, no. 15, Cluj-Napoca, 400020, Cluj county, Romania. Corresponding author* e-mail: stefan_ta@yahoo.com

***Abstract:*** *This paper presents the optimum sizing of a storage tank composed of a torus and a sphere, made of steel, intended for compressed natural gas (CNG) storage from the automotive industry. A design strategy was proposed to determine based on the finite element method, the optimum thicknesses of the torus and spherical coverings, with the correction of their thickness taking into account: the temperature variation, the corrosion action during the operation, the tolerances of execution of the sheet laminate, and the technological process used to manufacture the elements. Numerical simulations were carried out to determine the optimum form and sizing of the storage tank based on an objective optimization function to minimize the storage tank mass. For size dimensioning, the exploatation temperature was computed in function of the maximum effort Von Misses and the corresponding resulting linear deformation. The 3-D (three-dimensional) model (modelled using the AutoCAD Autodesk 2017 software), was imported for numerical analyses to SolidWorks 2017 software). The results of analyzed cases can improve the technical performances of these particular types of CNG storage tanks to meet the customers' requirements.*

***Keywords:*** *Automotive industry, compressed natural gas (CNG) storage tank, industrial engineering design, optimization methods, pressure vessel*

## 1. Introduction

In the last decades, the convergence of business models, technological developments and researches in the field of the fuel tank industry have revealed a fluent and coherent approach regarding the advanced design tools for the creation of new products with high performances and high quality [1-6].

The results of these researches are multifaceted. Not only is the demand for fuel storage tanks increasing, but the options available (such as the intended application, space constraints, weight, and cost price), safety and reliability considerations have become more sophisticated [7-11].

The dynamics of the storage tank markets has evolved in an upward direction both in the field of execution technology and in the strategy of qualitative innovation based on 3-D design, interdisciplinary and complex research in border areas that offers a competitive advantage [12-17].

In designing the fuel storage tanks, the researchers proposed and investigated through theoretical and experimental analyzes, models with different geometries (executed from various materials, with storage capacities and competitive prices to meet the customers' requirements [18-22].

Modeling prototypes of the fuel storage tanks used in the automotive industry with computer aided design (CAD) software and advanced design concepts allows avoiding the use of testing equipment and expensive tests performed with products under real conditions [23-27].

For the design, analysis and evaluation of storage tanks there are various software packages with virtual computer aided engineering (CAE) tools on the market, which offer users quick and precise projects for new tanks and evaluation of existing tanks in various environmental conditions, in accordance with the relevant guidelines and regulations outlined by the national/international standards [28-32]. Also, there are various valid implementations of mathematical methods in more efficient algorithms and programs [33-37] to find the optimized solution according the criterion of optimality to satisfy the general structural design [38-42] and certification rules [43, 44].

In our research, the optimum sizing of a fuel storage tank composed of a torus and a sphere, made of steel, intended for compressed natural gas (CNG) storage from the automotive industry was performed in accordance to the general structural design.

## 2. Design methodology

### 2.1 Basic geometry of the parametric 3-D model

Let's consider the parametric 3-D model of a CNG storage tank composed by a torus and a sphere as shown in fig. 1. By adopting the torus as a support element of the sphere, the aim is to achieve a constructive variant that can lead to the elimination of the sphere support system.

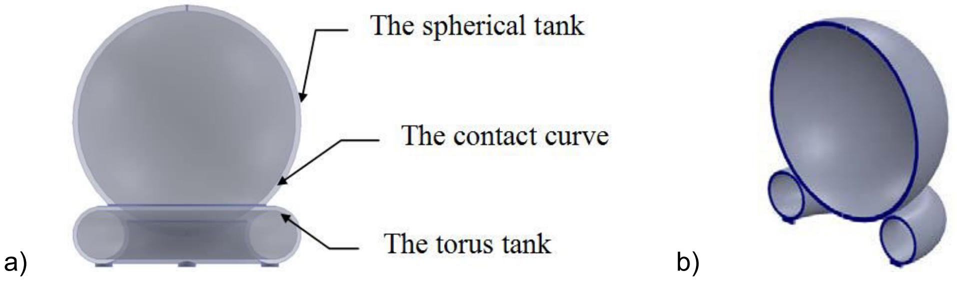

**Fig. 1.** The graphical representation of the parametric 3-D solid model: a) section; b) axonometric view

In this case, an intermediate bracelet type element (fig. 2a) was used, which supports the torus inside, and on the outside on the contoured surface of the sphere (fig. 2b and fig. 2c). In this way it was intended that the action of the forces generated by the sphere to discharge / towards the sole of the support element through its body without transmitting their action on the torus coverings.

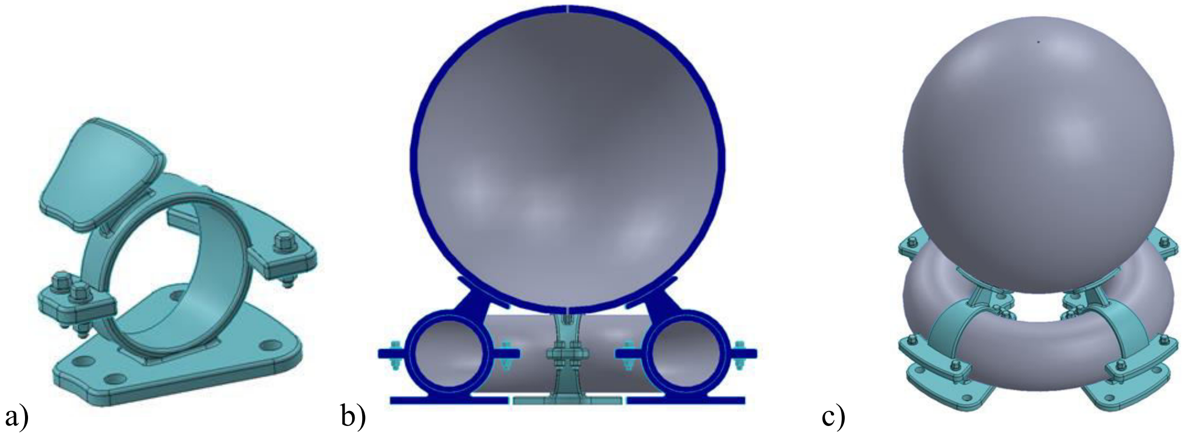

**Fig. 2.** The graphical representation of: a) the intermediate bracelet type element; b) section of 3-D solid model; c) axonometric view of 3-D solid model

In design, the aim was to determine the diameter of the sphere and the torus: the diameter of the cross-section and the diameter of the guiding curve of the cross-section needed to generate it.
Let's consider the dimensions B x H imposed in the cross-section of the storage tank and the depth dimension L1 (fig. 3).

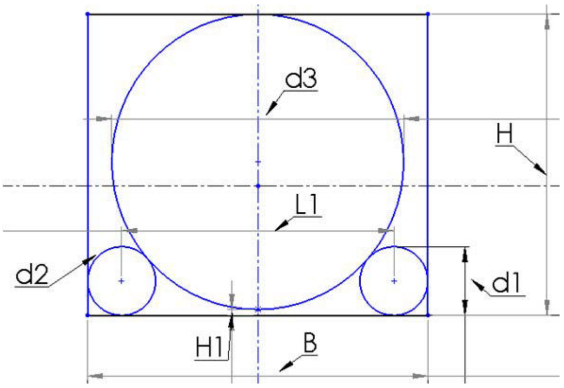

**Fig. 3.** The graphical representation of the dimensions B x H imposed in the cross-section of the storage tank and the depth dimension L1

The following parameters were applied as input parameters to the 3-D parametric model (fig. 3): a) H1 > 0; b) d1 = d2; c) B = H = L = 3000 mm.
The sizes d1, L1 and d3 will be determined considering a maximum total volume of storage tank (composed by a torus and a sphere). As a result of the variation of diameter d1 (which took into account the solution of construction of the support element) which decreased the radius of the cross-sectional storage section by Δd1 = 50 mm, the following dimensions were determined (shown in table 1).

**Table 1:** The constructive dimensions of the storage tank

| d1 [m] | H1 [m] | L1 [m] | d3 [m] | V1 [$m^3$] | V3 [$m^3$] | VT [$m^3$] | V [$m^3$] | $p_{vol}$ [%] | A1 [$m^2$] | A3 [$m^2$] | A_total [$m^2$] |
|---|---|---|---|---|---|---|---|---|---|---|---|
| 0.450 | 0.043 | 2.450 | 2.915 | 1.223 | 12.963 | 15.408 | 27.0 | 57.06 | 10.870 | 26.681 | 48.422 |
| 0.500 | 0.103 | 2.400 | 2.794 | 1.479 | 11.416 | 14.374 | 27.0 | 53.23 | 11.832 | 24.514 | 48.177 |
| 0.550 | 0.163 | 2.350 | 2.673 | 1.752 | 9.999 | 13.504 | 27.0 | 50.01 | 12.744 | 22.442 | 47.929 |
| 0.600 | 0.223 | 2.300 | 2.553 | 2.041 | 8.708 | 12.790 | 27.0 | 47.3 | 13.606 | 20.466 | 47.678 |
| 0.650 | 0.284 | 2.250 | 2.432 | 2.343 | 7.528 | 12.214 | 27.0 | 45.23 | 14.420 | 18.572 | 47.411 |
| 0.700 | 0.344 | 2.200 | 2.311 | 2.657 | 6.461 | 11.776 | 27.0 | 43.6 | 15.184 | 16.774 | 47.141 |
| 0.750 | 0.405 | 2.150 | 2.191 | 2.981 | 5.501 | 11.463 | 27.0 | 42.45 | 15.899 | 15.067 | 46.864 |
| 0.800 | 0.465 | 2.100 | 2.070 | 3.313 | 4.642 | 11.267 | 27.0 | 41.73 | 16.564 | 13.455 | 46.583 |
| 0.850 | 0.526 | 2.050 | 1.950 | 3.651 | 3.880 | 11.182 | 27.0 | 41.41 | 17.180 | 11.940 | 46.301 |
| 0.900 | 0.586 | 2.000 | 1.829 | 3.993 | 3.199 | 11.186 | 27.0 | 41.42 | 17.747 | 10.498 | 45.993 |
| 0.950 | 0.646 | 1.950 | 1.708 | 4.338 | 2.608 | 11.283 | 27.0 | 41.79 | 18.265 | 9.160 | 45.690 |
| 1.000 | 0.707 | 1.900 | 1.587 | 4.683 | 2.092 | 11.458 | 27.0 | 42.43 | 18.733 | 7.908 | 45.375 |
| 1.050 | 0.767 | 1.850 | 1.466 | 5.027 | 1.649 | 11.704 | 27.0 | 43.34 | 19.152 | 6.748 | 45.053 |
| 1.100 | 0.827 | 1.800 | 1.346 | 5.369 | 1.276 | 12.013 | 27.0 | 44.49 | 19.522 | 5.687 | 44.731 |
| 1.150 | 0.888 | 1.750 | 1.225 | 5.705 | 0.962 | 12.371 | 27.0 | 45.82 | 19.842 | 4.712 | 44.397 |
| 1.200 | 0.948 | 1.700 | 1.105 | 6.034 | 0.706 | 12.774 | 27.0 | 47.31 | 20.114 | 3.834 | 44.061 |
| 1.250 | 1.010 | 1.650 | 0.984 | 6.355 | 0.499 | 13.208 | 27.0 | 48.91 | 20.335 | 3.040 | 43.711 |
| 1.300 | 1.070 | 1.600 | 0.862 | 6.665 | 0.335 | 13.665 | 27.0 | 50.61 | 20.508 | 2.333 | 43.349 |
| 1.350 | 1.130 | 1.550 | 0.742 | 6.963 | 0.214 | 14.140 | 27.0 | 52.37 | 20.631 | 1.729 | 42.991 |
| 1.400 | 1.190 | 1.500 | 0.622 | 7.247 | 0.126 | 14.620 | 27.0 | 54.14 | 20.705 | 1.215 | 42.625 |

The graphs of H1 = f(d1), L1 = f(d1), d3 = f(d1), taking into account the results from Table 1, are graphically shown in fig. 4 and fig. 5.

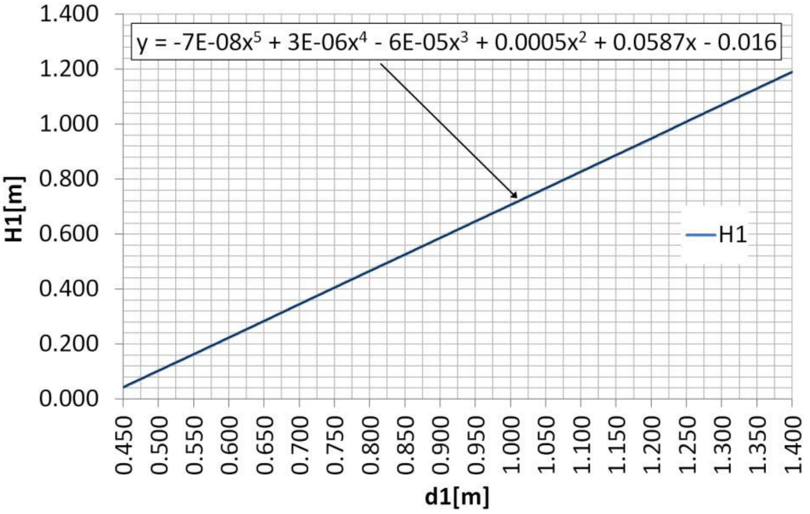

**Fig. 4.** The graph: H1 = f(d1)

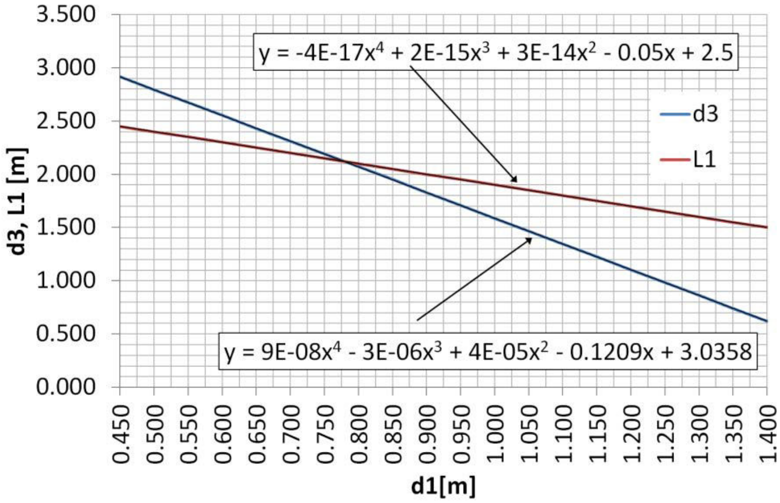

**Fig. 5.** The graphs: L1 = f(d1), d3 = f(d1)

The graphs of the variation of the volume of the torus V1 = f(d1), volume of the sphere V3 = f(d1), and the total volume of the tank VT = f(d1), are graphically shown in fig. 6. In fig. 7 the dependences of the torus area A1 = f(d1), the sphere A3 = f(d1), and the total area $A_T$ = f(d1) are represented.

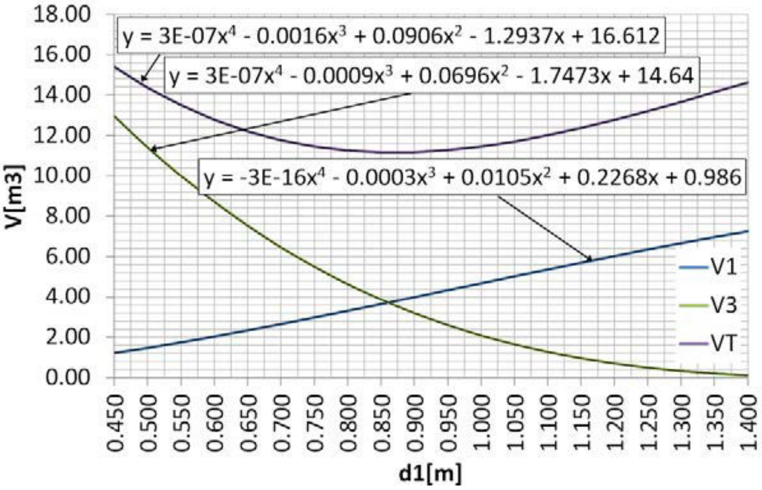

**Fig. 6.** The graphs: V1 = f(d1), V3 = f(d1), VT = f(d1)

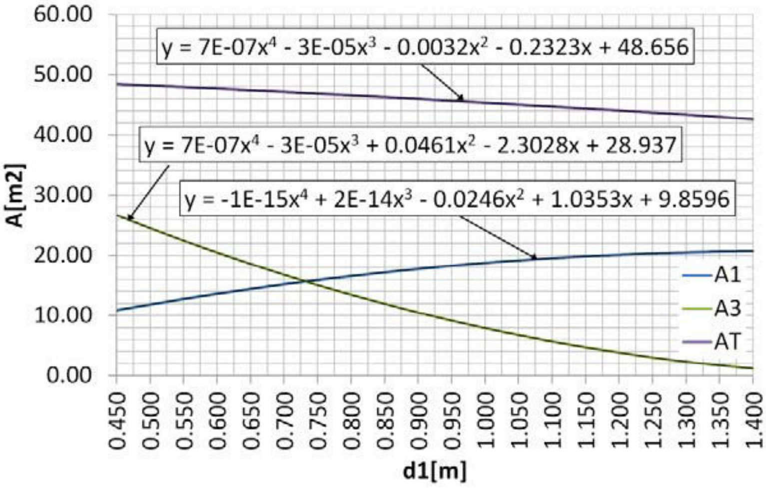

**Fig. 7.** The graphs: A1 = f(d1), A3 = f(d1), AT = f(d1)

In fig. 8 the dependence of the size of the percentage occupied by the volume of the tank (pv) from the maximum volume B x L x H are graphically shown.

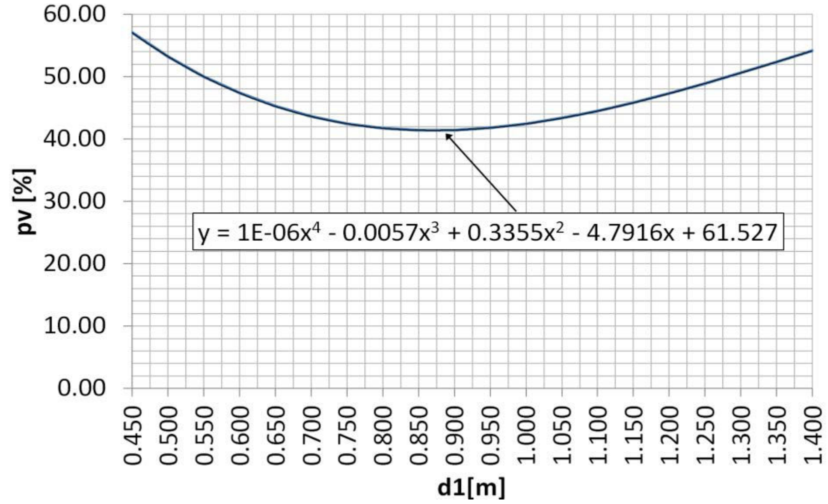

**Fig. 8.** The graph: pv = f(d1)

The optimal constructive dimensions of the storage tank are given in table 2.

**Table 2:** The optimal constructive dimensions of the storage tank

| d1 [m] | H1 [m] | L1 [m] | d3 [m] | V1 [$m^3$] | V3 [$m^3$] | VT [$m^3$] | V [$m^3$] | $p_{vol}$ [%] | A1 [$m^2$] | A3 [$m^2$] | A_total [$m^2$] |
|---|---|---|---|---|---|---|---|---|---|---|---|
| 0.450 | 0.043 | 2.450 | 2.915 | 1.223 | 12.963 | 15.408 | 27.0 | 57.06 | 10.870 | 26.681 | 48.422 |

## 2.2 Numerical analysis of the parametric 3-D model

Based on the physical model, the modeling was done in the AutoCAD Autodesk 2017 software [45] and the numerical analysis was performed with SolidWorks 2017 software [46] with the Static, Thermal and Design Study modules. The design data used were:

- the tank material is AISI 4340 steel; the intermediate bracelet type element is AISI 1045 steel;
- the maximum hydraulic test pressure: $p_{max}$ = 300 bar;
- the working temperature between the limits: T = -30 $^0$C up to T = 60 $^0$C;
- the period of the tank exploitation: $n_a$ = 20 years;
- the corrosion rate of the material: $v_c$ = 0.06 mm/years.
- the fuel stored in the tank is CNG with a density of $\rho$ = 20.5 kg / $m^3$.

In fig. 9 the parametric 3-D model of a CNG storage tank composed by a torus and a sphere with eight intermediate bracelets is graphically shown.

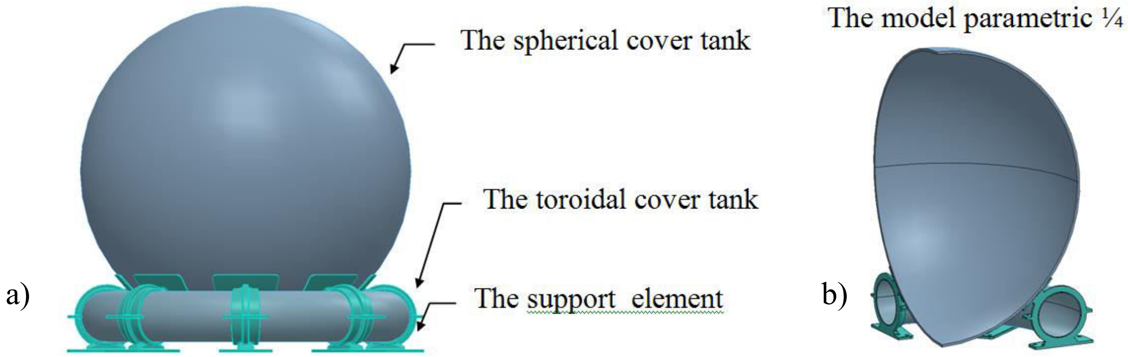

**Fig. 9.** The graphical representation of the parametric 3-D model of a CNG storage tank composed by a torus and a sphere with eight intermediate bracelets

The storage tank design takes into account the variation of the working temperature, the correction of the thickness of the cover material, the evolution of the corrosion process, the tolerance of the execution of the cover sheet, the thinning of the sheet thickness, and the exploitation period.
The parameterized model used in calculus is a section of ¼ from the initial cover (fig. 10a) and the corresponding surfaces to which the constraints and restrictions are applied are shown in fig. 10b.

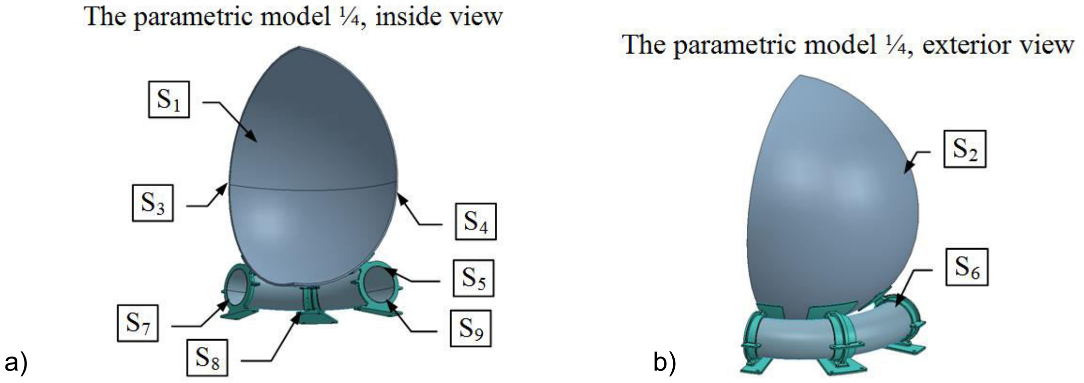
The parametric model ¼, inside view

The parametric model ¼, exterior view

**Fig. 10.** The graphical representation of the parametric 3-D model ¼: a) inside view; b) exterior view

The following parameters were applied as input parameters to the parametric model (fig. 10):

- the maximum pressure $p_{max}$ = 30 N/mm$^2$ on the inner surfaces $S_1$ and $S_5$;
- the temperature between the limits: T = -30 $^0$C to T = 60 $^0$C on the surfaces $S_2$ and $S_6$;
- the action of the weight force of the fuel F = 6953 N on the surface $S_1$, and F = 656 N on the surface $S_5$;
- the action of the force of weight of the metallic structure of the storage tank;
- the surface symmetry on $S_3$ and $S_4$;
- the fixing conditions on the surfaces: $S_7$, $S_8$ and $S_9$;
- an objective function of optimization to minimize the storage tank mass.

The applied optimization function is intended to achieve a minimum mass. The variable of optimization is the thickness of the cover *s* [mm].
The applied restrictions of constraints are:
a) for the cover material, the value of Von Mises effort $\sigma_{rez} \leq \sigma_a$ = 710 N/mm$^2$ ($\sigma_a$ - the admissible value of the traction stress of the cover material).
a) for the support element, the value of Von Mises effort $\sigma_{rez} \leq \sigma_a$ = 530 N/mm$^2$ ($\sigma_a$ - the admissible value of the traction stress of the support element).
After the optimization procedure, the obtained values are given in table 3.

**Table 3:** The optimal constructive dimensions of the cover of the torus and the sphere of the tank

| The type of constructive element | s | T | σ | $u_{rez}$ |
|---|---|---|---|---|
| | [mm] | [$^0$C] | [N/mm$^2$] | [mm] |
| **Sphere** | 32.5 | -30 | 709.35 | 4.93 |
| **Torus** | 6.2 | -30 | 707.45 | 3.17 |

Distributions of the state of stress and of the linear deformation are shown in figures 11 and 12.
The optimized thicknesses of the covers (torus and sphere) were corrected taking into account: the corrosion phenomenon, the tolerance of negative execution of the sheet laminate and the thinning of the sheet in the embossing process. The formula for calculating the thickness is the following:

$$s_{real} = s_{opt} + \Delta s_c + \Delta s_T + \Delta s_{am} = s_{opt} + v_c \cdot n_a + abs(A_i) + 0.1 \cdot s \quad (1)$$

where: $s_{opt}$, the optimal thickness; $\Delta s_c$, the loss of thickness by corrosion; $\Delta s_T$, the addition of thickness due to the tolerance of the laminate sheet; $v_c$, the corrosion velocity of the lateral cover, $v_c$ = 0.06 mm/year; $n_a$, the number of years of exploitation; $A_i$, the lower tolerance of the laminate sheet; s = 9 mm.

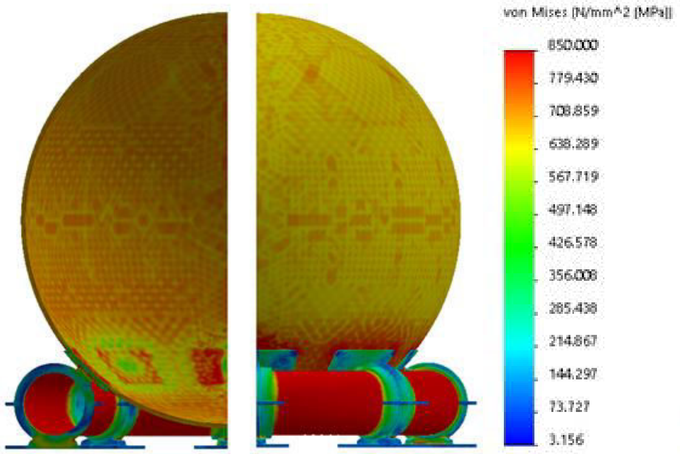

**Fig. 11.** The graph of Von Mises stress of lateral cover

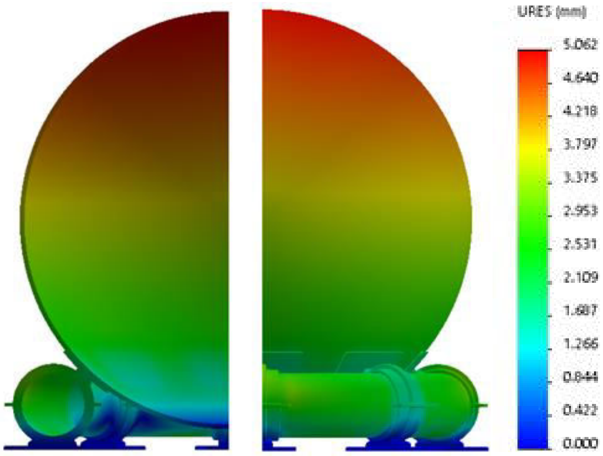

**Fig. 12.** The graph of linear deformation of lateral cover

The minimum value of the sheet thickness for the torus cover is determined as:

$$s_{real\ min} = 6.2 + 0.06 \cdot 20 + abs(-0.6) + 0.1 \cdot 9 = 8.9 \text{ mm} \quad (2)$$

A laminate sheet of AISI 4340 steel with a thickness of $s = 9^{0}_{-0.6}$ mm is chosen for analysis.
The minimum value of the sheet thickness for the sphere cover is determined as:

$$s_{real\ min} = 32.5 + 0.06 \cdot 20 + abs(-0.8) + 0.1 \cdot 32.5 = 37.75 \text{ mm} \quad (3)$$

A laminate sheet of AISI 4340 steel with a thickness of $s = 40^{+1.4}_{-0.8}$ mm is chosen for analysis.
After the end of the number of years of exploitation when $n_a = 20$ years, the toroidal envelope will have the thickness of s = 6.5 mm and the spherical one of s = 34 mm.
In this case for the real constructive solution after the exploitation periods are shown in fig. 13 and fig. 14, the Von Mises stress state and the resulting linear deformation state. Also their numerical values are shown in table 4.

**Table 4:** The real constructive dimensions of the cover of the torus and the sphere of the storage tank

| The type of constructive element | s | T | σ | $u_{rez}$ |
|---|---|---|---|---|
| | [mm] | [$^0$C] | [N/mm$^2$] | [mm] |
| **Sphere** | 34 | -30 | 676.1 | 3.138 |
| **Torus** | 6.5 | -30 | 684.3 | 2.94 |

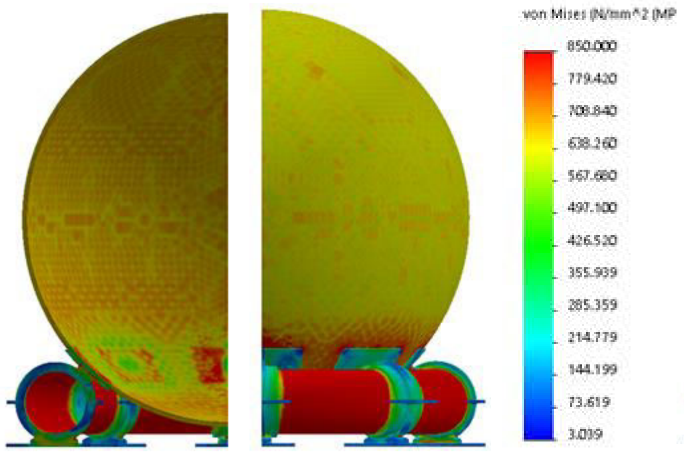

**Fig. 13.** The graph of real Von Mises stress of covers

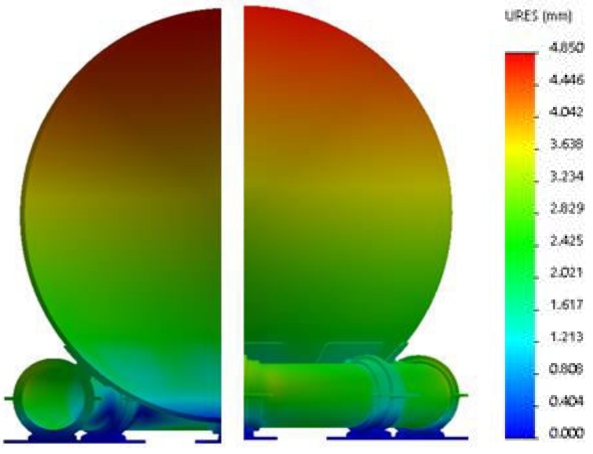

**Fig. 14.** The graph of real linear deformation of covers

The actual volume of storage of the tank, from the beginning of the exploitation period, is given in table 5.

**Table 5:** The volume constructive dimensions of the storage tank

| d1 | H1 | L1 | d3 | V1 | V3 | VT | V | $p_{vol}$ |
|---|---|---|---|---|---|---|---|---|
| [m] | [m] | [m] | [m] | [m$^3$] | [m$^3$] | [m$^3$] | [m$^3$] | [%] |
| 0.450 | 0.043 | 2.450 | 2.915 | 1.223 | 12.963 | 15.408 | 27.0 | 57.06 |
| 0.432 | 0.043 | 2.450 | 2.958 | 1.127 | 11.924 | 14.178 | 27 | 52.51 |

The parameters ΔV1, ΔV3, ΔVT, and $\Delta p_{vol}$, calculated in relation to the initial dimensions, are shown in table 6.

**Table 6:** The ΔV1, ΔV3, ΔVT, and $\Delta p_{vol}$, calculated in relation to the initial dimensions

| ΔV1 | ΔV3 | ΔVT | $\Delta p_{vol}$ |
|---|---|---|---|
| [%] | [%] | [%] | [%] |
| 7.84 | 8.01 | 7.98 | 7.98 |

## 3. Discussion

Following the numerical analyses and the resulting graphs for the parametric 3-D model structure through the method of finite elements it has been found that:
- the optimal design of the storage CNG tanks composed (such as a torus and a sphere) is efficient using the finite element method, on parameterized 3-D models for complex constructive variants;
- the use of the storage tanks with different storage spaces can obtain a percentage of occupancy of the maximum space. In our case the maximum initial value being $p_v$ = 57.06%, having a minimum of $p_v$ = 41.41% around to d1 = 0.850 m (fig. 8);
- the evolution of dimension H1 is strictly increasing (fig. 4), and for dimensions L1 and d3, these ones decrease to the value at d1 = 0.790 m (fig. 5);
- the total volume has a minimum value for d1 = 0.850 m (fig. 6 and table 1), and the total area has a decreasing evolution of the volume with the increase of d1;
- the calculation method used for optimization shows that the maximum stress state appears at the minimum negative temperature (table 3), for the minimal resulting linear deformation (fig. 11 and fig. 12);
- the dimensional correction of the actual constructive dimensions for the covers (table 5), determine the state of stress and of the linear deformation below the value admitted at the end of the exploitation period (table 4, fig.13 and fig.14);
- also the recalculation of the volume of the storage tank resulted by decreasing the calculated thickness of the covers from the initial volume of the tank shows that the volume reduction is with 7.98% (table 6).

## 4. Conclusions

The proposed method is efficient in the design phase of a storage tank composed of a torus and a sphere, made of steel, for compressed natural gas (CNG) fuel storage used in the automotive industry.

**Conflict of Interest:** The authors declare that they have no conflict of interest.

**ORCID**
Ştefan Ţălu, http://orcid.org/0000-0003-1311-7657.

**References**

[1] Ghiţă, C. Mirela, Anton C. Micu, Mihai Ţălu, and Ştefan Ţălu. "Shape optimization of a thoroidal methane gas tank for automotive industry." *Annals of Faculty of Engineering Hunedoara - International Journal of Engineering, Hunedoara, Romania*, Tome X, Fascicule 3 (2012): 295-297.

[2] Ghiţă, C. Mirela, Anton C. Micu, Mihai Ţălu, Ştefan Ţălu, and Ema I. Adam. “Computer-Aided Design of a classical cylinder gas tank for the automotive industry.“ *Annals of Faculty of Engineering Hunedoara - International Journal of Engineering, Hunedoara*, *Romania*, Tome XI, Fascicule 4 (2013): 59-64.

[3] Ghiţă, C. Mirela, Anton C. Micu, Mihai Ţălu, and Ştefan Ţălu. “3D modelling of a gas tank with reversed end up covers for automotive industry.“ *Annals of Faculty of Engineering Hunedoara - International Journal of Engineering, Hunedoara*, *Romania*, Tome XI, Fascicule 3 (2013): 195-200.

[4] Ghiţă, C. Mirela, Anton C. Micu, Mihai Ţălu, and Ştefan Ţălu. “3D modelling of a shrink fitted concave ended cylindrical tank for automotive industry.“ *Acta Technica Corviniensis – Bulletin of Engineering, Hunedoara, Romania*, Tome VI, Fascicule 4 (2013): 87-92.

[5] Ghiţă, C. Mirela, Ştefan C. Ghiță, Ştefan Ţălu, and Simona Rotaru, “Optimal design of cylindrical rings used for the shrinkage of vehicle tanks for compressed natural gas.“ *Annals of Faculty of Engineering Hunedoara - International Journal of Engineering, Hunedoara*, Tome XII, Fascicule 3 (2014): 243-250.

[6] Ghiţă, C. Mirela, Anton C. Micu, Mihai Ţălu, and Ştefan Ţălu. “Shape optimization of vehicle's methane gas tank.“ *Annals of Faculty of Engineering Hunedoara - International Journal of Engineering, Hunedoara, Romania*, Tome X, Fascicule 3 (2012): 259-266.

[7] Bică, Marin, Mihai Ţălu, and Ştefan Ţălu. “Optimal shapes of the cylindrical pressurized fuel tanks.” *Magazine of Hydraulics, Pneumatics, Tribology, Ecology, Sensorics, Mechatronics (HIDRAULICA)*, no. 4 (December 2017): 6-17.

[8] Vintilă, Daniela, Mihai Ţălu, and Ştefan Ţălu. “The CAD analyses of a torospheric head cover of a pressurized cylindrical fuel tank after the crash test.” *Magazine of Hydraulics, Pneumatics, Tribology, Ecology, Sensorics, Mechatronics (HIDRAULICA)*, no. 4 (December 2017): 57-66.

[9] Ţălu, Mihai. "The influence of the corrosion and temperature on the Von Mises stress in the lateral cover of a pressurized fuel tank." *Magazine of Hydraulics, Pneumatics, Tribology, Ecology, Sensorics, Mechatronics (HIDRAULICA)*, no. 4 (December 2017): 89-97.

[10] Ţălu, Ştefan, and Mihai Ţălu. "The influence of deviation from circularity on the stress of a pressurized fuel cylindrical tank." *Magazine of Hydraulics, Pneumatics, Tribology, Ecology, Sensorics, Mechatronics (HIDRAULICA)*, no. 4 (December 2017): 34-45.

[11] Ţălu, Mihai, and Ştefan Ţălu. "Analysis of temperature resistance of pressurized cylindrical fuel tanks." *Magazine of Hydraulics, Pneumatics, Tribology, Ecology, Sensorics, Mechatronics (HIDRAULICA)*, no. 1 (March 2018): 6-15.

[12] Ţălu, Mihai, and Ştefan Ţălu. "Design and optimization of pressurized toroidal LPG fuel tanks with variable section." *Magazine of Hydraulics, Pneumatics, Tribology, Ecology, Sensorics, Mechatronics (HIDRAULICA)*, no. 1 (March 2018): 32-41.

[13] Ţălu, Mihai, and Ştefan Ţălu. "The optimal CAD design of a 3D hexagonal toroid with regular hexagonal cross-section used in manufacturing of LPG storage tanks." *Magazine of Hydraulics, Pneumatics, Tribology, Ecology, Sensorics, Mechatronics (HIDRAULICA)*, no. 2 (June 2018): 49-56.

[14] Ţălu, Ştefan, and Mihai Ţălu. "Algorithm for optimal design of pressurized toroidal LPG fuel tanks with constant section described by imposed algebraic plane curves." *Magazine of Hydraulics, Pneumatics, Tribology, Ecology, Sensorics, Mechatronics (HIDRAULICA)*, no. 2 (June 2018): 14-21.

[15] Ţălu, Mihai, and Ştefan Ţălu. “The influence of corrosion and temperature variation on the minimum safety factor of a 3D hexagonal toroid with regular hexagonal cross-section used in manufacturing of LPG storage tanks.“ *Magazine of Hydraulics, Pneumatics, Tribology, Ecology, Sensorics, Mechatronics (HIDRAULICA)*, no. 3 (August 2018): 16-25.

[16] Ţălu, Ştefan, and Mihai Ţălu. "The influence of corrosion and pressure variation on the minimum safety factor of a 3D hexagonal toroid with regular hexagonal cross-section used in manufacturing of LPG storage tanks." *Magazine of Hydraulics, Pneumatics, Tribology, Ecology, Sensorics, Mechatronics (HIDRAULICA)*, no. 3 (August 2018): 39-45.

[17] Ţălu, Mihai, and Ştefan Ţălu. “The influence of corrosion and temperature variation on a CNG storage tank with a combined form consisting of a torus and a sphere.“ *Magazine of Hydraulics, Pneumatics, Tribology, Ecology, Sensorics, Mechatronics (HIDRAULICA)*, no. 4 (December 2019): 93-104.

[18] Ţălu, Mihai, and Ştefan Ţălu. “3D geometrical solutions for toroidal LPG fuel tanks used in automotive industry.“ *Advances in Intelligent Systems Research* 151 (2018): 189-193. DOI: 10.2991/cmsa-18.2018.44.

[19] Ţălu, Ştefan, and Mihai Ţălu. “Constructive CAD variants of toroidal LPG fuel tanks used in automotive Industry.“ *Advances in Intelligent Systems Research* 159 (2018): 27-30. DOI: 10.2991/mmsa-18.2018.7.

[20] Ţălu, Ştefan, and Mihai Ţălu. “The Influence of corrosion on the vibration modes of a pressurized fuel tank used in automotive industry.“ *DEStech Transactions on Materials Science and Engineering* (May 2018): 1-6. DOI: 10.12783/dtmse/icmsa2018/20560.

[21] Ţălu, Mihai, and Ştefan Ţălu. “Optimal engineering design of a pressurized paralepipedic fuel tank.“ *Annals of Faculty of Engineering Hunedoara - International Journal of Engineering, Hunedoara, Romania*, Tome XVI, Fascicule 2 (2018): 193-200.

[22] Malviya, Rupesh Kumar, and Muhamed Rushaid. "Consequence analysis of LPG storage tank." *Materials Today* 5, no. 2 (2018): 4359-4367. DOI: 10.1016/j.matpr.2017.12.003.

[23] Ţălu, Ştefan, and Mihai Ţălu. “CAD generating of 3D supershapes in different coordinate systems.“ *Annals of Faculty of Engineering Hunedoara - International Journal of Engineering, Hunedoara, Romania*, Tome VIII, Fascicule 3 (2010): 215-219.

[24] Ţălu, Ştefan, and Mihai Ţălu. “A CAD study on generating of 2D supershapes in different coordinate systems.“ *Annals of Faculty of Engineering Hunedoara - International Journal of Engineering, Hunedoara, Romania*, Tome VIII, Fascicule 3 (2010): 201-203.

[25] Niţulescu, Theodor, and Ştefan Ţălu. *Aplicaţii ale geometriei descriptive şi graficii asistate de calculator în desenul industrial / Applications of descriptive geometry and computer aided design in engineering graphics.* Cluj-Napoca, Risoprint Publishing House, 2001.

[26] Florescu-Gligore, Adrian, Ştefan Ţălu, and Dan Noveanu. *Reprezentarea şi vizualizarea formelor geometrice în desenul industrial / Representation and visualization of geometric shapes in industrial drawing).* Cluj-Napoca, U. T. Pres Publishing House, 2006.

[27] Ţălu, Ştefan, and Cristina Racocea. *Reprezentări axonometrice cu aplicaţii în tehnică / Axonometric representations with applications in technique.* Cluj-Napoca, MEGA Publishing House, 2007.

[28] Racocea, Cristina, and Ştefan Ţălu. *Reprezentarea formelor geometrice tehnice în axonometrie / The axonometric representation of technical geometric shapes.* Cluj-Napoca, Napoca Star Publishing House, 2011.

[29] Ţălu, Ştefan. *Geometrie descriptivă / Descriptive geometry.* Cluj-Napoca, Risoprint Publishing House, 2010.

[30] Florescu-Gligore, Adrian, Magdalena Orban, and Ştefan Ţălu. *Cotarea în proiectarea constructivă şi tehnologică / Dimensioning in technological and constructive engineering graphics.* Cluj-Napoca, Lithography of The Technical University of Cluj-Napoca, 1998.

[31] Ţălu, Ştefan. *Grafică tehnică asistată de calculator / Computer assisted technical graphics)*. Cluj-Napoca, Victor Melenti Publishing House, 2001.

[32] Ţălu, Ştefan. *Reprezentări grafice asistate de calculator / Computer assisted graphical representations.* Cluj-Napoca, Osama Publishing House, 2001.

[33] Țălu, Mihai. *Calculul pierderilor de presiune distribuite în conducte hidraulice / Calculation of distributed pressure loss in hydraulic pipelines.* Craiova, Universitaria Publishing House, 2016.

[34] Ţălu, Mihai. *Mecanica fluidelor. Curgeri laminare monodimensionale / Fluid mechanics. The monodimensional laminar flow.* Craiova, Universitaria Publishing House, 2016.

[35] Țălu, Mihai. *Pierderi de presiune hidraulică în conducte tehnice cu secțiune inelară. Calcul numeric și analiză C.F.D / Hydraulic pressure loss in technical piping with annular section. Numerical calculation and C.F.D.)*. Craiova, Universitaria Publishing House, 2016.

[36] Ţălu, Ştefan. *Limbajul de programare AutoLISP. Teorie şi aplicaţii / AutoLISP programming language. Theory and applications*. Cluj-Napoca, Risoprint Publishing House, 2001.

[37] Ţălu, Ştefan. *AutoCAD 2005*. Cluj-Napoca, Risoprint Publishing House, 2005.

[38] Ţălu, Ştefan, and Mihai Ţălu. *AutoCAD 2006. Proiectare tridimensională / AutoCAD 2006. Three-dimensional designing*. Cluj-Napoca, MEGA Publishing House, 2007.

[39] Ţălu, Ştefan. *AutoCAD 2017*. Cluj-Napoca, Napoca Star Publishing House, 2017.

[40] Nedelcu, Dorian. *Proiectare și simulare numerică cu SolidWorks / Digital Prototyping and Numerical Simulation with SolidWorks*. Timişoara, Eurostampa Publishing House, 2011.

[41] Ţălu, Ştefan. *Micro and nanoscale characterization of three dimensional surfaces. Basics and applications*. Cluj-Napoca, Napoca Star Publishing House, Romania, 2015.

[42] Bîrleanu, Corina, and Ştefan Ţălu. *Organe de maşini. Proiectare şi reprezentare grafică asistată de calculator / Machine elements. Designing and computer assisted graphical representations.* Cluj-Napoca, Victor Melenti Publishing House, 2001.

[43] *** Certification tests of LPG and CNG. Accessed August 23, 2018. http://vzlutest.cz/en/certification-tests-of-lpg-and-cng-c3.html.

[44] *** TANK software (https://cas.hexagonppm.com/solutions/tank).

[45] *** Autodesk AutoCAD 2017 software.

[46] *** SolidWorks 2017 software.

**ISSN 1453 – 7303** **"HIDRAULICA" (No. 4/2019)**
**Magazine *of Hydraulics, Pneumatics, Tribology, Ecology, Sensorics, Mechatronics***

# River-Bed Processes Numerical Analysis in the Influence Area of a Crossing Structure

Assist. dr.eng. **Alina-Ioana POPESCU-BUȘAN**[1], Assist. dr.eng. **Marie Alice GHIȚESCU**[2], Assoc.prof.dr.eng. **Albert Titus CONSTANTIN**[3], Lect.dr.eng. **Şerban-Vlad NICOARĂ**[4]

[1] University Politehica of Timisoara, Piata victoriei nr. 2, 300006 Timisoara, Romania, alina.popescu-busan@upt.ro
[2] University Politehica of Timisoara, Piata victoriei nr. 2, 300006 Timisoara, Romania, alice.ghitescu@upt.ro
[3] University Politehica of Timisoara, Piata victoriei nr. 2, 300006 Timisoara, Romania, albert.constantin@upt.ro
[4] University Politehica of Timisoara, Piata victoriei nr. 2, 300006 Timisoara, Romania, serban.nicoara@upt.ro

***Abstract:*** *There is described a 1D numerical study of scouring and sedimentation processes on a specific altered river sector. The model developed and analysed by the help of HEC-RAS software package is concerned by the immediate upstream and downstream vicinity of an existing road bridge. The general quasi-unsteady (transitory) flowing regime assimilates a given hydrologic development unfolding over a generous time period, from August 1st, 1985 to July 31st, 1988.*

*The present paper considers a casual approach by which the specific crossing structure is replaced by two characteristic cross-sections along the concrete bridge faces. The scourings expansion and depth or the silting spread and height can so be revealed especially along the bothering bridge span but also along the influenced river sector as modelled.*

***Keywords:*** *River flow, bridge hydraulics, highwaters flow, sediment transport, river-bed processes, numerical model.*

## 1. General site and model information

The 1D numerical model covers a sector of 352.20 m on Someș River, downstream of its confluence with Agrij tributary, as altered by a crossing driveway bridge right outside of Jibou Town building area, about 25 km from Zalău Municipality in the North-West of Romania. The Town of Jibou in Sălaj County, north-east of Romanian historical Province of Crișana, lays down on the left bank of Someș River, at about 25km north-east of the county administrative municipality, Zalău.

The Someș River crossing by the east side connecting roadway is arranged by a bridge of six gaps determined by concrete piers, the total span covering the streambed and the adjacent flood plains [1]. The bays have slightly variable gaps of about 33.40m, 25.40m, 26.30m, 24.90m, 25.80m and 23.80m, as going from left to right. The bridge stands on the two flanking abutments and the five piers (about 2.20m width, 5.20m length, 184.00mSL top level) founded by concrete blocks (top level at 175.05mSL).

The numerical analysis performed by the help of HEC-RAS 5.0.6 [2] considers the quasi-unsteady flow regime over the given time period spreading from August 1st, 1985 to July 31st, 1988.

A topographic database was created as given by a general situation plan (comprising 371 measured points) and five cross profiles. Covering the studied river path and its adjacent areas, this data reflects the geometrical configuration of the river sector cross-sections, offering also the proper image of the stream-bed and flood plains morphology.

As about the crossing structure presence in the performed model, it is going to be considered by its upstream and downstream faces river cross-sections initial geometry. Since there were no accessible measurements of the scouring/silting situation, it was first necessary to numerically estimate [3] a start configuration properly matching former visual observation on bridge site.

There was followed a facile approach with respect to graphical processing of the available measured topographical data under similar given circumstances with the studied river site [4,5]. The approach employs a specialised 2D graphical interpolation software extension (specified 0x and 0y directions) that can further on generate a 3D shape surface (.shx extension file). So, by considering the previously created topographic database, a 3D ground surface associated to the Someș River sector was shaped. Further on, this shape was meshed by the help of RAS Mapper module and the discrete river-path was endowed with a contained bridge type crossing structure [6].

The boundary conditions for a steady flow regime under existing conditions are represented by the maximum entering discharge of 226.53 m$^3$/s and the known hydro-dynamic gradient of 2.75‰ as corresponding to the outgoing section.

The piezometric line development along the river sector model resulted by running the numerical analysis. The option Type was then considered under Hydraulic Design Functions menu and, after checking the Bridge Scour box, the input values of corresponding parameters were specified.

As following considered by the present paper, the analysis regarding the movable river-bed local washing capacity under transited flow and the effect of local stream contractions at piers and abutments is revealed by running the Compute command. The total maximum scouring amount reached at the crossing bridge (river station 148), i.e. Pier scour + Contraction scour = 1.59 m, as a parameter defining the simulated reference cross-sections at the bridge faces that follows to be considered in the sediments transport analysis, is revealed by the graphical representation in figure 1.

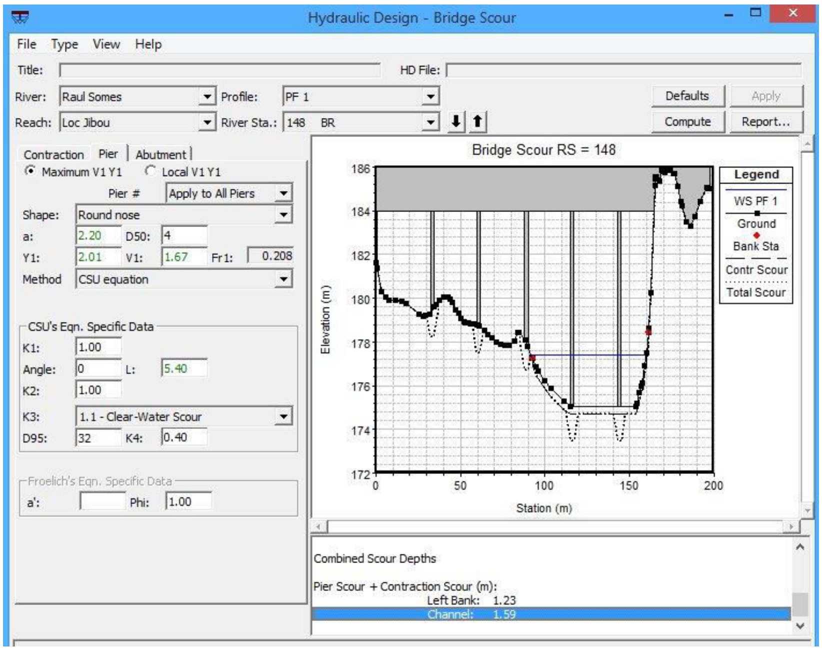

Title:
HD File:
River: Raul Somes
Profile: PF 1
Reach: Loc Jibou
River Sta.: 148 BR

● Maximum V1 Y1 ○ Local V1 Y1
Pier #: Apply to All Piers
Shape: Round nose
a: 2.20 D50: 4
Y1: 2.01 V1: 1.67 Fr1: 0.208
Method: CSU equation

CSU's Eqn. Specific Data
K1: 1.00
Angle: 0 L: 5.40
K2: 1.00
K3: 1.1 - Clear-Water Scour
D95: 32 K4: 0.40

Froelich's Eqn. Specific Data
a':
Phi: 1.00

Combined Scour Depths

Pier Scour + Contraction Scour (m):
Left Bank: 1.23
Channel: 1.59

**Fig. 1.** Total scouring amount numerically revealed at the crossing road bridge, as to be considered for the sediments transport analysis

As about the sediment transport study, since available specific information is relatively uncertain and the driving theory is considerably empirical and parameters sensitive, it could be a difficult problem [3]. HEC-RAS 5.0.6 covers also sediments transport capacities related to the ground movable surface, successively adjusting the river cross-sections geometry as a response to solid material dynamics. The software combines the sediments transport computations with the unsteady or quasi-unsteady hydraulics.

By considering the quasi-unsteady flow regime, the hydrodynamics is simplified as the continuous hydrograph is modelled as a series of constant discrete flow values. So, for each registered constant flow the software makes the sediment transport calculations along the corresponding stated time interval. Specifically, each constant flow time interval is sub-divided by a user defined computational increment representing the sediment transport calculation time step. The system’s hydraulic and corresponding cross-section geometry is so successively updated for each computational increment. This time step covers several mixing stages at the level of the movable ground surface for the river-bed layers.

## 2. Accomplishment of the liquid and sediment transport 1D numerical model

Once the geographic coordinates established, the final ground surface shape (an ".FLT" extension file) is uploaded in the graphical window of HEC-RAS 5.0.6 by the help of RAS Mapper facility [1]. The 1D numerical model is generated by following the specific operations (river path drawing and cross-sections geometry, sequential generating procedure, conversion procedure, river banks or cross-sections alteration procedure etc.) given by HEC-RAS options [7,4]. The graphical visualization is achieved by the main menu, following the associated "Lid to XS" option (figures 2 and 3).

The two images in figure 3 show the significant river cross-sections – River Stations 151 and 146 – defined at the bridge faces to simulate the crossing structure. The specific area under the concrete bridge (of about 5.2m width) is covered by the geometric interval ∆L = 153.7 - 142.5 = 11.2m and its movable river-bed numerical characteristics are going to be updated only by extending the framing 153.7 and 142.5 cross-sections characteristics (and not by actual calculation). Thus, by establishing these simulated cross-sections, the river-bed levels on the particularly concerning bridge area are successively adjusted along the entire running period, allowing so the study of scouring as crossing structure effect.

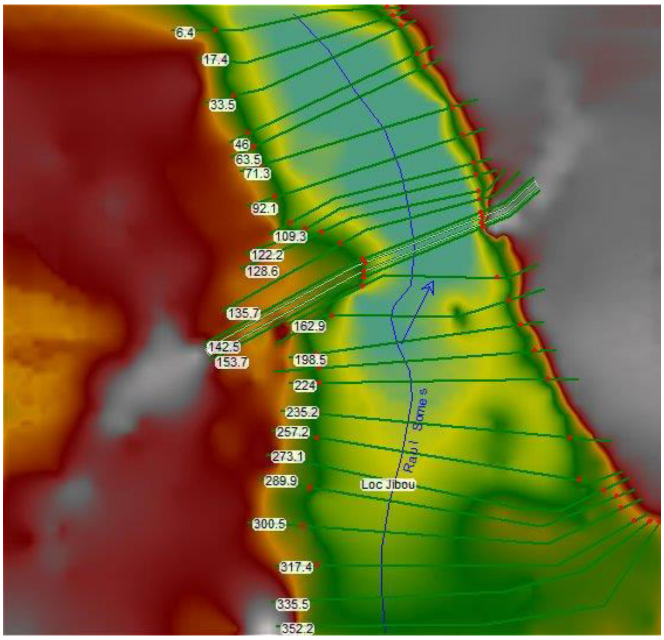

**Fig. 2.** Plan view of the 1D numerical model for the analysed Someș River sector indicating the cross-sections (river stations)

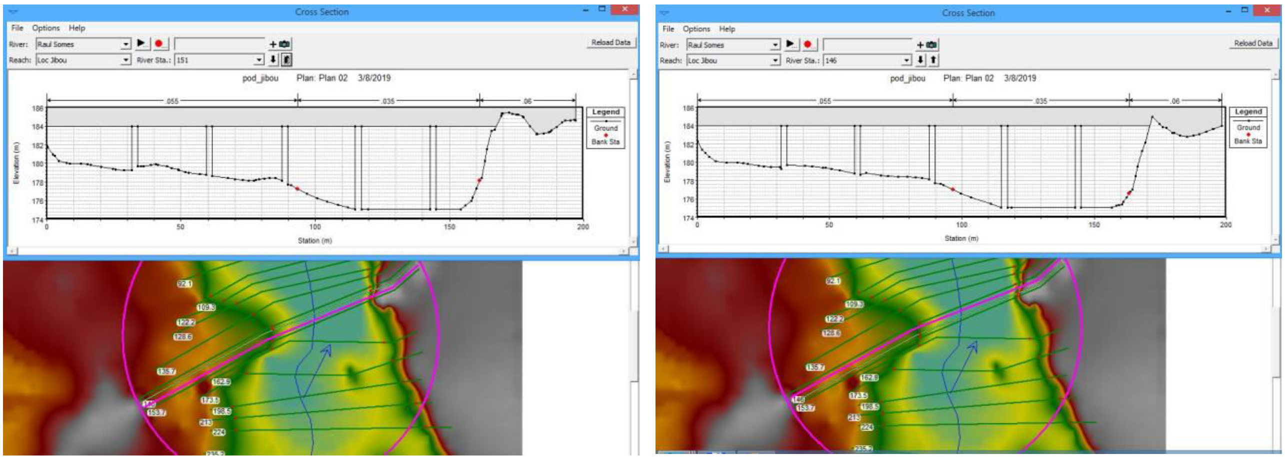

River: Raul Somes
Reach: Loc Jibou River Sta.: 151
pod_jibou Plan: Plan 02 3/8/2019

River: Raul Somes
Reach: Loc Jibou River Sta.: 146
pod_jibou Plan: Plan 02 3/8/2019

**Fig. 3.** Detail view of the Someș River sector numerical model indicating the two special river cross-sections defined at the upstream and downstream bridge faces (River Stations 151 and 146)

Figures 5 and 6 indicate the approaching ways for uploading the three years flowing hydrograph of the quasi-unsteady regime and the corresponding temperature series respectively. The hydrograph development on the studied site on Someș River reaches the maximum value of 226.53 m$^3$/s.

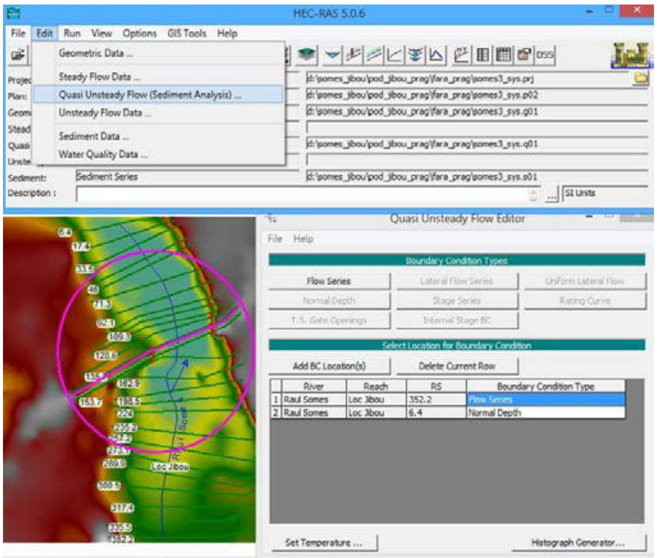

Project: d:\somes_jibou\pod_jibou_prag\fara_prag\somes3_sys.prj
Plan: d:\somes_jibou\pod_jibou_prag\fara_prag\somes3_sys.p02
Geometry: d:\somes_jibou\pod_jibou_prag\fara_prag\somes3_sys.g01
Quasi: d:\somes_jibou\pod_jibou_prag\fara_prag\somes3_sys.q01
Sediment: Sediment Series d:\somes_jibou\pod_jibou_prag\fara_prag\somes3_sys.s01
Description: SI Units

| | River | Reach | RS | Boundary Condition Type |
|---|---|---|---|---|
| 1 | Raul Somes | Loc Jibou | 352.2 | Flow Series |
| 2 | Raul Somes | Loc Jibou | 6.4 | Normal Depth |

**Fig. 4.** Flowing hydrograph approaching way as considering a quasi-unsteady regime

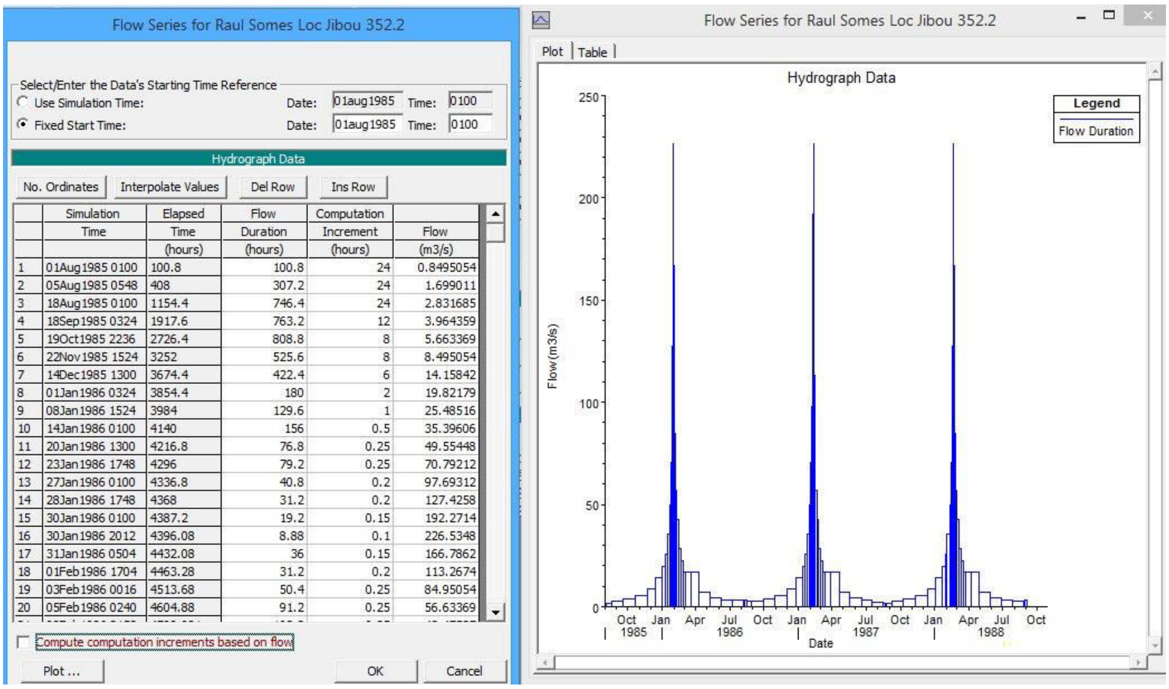

Flow Series for Raul Somes Loc Jibou 352.2

Select/Enter the Data's Starting Time Reference
○ Use Simulation Time: Date: 01aug1985 Time: 0100
● Fixed Start Time: Date: 01aug1985 Time: 0100

| | Simulation Time | Elapsed Time (hours) | Flow Duration (hours) | Computation Increment (hours) | Flow (m3/s) |
|---|---|---|---|---|---|
| 1 | 01Aug1985 0100 | 100.8 | 100.8 | 24 | 0.8495054 |
| 2 | 05Aug1985 0548 | 408 | 307.2 | 24 | 1.699011 |
| 3 | 18Aug1985 0100 | 1154.4 | 746.4 | 24 | 2.831685 |
| 4 | 18Sep1985 0324 | 1917.6 | 763.2 | 12 | 3.964359 |
| 5 | 19Oct1985 2236 | 2726.4 | 808.8 | 8 | 5.663369 |
| 6 | 22Nov1985 1524 | 3252 | 525.6 | 8 | 8.495054 |
| 7 | 14Dec1985 1300 | 3674.4 | 422.4 | 6 | 14.15842 |
| 8 | 01Jan1986 0324 | 3854.4 | 180 | 2 | 19.82179 |
| 9 | 08Jan1986 1524 | 3984 | 129.6 | 1 | 25.48516 |
| 10 | 14Jan1986 0100 | 4140 | 156 | 0.5 | 35.39606 |
| 11 | 20Jan1986 1300 | 4216.8 | 76.8 | 0.25 | 49.55448 |
| 12 | 23Jan1986 1748 | 4296 | 79.2 | 0.25 | 70.79212 |
| 13 | 27Jan1986 0100 | 4336.8 | 40.8 | 0.2 | 97.69312 |
| 14 | 28Jan1986 1748 | 4368 | 31.2 | 0.2 | 127.4258 |
| 15 | 30Jan1986 0100 | 4387.2 | 19.2 | 0.15 | 192.2714 |
| 16 | 30Jan1986 2012 | 4396.08 | 8.88 | 0.1 | 226.5348 |
| 17 | 31Jan1986 0504 | 4432.08 | 36 | 0.15 | 166.7862 |
| 18 | 01Feb1986 1704 | 4463.28 | 31.2 | 0.2 | 113.2674 |
| 19 | 03Feb1986 0016 | 4513.68 | 50.4 | 0.25 | 84.95054 |
| 20 | 05Feb1986 0240 | 4604.88 | 91.2 | 0.25 | 56.63369 |

☐ Compute computation increments based on flow

**Fig. 5.** Accustomed flow hydrograph over the total simulation period, August 1st, 1985 ÷ July 31st, 1988

Besides three regular files developed by a HEC-RAS 5.0.6 modelling – the flow one (constant or unsteady), the geometry one and the plan model one (as bonding the data files), the sediment transport analysis requires a fourth file covering the solid material data. Figure 7 illustrates the uploaded sediment data and the specific geometry elements. The sediment data editor shows three facilities: Initial Conditions and Transport Parameters, Boundary Conditions and USDA-ARS Bank Stability and Erosion Model (BSTEM), the first two needing to be always accessed in a sediment transport model, while the third one being required only for an analysis concerning river-banks failing processes.

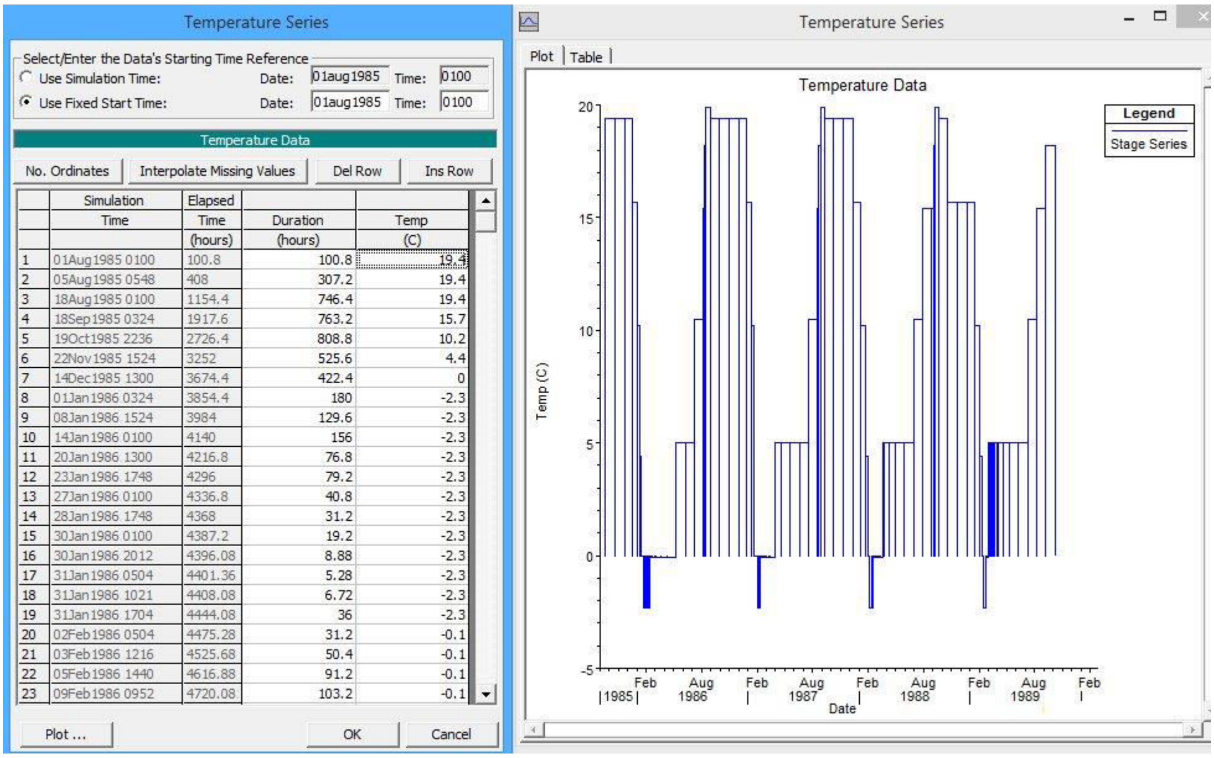

Temperature Series

Select/Enter the Data's Starting Time Reference
○ Use Simulation Time: Date: 01aug1985 Time: 0100
● Use Fixed Start Time: Date: 01aug1985 Time: 0100

Temperature Data

| | Simulation Time | Elapsed Time (hours) | Duration (hours) | Temp (C) |
|---|---|---|---|---|
| 1 | 01Aug1985 0100 | 100.8 | 100.8 | 19.4 |
| 2 | 05Aug1985 0548 | 408 | 307.2 | 19.4 |
| 3 | 18Aug1985 0100 | 1154.4 | 746.4 | 19.4 |
| 4 | 18Sep1985 0324 | 1917.6 | 763.2 | 15.7 |
| 5 | 19Oct1985 2236 | 2726.4 | 808.8 | 10.2 |
| 6 | 22Nov1985 1524 | 3252 | 525.6 | 4.4 |
| 7 | 14Dec1985 1300 | 3674.4 | 422.4 | 0 |
| 8 | 01Jan1986 0324 | 3854.4 | 180 | -2.3 |
| 9 | 08Jan1986 1524 | 3984 | 129.6 | -2.3 |
| 10 | 14Jan1986 0100 | 4140 | 156 | -2.3 |
| 11 | 20Jan1986 1300 | 4216.8 | 76.8 | -2.3 |
| 12 | 23Jan1986 1748 | 4296 | 79.2 | -2.3 |
| 13 | 27Jan1986 0100 | 4336.8 | 40.8 | -2.3 |
| 14 | 28Jan1986 1748 | 4368 | 31.2 | -2.3 |
| 15 | 30Jan1986 0100 | 4387.2 | 19.2 | -2.3 |
| 16 | 30Jan1986 2012 | 4396.08 | 8.88 | -2.3 |
| 17 | 31Jan1986 0504 | 4401.36 | 5.28 | -2.3 |
| 18 | 31Jan1986 1021 | 4408.08 | 6.72 | -2.3 |
| 19 | 31Jan1986 1704 | 4444.08 | 36 | -2.3 |
| 20 | 02Feb1986 0504 | 4475.28 | 31.2 | -0.1 |
| 21 | 03Feb1986 1216 | 4525.68 | 50.4 | -0.1 |
| 22 | 05Feb1986 1440 | 4616.88 | 91.2 | -0.1 |
| 23 | 09Feb1986 0952 | 4720.08 | 103.2 | -0.1 |

**Fig. 6.** Temperature series development covering the simulation period

Some sediment parameters need to be defined for each of the numerical model cross-section, the two simulated ones including. The following elements were adopted for the sediment transport analysis: the Yang transport function, the Thomas river-bed mixing method and the Rubey fall velocity computation method.

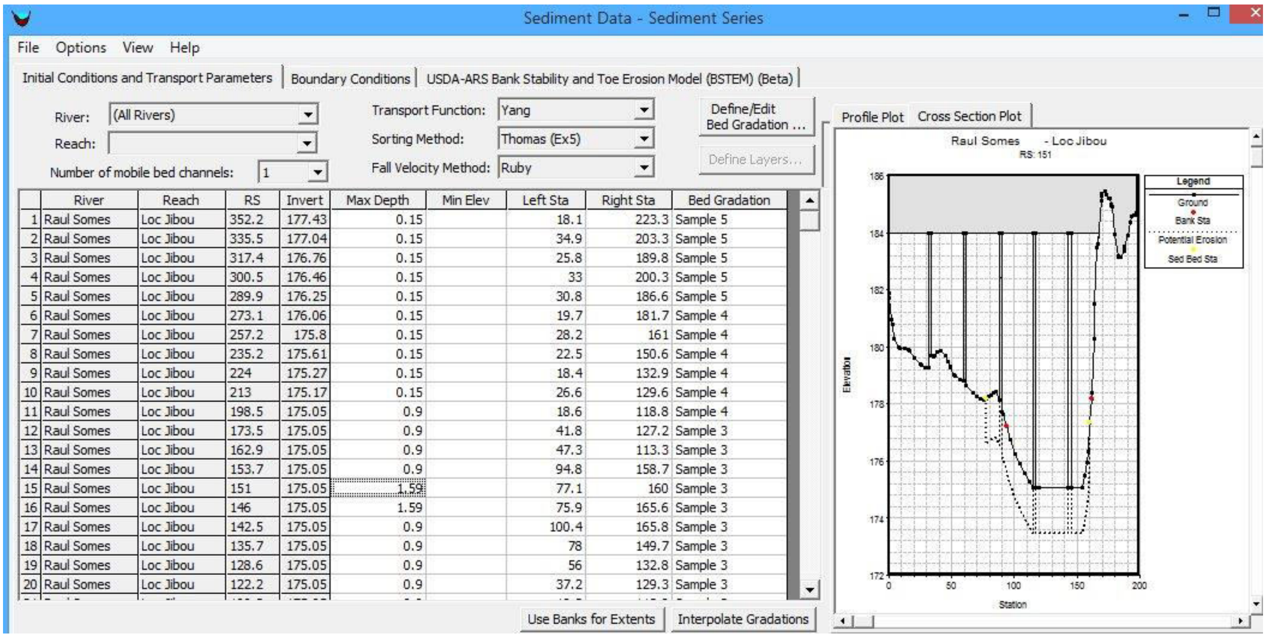

Sediment Data - Sediment Series

River: (All Rivers)
Reach:
Number of mobile bed channels: 1
Transport Function: Yang
Sorting Method: Thomas (Ex5)
Fall Velocity Method: Ruby

| | River | Reach | RS | Invert | Max Depth | Min Elev | Left Sta | Right Sta | Bed Gradation |
|---|---|---|---|---|---|---|---|---|---|
| 1 | Raul Somes | Loc Jibou | 352.2 | 177.43 | 0.15 | | 18.1 | 223.3 | Sample 5 |
| 2 | Raul Somes | Loc Jibou | 335.5 | 177.04 | 0.15 | | 34.9 | 203.3 | Sample 5 |
| 3 | Raul Somes | Loc Jibou | 317.4 | 176.76 | 0.15 | | 25.8 | 189.8 | Sample 5 |
| 4 | Raul Somes | Loc Jibou | 300.5 | 176.46 | 0.15 | | 33 | 200.3 | Sample 5 |
| 5 | Raul Somes | Loc Jibou | 289.9 | 176.25 | 0.15 | | 30.8 | 186.6 | Sample 5 |
| 6 | Raul Somes | Loc Jibou | 273.1 | 176.06 | 0.15 | | 19.7 | 181.7 | Sample 4 |
| 7 | Raul Somes | Loc Jibou | 257.2 | 175.8 | 0.15 | | 28.2 | 161 | Sample 4 |
| 8 | Raul Somes | Loc Jibou | 235.2 | 175.61 | 0.15 | | 22.5 | 150.6 | Sample 4 |
| 9 | Raul Somes | Loc Jibou | 224 | 175.27 | 0.15 | | 18.4 | 132.9 | Sample 4 |
| 10 | Raul Somes | Loc Jibou | 213 | 175.17 | 0.15 | | 26.6 | 129.6 | Sample 4 |
| 11 | Raul Somes | Loc Jibou | 198.5 | 175.05 | 0.9 | | 18.6 | 118.8 | Sample 4 |
| 12 | Raul Somes | Loc Jibou | 173.5 | 175.05 | 0.9 | | 41.8 | 127.2 | Sample 3 |
| 13 | Raul Somes | Loc Jibou | 162.9 | 175.05 | 0.9 | | 47.3 | 113.3 | Sample 3 |
| 14 | Raul Somes | Loc Jibou | 153.7 | 175.05 | 0.9 | | 94.8 | 158.7 | Sample 3 |
| 15 | Raul Somes | Loc Jibou | 151 | 175.05 | 1.59 | | 77.1 | 160 | Sample 3 |
| 16 | Raul Somes | Loc Jibou | 146 | 175.05 | 1.59 | | 75.9 | 165.6 | Sample 3 |
| 17 | Raul Somes | Loc Jibou | 142.5 | 175.05 | 0.9 | | 100.4 | 165.8 | Sample 3 |
| 18 | Raul Somes | Loc Jibou | 135.7 | 175.05 | 0.9 | | 78 | 149.7 | Sample 3 |
| 19 | Raul Somes | Loc Jibou | 128.6 | 175.05 | 0.9 | | 56 | 132.8 | Sample 3 |
| 20 | Raul Somes | Loc Jibou | 122.2 | 175.05 | 0.9 | | 37.2 | 129.3 | Sample 3 |

**Fig. 7.** Cross-sections sediment specific data

The movable river-bed surface was defined by six bed layers gradation templates, specifying the shallow ground granulometry. The graphical representation of figure 8 exemplifies the ground gradation curve in the crossing structure area (Sample 3) according to the associated granulometry.

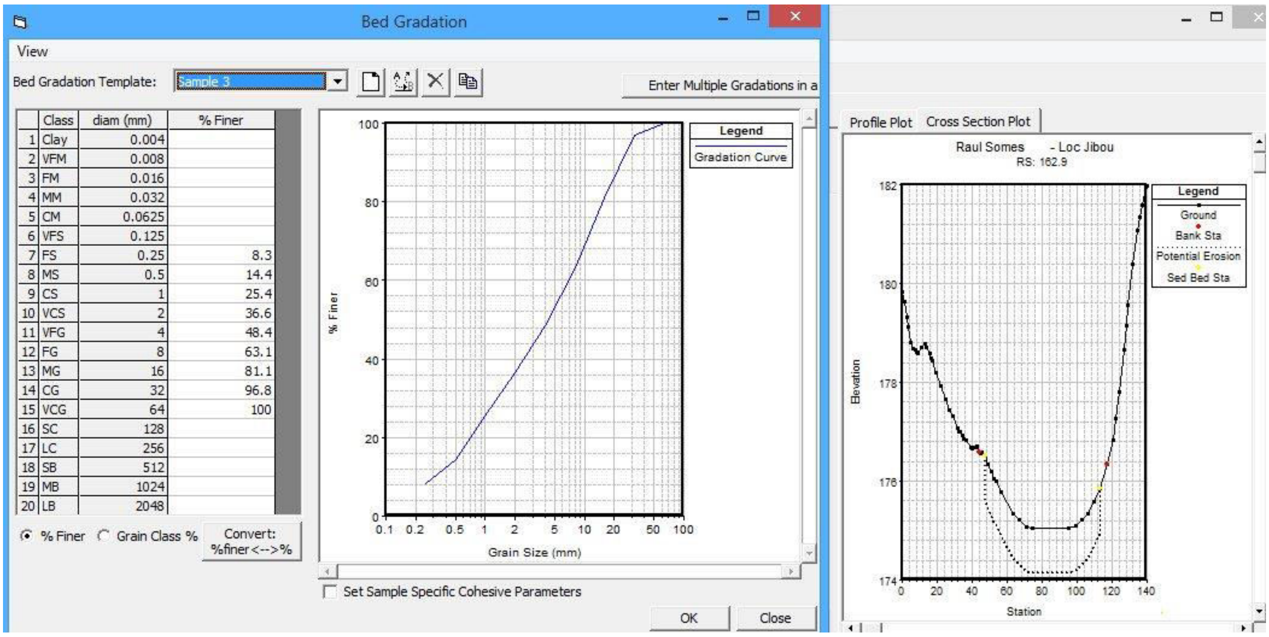

Bed Gradation Template: Sample 3

| | Class | diam (mm) | % Finer |
|---|---|---|---|
| 1 | Clay | 0.004 | |
| 2 | VFM | 0.008 | |
| 3 | FM | 0.016 | |
| 4 | MM | 0.032 | |
| 5 | CM | 0.0625 | |
| 6 | VFS | 0.125 | |
| 7 | FS | 0.25 | 8.3 |
| 8 | MS | 0.5 | 14.4 |
| 9 | CS | 1 | 25.4 |
| 10 | VCS | 2 | 36.6 |
| 11 | VFG | 4 | 48.4 |
| 12 | FG | 8 | 63.1 |
| 13 | MG | 16 | 81.1 |
| 14 | CG | 32 | 96.8 |
| 15 | VCG | 64 | 100 |
| 16 | SC | 128 | |
| 17 | LC | 256 | |
| 18 | SB | 512 | |
| 19 | MB | 1024 | |
| 20 | LB | 2048 | |

● % Finer ○ Grain Class % Convert: %finer<-->%

☐ Set Sample Specific Cohesive Parameters

**Fig. 8.** Gradation curve of the movable river-bed shallow ground corresponding to the crossing bridge area on Someș River analysed sector, as attached to River Station 162.9

It must be mentioned that the employed data regarding the solid flow and the movable river-bed layers gradation was only adjusted from other similar river courses and sites, following recommendations and eloquent templates [2]. Even if the values modelling these parameters closely follow a possible natural case on the studied site, still they are not obtained by authorized monitoring and measurements. Similarly, the adopted temperature development generally complies with thermal monthly evolution in the specific geographical area of Jibou Town.

As about the model boundary initial conditions, they were edited in the Sediment Analysis sub-menu by employing the BC Line option with respect to the upstream entering river cross-section (River Station 352.2). The constant flow values and the flow steps duration, as modelling the natural hydrograph, together with the computation increment of each step were assigned there (figure 9).

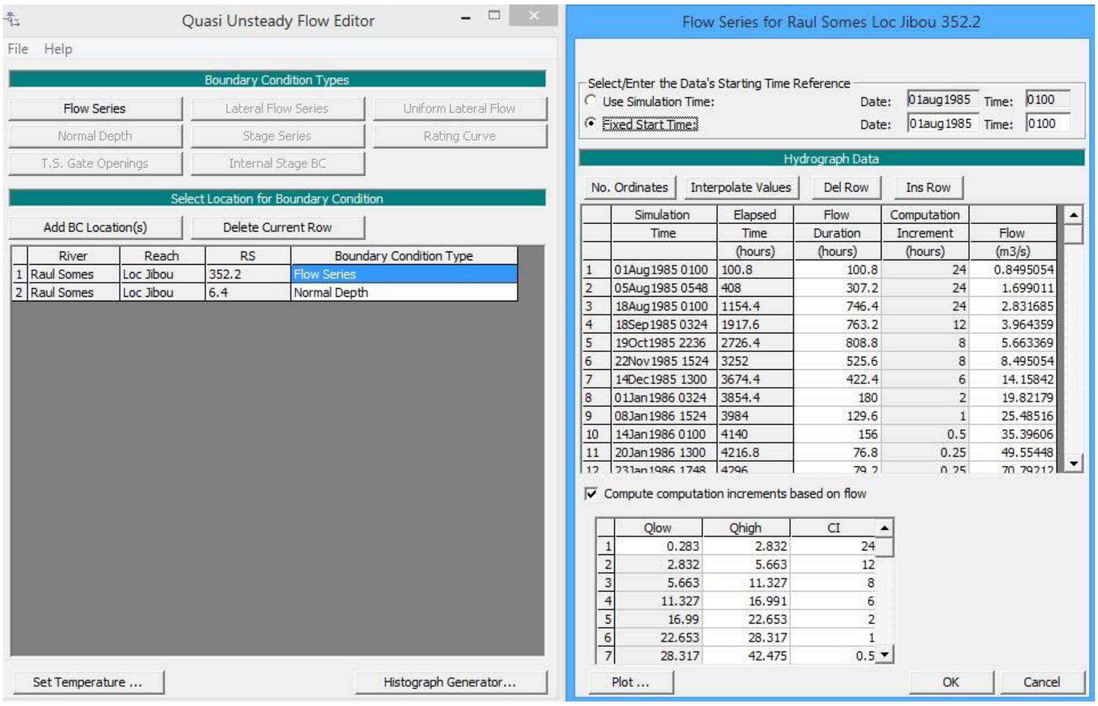

| | River | Reach | RS | Boundary Condition Type |
|---|---|---|---|---|
| 1 | Raul Somes | Loc Jibou | 352.2 | Flow Series |
| 2 | Raul Somes | Loc Jibou | 6.4 | Normal Depth |

Select/Enter the Data's Starting Time Reference
○ Use Simulation Time: Date: 01aug1985 Time: 0100
● Fixed Start Time: Date: 01aug1985 Time: 0100

| | Simulation Time | Elapsed Time (hours) | Flow Duration (hours) | Computation Increment (hours) | Flow (m3/s) |
|---|---|---|---|---|---|
| 1 | 01Aug1985 0100 | 100.8 | 100.8 | 24 | 0.8495054 |
| 2 | 05Aug1985 0548 | 408 | 307.2 | 24 | 1.699011 |
| 3 | 18Aug1985 0100 | 1154.4 | 746.4 | 24 | 2.831685 |
| 4 | 18Sep1985 0324 | 1917.6 | 763.2 | 12 | 3.964359 |
| 5 | 19Oct1985 2236 | 2726.4 | 808.8 | 8 | 5.663369 |
| 6 | 22Nov1985 1524 | 3252 | 525.6 | 8 | 8.495054 |
| 7 | 14Dec1985 1300 | 3674.4 | 422.4 | 6 | 14.15842 |
| 8 | 01Jan1986 0324 | 3854.4 | 180 | 2 | 19.82179 |
| 9 | 08Jan1986 1524 | 3984 | 129.6 | 1 | 25.48516 |
| 10 | 14Jan1986 0100 | 4140 | 156 | 0.5 | 35.39606 |
| 11 | 20Jan1986 1300 | 4216.8 | 76.8 | 0.25 | 49.55448 |
| 12 | 23Jan1986 1748 | 4296 | 79.2 | 0.25 | 70.79212 |

☑ Compute computation increments based on flow

| | Qlow | Qhigh | CI |
|---|---|---|---|
| 1 | 0.283 | 2.832 | 24 |
| 2 | 2.832 | 5.663 | 12 |
| 3 | 5.663 | 11.327 | 8 |
| 4 | 11.327 | 16.991 | 6 |
| 5 | 16.99 | 22.653 | 2 |
| 6 | 22.653 | 28.317 | 1 |
| 7 | 28.317 | 42.475 | 0.5 |

**Fig. 9.** Assignment of upstream entering river station boundary conditions – constant flow series

The computation increment value is estimated as related to the constant flow level, decreasing with the flow value increase (Compute computation increments based on flow facility). In the same time, a downstream boundary condition was edited by assigning the given 2.75‰ hydro-dynamic gradient to the model outgoing river cross-section (River Station 6.4).

The solid flow sets of values (tons/day), as estimated in relation to the liquid one ($m^3/s$), were uploaded as boundary conditions of the numerical model by following the given sequence of software menus: Sediment Data → Data sediment – Sediment Series → Boundary Conditions → Rating Curve. There were considered five sets, for each being specified the fractions contribution in the sediment load according to the material granulometry (figure 10), which were assigned as boundary condition to the river sector entering cross-section (River Station 352.2).

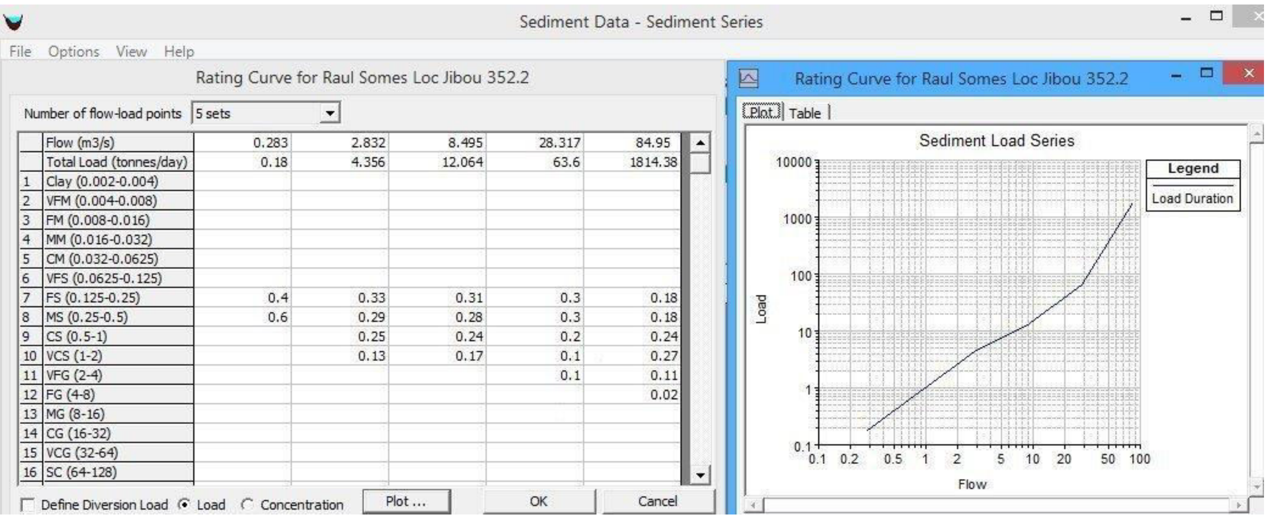

| | | | | | | |
|---|---|---|---|---|---|---|
| | Flow (m3/s) | 0.283 | 2.832 | 8.495 | 28.317 | 84.95 |
| | Total Load (tonnes/day) | 0.18 | 4.356 | 12.064 | 63.6 | 1814.38 |
| 1 | Clay (0.002-0.004) | | | | | |
| 2 | VFM (0.004-0.008) | | | | | |
| 3 | FM (0.008-0.016) | | | | | |
| 4 | MM (0.016-0.032) | | | | | |
| 5 | CM (0.032-0.0625) | | | | | |
| 6 | VFS (0.0625-0.125) | | | | | |
| 7 | FS (0.125-0.25) | 0.4 | 0.33 | 0.31 | 0.3 | 0.18 |
| 8 | MS (0.25-0.5) | 0.6 | 0.29 | 0.28 | 0.3 | 0.18 |
| 9 | CS (0.5-1) | | 0.25 | 0.24 | 0.2 | 0.24 |
| 10 | VCS (1-2) | | 0.13 | 0.17 | 0.1 | 0.27 |
| 11 | VFG (2-4) | | | | 0.1 | 0.11 |
| 12 | FG (4-8) | | | | | 0.02 |
| 13 | MG (8-16) | | | | | |
| 14 | CG (16-32) | | | | | |
| 15 | VCG (32-64) | | | | | |
| 16 | SC (64-128) | | | | | |

**Fig. 10.** Definition of the five sets of sediment load as corresponding to the liquid flow level, assigned to the upstream entering river station

## 3. Numerical simulation and results

The liquid and solid transport numerical simulation along the specific river sector was performed over a three years given period, from 01:00 of August 1st, 1985, to 23:00 of July 31st, 1988. The steady and time dependent representative flowing parameters – water level, velocity and discharge – along the entire modelled river sector were revealed by running the numerical simulation.

Particular files of numerical values were created by performing the output regular processing operations [1,5,6]. As specifically looking to study the effect of considering the two simulated bridge framing crossing-sections with respect to a reference situation when the model considers the actual crossing structure (analysed by Popescu-Buşan et.al., 2019, under the same flow and sediment loading conditions [1]), the numerically reached results are going to be fairly presented further on.

Since the analysed phenomenon runs over a relatively long period of time, for expressiveness reasons, there were considered six particular moments of given constant liquid flow (figure 11): August 18th, 1985, of 2.83$m^3/s$ transported flow, January 8th, 1986, of 25.485$m^3/s$, January 30th, 1986, of 226.53$m^3/s$, August 5th, 1986, of 2.83$m^3/s$, February 20th, 1987, of 186.79$m^3/s$, and February 20th, 1988, of 226.53$m^3/s$.

As comparatively examining the numerical output regarding scouring depths (or silting heights, at some moment) in the immediate bridge area (geometric interval $\Delta L$ = 153.7 - 142.5 = 11.2m), one would notice that the values reached by the presently described model are slightly different from the values given by the reference model (table no.1).

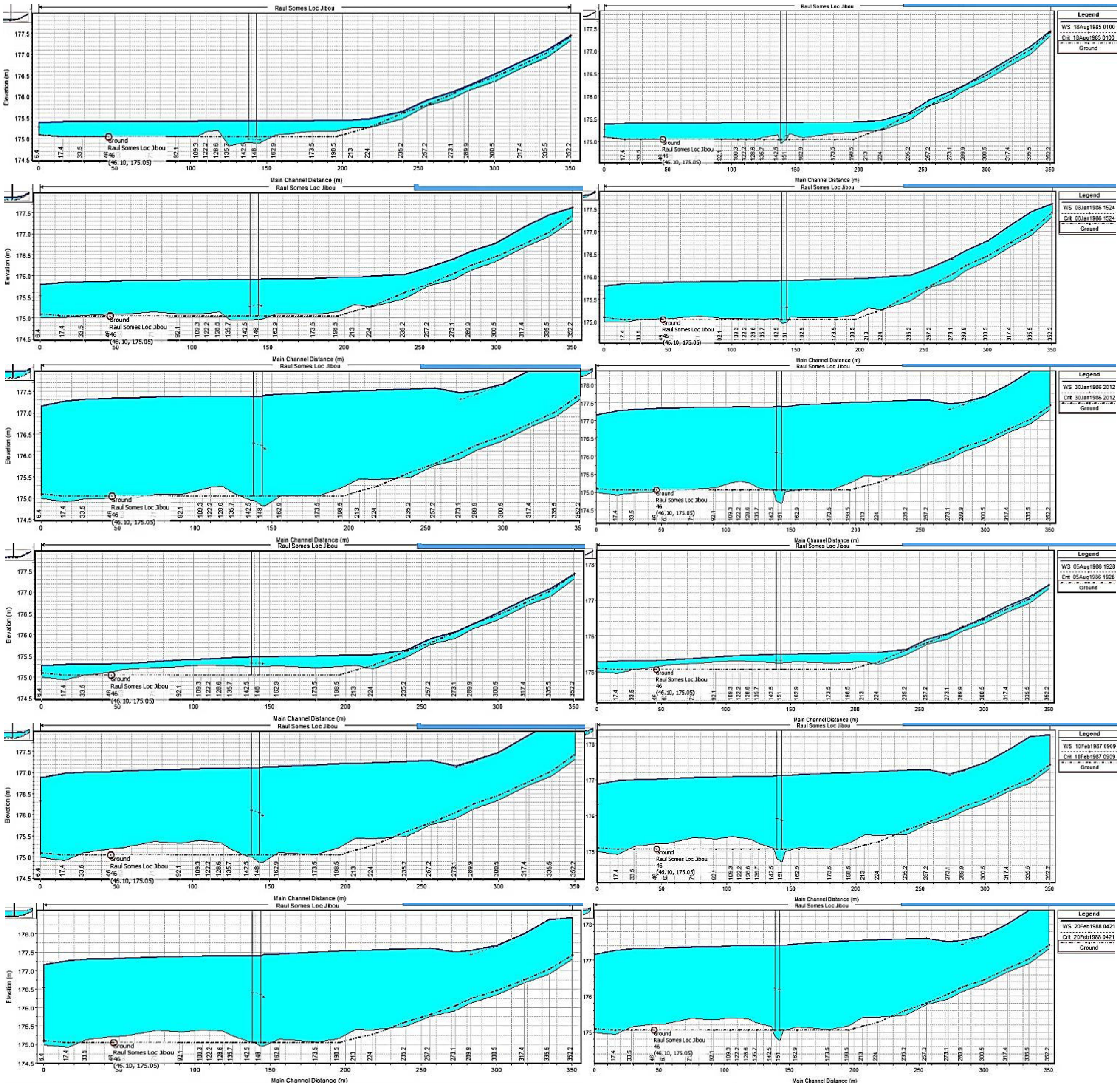

**Fig. 11.** Comparative water surface and river-bed longitudinal profiles (reference model on the left side) on the Someș River analysed sector at six particular moments along the liquid and solid transport simulation period: August 18th, 1985, January 8th, 1986, January 30th, 1986, August 5th, 1986, February 10th, 1987, and February 20th, 1988

Even if the values are in the expected range and so not outsize for the analysed phenomenon under the given judicious circumstances, there is still noticed that the major difference appear as larger scourings – January 30th, 1986 → $\Delta$ = 9cm, February 10th, 1987 → $\Delta$ = 19cm or February 20th, 1988 → $\Delta$ = 18.6cm.

Regarding the concerning river cross-section right at the bridge upstream face, tagged as River Station 151, the correlated river-bed minimum level – water surface maximum level time development revealed by the presented model (figure 12) show a general tendency of scouring decreasing with respect to the foundation structure top level (175.05mSL) from about 38cm, in the first part of the considered three years simulation period, to about 22cm, as the maximum depth towards the ending part.

**Table 1:** Movable river-bed levels in the bridge area at several moments

| | River Station | Movable river-bed level (mSL) | | | | | |
|---|---|---|---|---|---|---|---|
| | | August 18th, 1985 | January 8th, 1986 | January 30th, 1986 | August 25th, 1986 | February 10th, 1987 | February 20th, 1988 |
| Reference model | 153.70 | 174.9000 | 174.9700 | 174.8100 | 175.2400 | 174.8900 | 174.9700 |
| | 151 | 174.9000 | 174.9700 | 174.8100 | 175.2400 | 174.8900 | 174.9700 |
| | 146 | 174.9100 | 174.9100 | 174.9300 | 175.2600 | 175.0200 | 175.0900 |
| | 142.50 | 174.9100 | 174.9100 | 174.9300 | 175.2600 | 175.0200 | 175.0900 |
| difference from the minimum bed level to foundation block top level (175.05mSL) | | - 15.0cm scouring | - 14.0cm scouring | - 24.0cm scouring | + 19.0cm silting | - 16.0cm scouring | - 9.8cm scouring |
| Present model | 153.70 | 175.2010 | 175.0994 | 175.1198 | 175.2991 | 175.0052 | 175.0440 |
| | 151 | 174.9879 | 174.9705 | 174.7200 | 175.2353 | 174.7000 | 174.7664 |
| | 146 | 174.9378 | 174.9623 | 174.7900 | 175.2444 | 174.8195 | 174.8862 |
| | 142.50 | 175.1721 | 175.0986 | 175.0861 | 175.2476 | 175.1111 | 175.1564 |
| difference from the minimum bed level to foundation block top level (175.05mSL) | | - 11.2cm scouring | - 8.8cm scouring | - 33.0cm scouring | + 18.5cm silting | - 35.0cm scouring | - 28.4cm scouring |
| deviation with respect to reference model | | 3.8cm | 5.2cm | 9.0cm | 0.5cm | 19.0cm | 18.6cm |

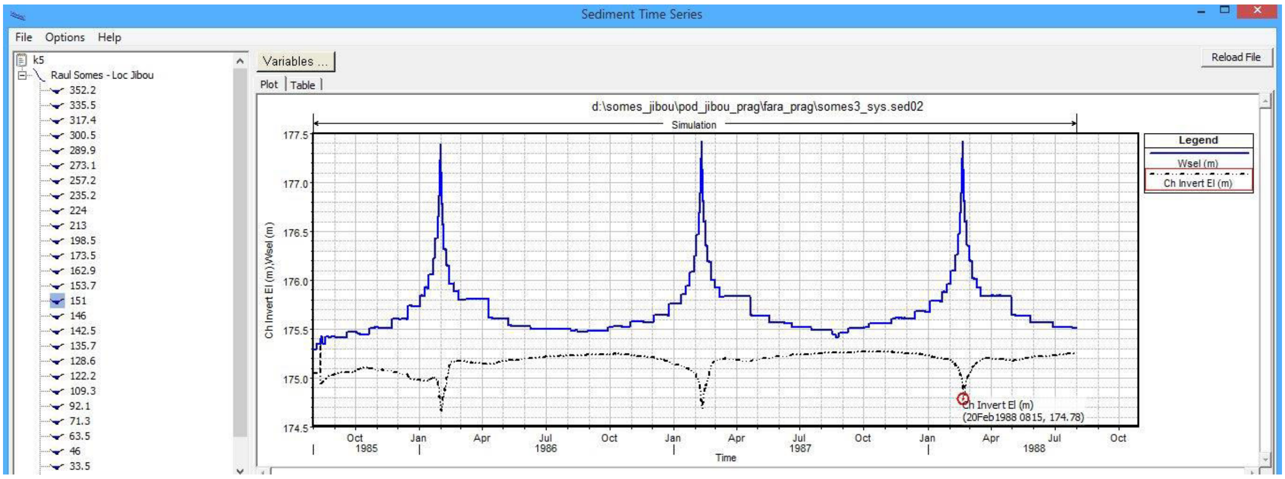

**Fig. 12.** Correlated river-bed minimum level – water surface maximum level time development on the bridge upstream face river station 151 along the three years simulation period

## 4. Conclusions

By performing the liquid and solid transport numerical study for the bridge influenced Someș River sector in order to analyse the river-bed dynamic processes, one can conclude that in case of lack of specific local geometry information (e.g. new river crossing structures on other sites) there is possible to engage a two steps modelling. In order to reach a potential local scouring estimation for the bridge area, the first model step considered the explicit bridge structure under transited by the steady maximum flow of 226.53m$^3$/s and led to the total maximum scour depth of 1.59m with respect to piers foundation top level. This under bridge river-bed geometry, obtainable only by involving the actual crossing structure model, is to be further on engaged to define the required parameters for the second model step. Thus, the actual crossing structure was than replaced by two simulated framing river cross-sections bearing also the bridge supporting piers structural shape. The altered numerical model of the second step is recommended for a liquid and sediment transport analysis.

The comparative study of the outcome revealed by the proposed two steps model and the results of a previously performed numerical simulation under similar flowing conditions, which however considered a given state of river-bed and bridge structure, shows a considerable reversion of the starting local scouring limits but also significant differences (maximum about 19cm) regarding the scouring depths, mainly larger for the present approach.

As it was already suggested by the former analysis results, looking at the presently reached outcome it may be once again concluded that the accomplishment of a bridge downstream bottom step would be required in order to improve the general river-bed processes development over time. Its location may be estimated by the help of the graphical longitudinal output, meaning on the inflection point parting the silting and scouring sections in the bridge downstream area (about River Station 46). The bottom step optimum height may be further on proposed by performing some successive additional analysis.

## References

[1] Popescu-Buşan, A.I., Gh.I. Lazăr, A.T. Constantin, and Ş.V. Nicoară. "Numerical simulation of sediments transport on a river sector as distorted by a crossing structure." Paper presented at World Multidisciplinary Earth Sciences Symposium - WMESS 2019, Praga, Cehia, September 3- 9, 2019.
[2] Brunner, G.W. *HEC–RAS 5.0.6*. US Army Corps of Engineers, November 2018.
[3] Brunner, G.W. *HEC–RAS River Analysis System, Hydraulic Reference Manual.* Version 5.0. US Army Corps of Engineers, February 2016.
[4] Nicoară, Ş.V., Gh.I. Lazăr, and A.T. Constantin. "Comparative study of a 1D and 2D numerical analysis modelling a water flow at a river confluence under accidental high waters." *Hidraulica - Magazine of Hydraulics, Pneumatics, Tribology, Ecology, Sensorics, Mechatronics*, no. 4 (December 2018): 90-97.
[5] Nicoară, Ş.V., Gh.I. Lazăr, and A.T. Constantin. "Computer analysis of water flow transition under existing conditions on a river sector in the range of a bridge structure." *Hidraulica - Magazine of Hydraulics, Pneumatics, Tribology, Ecology, Sensorics, Mechatronics*, no.1 (March 2019): 98-106.
[6] Ghiţescu, M.A., Gh.I. Lazăr, A.T. Constantin, and Ș.V. Nicoară. "Numerical Model of Transitory Flood Flow in 2005 on River Timiș." Paper presented at World Multidisciplinary Civil Engineering – Architecture – Urban Planning Symposium (WMCAUS), Eco-Friendly Symposium, Prague, Czech Republic, June 12–16, 2017.
[7] Brunner, G.W. *Combined 1D and 2D Modelling with HEC–RAS.* Version 5.0. US Army Corps of Engineers, October 2016.

**ISSN 1453 – 7303** **"HIDRAULICA" (No. 4/2019)**
**Magazine *of Hydraulics, Pneumatics, Tribology, Ecology, Sensorics, Mechatronics***

# The Influence of Corrosion and Temperature Variation on a CNG Storage Tank with a Combined Form consisting of a Torus and a Sphere

Assoc. Prof. PhD. Eng. **Mihai ŢĂLU**[1], Assoc. Prof. PhD. Eng. **Ștefan ŢĂLU**[2,*]

[1] University of Craiova, Faculty of Mechanics, Department of Applied Mechanics and Civil Engineering, Calea București Street, no. 107, 200512 Craiova, Dolj county, Romania. E-mail: mihai_talu@yahoo.com

[2] Technical University of Cluj-Napoca, The Directorate of Research, Development and Innovation Management (DMCDI), Constantin Daicoviciu Street, no. 15, Cluj-Napoca, 400020, Cluj county, Romania. Corresponding author* e-mail: stefan_ta@yahoo.com

***Abstract:*** *The objective of this paper is to study the influence of corrosion and temperature variation on a CNG storage tank with a combined form consisting of a torus and a sphere, made of steel, for compressed natural gas (CNG) storage from the automotive industry. Numerical simulations had been performed to assess the influence of the corrosion and temperature variation on the state of stress and of the linear deformation values. A polynomial interpolation was applied to provide a comparison between the surfaces or curves.The 3-D (three-dimensional) model (modelled using the AutoCAD Autodesk 2017 software), was imported for numerical analyses to SolidWorks 2017 software). The results of analyzed cases can improve the fundamental understanding of the corrosion behavior of CNG storage tanks in exploatation environments.*

***Keywords:*** *Automotive industry, compressed natural gas (CNG) storage tank, industrial engineering design, optimization methods, pressure vessel*

## 1. Introduction

In the last few decades, the process of deterioration of materials due to the storage fuel tank's interaction with interconnected components and corrosive environmental conditions has been deeply studied in the scientific literature, both theoretically and experimentally, in relation with a lot of factors (such as erosion, the degree of saturation with water, the elastic properties and the strength of the material, the pore structure of the material, volume change of the material, the volume changes of the material in pores, dissolution of a material and the associated chemical changes) [1]. Furthermore, in the scientific literature are presented new models for the competitive market of fuel storage tanks designed based on suitable strategies for reducing the impact of corrosion, and preserving the material integrity [2-7].

Generally, the fuel storage tanks are made of materials with good mechanical and chemical resistance; they have simple or complex geometric configurations, in a wide range of dimensions, with various engineering specifications, which combines design, functionality and performance [8-12].

Modern computer aided design (CAD) and computer aided engineering (CAE) analyses used in designing of the storage fuel tanks have become a part of product development process that offer a competitive advantage, without substantial investments, for reducing product design cycle by saving time, costs in set ups and manufacturing the physical prototypes [13-16].

In the design and manufacturing strategies of the storage fuel tanks, priority research directions include optimization theory and algorithms for analysis, methodologies for multiscale deterministic models; alternative models of uncertainty and risk; integration of data and modeling [17-21].

For the 3-D (three-dimensional) design of the storage fuel tanks in accordance with the relevant guidelines and procedures outlined by the national/international standards [22-26] there are various valid implementations of mathematical methods [27-31] in more efficient algorithms and programs [32-36] to find the optimized solution according the criterion of optimality to satisfy the general structural design (In a hierarchical approach, the system, subsystems, components) [37-42] and certification rules [43, 44].

In our research, the influence of corrosion and temperature variation on a CNG storage tank with a combined form consisting of a torus and a sphere, made of steel, for compressed natural gas (CNG) storage from the automotive industry was performed in accordance to the general structural design.

## 2. Design methodology

### 2.1 Basic geometry of the parametric 3-D model

Let's consider the parametric 3-D model of a CNG storage tank composed by a torus and a sphere with eight intermediate bracelets as shown in fig. 1, as described in Ref. [18].

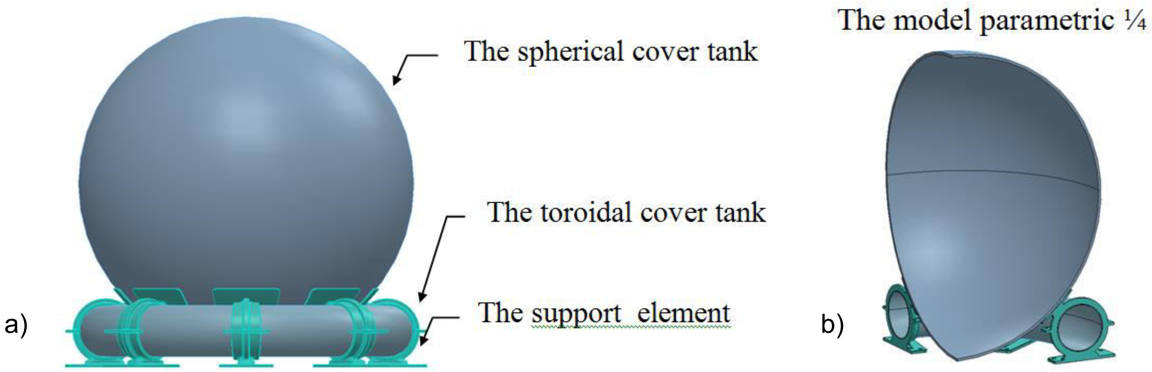

**Fig. 1.** The graphical representation of the parametric 3-D model of a CNG storage tank composed by a torus and a sphere with eight intermediate bracelets

### 2.2 Numerical analysis of the parametric 3-D model

Based on the physical model, the modeling was done in the AutoCAD Autodesk 2017 software [45] and the numerical analysis was performed with SolidWorks 2017 software [46] with the Static, Thermal and Design Study modules. The design data used were:

- the tank material is AISI 4340 steel; the intermediate bracelet type element is AISI 1045 steel;
- the maximum hydraulic test pressure: $p_{max}$ = 300 bar;
- the working temperature between the limits: T = -30 $^0$C up to T = 60 $^0$C;
- the period of the tank exploitation: $n_a$ = 20 years;
- the corrosion rate of the material: $v_c$ = 0.06 mm/years.
- the fuel stored in the tank is CNG with a density of ρ = 20.5 kg / m$^3$.

The values of the state of stress Von Mises for spherical and toroidal covers determined by the finite element method are shown in tables 1 and 2.

**Table 1:** The Von Misess effort for the spherical cover

| σ [MPa] | $n_a$ years] | The spherical cover | | | |
|---|---|---|---|---|---|
| T [°C] | 0 | 5 | 10 | 15 | 20 |
| -30 | 650.99 | 655.91 | 665.28 | 669.9 | 672.79 |
| -20 | 646.53 | 651.54 | 660.33 | 665.2 | 668.34 |
| -10 | 642.09 | 647.19 | 655.41 | 660.52 | 663.9 |
| 0 | 637.67 | 642.87 | 650.51 | 655.87 | 659.49 |
| 10 | 633.28 | 638.57 | 645.23 | 651.25 | 655.1 |
| 20 | 628.92 | 634.29 | 640.81 | 646.65 | 650.74 |
| 30 | 624.58 | 630.04 | 636.42 | 642.09 | 646.41 |
| 40 | 620.27 | 625.82 | 632.06 | 637.56 | 642.1 |
| 50 | 615.99 | 621.63 | 627.72 | 633.06 | 637.83 |
| 60 | 611.75 | 617.47 | 623.42 | 628.59 | 633.59 |

**Table 2:** The Von Misess effort for the toroidal cover

| σ [MPa] | $n_a$ years] | The toroidal cover | | | |
|---|---|---|---|---|---|
| **T [°C]** | **0** | **5** | **10** | **15** | **20** |
| -30 | 558.44 | 570.27 | 613.23 | 636.09 | 625.65 |
| -20 | 550.12 | 562.4 | 609.99 | 632.87 | 622.5 |
| -10 | 542.02 | 544.73 | 606.88 | 629.8 | 619.49 |
| 0 | 534.14 | 547.3 | 603.92 | 626.9 | 616.63 |
| 10 | 526.53 | 540.12 | 606.41 | 624.18 | 613.93 |
| 20 | 519.22 | 533.24 | 603.89 | 621.67 | 611.41 |
| 30 | 512.23 | 526.67 | 601.59 | 619.36 | 609.09 |
| 40 | 505.61 | 520.44 | 599.52 | 617.27 | 606.98 |
| 50 | 499.44 | 514.62 | 597.7 | 615.41 | 605.11 |
| 60 | 493.7 | 509.02 | 596.11 | 613.79 | 603.48 |

The graphs and laws of the variance of the Von Misess effort, calculated through a polynomial interpolation using Microsoft Excel 2017, taking into account the results from table 1 and 2, are graphically shown in fig. 2.

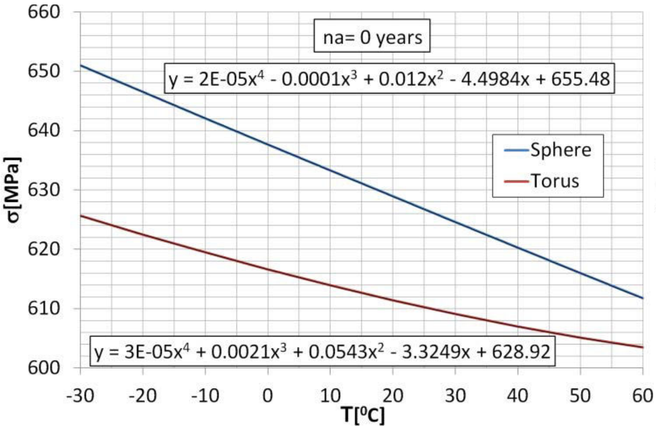

a)

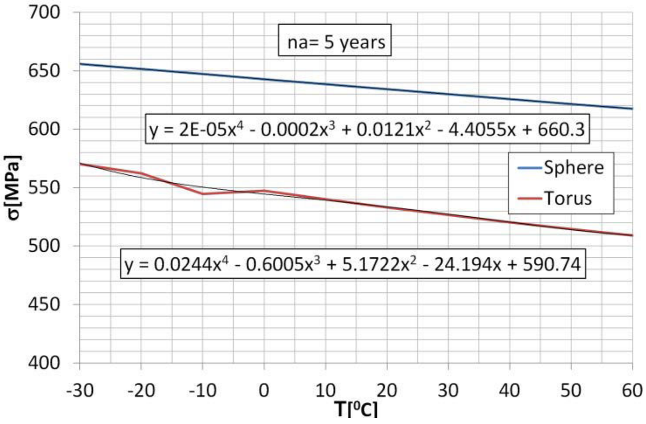

b)

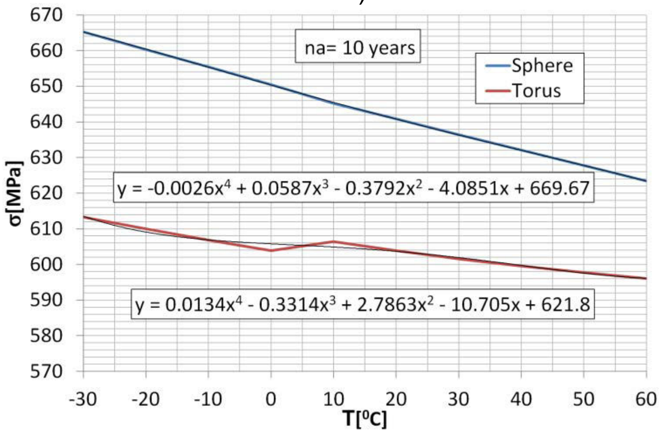

c)

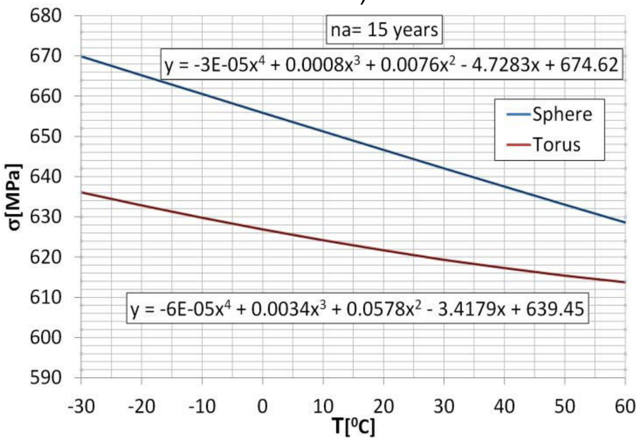

d)

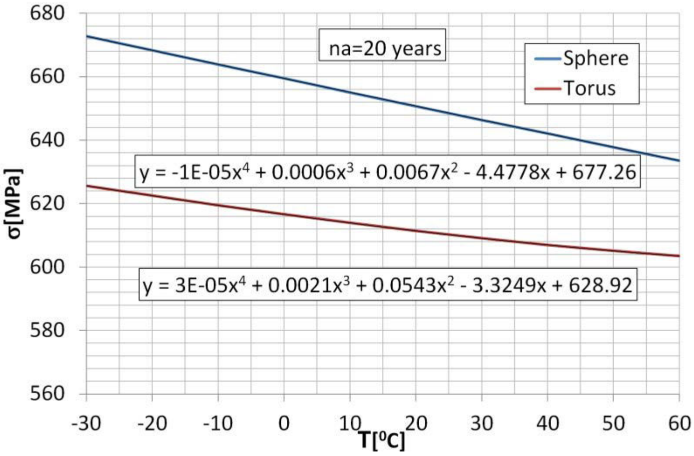

e)

**Fig. 2.** The graph of Von Mises stress $\sigma = f(T)$ for spherical and toroidal covers

The graphs of 3-D surfaces corresponding to the Von Mises effort $\sigma = f(T, n_a)$ taking into account the results from table 1 and 2, are graphically shown in fig. 3.

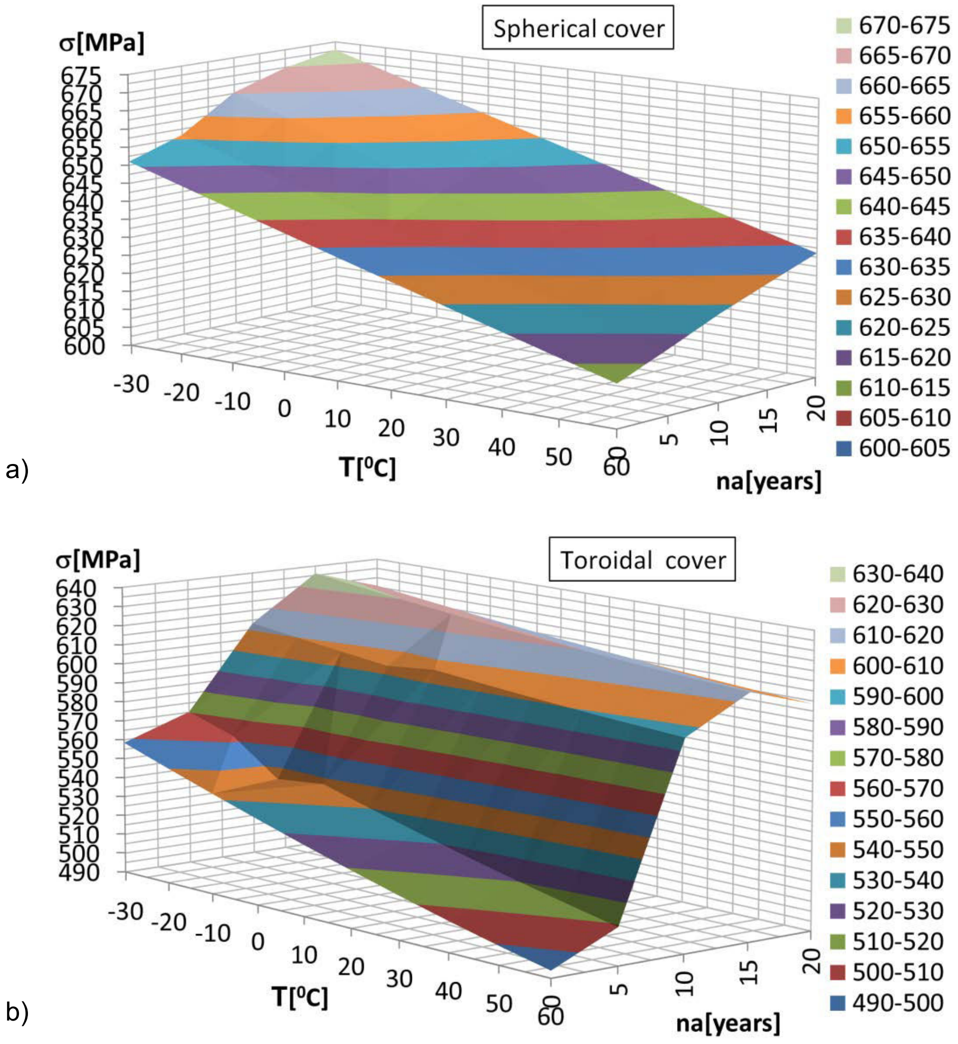

**Fig. 3.** The graphs of 3-D surfaces corresponding to the Von Mises effort $\sigma = f(T, n_a)$ for: a) spherical and b) toroidal covers

The resulting value of maximum Von Mises stress occurs at a minimum temperature of T = -30 $^0$C and a maximum linear deformation at a temperature of T = 60 $^0$C.

Distributions of the state of Von Mises stress for the storage tank corresponding for $n_a = \{0, 5, 10, 15, 20\}$ years are shown in fig. 4.

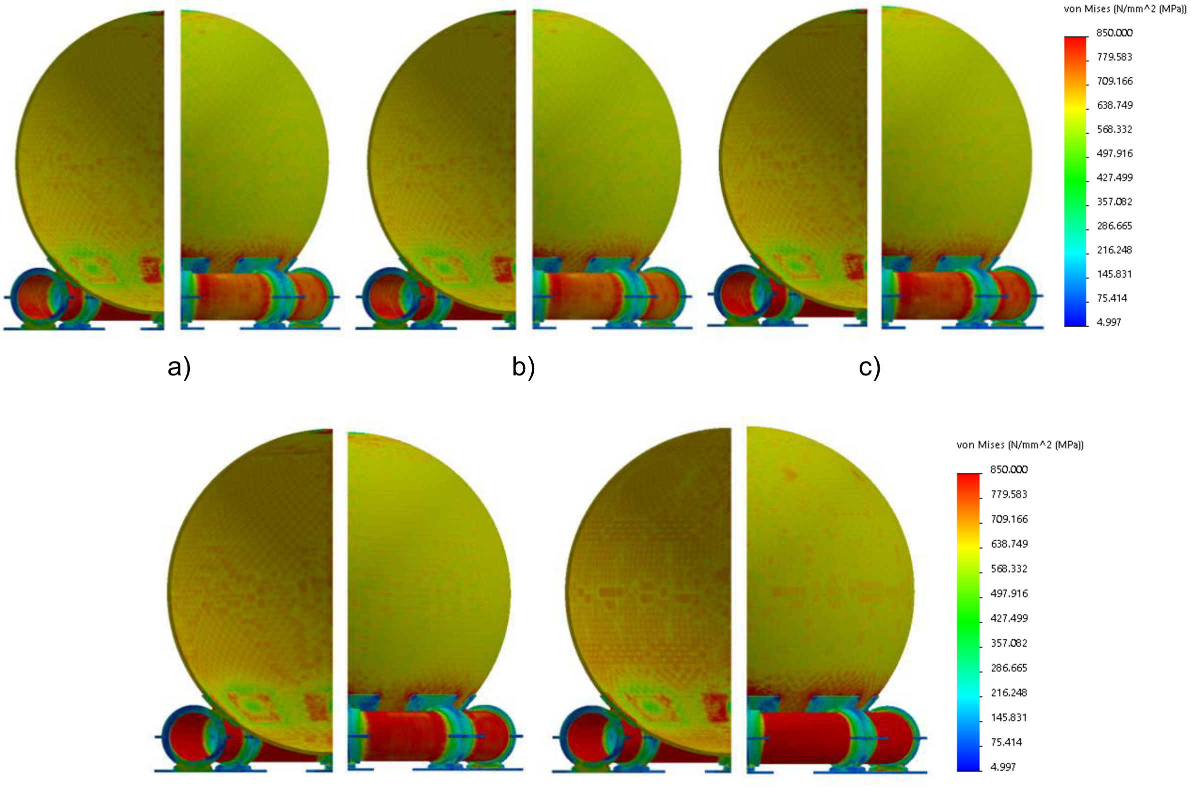

a) b) c)

d) e)

**Fig. 4.** The graphs of distributions of Von Mises stress $\sigma = f(n_a)$ for the storage tank: a) $n_a$ = 0 years; b) $n_a$ = 5 years; c) $n_a$ = 10 years; d) $n_a$ = 15 years; e) $n_a$ = 20 years

The values of the resultant linear deformation for spherical and toroidal covers determined by numerical analyses are shown in tables 3 and 4.

**Table 3:** The resultant liniar deformation for the spherical cover

| **u [mm]** | **$n_a$ years]** | **The spherical cover** | | | |
|---|---|---|---|---|---|
| **T [°C]** | **0** | **5** | **10** | **15** | **20** |
| -30 | 2.809 | 2.837 | 2.983 | 2.832 | 2.920 |
| -20 | 2.879 | 2.907 | 3.056 | 2.899 | 2.997 |
| -10 | 2.949 | 2.977 | 3.129 | 2.966 | 3.069 |
| 0 | 3.018 | 3.047 | 3.202 | 3.034 | 3.141 |
| 10 | 3.088 | 3.118 | 3.500 | 3.101 | 3.212 |
| 20 | 3.158 | 3.188 | 3.575 | 3.169 | 3.284 |
| 30 | 3.228 | 3.258 | 3.650 | 3.236 | 3.356 |
| 40 | 3.298 | 3.328 | 3.725 | 3.304 | 3.428 |
| 50 | 3.368 | 3.399 | 3.800 | 3.371 | 3.500 |
| 60 | 3.438 | 3.469 | 3.875 | 3.439 | 3.573 |

**Table 4:** The resultant liniar deformation for the toroidal cover

| **u [mm]** | **$n_a$ [years]** | **The toroidal cover** | | | |
|---|---|---|---|---|---|
| **T [°C]** | **0** | **5** | **10** | **15** | **20** |
| -30 | 1.571 | 1.589 | 1.718 | 1.703 | 1.740 |
| -20 | 1.588 | 1.606 | 1.735 | 1.718 | 1.757 |
| -10 | 1.606 | 1.624 | 1.751 | 1.733 | 1.774 |
| 0 | 1.623 | 1.641 | 1.768 | 1.748 | 1.792 |
| 10 | 1.641 | 1.659 | 1.955 | 1.763 | 1.809 |
| 20 | 1.659 | 1.677 | 1.972 | 1.779 | 1.827 |
| 30 | 1.677 | 1.694 | 1.990 | 1.795 | 1.845 |
| 40 | 1.695 | 1.712 | 2.008 | 1.811 | 1.741 |
| 50 | 1.713 | 1.731 | 2.026 | 1.827 | 1.881 |
| 60 | 1.731 | 1.749 | 2.045 | 1.843 | 1.900 |

The graphs and laws of the variance of the resultant linear deformation, calculated through a polynomial interpolation using Microsoft Excel 2017, taking into account the results from tables 3 and 4, are graphically shown in fig. 5.

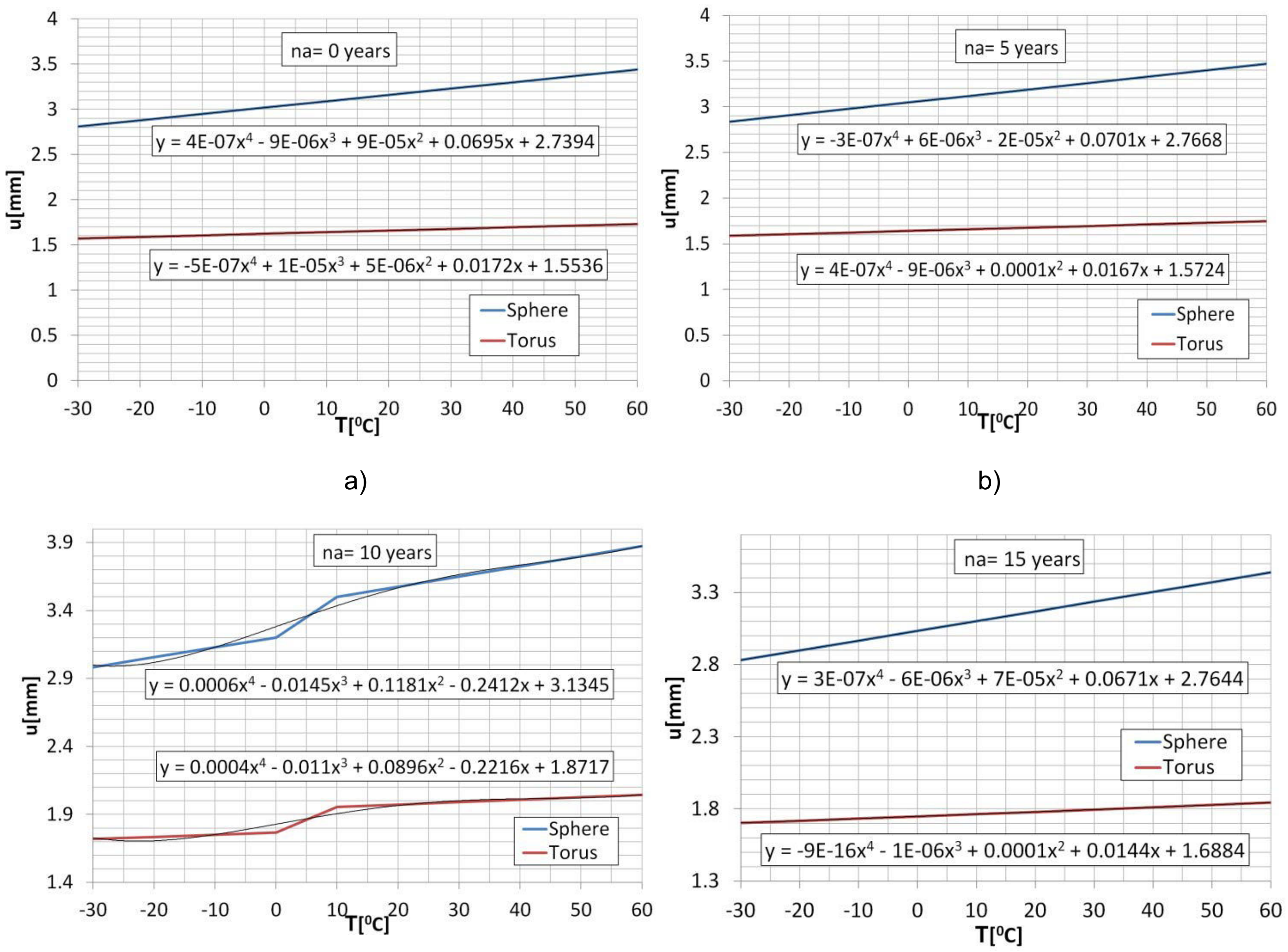

a)

b)

c)

d)

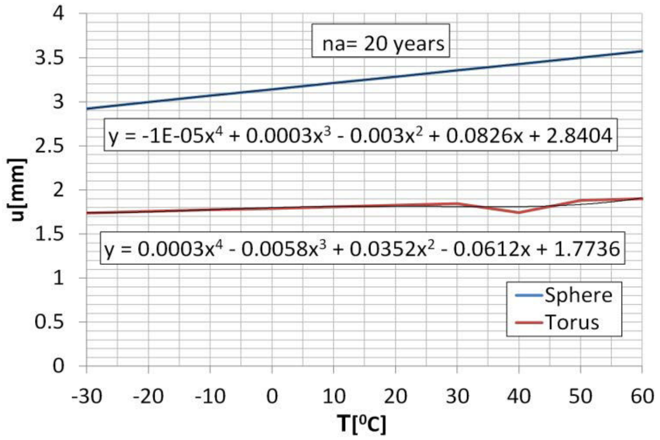

e)

**Fig. 5.** The graphs and laws of the variance of the resultant linear deformation u = f(T) for spherical and toroidal covers

The graphs of 3-D surfaces corresponding to the resultant linear deformation u = f(T, $n_a$) taking into account the results from tables 3 and 4, are graphically shown in fig. 6.

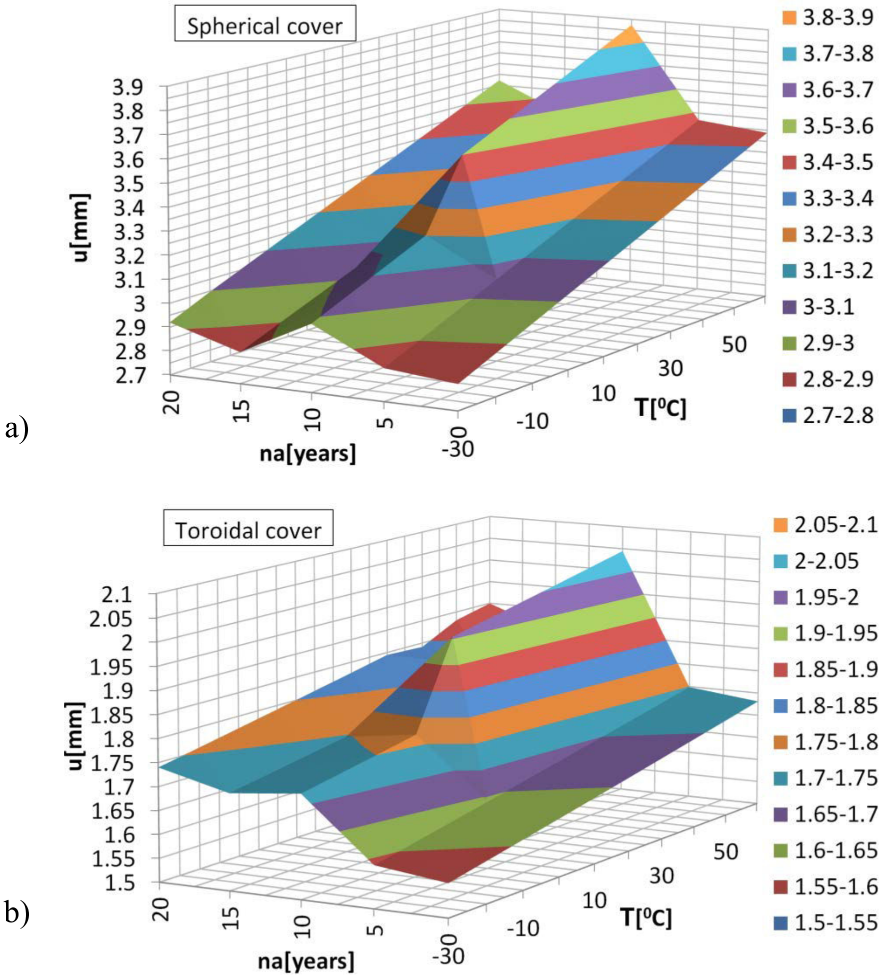

**Fig. 6.** The graphs of 3-D surfaces corresponding to the resultant linear deformation u = f(T, $n_a$) for: a) spherical and b) toroidal covers

Distributions of the resultant maximum liniar deformation at a temperature of T = 60 $^0$C for the storage tank corresponding for $n_a = \{0, 5, 10, 15, 20\}$ years are shown in fig. 7.

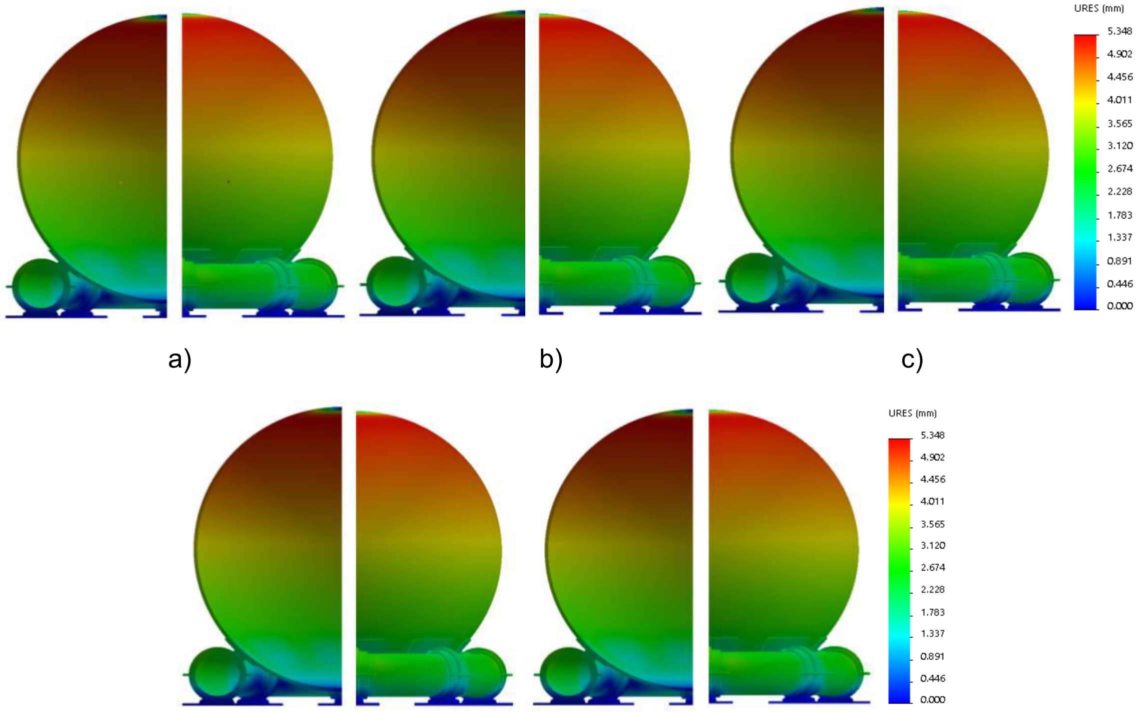

a) b) c)

d) e)

**Fig. 7.** The graphs of distributions of the resultant liniar deformation at a temperature of T = 60 $^0$C, $u = f(n_a)$ for the storage tank: a) $n_a$ = 0 years; b) $n_a$ = 5 years; c) $n_a$ = 10 years; d) $n_a$ = 15 years; e) $n_a$ = 20 years

The parameters $\Delta\sigma = f(T, n_a)$ and $\Delta u = f(T, n_a)$ for the spherical cover are given in tables 5 and 6.

**Table 5:** The variation of the Von Mises effort $\Delta\sigma = f(T, n_a)$ for the spherical cover

| **Δσ [%]** | **T [°C]** | **The spherical cover** | | | | | | | | |
|---|---|---|---|---|---|---|---|---|---|---|
| **$n_a$ [years]** | **-30** | **-20** | **-10** | **0** | **10** | **20** | **30** | **40** | **50** | **60** |
| 0 | 0.00 | 0.00 | 0.00 | 0.00 | 0.00 | 0.00 | 0.00 | 0.00 | 0.00 | 0.00 |
| 5 | 0.76 | 0.77 | 0.79 | 0.82 | 0.84 | 0.85 | 0.87 | 0.89 | 0.92 | 0.94 |
| 10 | 2.15 | 2.09 | 2.03 | 1.97 | 1.85 | 1.86 | 1.86 | 1.87 | 1.87 | 1.87 |
| 15 | 2.82 | 2.81 | 2.79 | 2.77 | 2.76 | 2.74 | 2.73 | 2.71 | 2.70 | 2.68 |
| 20 | 3.24 | 3.26 | 3.29 | 3.31 | 3.33 | 3.35 | 3.38 | 3.40 | 3.42 | 3.45 |

**Table 6:** The variation of the resultant liniar deformation $\Delta u = f(T, n_a)$ for the spherical cover

| **Δu [%]** | **T [°C]** | **The spherical cover** | | | | | | | | |
|---|---|---|---|---|---|---|---|---|---|---|
| **$n_a$ [years]** | **-30** | **-20** | **-10** | **0** | **10** | **20** | **30** | **40** | **50** | **60** |
| 0 | 0.00 | 0.00 | 0.00 | 0.00 | 0.00 | 0.00 | 0.00 | 0.00 | 0.00 | 0.00 |
| 5 | 0.76 | 0.99 | 0.98 | 0.97 | 0.95 | 0.95 | 0.93 | 0.92 | 0.92 | 0.91 |
| 10 | 2.15 | 5.84 | 5.80 | 5.77 | 5.74 | 11.76 | 11.65 | 11.55 | 11.45 | 11.35 |
| 15 | 2.82 | 0.79 | 0.69 | 0.59 | 0.50 | 0.41 | 0.33 | 0.24 | 0.16 | 0.09 |
| 20 | 3.24 | 3.80 | 3.95 | 3.92 | 3.89 | 3.86 | 3.84 | 3.81 | 3.79 | 3.77 |

The graphs of 3-D surfaces corresponding to the parameters $\Delta\sigma = f(T, n_a)$ and $\Delta u = f(T, n_a)$ for the spherical cover taking into account the results from tables 5 and 6, are graphically shown in fig. 8.

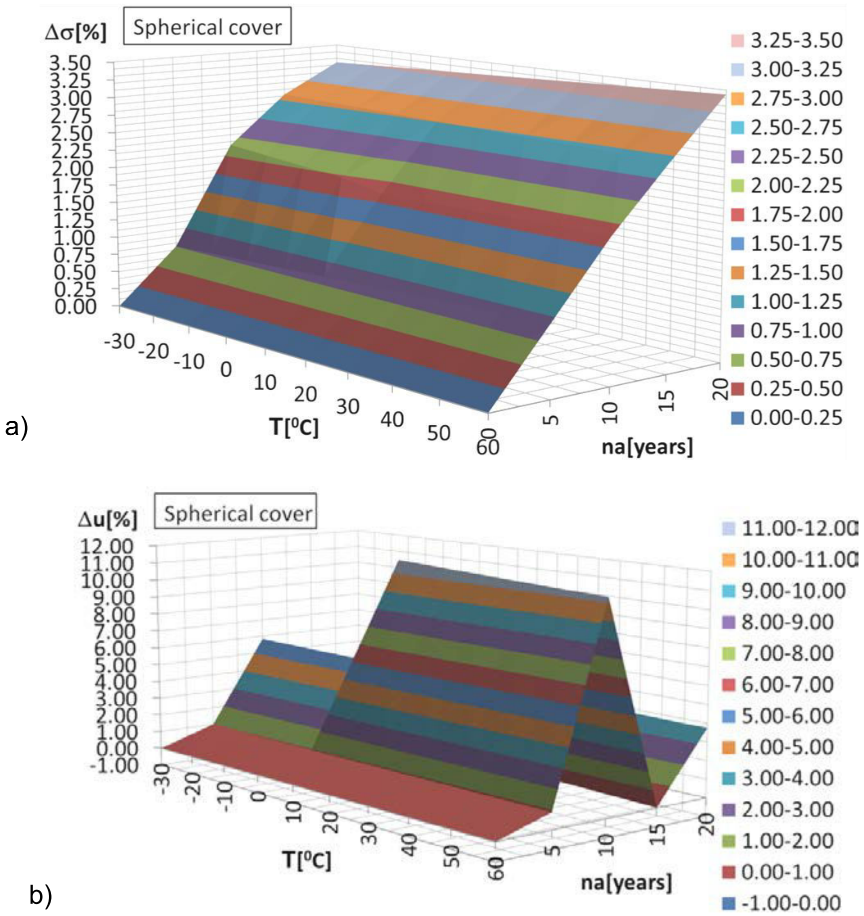

a)

b)

**Fig. 8.** The graphs of 3-D surfaces corresponding for the spherical cover: a) $\Delta\sigma = f(T, n_a)$, and b) $\Delta u = f(T, n_a)$

The parameters $\Delta\sigma = f(T, n_a)$ and $\Delta u = f(T, n_a)$ for the toroidal cover are given in tables 7 and 8.

**Table 7:** The variation of the Von Mises effort $\Delta\sigma = f(T, n_a)$ for the toroidal cover

| **Δσ [%]** | **T [°C]** | **The toroidal cover** | | | | | | | | |
|---|---|---|---|---|---|---|---|---|---|---|
| **$n_a$ [years]** | **-30** | **-20** | **-10** | **0** | **10** | **20** | **30** | **40** | **50** | **60** |
| 0 | 0.00 | 0.00 | 0.00 | 0.00 | 0.00 | 0.00 | 0.00 | 0.00 | 0.00 | 0.00 |
| 5 | 2.12 | 2.23 | 0.50 | 2.46 | 2.58 | 2.70 | 2.82 | 2.93 | 3.04 | 3.10 |
| 10 | 8.93 | 9.81 | 10.69 | 11.55 | 13.17 | 14.02 | 14.85 | 15.66 | 16.44 | 17.18 |
| 15 | 12.21 | 13.08 | 13.94 | 14.80 | 15.64 | 16.48 | 17.30 | 18.09 | 18.84 | 19.57 |
| 20 | 10.74 | 11.63 | 12.51 | 13.38 | 14.24 | 15.08 | 15.90 | 16.70 | 17.46 | 18.19 |

**Table 8:** The variation of the resultant liniar deformation $\Delta u = f(T, n_a)$ for the toroidal cover

| **Δu [%]** | **T [°C]** | **The toroidal cover** | | | | | | | | |
|---|---|---|---|---|---|---|---|---|---|---|
| **$n_a$ [years]** | **-30** | **-20** | **-10** | **0** | **10** | **20** | **30** | **40** | **50** | **60** |
| 0 | 0.00 | 0.00 | 0.00 | 0.00 | 0.00 | 0.00 | 0.00 | 0.00 | 0.00 | 0.00 |
| 5 | 1.18 | 1.15 | 1.13 | 1.12 | 1.10 | 1.09 | 1.07 | 1.05 | 1.03 | 1.02 |
| 10 | 8.59 | 8.45 | 8.32 | 8.20 | 16.06 | 15.90 | 15.75 | 15.61 | 15.47 | 15.33 |
| 15 | 7.76 | 7.54 | 7.34 | 7.15 | 6.95 | 6.77 | 6.59 | 6.42 | 6.25 | 6.09 |
| 20 | 9.72 | 9.62 | 9.51 | 9.41 | 9.30 | 9.21 | 9.11 | 2.68 | 8.95 | 8.87 |

The graphs of 3-D surfaces corresponding to the parameters $\Delta\sigma = f(T, n_a)$ and $\Delta u = f(T, n_a)$ for the toroidal cover taking into account the results from tables 7 and 8, are graphically shown in fig. 9.

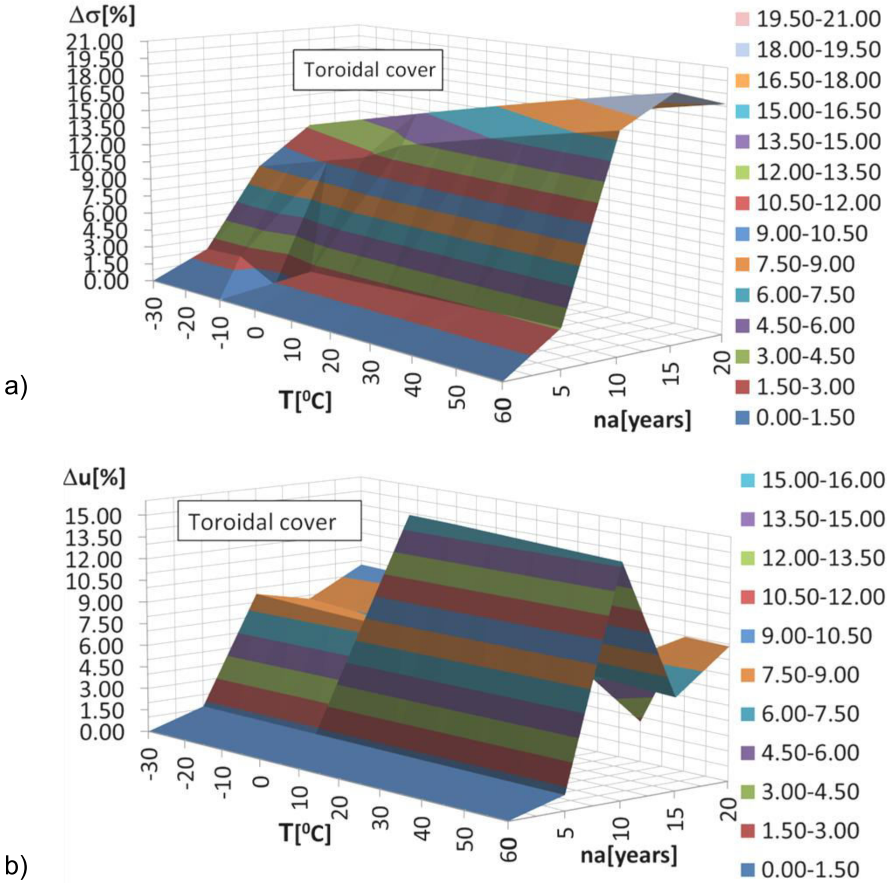

**Fig. 9.** The graphs of 3-D surfaces corresponding for the toroidal cover: a) $\Delta\sigma = f(T, n_a)$, and b) $\Delta u = f(T, n_a)$

## 3. Discussion

Following the numerical analyses and the resulting graphs it has been found that:
- the evolution of corrosion over time implies the decreasing of the thickness of the tank covers, which directly determine the increasing of the Von Mises stress state (tables 1-4);
- with the decrease of the temperature, the state of effort increases and reaches a maximum value corresponding to T = -30 $^0$C; at the same time, a decrease of the state of effort is observed with the increasing of the temperature, reaching an appropriate minimum value for T = 60 $^0$C (fig. 2).
- the resulting linear deformation decreases at negative temperatures and increases at positive temperatures (fig. 5); also the increase of the corrosion always determines the increase of the state of deformation due to the decrease of the thickness of the walls (under a constant pressure);
- the parameter $\Delta\sigma$ increases with the increase of the $n_a$ parameter in the tank covers (fig. 8), with higher values in the toroidal cover; also in the toroidal cover the parameter $\Delta u$ increases with the increase of the $n_a$ parameter (fig. 9).

## 4. Conclusions

These numerical analyses can be applied in the design phase of a CNG storage tank composed of a torus and a sphere, made of steel, used in the automotive industry.

**Conflict of Interest:** The authors declare that they have no conflict of interest.

**ORCID:** Ştefan Ţălu, http://orcid.org/0000-0003-1311-7657.

## References

[1] Moncmanová, A. “Environmental factors that influence the deterioration of materials.“ *WIT Transactions on State of the Art in Science and Engineering* 28 (2007). DOI: 10.2495/978-1-84564-032-3/01.

[2] Ghiţă, C. Mirela, Anton C. Micu, Mihai Ţălu, Ştefan Ţălu, and Ema I. Adam. “Computer-Aided Design of a classical cylinder gas tank for the automotive industry.“ *Annals of Faculty of Engineering Hunedoara - International Journal of Engineering, Hunedoara*, *Romania*, Tome XI, Fascicule 4 (2013): 59-64.

[3] Ghiţă, C. Mirela, Anton C. Micu, Mihai Ţălu, and Ştefan Ţălu. “3D modelling of a shrink fitted concave ended cylindrical tank for automotive industry.“ *Acta Technica Corviniensis – Bulletin of Engineering, Hunedoara, Romania*, Tome VI, Fascicule 4 (2013): 87-92.

[4] Ghiţă, C. Mirela, Anton C. Micu, Mihai Ţălu, and Ştefan Ţălu. “Shape optimization of a thoroidal methane gas tank for automotive industry.” *Annals of Faculty of Engineering Hunedoara - International Journal of Engineering, Hunedoara, Romania*, Tome X, Fascicule 3 (2012): 295-297.

[5] Ghiţă, C. Mirela, Anton C. Micu, Mihai Ţălu, and Ştefan Ţălu. “3D modelling of a gas tank with reversed end up covers for automotive industry.“ *Annals of Faculty of Engineering Hunedoara - International Journal of Engineering, Hunedoara*, *Romania*, Tome XI, Fascicule 3 (2013): 195-200.

[6] Ghiţă, C. Mirela, Anton C. Micu, Mihai Ţălu, and Ştefan Ţălu. “Shape optimization of vehicle's methane gas tank.“ *Annals of Faculty of Engineering Hunedoara - International Journal of Engineering, Hunedoara, Romania*, Tome X, Fascicule 3 (2012): 259-266.

[7] Ghiţă, C. Mirela, Ştefan C. Ghiță, Ştefan Ţălu, and Simona Rotaru, “Optimal design of cylindrical rings used for the shrinkage of vehicle tanks for compressed natural gas.“ *Annals of Faculty of Engineering Hunedoara - International Journal of Engineering, Hunedoara*, Tome XII, Fascicule 3 (2014): 243-250.

[8] Bică, Marin, Mihai Ţălu, and Ştefan Ţălu. “Optimal shapes of the cylindrical pressurized fuel tanks.” *Magazine of Hydraulics, Pneumatics, Tribology, Ecology, Sensorics, Mechatronics (HIDRAULICA)*, no. 4 (December 2017): 6-17.

[9] Ţălu, Mihai. "The influence of the corrosion and temperature on the Von Mises stress in the lateral cover of a pressurized fuel tank." *Magazine of Hydraulics, Pneumatics, Tribology, Ecology, Sensorics, Mechatronics (HIDRAULICA)*, no. 4 (December 2017): 89-97.

[10] Ţălu, Mihai, and Ştefan Ţălu. "Analysis of temperature resistance of pressurized cylindrical fuel tanks." *Magazine of Hydraulics, Pneumatics, Tribology, Ecology, Sensorics, Mechatronics (HIDRAULICA)*, no. 1 (March 2018): 6-15.

[11] Vintilă, Daniela, Mihai Ţălu, and Ştefan Ţălu. “The CAD analyses of a torospheric head cover of a pressurized cylindrical fuel tank after the crash test.” *Magazine of Hydraulics, Pneumatics, Tribology, Ecology, Sensorics, Mechatronics (HIDRAULICA)*, no. 4 (December 2017): 57-66.

[12] Ţălu, Ştefan, and Mihai Ţălu. "The influence of deviation from circularity on the stress of a pressurized fuel cylindrical tank." *Magazine of Hydraulics, Pneumatics, Tribology, Ecology, Sensorics, Mechatronics (HIDRAULICA)*, no. 4 (December 2017): 34-45.

[13] Ţălu, Mihai, and Ştefan Ţălu. “The influence of corrosion and temperature variation on the minimum safety factor of a 3D hexagonal toroid with regular hexagonal cross-section used in manufacturing of LPG storage tanks.“ *Magazine of Hydraulics, Pneumatics, Tribology, Ecology, Sensorics, Mechatronics (HIDRAULICA)*, no. 3 (August 2018): 16-25.

[14] Ţălu, Mihai, and Ştefan Ţălu. "Design and optimization of pressurized toroidal LPG fuel tanks with variable section." *Magazine of Hydraulics, Pneumatics, Tribology, Ecology, Sensorics, Mechatronics (HIDRAULICA)*, no. 1 (March 2018): 32-41.

[15] Ţălu, Ştefan, and Mihai Ţălu. "Algorithm for optimal design of pressurized toroidal LPG fuel tanks with constant section described by imposed algebraic plane curves." *Magazine of Hydraulics, Pneumatics, Tribology, Ecology, Sensorics, Mechatronics (HIDRAULICA)*, no. 2 (June 2018): 14-21.

[16] Ţălu, Mihai, and Ştefan Ţălu. "The optimal CAD design of a 3D hexagonal toroid with regular hexagonal cross-section used in manufacturing of LPG storage tanks." *Magazine of Hydraulics, Pneumatics, Tribology, Ecology, Sensorics, Mechatronics (HIDRAULICA)*, no. 2 (June 2018): 49-56.

[17] Ţălu, Ştefan, and Mihai Ţălu. "The influence of corrosion and pressure variation on the minimum safety factor of a 3D hexagonal toroid with regular hexagonal cross-section used in manufacturing of LPG storage tanks." *Magazine of Hydraulics, Pneumatics, Tribology, Ecology, Sensorics, Mechatronics (HIDRAULICA)*, no. 3 (August 2018): 39-45.

[18] Ţălu, Mihai, and Ştefan Ţălu. “Optimal design of a CNG storage tank with a combined form consisting of a torus and a sphere.“ *Magazine of Hydraulics, Pneumatics, Tribology, Ecology, Sensorics, Mechatronics (HIDRAULICA)*, no. 4 (December 2019): 73-82.

[19] Ţălu, Mihai, and Ştefan Ţălu. “3D geometrical solutions for toroidal LPG fuel tanks used in automotive industry.“ *Advances in Intelligent Systems Research* 151 (2018): 189-193. DOI: 10.2991/cmsa-18.2018.44.

[20] Ţălu, Ştefan, and Mihai Ţălu. “The Influence of corrosion on the vibration modes of a pressurized fuel tank used in automotive industry.“ *DEStech Transactions on Materials Science and Engineering* (May 2018): 1-6. DOI: 10.12783/dtmse/icmsa2018/20560.
[21] Ţălu, Ştefan, and Mihai Ţălu. “Constructive CAD variants of toroidal LPG fuel tanks used in automotive Industry.“ *Advances in Intelligent Systems Research* 159 (2018): 27-30. DOI: 10.2991/mmsa-18.2018.7.
[22] Ţălu, Mihai, and Ştefan Ţălu. “Optimal engineering design of a pressurized paralepipedic fuel tank.“ *Annals of Faculty of Engineering Hunedoara - International Journal of Engineering, Hunedoara, Romania*, Tome XVI, Fascicule 2 (2018): 193-200.
[23] Ţălu, Ştefan, and Mihai Ţălu. “CAD generating of 3D supershapes in different coordinate systems.“ *Annals of Faculty of Engineering Hunedoara - International Journal of Engineering, Hunedoara, Romania*, Tome VIII, Fascicule 3 (2010): 215-219.
[24] Niţulescu, Theodor, and Ştefan Ţălu. *Aplicaţii ale geometriei descriptive şi graficii asistate de calculator în desenul industrial / Applications of descriptive geometry and computer aided design in engineering graphics.* Cluj-Napoca, Risoprint Publishing House, 2001.
[25] Ţălu, Ştefan, and Mihai Ţălu. “A CAD study on generating of 2D supershapes in different coordinate systems.“ *Annals of Faculty of Engineering Hunedoara - International Journal of Engineering, Hunedoara, Romania*, Tome VIII, Fascicule 3 (2010): 201-203.
[26] Florescu-Gligore, Adrian, Ştefan Ţălu, and Dan Noveanu. *Reprezentarea şi vizualizarea formelor geometrice în desenul industrial / Representation and visualization of geometric shapes in industrial drawing.* Cluj-Napoca, U. T. Pres Publishing House, 2006.
[27] Ţălu, Ştefan, and Cristina Racocea. *Reprezentări axonometrice cu aplicaţii în tehnică / Axonometric representations with applications in technique.* Cluj-Napoca, MEGA Publishing House, 2007.
[28] Ţălu, Ştefan. *Geometrie descriptivă / Descriptive geometry.* Cluj-Napoca, Risoprint Publishing House, 2010.
[29] Racocea, Cristina, and Ştefan Ţălu. *Reprezentarea formelor geometrice tehnice în axonometrie / The axonometric representation of technical geometric shapes.* Cluj-Napoca, Napoca Star Publishing House, 2011.
[30] Ţălu, Ştefan. *Grafică tehnică asistată de calculator / Computer assisted technical graphics*. Cluj-Napoca, Victor Melenti Publishing House, 2001.
[31] Florescu-Gligore, Adrian, Magdalena Orban, and Ştefan Ţălu. *Cotarea în proiectarea constructivă şi tehnologică / Dimensioning in technological and constructive engineering graphics.* Cluj-Napoca, Lithography of The Technical University of Cluj-Napoca, 1998.
[32] Ţălu, Ştefan. *Reprezentări grafice asistate de calculator / Computer assisted graphical representations.* Cluj-Napoca, Osama Publishing House, 2001.
[33] Ţălu, Mihai. *Mecanica fluidelor. Curgeri laminare monodimensionale / Fluid mechanics. The monodimensional laminar flow.* Craiova, Universitaria Publishing House, 2016.
[34] Țălu, Mihai. *Calculul pierderilor de presiune distribuite în conducte hidraulice / Calculation of distributed pressure loss in hydraulic pipelines.* Craiova, Universitaria Publishing House, 2016.
[35] Țălu, Mihai. *Pierderi de presiune hidraulică în conducte tehnice cu secțiune inelară. Calcul numeric și analiză C.F.D. / Hydraulic pressure loss in technical piping with annular section. Numerical calculation and C.F.D.* Craiova, Universitaria Publishing House, 2016.
[36] Ţălu, Ştefan. *Limbajul de programare AutoLISP. Teorie şi aplicaţii / AutoLISP programming language. Theory and applications*. Cluj-Napoca, Risoprint Publishing House, 2001.
[37] Ţălu, Ştefan, and Mihai Ţălu. *AutoCAD 2006. Proiectare tridimensională / AutoCAD 2006. Three-dimensional designing*. Cluj-Napoca, MEGA Publishing House, 2007.
[38] Ţălu, Ştefan. *AutoCAD 2005*. Cluj-Napoca, Risoprint Publishing House, 2005.
[39] Ţălu, Ştefan. *AutoCAD 2017*. Cluj-Napoca, Napoca Star Publishing House, 2017.
[40] Bîrleanu, Corina, and Ştefan Ţălu. *Organe de maşini. Proiectare şi reprezentare grafică asistată de calculator / Machine elements. Designing and computer assisted graphical representations*. Cluj-Napoca, Victor Melenti Publishing House, 2001.
[41] Nedelcu, Dorian. *Proiectare și simulare numerică cu SolidWorks / Digital Prototyping and Numerical Simulation with SolidWorks*. Timişoara, Eurostampa Publishing House, 2011.
[42] Ţălu, Ştefan. *Micro and nanoscale characterization of three dimensional surfaces. Basics and applications*. Napoca Star Publishing House, Cluj-Napoca, Romania, 2015.
[43] *** Certification tests of LPG and CNG. Accessed August 23, 2018. http://vzlutest.cz/en/certification-tests-of-lpg-and-cng-c3.html.
[44] *** TANK software (https://cas.hexagonppm.com/solutions/tank).
[45] *** Autodesk AutoCAD 2017 software.
[46] *** SolidWorks 2017 software.

**ISSN 1453 – 7303** **"HIDRAULICA" (No. 4/2019)**
**Magazine *of Hydraulics, Pneumatics, Tribology, Ecology, Sensorics, Mechatronics***

# Aspects of the Operation of the Blade Pumps Used in Agricultural Irrigation Applications

Assistant professor **Fănel Dorel ȘCHEAUA**[1]

[1] "Dunărea de Jos" University of Galați, fanel.scheaua@ugal.ro

***Abstract:** The population increase rate represents a factor of progress registered as a result of the people living standard improvement. This increase must be sustained worldwide through improved agricultural practices that allow to obtain optimum yields on cultivated lands that guarantee the well-being of human communities first and foremost in terms of providing food and related economic activities. The agricultural productions have had remarkable increases on the units of cultivated areas in the last years, which denotes the use of agricultural techniques that give good results regarding the quality of the seeds used, the land quality but also of the water resources that allow the irrigation of the cultivated surfaces so that optimum results are obtained from agriculture. In this paper are presented constructive and functional aspects of the primary component of the irrigation plant of the cultivated areas of agricultural land represented by the pump. This is a constructive version of a blade pump that is used for the water supply in a pumping plant intended for agricultural irrigation.*

***Keywords:** Agriculture irrigation, water flow, blade pump, three-dimensional modelling, CFD*

## 1. Introduction

The sustained development in the field of agriculture of the last period was possible due to the specific techniques applied strictly regarding the scheduling of the necessary works for the cultivation of agricultural lands.The scientific principles underlying agricultural engineering have been pursued and applied in order to obtain optimal results that are better compared to previous decades in terms of obtaining crops from cultivated land for the benefit of human communities.

Emphasis is placed on agronomic engineering in order to obtain the best possible harvests with much smaller water resources through efficient water use, thus avoiding high values of water and energy consumption. This is because many areas around the world are increasingly facing the lack of water as a natural resource and irrigation systems contribute to a specific consumption that determines an impact on the natural system. It is necessary that the irrigation systems be properly sized, continuously monitored and the operation be directed not only to the benefit of the user but also of the whole community.

The efficiency of the irrigation system of agricultural lands is a function of several factors such as water losses along the length of the irrigation column or the water transport channels through infiltration, the type of water distribution systems and the type of pumping solution adopted to be used in water conveyance from the main supply basin. [1]

The model of a blade pump used within an pumping installation adopted for the conveyance of water for irrigation of agricultural land is presented in this paper. The constructive and functional model of the blade pump determines the water circulation on the hydrodynamic principle with the mass flow rate and water flow velocity components, which transforms the mechanical energy taken at the pump rotor axis from the energy source into kinetic energy of the water.

The blade pump model from a constructive and functional point of view is analyzed in this paper, presenting the kinematic structure of the water currents formed during operation.

## 2. Blade pump principal characteristics

The model of pumping system is presented which has the main component represented by a blade pump.

The main parameters that define the operation of the pumping system are the pumping height, static or geodesic height and the power at the pump axis.

The pumping height, $\left(H_P\right)$ represents the difference between the specific energies of the water in the discharge basin and the suction basins of the pump, where the total local and distributed load losses, $\left(h_r\right)$ are considered along the suction and discharge water pathlines within the supply basin. [2][3][4]

$$H_p = H_{st} + h_r \tag{1}$$

$$h_r = h_{ra} + h_{rr} \tag{2}$$

The pressure values determination at the connection with the discharge pipe is made by installing a manometer and at the suction connection a vacuummeter for the case where the pump operates without back pressure and the pressure on the suction pipe is below atmospheric pressure value. Thus, two pressure values will be read on the devices mounted on the pressure gauge in terms of the pumped water column $\left(p_M\right)$ and on the vacuum gauge in terms of the suction water column $\left(p_V\right)$ and the relation for the pumping height is of the form:[3][5]

$$H_P = p_M - p_V + (z_M - z_V) + \frac{v_2^2 - v_1^2}{2g} \tag{3}$$

Because for the pumping installations the term $\left(\frac{v_2^2 - v_1^2}{2g}\right)$ has a reduced value, the relation for the pumping height of simplified form can be considered as: [3][5]

$$H_P = p_M - p_V + (z_M - z_V) \tag{4}$$

The static or geodesic height represents the difference between the water level in the discharge basin positioned in the upper position and the suction basin positioned in the lower position, being calculated with the relation: [3][5]

$$H_S = z_{Br} - z_{Ba} \tag{5}$$

For the case where the installation works under the conditions where the pressure values on the free water surface in the suction region $\left(p_{Ba}\right)$ and discharge basin $\left(p_{Br}\right)$ are different the relation of static height $\left(H_s\right)$ becomes: [3][5]

$$H_S = z_{Br} - z_{Ba} + \frac{p_{Br} - p_{Ba}}{\gamma_a} \tag{6}$$

The determination of the power values at the pump shaft is made taking into account the specific water weight $\left(\gamma_a\right)$, the pump flow rate $\left(Q_P\right)$, the pumping height $\left(H_P\right)$ and the total efficiency of the pump $\left(\eta_P\right)$ using the relation: [3][5]

$$N_P = \frac{\gamma_a Q_P H_P}{100\eta_P} \tag{7}$$

The kinematic structure of currents for the case of centrifugal pumps is shown in Figure 1.

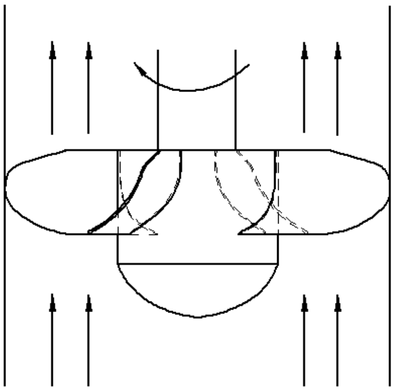

**Fig. 1.** Operational principle of blade pump

For the inlet section area the water velocity values are close to the radial direction. The velocity parallelogram of water circulation is constructed if the water velocity $(v_1)$ is decomposed on components represented by the transport velocity $(u_1)$ and the relative velocity$(\omega_1)$. On the output edge of the rotor blades the absolute velocity $(v_2)$ is determined by constructing the parallelogram with the relative velocity $(\omega_2)$ and the transport speed$(u_2)$.

$$u_1 = \frac{\pi D_1 n}{60}; u_2 = \frac{\pi D_2 n}{60} \tag{8}$$

The velocity parallelogram at the rotor blade contour is shown in figure 2

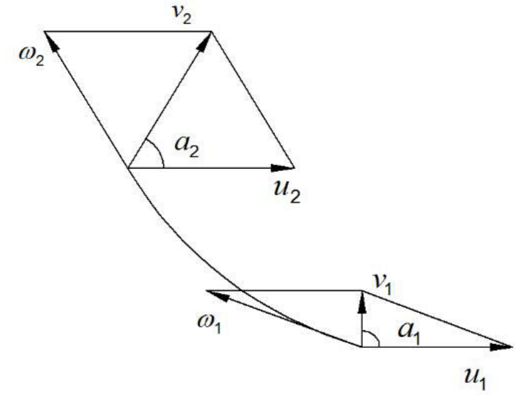

**Fig. 2.** Velocity parallelogram

The fluid is entrained into the enclosure by the rotor blades in rotational motion and at the entrance to the rotor area the velocity $(v_1)$is directed parallel to the axis and at the rotor exit the velocity $(v_2)$ is inclined at an angle relative to the rotor axis which means that the fluid is driven in rotational motion with respect to the axis but also with advance movement in relation to the axis. In order to eliminate the rotational movement of the fluid stream, an auxiliary device is usually installed which has the role of stopping the rotational movement and driving the fluid parallel to the rotor axis.

The Euler equation describes the connection between the transmitted energy to convey a fluid at a certain pumping height value $(H_P)$and the velocity parallelograms:[3][5]

$$H_P = \eta_h \left( \frac{u_2 v_2 \cos a_2 - u_1 v_1 \cos a_1}{g} \right) \tag{9}$$

where $\eta_h$ is hydraulic efficiency of the pump unit.

Considering the value of the velocity circulation $(\Upsilon)$ with the components $(\Upsilon_1),(\Upsilon_2)$ representing the velocity circulation of the fluid on a contour before and after entering the rotor having the angular velocity $(\omega)$ it can be considered: [3][5]

$$H_P = \eta_h \left\lfloor \frac{\omega}{2\pi g} (\Upsilon_2 - \Upsilon_1) \right\rfloor \tag{10}$$

Because at the inlet of the pump rotor the fluid velocity circulation is considered to be null value $(\Upsilon_1 \cong 0)$, it can be written: [3][5]

$$H_P = \eta_h \frac{\omega}{2\pi g} \Upsilon_2 \tag{11}$$

The optimum operating conditions for the pump are established for the situation where the fluid is admitted into the rotor enclosure without shocks. Therefore, the relative velocity direction must coincide with the tangent direction at the blade contour at the level of the rotor enclosure inlet region.

## 4. Fluid flow aspects within lobe pump virtual model

Aspects of fluid flow through the blade pump enclosure related to the operation of these volumetric units are highlighted through a CFD analysis on the overall virtual model of the blade pump rotor.
The overall 3D virtual model was developed and introduced in the analysis with the Ansys CFX analysis program.
Figure 3 shows the overall rotor model and the mesh network with a number of 495875 nodes and 2261255 elements of triangular form.

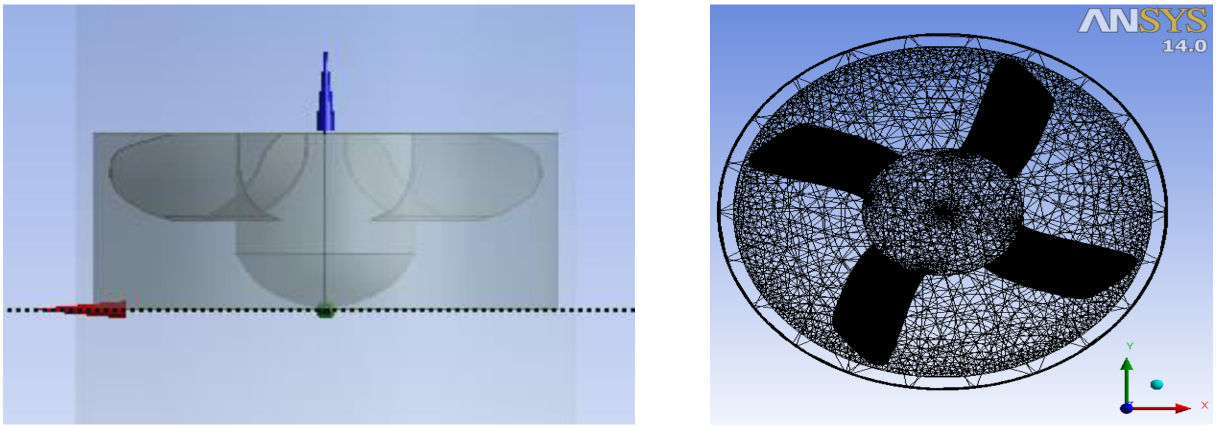

a) imported model b) mesh network of triangular elements

**Fig. 3.** Assembly model for water flow analysis

The operating principle for this volumetric unit is based on the rotational motion which engage the fluid in motion along the casing wall. The pressure at the inlet is considered as atmospheric pressure, while the rotational velocity is declared at 1500 rot/min.

The flow rate values of liquid circulation is according with the volumetric capacity at a single rotation of pump shaft.

The analysis main domains are represented by fluid region declared as water, and the immersed solid represented by the rotor, material steel.

The analyzed fluid model has an inlet port for the working fluid (water) and one outlet port while the enclosure cylinder is declared as wall.

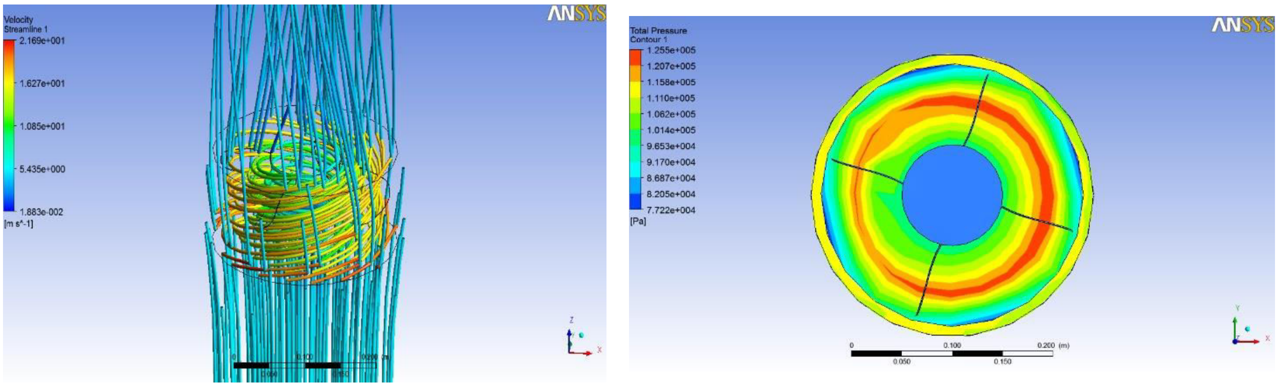

a) water velocity on streamlines

b) total pressure on rotor fluid contour

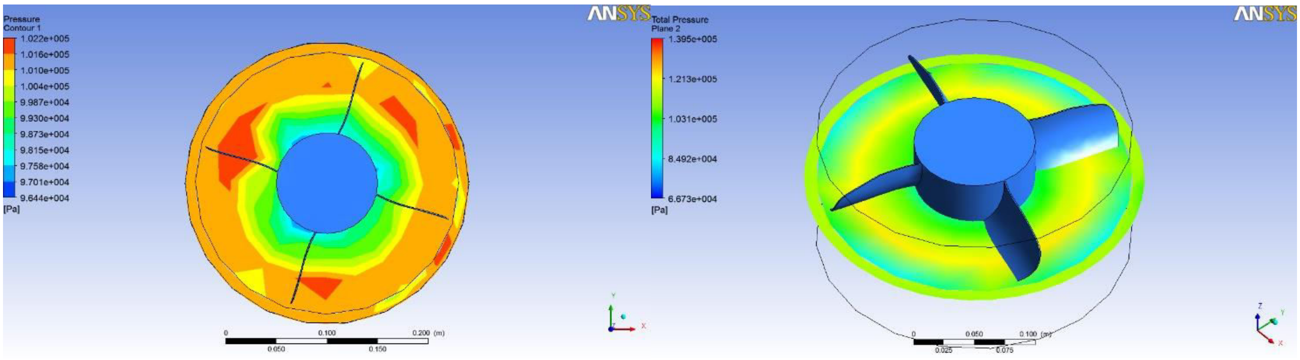

c) pressure values on rotor fluid contour

d) total pressure on XY cutting plane

**Fig. 4.** Water flow analysis result values

The results are presented in terms of total pressure and water velocity and pressure values as shown in figure 4. The fluid stream path lines created as a result of the rotor movement that draws the water according to the blades shape in rotary motion are highlighted. The pressure values are not very high, the analyzed fluid region considers the water entrainment and exit to the discharge duct.

The operation of the blade pump model presented is based on the rotor speed which has the possibility to vehiculate water due to the specific geometry of the rotor blades, the unit operating on the hydrodynamic principle that ensures the kinetic energy of the fluid conveyed in the form of mass flow rate and flow velocity.

The mass flow rate of water at the rotor outlet enclosure is calculated at 213.5 kg/s and water entrainment velocity of up to 2.5 m/s.

## 5. Conclusions

Theoretical aspects related to the constructive and functional particularities for the model of a blade pump were presented in this paper.
The blade pump model is the primary component of a water pump unit for irrigation in agriculture. On the basis of a three-dimensional virtual model, an analysis of the water flow inside the pump rotor blades enclosure was performed, with specific results of the flow velocity and water pressure recorded. Are emphasized the flow pathlines at the rotor level, formed due to rotational motion declared at the rotor shaft.
Based on the results obtained from water flow analysis on the virtual model of the blade pump are created the premises of optimizing the constructive shape of the blade contour in order to allow uniformity of the relative velocity during rotor motion ensuring in this manner the optimization of pump operation, thus improving the values for the operating efficiency for the blade pump assembly.

### References

[1] Ali, Hossain. *Practices of irrigation & on-farm water management*. Springer Science & Business Media, 2011.
[2] Axinti, G., and A.S. Axinti. *Hydraulic and pneumatic drives - Components and systems, Functions and characteristics*. / *Acţionări hidraulice şi pneumatice – Componente și sisteme, Funcții și caracteristici*. Chişinău, Tehnica-Info Publishing House, 2008.
[3] Kiselev, P.G., and S. Hancu. *Guide for hydraulic calculations / Indreptar pentru calcule hidraulice*. Bucharest, Technical Publishing House, 1988.
[4] Axinti, S., and F.D. Scheaua. *Introduction to industrial hydraulics / Introducere în hidraulica industrială*. Galați, Galați University Press, 2015.
[5] Axinti, G., and A.S. Axinti. *Hydraulic and pneumatic drives - Calculation, Design, Exploitation, Reliability and Drive Diagrams / Acţionări hidraulice şi pneumatice – Baze de Calcul, Proiectare, Exploatare, Fiabilitate și Scheme de Acționare*. Chişinău, Tehnica-Info Publishing House, 2009.
[6] Florea, J., and V. Panaitescu. *Fluid Mechanics / Mecanica Fluidelor*. Bucharest, Didactic and Pedagogical Publishing House, 1979.
[7] Axinti, G., and A.S. Axinti. *Hydraulic and pneumatic drives - Dynamics of equipment and systems / Acţionări hidraulice şi pneumatice –Dinamica echipamentelor și sistemelor*. Vol III. Chişinău, Tehnica-Info Publishing House, 2008.
[8] Vasilescu, Al.A. *Fluid Mechanics / Mecanica Fluidelor*. Ministry of Education, Galați, University of Galați, 1979.
[9] Bacharoudis, E.C., A.E. Filios, M.D. Mentzos, and D.P. Margaris. "Parametric study of a centrifugal pump impeller by varying the outlet blade angle." *The Open Mechanical Engineering Journal* 2 (2008): 75-83.
[10] Jensen, Marvin E., et al. (ed.). *Design and operation of farm irrigation systems*. American Society of Agricultural Engineers, 1980.

**ISSN 1453 – 7303** **"HIDRAULICA" (No. 4/2019)**
**Magazine *of Hydraulics, Pneumatics, Tribology, Ecology, Sensorics, Mechatronics***

# The Construction of Systems for Air Dispersion in Wastewater

PhD Student **Titu - Cătălin CIOIENARU**[1], Prof. Dr. Eng. **Nicolae BĂRAN**[1],
Prof. Dr. Eng. **Octavian DONȚU**[1], Conf. Dr. Eng. **Daniel BESNEA**[1], Dr. Eng. **Corina MOGA**[2],
PhD Student **Mihaela PETROȘEL**[1], Sl. Dr. Eng**. Mihaela CONSTANTIN**[1]

[1] University Politehnica of Bucharest, i.mihaelaconstantin@gmail.com

[2] DFR Systems SRL, Bucharest, corinamoga@yahoo.com

***Abstract:*** *For an efficient aeration of wastewater, two options are proposed:*
*1) In the case of stagnant waters, the use of fine bubble generators; these fine bubble generators ensure accurate and uniform air dispersion;*
*2) In the case of the water flowing through the pipes, the aeration of the water will take place right inside the pipes, thus eliminating those huge aeration tanks used for water treatment.*
*The pipes carrying the wastewater can be placed horizontally or vertically; only horizontal pipes will be analysed in the paper.*

***Keywords:*** *Fine air bubble generator, water aeration.*

## 1. Introduction

Water aeration is a process of mass transfer of oxygen from atmospheric air to a volume of water; in this way the concentration of dissolved oxygen in the water will increase.
Water aeration systems determine certain energy consumption; by using the modern technologies of construction of these systems, a reduction of the energy consumption can be obtained.
In specialized papers [1], [2], [3] it is noted that the pneumatic aeration is clearly superior to the mechanical aeration systems.
The best performing aeration systems are those that produce fine air bubbles [4], [5]. The paper proposes the aeration achievement of the wastewaters by introducing the compressed air into the pipes that carry these wastewaters.
This constructive solution eliminates those aeration tanks with volumes of hundreds of $m^3$, thus reducing the investment and operating costs of wastewater treatment plants.
In a two-phase system the transfer of a component takes place between areas where there are different phases; for example, the transfer of a gas into a liquid (air-water) [6], [7], [8]. In this case the mass transfer is interfacial. Table 1 shows a classification of the mass transfer (diffusion) phenomena encountered in technical engineering.

**Table 1:** Classification of mass transfer processes

| Fluid in which diffusion takes place | Flow type | Flow regime | Mass transfer takes place through: |
|---|---|---|---|
| 1- Stagnant fluid<br>($w = 0$) | - | - | Molecular diffusion |
| 2- Fluid in flow<br>($w \neq 0$) | Free flow | - | Convective natural diffusion |
| | | Laminar regime | Convective forced diffusion |
| | | Turbulent regime | Convective forced diffusion |

In biphasic systems, at low speeds of the system phases, molecular diffusion predominates, and at high speeds convective diffusion predominates.

## 2. Analysis of two-phase fluid flow through pipes

### 2.1 The purpose of the researches and initial data for the two-phase fluid flow process

The paper aims to present two water aeration systems:
- Option 1: Water aeration is performed with a fine bubble generator (FBG) placed in a tank with volume $V = 0.125\ m^3$.
- Option 2: The aeration of the water is carried out on the flow by the installation in a pipe of an air dispersion device in the wastewater; the volume of water that will flow will be all $V = 0.125\ m^3$.

Other common initial values for the two options are:

- Air flow in the water: $\dot{V} = 0.6\ m^3/h$;
- The area of the air outlet section in water $A = 1.2 \cdot 10^{-6}\ m^2$, orifices number = 17;
- Hydrostatic load 0.5 m;
- Water temperature: t = 24 °C;
- Initial dissolved oxygen concentration in water $C_0 = 5.48\ mg/dm^3$;
- Experience duration: $\tau = 120$ minutes;
- For t = 24 °C for water, a value of the dissolved oxygen concentration in water was obtained [9]: $C_s = 8.4\ mg/dm^3$.

### 2.2 Establishing the flow regime of the two-phase fluid

From previous experimental researches it is considered that the water volume to be aerated in time ($\tau$) of two hours is $V = 0.125\ m^3$.

This volume will flow through a pipe with an internal diameter of 44 mm; consequently, the volumetric flow rate ($\dot{V}$) and the water velocity (w) in the pipe will be [10] [11]:

$$\dot{V} = \frac{V}{\tau} = \frac{0.125}{2 \cdot 3600} = 0.01736 \cdot 10^{-3}\ m^3/s \tag{1}$$

$$w = \frac{\dot{V}}{\frac{\pi}{4} d^2} = \frac{0.0173 \cdot 10^{-3}}{0.786(0.044)^2} = 0.0115\ m/s \tag{2}$$

For water at 20°C, the kinematic viscosity is [12]: $\nu = 1 \cdot 10^{-6}\ m^2/s$, so the Reynolds number will be:

$$\mathrm{Re} = \frac{wd}{\nu} = \frac{0.0115 \cdot 0.044}{1 \cdot 10^{-6}} = 506 \tag{3}$$

So, the flow regime for water is laminar (Re <2320). The air flow rate in the water:

$$\dot{V}_{air} = \frac{0.6}{3600} = 0.0001666\ m^3/s \tag{4}$$

This value is very small, as a result, it does not change the flow regime previously established.

### 2.3 Structure of two-phase fluid flow (air + water)

It is considered that the air and water flow rates that are transported through the pipe remain constant i time, and the water and air temperature are approximately equal to the ambient temperature. In the case of two-phase fluid flow (water + air), there can be several types of flows that have a different architecture (Figures 1, 2, 3) as follows:

A) Bubble flow (figure 1). If the motion of the air bubbles is superimposed over the liquid flow, an image of the two-phase flow is obtained:

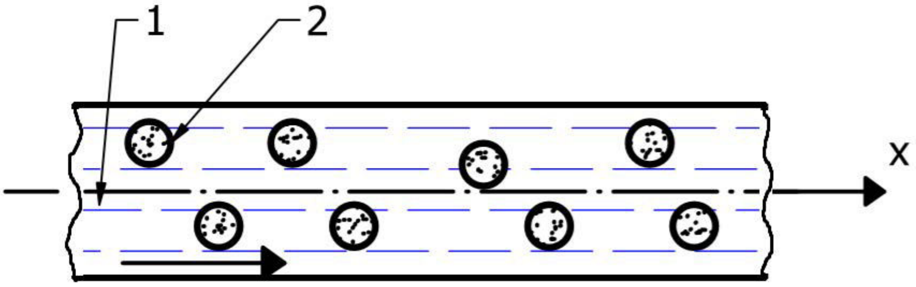

**Fig. 1.** Bubble flow

1- liquid (water); 2- air bubbles

The gas is dispersed as bubbles in the liquid; in their movement the air bubbles tend to rise at the top of the pipe. The study takes into account the horizontal pipe expected for the experimental installation that has Ø 50 x 3 mm, so an internal diameter of 44 mm.

B) Flow with gas plugs (figure 2).

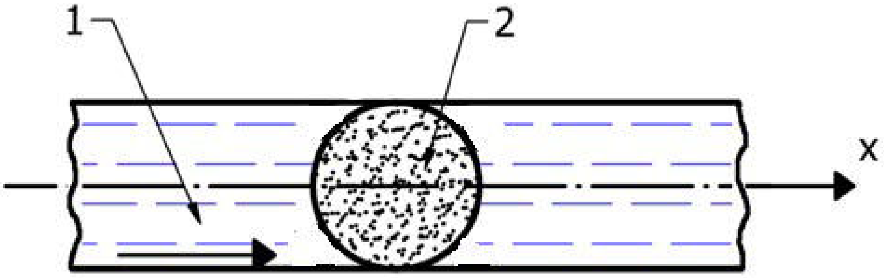

**Fig. 2.** Flow with gas plugs

1- liquid phase (water); 2- gas phase (air)

The gas bubbles unite and form plugs that move at a speed equal to that of water.

C) Layered flow (Figure 3).

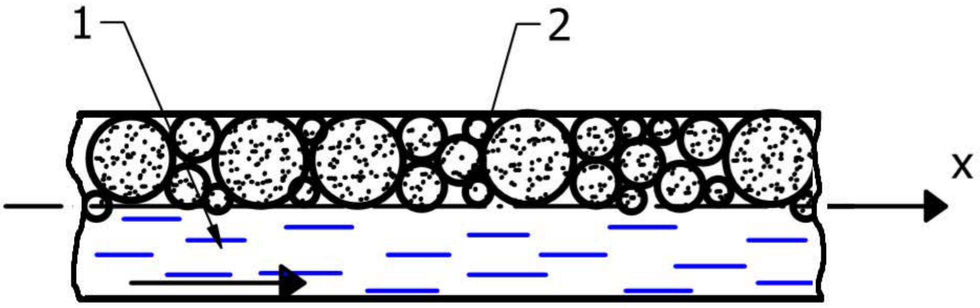

**Fig. 3.** Layered flow

1- liquid (water); 2- gas bubbles (air)

The flow has a separation surface between the liquid at the bottom of the pipe and the gas at the top ($\rho_{water} > \rho_{air}$).

## 3. Air dispersion devices in water

### 3.1 Aeration of stagnant water using the fine bubble generator (option 1)

Figure 4 shows an overview of a fine bubble generator.

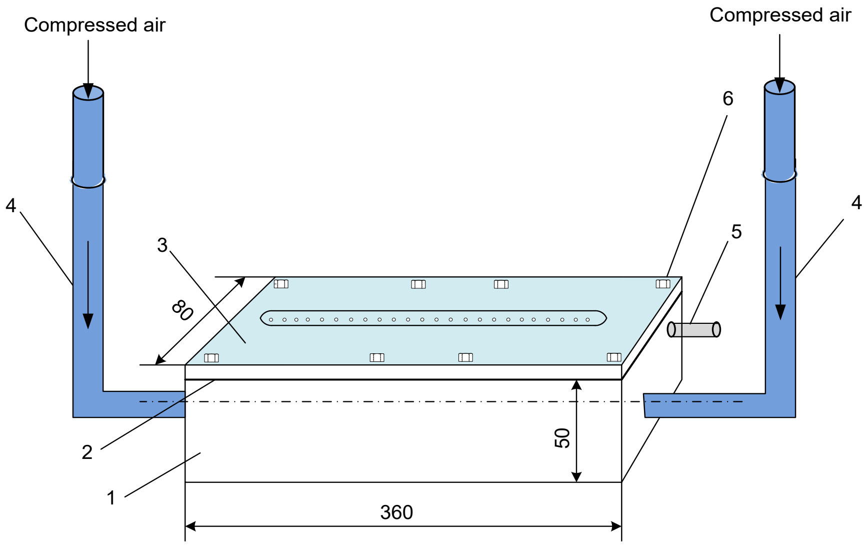

**Fig. 4.** Fine air bubble generator

1 - compressed air tank; 2 - sealing gasket; 3 - orifice plate; 4 - compressed air supply pipe of FBG ø 18 mm; 5 - compressed air pressure connection; 6 - screws for fixing the plate with orifices in the tank frame

Compressed air enters the tank through the FBG with a plate with orifices (Figure 5). The distance between the orifices is 6 mm and the thickness of the aluminium plate is 2 mm.

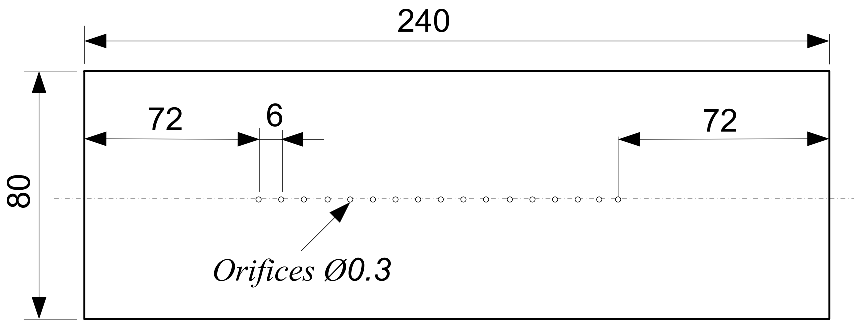

**Fig. 5.** Perforated plate with 17 orifices Ø 0.3 mm

In both options the location of the orifices must meet two conditions [4] [12]:

$$\frac{s}{d_0} > 3 \tag{5}$$

$$\frac{d}{d_0} > 8 \tag{6}$$

where:
s - the thickness of the metal wall;
$d_0$ - the diameter of the orifice through which the air exits into the water;
d - the distance between two successive orifices.

For the presented bubble generator: s = 2 mm, $d_0$ = 0.3 mm, d = 6 mm; one obtains:

$$\frac{s}{d_0} = \frac{2}{0.3} = 6.66 > 3 \tag{7}$$

$$\frac{d}{d_0} = \frac{6}{0.3} = 20 > 8 \tag{8}$$

From the constructive solutions achieved in previous researches [13] [14], a fine bubble generator with n = 17 orifices with a diameter of 0.3 mm was chosen.

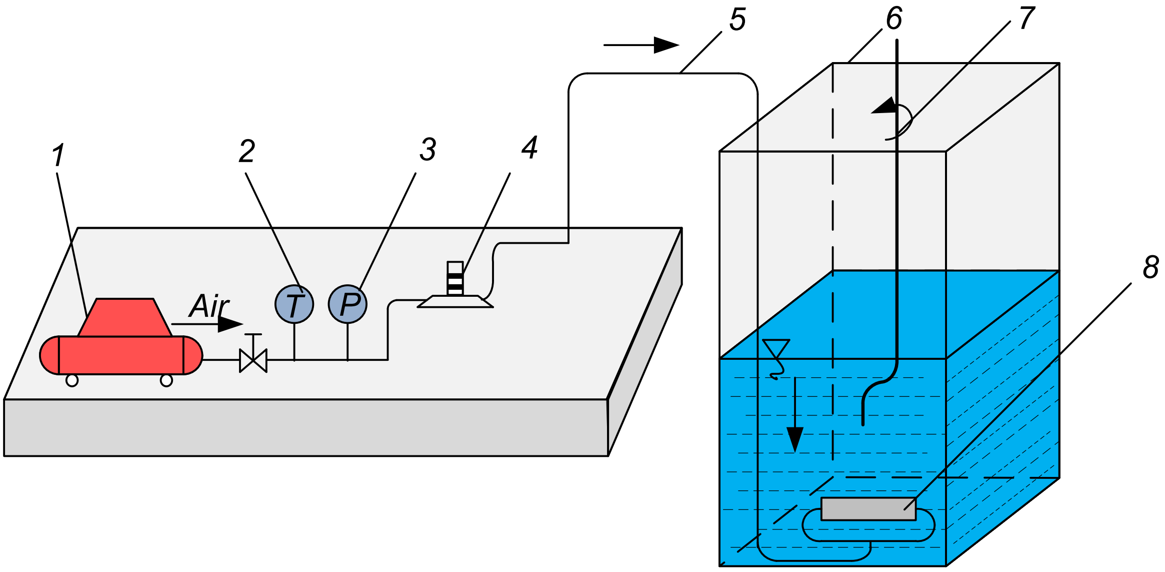

**Fig. 6.** Sketch of the experimental installation for the introduction of atmospheric air in water

1 - air compressor; 2 - thermometer; 3 - manometer; 4 - rotameter; 5 - compressed air supply line of the bubble generator; 6 - parallelepiped water tank; 7 - oxygen meter probe; 8 - of fine bubbles generator with 17 orifices

The device of dispersing the air in the water flowing through a pipe will have the same number of orifices.

### 3.2 Aeration of water flowing through pipes

In this option, for the uniform and controlled introduction of air into the water, a flat spiral has been designed and built which is mounted inside the pipe.

The spiral follows approximately the shape of three circles with diameters of 16 mm, 26 mm, 36 mm and lengths of 50.24 mm, 81.64 mm and 113.24 mm, their total length is L = 244.92 mm.

As a result, the distance between two orifices will be:

$$l = \frac{L}{n} = \frac{244.92}{17} = 14.4\,m \tag{9}$$

A number of orifices will be placed on each circle:

$$n_1 = \frac{L_1}{l} = \frac{50.24}{14.4} \approx 3\,orifices \tag{10}$$

$$n_2 = \frac{L_2}{l} = \frac{81.64}{14.4} \approx 6\,orifices \tag{11}$$

$$n_3 = \frac{L_3}{l} = \frac{113.24}{14.4} \approx 8\,orifices \tag{12}$$

In total, there are 17 orifices of Ø 0.3 mm (figure 7).

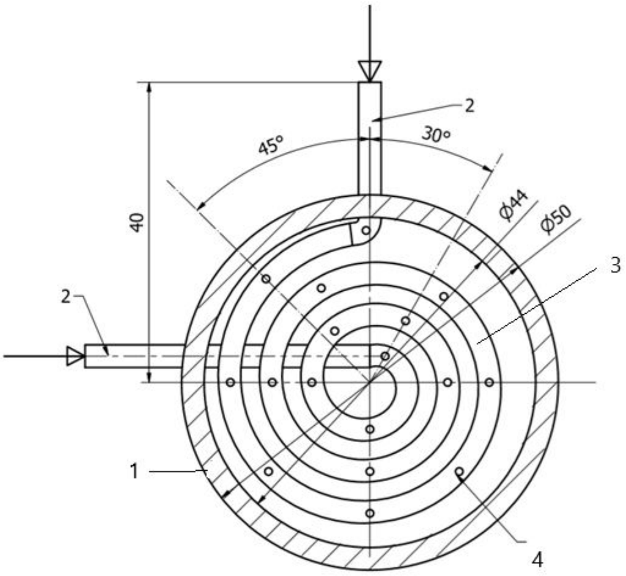

**Fig. 7.** Cross section through the pipe in the area where the spiral is located.
1- pipe Ø 50x3 mm; 2- compressed air inlet connections;
3- spiral; 4- orifices Ø 0.3 mm

The spiral is made of a capillary tube (figure 8) with an outer diameter of 3 mm and an inner diameter of 1 mm; the two conditions for placing the orifices presented above are verified:.

$$\frac{s}{d_0}=\frac{2}{0.3}=6.66>3 \tag{13}$$

$$\frac{d}{d_0}=\frac{6}{0.3}=20>8 \tag{14}$$

**Fig. 8.** Plan view of the spiral with 17 orifices Ø 0.3 mm

Figure 9 shows the experimental installation built for the purpose of measuring the dissolved oxygen concentration in water; the measurement is performed with the electrical or optical method [15].

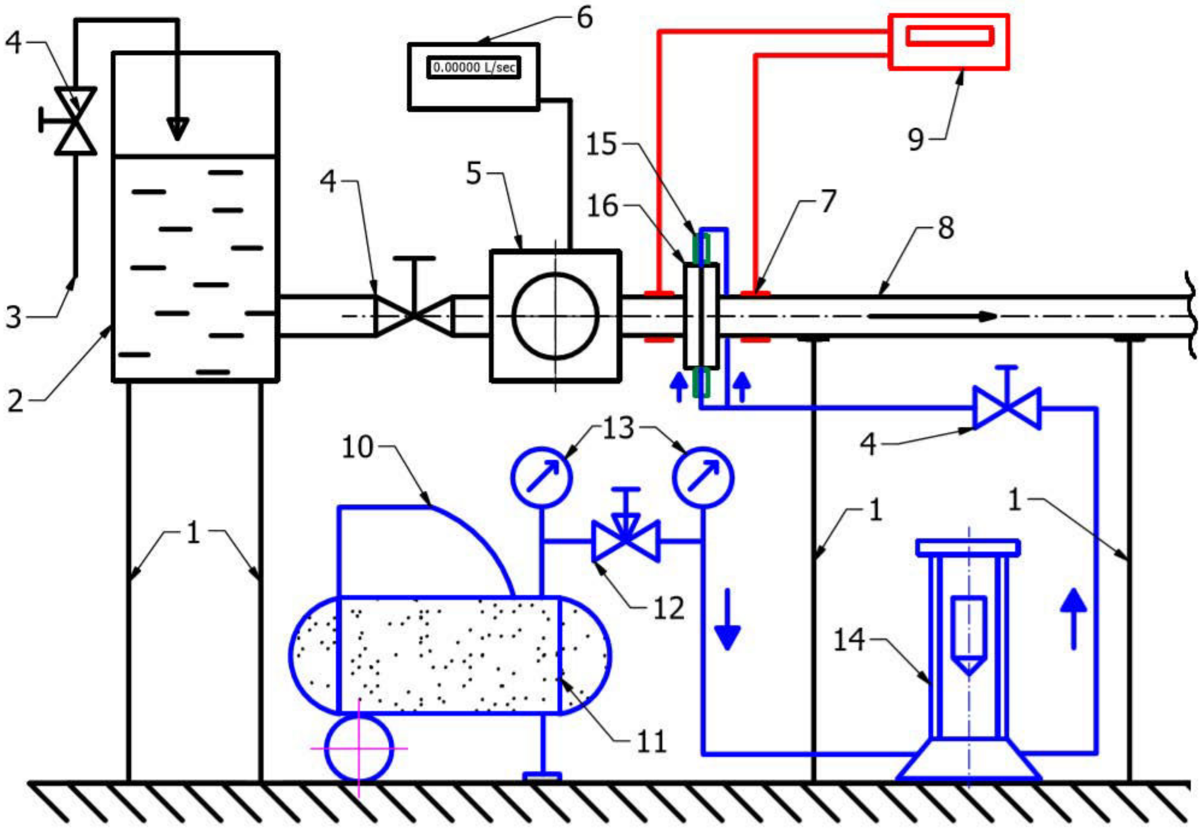

**Fig. 9.** Sketch of the experimental installation
1- supports; 2- water tank; 3- connection for mains water supply; 4- tap; 5- flow meter sensor; 6- flow meter with digital indication; 7- sensors for measuring the dissolved oxygen concentration in water; 8- transparent plexiglass pipe; 9- oxygenometer; 10- electro compressor; 11- compressed air tank; 12- pressure reducer; 13- manometers; 14- rotameter; 15- connection from the coil; 16- serpentine fixed between the flanges of the pipe.

For the flow rate measurement, a flow rate sensor with a Hall sensor was provided which sends 7.5 pulses at 1 $dm^3$ / min. The sensor sends a signal to an arduino microcontroller with a display; the controller shows the flow rate within an interval of one second and 5 seconds for greater accuracy.
Before and after the coil the dissolved oxygen concentration in water is measured using the oxygenometer.

## 4. Conclusions

1. The paper presents two constructive options of water aeration for stationary water and for water flowing through pipes.
2. Option 2 is more favourable because it removes the aeration tanks from the water treatment plants.
3. The experimental researches that will be presented in a paper published in 2020 will determine precisely which constructive solution is more favourable.

### Acknowledgments

This work was supported by a grant of the Romanian National Authority for Scientific Research and Innovation, CCCDI – UEFISCDI, project number Manunet – MNET17/ENER2307 – CEBIOTREAT, within PNCDI III.

## References

[1] Oprina, Gabriela. “Contribuții la hidro-gazo-dinamica difuzoarelor poroase.” PhD Thesis. Politehnica University of Bucharest, 2007.

[2] Mateescu, Gabriela Maria. “Hidro-gazo-dinamica generatoarelor de bule fine”. PhD Thesis. Politehnica University of Bucharest, 2011.

[3] Law, C.N.S., and B.C. Khoo. “Transport across a turbulent air-water interface.” *AICHE Journal* 48, no. 9 (2002): 1856-1868.

[4] Băran, Nicolae, Mihaela Călușaru, and Gabriela Mateescu. “Influence of the architecture of fine bubble generators on the variation of the concentration of oxygen dissolved in water.” *Buletinul Științific al Universității POLITEHNICA din București*, *Seria D, Inginerie Mecanică* 75, no. 3 (2013): 225-236.

[5] Tănase, Beatrice Elena. “Influența compoziției gazului insuflat în apă asupra conținutului de oxigen dizolvat.” PhD Thesis. Politehnica University of Bucharest, 2017.

[6] Marinescu, Mircea, et al. *Mass and heat transfer / Transfer de masă și căldură*. Bucharest, Politehnica Press, 2000.

[7] Chanson, Hubert. “Air-Water Interface Area in Self-Aerated Flows.” *Water Res* 28, no. 4 (April 1994): 923-929.

[8] Pătulea, Alexandru. “Influence of the functional parameters and the architecture of the fine bubble generators on the efficiency of the aeration systems” / “Influența parametrilor funcționali și a arhitecturii generatoarelor de bule fine asupra eficienței instalațiilor de aerare.” PhD Thesis, Politehnica University of Bucharest, 2012.

[9] Oprina, G., I. Pincovschi, and Gh. Băran. *Hydro-Gas-Dynamics of aeration systems equipped with bubble generators / Hidro-Gazo-Dinamica Sistemelor de aerare echipate cu generatoare de bule*. Bucharest, Politehnica Press, 2009.

[10] Dobrovicescu, Alexandru, Nicolae Băran, et al*. Elements of Technical Thermodynamics / Elemente de Termodinamică Tehnică*. Bucharest, Politehnica Press, 2009.

[11] Isbășoiu, E.C.Gh. *Handbook of Fluid Mechanics / Tratat de mecanica fluidelor*. Bucharest, AGIR Publishing House, 2011.

[12] Miyahara, T., Y. Matsuha, and T. Takahashi. “The size of bubbles generated from perforated plates.“ *International Chemical Engineering* 23 (1983): 517-523.

[13] Căluşaru, I.M. “Influence of the physical properties of the fluid on the efficiency of oxygenation processes” / “Influenţa proprietăţilor fizice ale lichidului asupra eficienţei proceselor de oxigenare.“ PhD Thesis, Politehnica University of Bucharest, 2014.

[14] Băran, N., Gh. Băran, and G. Mateescu. “Research Regarding a New Type of Fine Bubble Generator.“ *Revista de Chimie* 61, no. 2 (2010): 196-199.

[15] Pătulea, Alexandru, Ionela Mihaela Căluşaru, and Nicolae Băran. “Researches regarding the measurements of the dissolved concentration in water.“ *Advanced Material Research* 550-553 (2012): 3388-3394.

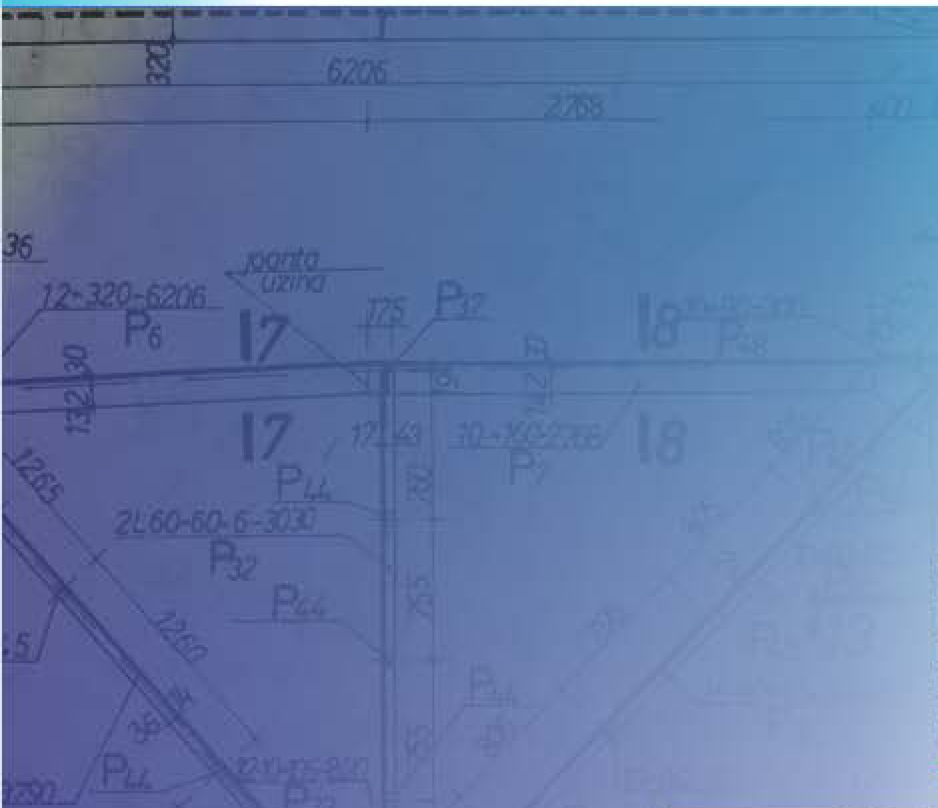

hidraulica.fluidas.ro